Task-Based Comparison of Parallel Translational Kinematic Structures

Aufgabenbasierter Vergleich von translatorischen, parallelkinematischen Strukturen

Von der Fakultät für Maschinenwesen der Rheinisch-Westfälischen Technischen Hochschule Aachen zur Erlangung des akademischen Grades einer Doktorin der Ingenieurwissenschaften genehmigte Dissertation

vorgelegt von

Isabel Prause

Berichter: Univ.-Prof. Dr.-Ing. Dr. h. c. Burkhard Corves
Prof. Dr.-Ing. Just Herder
Tag der mündlichen Prüfung: 14. November 2016

Diese Dissertation ist auf den Internetseiten der Universitätsbibliothek online verfügbar.

Acknowledgment

The present thesis was carried out between 2011 and 2015 as part of my research activities at the Department of Mechanism Theory and Dynamics of Machines (IGM) at Aachen University.

Foremost, I would like to express my sincere gratitude to my advisor Univ.-Prof. Dr.-Ing. Dr. h. c. Burkhard Corves for the continuous support of my Ph.D study and the freedom he gave me regarding topic and structure of my research. Besides my advisor, I would like to thank the rest of my thesis committee: Prof. Dr.-Ing. Just Herder for being the second referee and Univ.-Prof. Dr.-Ing. Robert Heinrich Schmitt for taking the chair.

Moreover, thanks to the chief engineer Prof. Dr.-Ing. Mathias Hüsing as an important and expert contact person for his advices and support and to the technical employees for helping me out with any problems regarding software, hardware, design and manufacturing. Special thanks are also due to all my students who made a significant contribution to the success of this thesis.

Many thanks to the institute management, the technical employees and all research assistants for the good working environment and the pleasant atmosphere at the department. I am very glad that former colleagues became friends over the past years and that we still meet for skiing, climbing or other fun activities. Thank you for being part of my life and for all professional and personal discussions we had and still have.

I will keep good memory of my time at the IGM and I am excited what the forthcoming years hold in store for me.

Last but not least, I would like to thank my family for their support throughout my life.

Bolton, May 2017

Isabel Prause

Summary

Well known is Clavel's DELTA robot, but there are other parallel kinematic structures (PKS) with three translational degrees of freedom. They differ in the assembly and the limb structure. A broad range of PKS based on different joint and limb arrangements has been synthesized in the past years, but only a small number has been further investigated in research.

Therefore, in this thesis, a structure catalog comprising different PKS with their respective characteristics is created. The selection is based on lists of previously synthesized PKS. Furthermore, different frame configurations are investigated. For in total 25 different PKS the structure catalog is expanded by mathematical descriptions.

In a first step, the kinematic dimensions are optimized with respect to two load cases: 1) rectangular workspace with low external forces and 2) cylindrical workspace with higher external forces. The results show that not all selected PKS possess good transmission qualities. Hence, some PKS are excluded from further analysis.

Then, a general research study of the selected structures is performed. Different dimensions of the PKS are considered and analyzed to identify the influence of selected parameter configurations on the overall performance. To do so, various criteria are applied within a prescribed workspace. This analysis and the comparison afterwards result in further reduction of the PKS for the final task-adapted dimensional synthesis. Three tasks and trajectories respectively are considered: pick & place, positioning and guidance task.

The optimization of the kinematic dimensions is based on a flexible objective function that allows adjusting the function value by including different criteria with adaptable weights. To select appropriate criteria, a compilation of criteria to measure, analyze and compare the performance of PKS is presented. Finally, the performance of the PKS along the trajectories or within the prescribed workspace is analyzed. The optimization and analysis results show that some of the selected PKS can fulfill the described tasks and that no "best" PKS can be found.

Zusammenfassung

Bekannt ist Clavels DELTA Roboter, aber es gibt noch andere parallelkinematische Strukturen (PKS) mit drei translatorischen Freiheitsgraden. Diese unterscheiden sich im Zusammenbau und im Aufbau ihrer kinematischen Ketten. Viele PKS, die auf unterschiedlichen Gelenk- und Gliedanordnungen basieren, sind das Ergebnis von Struktursynthesen der letzten Jahre. Allerdings wurde nur eine sehr geringe Anzahl davon tiefergehend in der Forschung untersucht.

Daher ist es das Ziel dieser Arbeit einen Strukturkatalog zu erstellen, in dem unterschiedliche PKS mit ihren entsprechenden Eigenschaften beschrieben werden. Die Auswahl basiert auf Listen von bereits synthetisierten PKS. Darüberhinaus werden unterschiedliche Gestellanordnungen untersucht. Für insgesamt 25 unterschiedliche PKS wird der Strukturkatalog mit mathematischen Beschreibungen erweitert.

In einem ersten Schritt werden dann die kinematischen Abmessungen hinsichtlich zwei unterschiedlicher Lastfälle optimiert: 1) rechteckiger Arbeitsraum mit geringen externen Kräften und 2) zylindrischer Arbeitsraum mit höheren externen Kräften. Die Ergebnisse zeigen, dass nicht alle PKS gute Übertragungseigenschaften aufweisen. Als Folge dessen werden einige PKS von einer weiteren Analyse ausgeschlossen.

Desweiteren wird eine allgemeine Untersuchung der ausgewählten Strukturen durchgeführt. Unterschiedliche Abmessungen der PKS werden betrachtet und analysiert um den Einfluss von der gewählten Parameterkonfiguration auf die Gesamtperformance zu identifizieren. Dafür werden verschiedene Kriterien innerhalb eines vorgegebenen Arbeitsraums angewandt. Diese Analyse und ein anschließender Vergleich führen zu einer weiteren Einschränkung der PKS, die für die finale, aufgabenangepasste Maßsynthese in Betracht gezogen werden. Drei Handhabungsaufgaben werden betrachtet: eine Pick & Place Aufgabe, eine Positionier- und eine Führungsaufgabe.

Die Optimierung der kinematischen Abmessungen basiert auf einer flexiblen Zielfunktion, bei der der Funktionswert durch entsprechende Gewichtung der Kriterien angepasst werden kann. Um geeignete Kriterien auszuwählen, wird eine vollständige Übersicht von Kriterien zum Messen, Analysieren und Vergleichen der Leistungsfähigkeit von PKS vorgestellt. Anschließend wird das Übertragungsverhalten der PKS entlang der Trajektorien oder innerhalb eines vorgegebenen Arbeitsraums analysiert. Die Optimierungs- und Analyseergebnisse zeigen, dass einige der PKS die Handhabungsaufgaben erfüllen können und dass es keine Struktur gibt, die als die „Beste“ bezeichnet werden kann.

Contents

Symbols and Indices **ix**

List of abbreviations **xvii**

1 Introduction **1**
1.1 Research issue and motivation 1
1.2 Structure of the thesis 5

2 Industrial robotics **7**
2.1 Serial robots in industry 7
2.2 Parallel robots in industry 9
2.3 Comparison of serial and parallel robots in the industrial environment . . . 12
2.4 Available software for dimensioning and design of robots 13

3 Selection and evaluation methods **15**

4 Structure selection **23**
4.1 Structural synthesis methods 23
4.1.1 Screw-based approaches 24
4.1.2 Displacement group theory 27
4.1.3 Single-opened-chain theory 28
4.1.4 Structural synthesis based on Gogu 29
4.1.5 Structural synthesis based on the DoF 29
4.2 Selection scheme 31
4.2.1 Selection based on Tsai and Neugebauer 35
4.3 Considered structures 36
4.4 Frame configurations 38
4.4.1 3R-1P 39
4.4.2 2R-2P 40
4.4.3 4R-1P 41
4.4.4 5R 42
4.5 Summary and final selection 42

5 Study on typical manipulation tasks 45
5.1 General requirements . . . 45
5.2 General manipulation tasks . . . 50
5.3 Description of selected manipulation tasks . . . 53
5.3.1 Handling (pick & place) . . . 53
5.3.2 Positioning (quasistatic positioning) . . . 53
5.3.3 Guidance (3D fiber injection plant) . . . 54
5.4 Reference structures from industry . . . 57

6 Derivation and implementation of calculation methods 61
6.1 Definition of parameters . . . 61
6.2 Calculation methods and models . . . 63
6.2.1 Kinematics . . . 63
6.2.2 Jacobian matrix . . . 63
6.2.3 Stiffness model . . . 64
6.2.4 Dynamics . . . 64
6.2.5 Multi-body simulation model . . . 65

7 Analysis and evaluation criteria 69
7.1 Compilation of relevant criteria . . . 69
7.1.1 Criteria based on the robotic structure . . . 69
7.1.2 Criteria based on the kinematic model . . . 70
7.1.3 Criteria based on the Jacobian matrix . . . 71
7.1.4 Criteria based on the stiffness model . . . 77
7.1.5 Criteria based on the dynamic model . . . 78
7.2 Final selection for further analysis . . . 80

8 First analysis and comparison of selected structures 83
8.1 General assumptions . . . 83
8.2 Optimization method . . . 86
8.3 Analysis procedure . . . 88
8.4 Results . . . 90
8.4.1 Geometrical parameters . . . 90
8.4.2 Workspace . . . 92
8.4.3 Performance . . . 92
8.5 Conclusion and summary . . . 94

9 General research study of selected structures 97
9.1 Methodology . . . 97
9.1.1 Bisection method . . . 99
9.1.2 Largest enclosed object . . . 101
9.1.3 Singularities . . . 103
9.1.4 Applied criteria . . . 103
9.2 Results and evaluation . . . 104
9.3 Discussion . . . 110
9.4 Conclusion and summary . . . 111

10 Task adapted dimensional synthesis 113
10.1 Preliminary studies . . . 113
10.2 Components and stiffness modeling . . . 115
10.3 Optimization concept . . . 122
10.4 Results . . . 125
10.4.1 Handling task (pick & place) . . . 125
10.4.2 Positioning task (quasistatic positioning) . . . 128
10.4.3 Guidance task (3D fiber injection plant) . . . 130
10.5 Evaluation . . . 131
10.5.1 Handling task (pick & place) . . . 132
10.5.2 Positioning task (quasistatic positioning) . . . 134
10.5.3 Guidance task (3D fiber injection plant) . . . 138
10.6 Detailed stiffness modeling . . . 139
10.7 Conclusion and Summary . . . 140

11 Summary and outlook 143
11.1 Summary . . . 143
11.2 Discussion . . . 144
11.3 Conclusion . . . 147

Bibliography 151

List of Tables 183

List of Figures 185

Figures 189

Tables **219**

Mathematical descriptions of PKS **229**

1 RRC . . . 229
2 CRR . . . 232
2.1 Δ configuration . . . 232
2.2 $\|$ configuration . . . 236
2.3 $\star$ configuration . . . 237
3 RPC . . . 240
4 CPR . . . 241
4.1 Δ configuration . . . 241
4.2 $\star$ configuration . . . 244
5 PRC . . . 248
6 UUP . . . 251
7 URC . . . 253
8 UCR . . . 254
9 UPU . . . 257
10 CRU . . . 260
10.1 Δ configuration . . . 260
10.2 $\star$ configuration . . . 263
11 PUU . . . 263
12 RUC . . . 266
13 CUR . . . 269
13.1 Δ configuration . . . 269
13.2 $\|$ configuration . . . 270
13.3 $\star$ configuration . . . 272
14 URU . . . 277
15 UUR . . . 278
16 RUU . . . 281

Index **285**

Symbols and Indices

Latin lowercase letters

$\mathbf{a}_i$	m	vector pointing to the first joint of limb i in R_0
$\mathbf{a}_1$	$\frac{\mathrm{m}}{\mathrm{s}^2}$	acceleration vector of link 1
$\mathbf{a}_2$	$\frac{\mathrm{m}}{\mathrm{s}^2}$	acceleration vector of link 2
${}^p\mathbf{b}_i$	m	vector pointing to end-effector joint of limb i (in R_p)
c_q	$\frac{\mathrm{m}}{\mathrm{N}}, \frac{\mathrm{rad}}{\mathrm{Nm}}$	compliance of actuator
$\mathbf{d}_0$	$-$	unit vector of prismatic/cylindrical joint axis
d	m	mean diameter
d_{ex}	m	outer diameter of cylinder
d_i	m	stroke length of prismatic/cylindrical joint
d_{in}	m	inner diameter of cylinder
$\dot{d}_i$	$\frac{\mathrm{m}}{\mathrm{s}}$	velocity of prismatic/cylindrical joint
$\ddot{d}_i$	$\frac{\mathrm{m}}{\mathrm{s}^2}$	acceleration of prismatic/cylindrical joint
e	$-$	unit vector
f	$-$	number of joints
f_q	N	actuator force
f_i	$-$	DoF of leg i
$\mathbf{f}_{EE}$	N	applied force vector
fi		fitness
g_h		function value of tested boundary condition
$\mathbf{g}$	$-, \frac{\mathrm{m}}{\mathrm{s}^2}$	auxiliary vector, gravity vector
h	$-$	pitch of the screw
$\mathbf{h}$		auxiliary vector

j	$-$	number of joints
k	$-$	number of identical objects
k_{at}	kg	acceleration capability
$k_{i,ax}$	$\frac{\mathrm{N}}{\mathrm{m}}$	axial stiffness
$k_{i,rad}$	$\frac{\mathrm{N}}{\mathrm{m}}$	radial stiffness
$k_{rot,x}$	$\frac{\mathrm{Nm}}{\mathrm{rad}}$	torsional stiffness about local x-axis
$k_{rot,y}$	$\frac{\mathrm{Nm}}{\mathrm{rad}}$	torsional stiffness about local y-axis
$k_{rot,z}$	$\frac{\mathrm{Nm}}{\mathrm{rad}}$	torsional stiffness about local z-axis
k_s	$\mathrm{kg}^{-3}\mathrm{m}^{-2}$	swiftness
k_{tilt}	$\frac{\mathrm{Nm}}{\mathrm{rad}}$	tilting stiffness
k_x	$\frac{\mathrm{N}}{\mathrm{m}}$	stiffness in local x-direction
k_y	$\frac{\mathrm{N}}{\mathrm{m}}$	stiffness in local y-direction
k_z	$\frac{\mathrm{N}}{\mathrm{m}}$	stiffness in local z-direction
lb		lower bound
l_b	m	distance between two single ball bearings
l_i	m	link length of link i
$\mathbf{l}_{k0i}$	$-$	unit vector of link k of limb i
m	kg	mass
n	$-$	number of objects resp. links
$\mathbf{n}$	$-$	vector of transmission axis
$\mathbf{p}$	m	position vector of end-effector
$\dot{p}$	$\frac{\mathrm{m}}{\mathrm{s}}$	absolute velocity value (applied at the end-effector)
$\dot{\mathbf{p}}$	$\frac{\mathrm{m}}{\mathrm{s}}$	end-effector velocity vector
$\ddot{\mathbf{p}}$	$\frac{\mathrm{m}}{\mathrm{s}^2}$	end-effector acceleration vector
$\mathbf{pw}$	W	power vector
q	m, °, rad	drive position
$\mathbf{q}$	m, °, rad	drive position vector

$\dot{q}$	$\frac{\mathrm{m}}{\mathrm{s}}, \frac{1}{\mathrm{s}}$	drive velocity
$\dot{\mathbf{q}}$	$\frac{\mathrm{m}}{\mathrm{s}}, \frac{1}{\mathrm{s}}$	drive velocity vector
r	m	position vector to point on screw axis
r_A	m	frame size (radius)
r_B	m	size of end-effector (radius)
ub		upper bound
s	–	singularity index
$\mathbf{s}_0$	–	unit vector of prismatic/cylindrical joint axis
s_i	m	stroke length of prismatic/cylindrical joint
$\dot{s}_i$	$\frac{\mathrm{m}}{\mathrm{s}}$	velocity of prismatic/cylindrical joint
$\ddot{s}_i$	$\frac{\mathrm{m}}{\mathrm{s}^2}$	acceleration of prismatic/cylindrical joint
t	m	thickness
v	$\frac{\mathrm{m}}{\mathrm{s}}$	linear velocity amplification
v_q	m/s	actuator velocity
$\mathbf{v}_{EE}$	$\frac{\mathrm{m}}{\mathrm{s}}$	applied velocity vector
w	–	weighting factor
$\mathbf{w}$	–	unit vector of rotational axis
$\mathbf{x}$	–	technical value
$\mathbf{y}$	–	economical value
z_{MS}	m	distance between reference frame R_0 and R_p

Latin capital letters

A	m^2	cross-sectional area of the link
C		constant value
C_k	–	connectivity
$\mathbf{C}$	$\frac{\mathrm{m}}{\mathrm{N}}, \frac{\mathrm{rad}}{\mathrm{Nm}}$	compliance matrix, matrix including all non-linear forces
E	$\frac{\mathrm{N}}{\mathrm{mm}^2}$	Young's modulus
$\mathbf{E}$	–	identity matrix
F	N	force amplification, force
$\mathbf{F}$	N	force vector
G	$\frac{\mathrm{N}}{\mathrm{mm}^2}$	shear modulus
$\mathbf{G}$	–	weighting matrix
$\mathbf{I}$	kgm^2	inertia tensor
$\mathbf{J}$		Jacobian matrix
$\mathbf{J}_d$		tolerance transmission matrix
$\mathbf{J}_h$		homogenized Jacobian matrix
$\mathbf{J}_p$		Jacobian matrix of force transmission
$\mathbf{K}$	$\frac{\mathrm{N}}{\mathrm{m}}, \frac{\mathrm{Nm}}{\mathrm{rad}}$	stiffness matrix
L	m	characteristic link length
$\mathbf{M}$	$\mathrm{kgm}^2, \mathrm{Nm}$	inertia matrix, torque vector
$\mathbf{N}_{ji}$	$\frac{\mathrm{m}}{\mathrm{N}}, \frac{\mathrm{rad}}{\mathrm{Nm}}$	compliance matrix of link j of limb i
O	–	origin
P	–	point
$\mathbf{R}$	–	rotation matrix
R_0	–	initial reference frame
R_p	–	end-effector reference frame
R_e	–	limb reference frame
\$	–	screw vector

S	–	unit vector along the axis of the screw
T	–	twist system
$\ddot{\mathbf{U}}$	–	transmission quality
W	–	wrench system
W_{pre}	–	Prescribed workspace
X	–	Benchmark value

Greek lowercase letters

α	$^\circ$, rad	geometric parameter
β	$^\circ$, rad	geometric parameter
δ	$^\circ$, rad	inclination angle
$\delta\mathbf{e}$	m	vector of length tolerances
$\delta\mathbf{p}$	m	positioning displacement (end-effector)
δq_i	m, rad	positioning error of drive i
$\delta\mathbf{q}$	m, rad	vector of positioning error (drives)
κ	–	condition number
λ	–	Eigenvalue, manipulability index, motion parameter
η	–	global dexterity index
ν	–	local dexterity index, sensitivity index
ϕ	$^\circ$, rad	rotation angle
ω	$\frac{1}{\mathrm{s}}$	angular velocity amplification, manipulability measure
$\boldsymbol{\omega}$	$\frac{1}{\mathrm{s}}$	angular velocity vector
$\dot{\boldsymbol{\omega}}$	$\frac{1}{\mathrm{s}}$	angular acceleration vector
ω_d	?	dynamic manipulability measure
ω_q	$\frac{1}{\mathrm{s}}$	angular velocity of actuator
ψ	$^\circ$, rad	inclination angle

ρ	$\frac{\mathrm{g}}{\mathrm{cm}^3}$	density
σ	–	singular value
τ	Nm	moment amplification
τ_q	Nm	actuator torque
$\boldsymbol{\tau}$	N, Nm	vector of actuator forces/moments
ξ	–	twist
ζ	–	wrench

Greek capital letters

$\Delta\mathbf{p}$	m	vector of end-effector displacements
$\Delta\mathbf{p}$	m	vector of actuator displacements
Θ	$^\circ$, rad	joint angle
$\dot{\Theta}$	$\frac{^\circ}{\mathrm{s}}$, $\frac{\mathrm{rad}}{\mathrm{s}}$	anglular velocity
$\ddot{\Theta}$	$\frac{^\circ}{\mathrm{s}^2}$, $\frac{\mathrm{rad}}{\mathrm{s}^2}$	anglular acceleration

Indices after symbols

c	kinematic condition
ext	external
EE	end-effector related
i	counter variable
int	internal
j	counter variable
m	counter variable
max	maximum
min	minimum

n	counter variable
p	position
q	actuator related
tot	total
T	transpose
T	workspace related
F	Frobenius norm
Φ	orientation
0	rotation (ξ), force (ζ)
∞	shift(ξ), coaxial moment (ζ)

List of abbreviations

BC	Boundary Condition
CAD	Computer Aided Design
C	Cylindrical joint
DoF	Degree of Freedom
GC	Geometrical Condition
IGM	Department of Mechanism Theory and Dynamics of Machines
IKV	Institute of Plastic Processing
MSA	Matrix Structure Analysis
PKS	Parallel Kinematic Structure
P	Prismatic joint
PI	Performance Index
R	Revolute joint
SOC	Single-Opened-Chain
TCP	Tool Center Point
U	Universal joint

1 Introduction

1.1 Research issue and motivation

Due to the growing trend of automation, the need for industrial robots increases. The sales within the last years with an average annual growth rate of 9 % prove this fact (Fig. 1.1). 70 % of all these sales arose in five countries: Japan, China, United States, South Korea and Germany. In 2012, 75 % of the sales in Germany were jointed-arm robots, followed by ∼14 % of portal systems and ∼9 % of SCARA robots. Only 1.4 % of the sales were generated by parallel robots. Nevertheless, the development of parallel robots with given motion characteristics and less than six degrees of freedom (DoF) attracted a lot of interest in fundamental research [FT02; FT04; HL02; HL03; JY04; KG04b]. These robots are characterized primarily by a simpler structure containing less limbs and drives and consequently they are cheaper to manufacture [CP03a; FT04; HL01; HL03; LHH04].

For example, many 3-DoF mechanisms have already been developed: structures with pure translational (e.g. DELTA (3-RPS), Tsai's (3-UPU)) or pure rotational motion, as well as structures with one translational and two rotational DoF [CP03a; HL01; HL03]. Even structures with four or five DoF can be found in the field of research and industry, e.g. [Tri14; Nef10]. But the synthesis of parallel manipulators with less than six DoF and good structural properties was performed unsystematically over a long period of time.

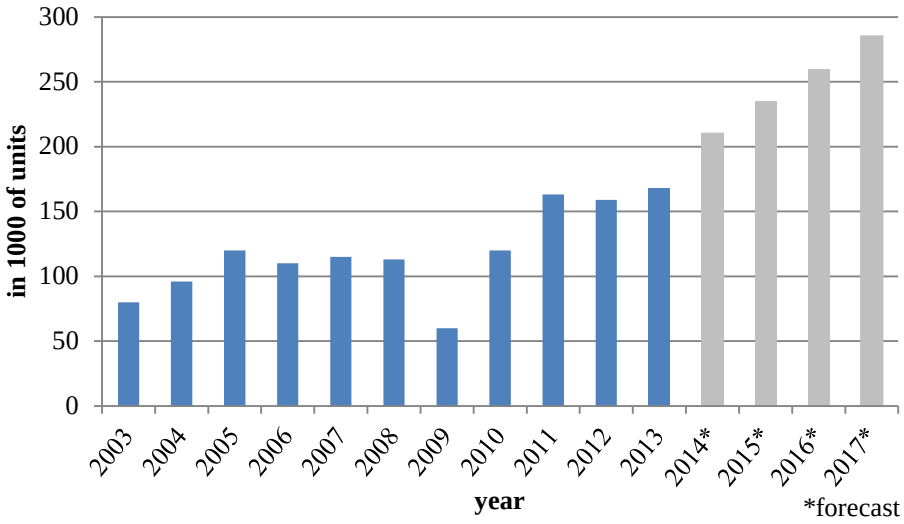

Fig. 1.1: Worldwide annual supply of industrial robots [IFR14]

Therefore, at the beginning of this century the emphasis was placed on the development of methods allowing the synthesis of new parallel kinematic structures with less than six DoF [Gog09; HL01; KG07]. Mainly, a symmetrical design, i.e. with identical limbs (kinematic chains), and the coverage of all possible joint combinations were envisaged [HL02]. Hence, the development of new kinematic chains for the limbs can lead to an expansion of structure types with possibly higher performance [JY04]. However, only a small number of the synthesized structures have been further investigated in research; an even lower number is industrially implemented. Well known is Clavel's DELTA robot, but are there any other parallel manipulators suitable for specific tasks?

This raises further questions:

- What are possible parallel kinematic structures and how do they differ, i.e. what are their characteristics?
- Can their suitability for special handling tasks be derived based on their characteristic properties?

In order to answer these questions, a selection of structures should be made first (Chapter 4), so that within the scope of this thesis, due to the high amount of possible parallel kinematic structures (PKS), only a subset of PKS will be addressed: those that have three translational DoF and a symmetrical assembly with three limbs (Section 4.3). The aim is to create a structure catalog comprising different PKS with their respective characteristics and to compare these structures with regard to their properties by metrics. First, the different structural synthesis methods must be examined further (Section 4.1) and the structures that already have been synthesized need to be classified (Section 4.3 and 4.4). Then the structure catalog should be expanded by mathematical descriptions (Chapter 6) so that a comparison of the structures with one another is possible, also with regard to already industrially implemented robots (Chapter 2). Here, a comparison based on metrics should be used. Referring to this, some comparisons of different structures were already carried out in the last 20 years, as the following examples show.

McCloy [McC90] compares a planar serial with two planar parallel kinematic structures: the serial structure RR and the parallel structures RRRPR as well as RRRRR. The analyzed criteria are the size of the workspace, the required performance of the actuators, as well as the stiffness of the structure, assuming all limbs except the drives as ideally rigid. For a comparison of the different structures, a global task is defined. A common type of load is selected and the presented criteria are finally combined to a general performance criterion. Gosselin [GRN95] compares different parallel manipulators with six DoF based on their workspace and kinematic properties. The translational and rotational workspaces as well as the stiffness properties of the structures are used as evaluation criteria. To carry

out a comparison, the structures are normalized by the definition of a maximum actuator load for each actuator. Tsai [TJ01] performs a comparison of four parallel manipulators with three translational DoF. These include the 3-RUU, the 3-UPU, the 3-PUU (with intersecting rails) and the 3-PUU (with parallel rails) manipulator. A dimensional synthesis is executed in terms of the maximum, however, well-conditioned workspace. The rigidity of the structures, as well as the mass inertia properties are also considered. To a great extent none of the analyzed structures is better than the others. Only the 3-PUU manipulator with intersecting rails shows a generally good, balanced performance. A similar approach can be found in [JT03]. The aim here is the comparison between two PKS with three DoF, of which one has three, the other four limbs. The optimization of a well-conditioned workspace using the global conditioning index is the most important criterion. Furthermore, a comparison of stiffness properties, based on stiffness matrices, derived from the virtual work, is carried out. In [GMD07] a general set of benchmark criteria is created. The following criteria are included: the ratio of workspace to installation space, the stiffness (determined by measurements), the smallest occurring natural angular frequency (determined by experiments), as well as the maximum possible acceleration of the end-effector, considering that any actuator has the same motion pattern. In [GMD07] parallel manipulators from the Multipteron family, i.e. the Tripteron [KG02] and the Quadrupteron [RGK06], are compared. In case of both structures, forward and inverse kinematics are independent of the link lengths. Thus, the transmission behavior of the end-effector is not influenced by manufacturing tolerances of the links.

However, these examples show that a comprehensive comparison of different parallel kinematic structures is missing. Furthermore, it becomes clear that such a comparison raises problems: not only that diverse criteria may be relevant for a certain task (Chapter 7), but the PKS must also be adapted to the respective performance features of the defined task [TJ01] (Section 5.3). Thus, the following research questions arise:

- How can parallel kinematic structures be compared in a coherent and comprehensive way?
- Which criteria allow the description, analysis and comparison of PKS?

For such comparison, it is necessary that the PKS are completely described. This requires different calculation methods (Chapter 6). The forward and inverse kinematics, dynamic and stiffness models, or even multi-body simulation models are among the important calculation procedures. Furthermore, the Jacobian matrix as a structure describing matrix is important. To expand the structure catalog with appropriate information, it must be identified which of these calculation procedures were already derived and implemented for various structures and where gap filling is necessary (Tab. 6.1). If possible, the mentioned calculation procedures should be generalized so that they can be applied to other struc-

tures easily. Once the mathematical descriptions of the structures are completed (annex, 11.3), for example, the distribution of certain properties over a prescribed workspace can be determined.

A further challenge is to determine the optimal kinematic dimensions for the structures, i.e. to perform a dimensional synthesis [GGZ96; Mer97; LW07; LWK06] (Chapters 8 and 9). To fulfill all requirements imposed on the mechanism, a parameter configuration (including link lengths) must be selected in such a way, that the structures have good properties with regard to various criteria (e.g. transmission behavior) over a wide range (e.g. workspace) [TTE95] (Section 9). Different performance characteristics highly depend on the selected parameter combination and are often contrary (Chapter 7). In many cases, for example, a large workspace with respect to the link lengths is desired [RR01; BG99; TTE93]. However, the problem of unwanted properties, such as poor transmission quality at certain points within the workspace, faces maximizing the workspace. Thereby, one more question comes up:

- How to find the “optimal” parameter settings?

First of all, the requirements that play an important role in the design must be defined so that not only from a technical perspective (e.g. max. actuator forces or torques respectively), but also from an economic point of view (e.g. costs) an optimal solution and configuration can be found (Chapter 5).

For practical relevance it is necessary to define typical manipulation tasks (Section 5.2). This includes the analysis of trajectories and specific requirements. If these requirements are known, valuable boundary conditions for the dimensional synthesis can be applied (e.g. Section 8.2 or 10.3). Further design boundaries result from the used components, e.g. drives, joints or links (Section 10.2).

Since not all PKS are suitable for all tasks, a preselection should be performed before starting with the dimensional synthesis (Section (4.2)). So, the number of PKS and the calculation costs are reduced. This preselection can be based, for example, on pre-calculated indicators (Chapter 9). But,

- how to define and calculate such indicators?

1.2 Structure of the thesis

The work in hand is organized as follows. Chapter 2 gives a brief overview of industrial robots. Serial and parallel robots are compared regarding their characteristic properties. The last part of this chapter includes a summary of available software for dimensioning and designing robots.

Since evaluation and benchmark procedures are important for this thesis, common methods are shortly summarized in Chapter 3. In Chapter 4 general type synthesis methods are described and possible structure configurations are presented. Afterwards, a selection scheme is introduced allowing to reduce the number of considered structures. Furthermore, the remaining PKS are presented with regard to different frame configurations.

A study on typical manipulation tasks follows in Chapter 5. This includes not only the compilation of typical manipulation tasks but also their analysis. The obtained results enable the creation of requirement profiles used for the further analysis of the considered structures.

To analyze and compare the selected PKS, relevant analytic calculation models such as inverse kinematics and dynamics, Jacobian matrix or stiffness models, have to be derived and implemented. The procedures are described in Chapter 6. Thereafter, Chapter 7 summarizes, analyzes and reviews relevant evaluation criteria for robotic structures. A part hereof will be used in the further course of this thesis. A first analysis and comparison of the selected PKS is carried out in Chapter 8. As a result, the number of PKS, which are suitable for different manipulation tasks, can be reduced further. In this way the selection scheme of Chapter 4 is extended.

In Chapter 9 a general research study of the selected structures is performed. Since the performance highly depends on the selected parameter configuration, different dimensions for the PKS are considered and analyzed. Based on a prescribed workspace inside the reachable workspace various criteria are applied. Afterwards, important and meaningful criteria are selected in order to perform a task-adapted dimensional synthesis and optimization in Chapter 10. An evaluation and benchmark study for the final selection of PKS is also included in this chapter.

Finally, Chapter 11 concludes with a short summary of the obtained results and gives an outlook on further research. The main parts of this thesis are illustrated in Fig. 1.2.

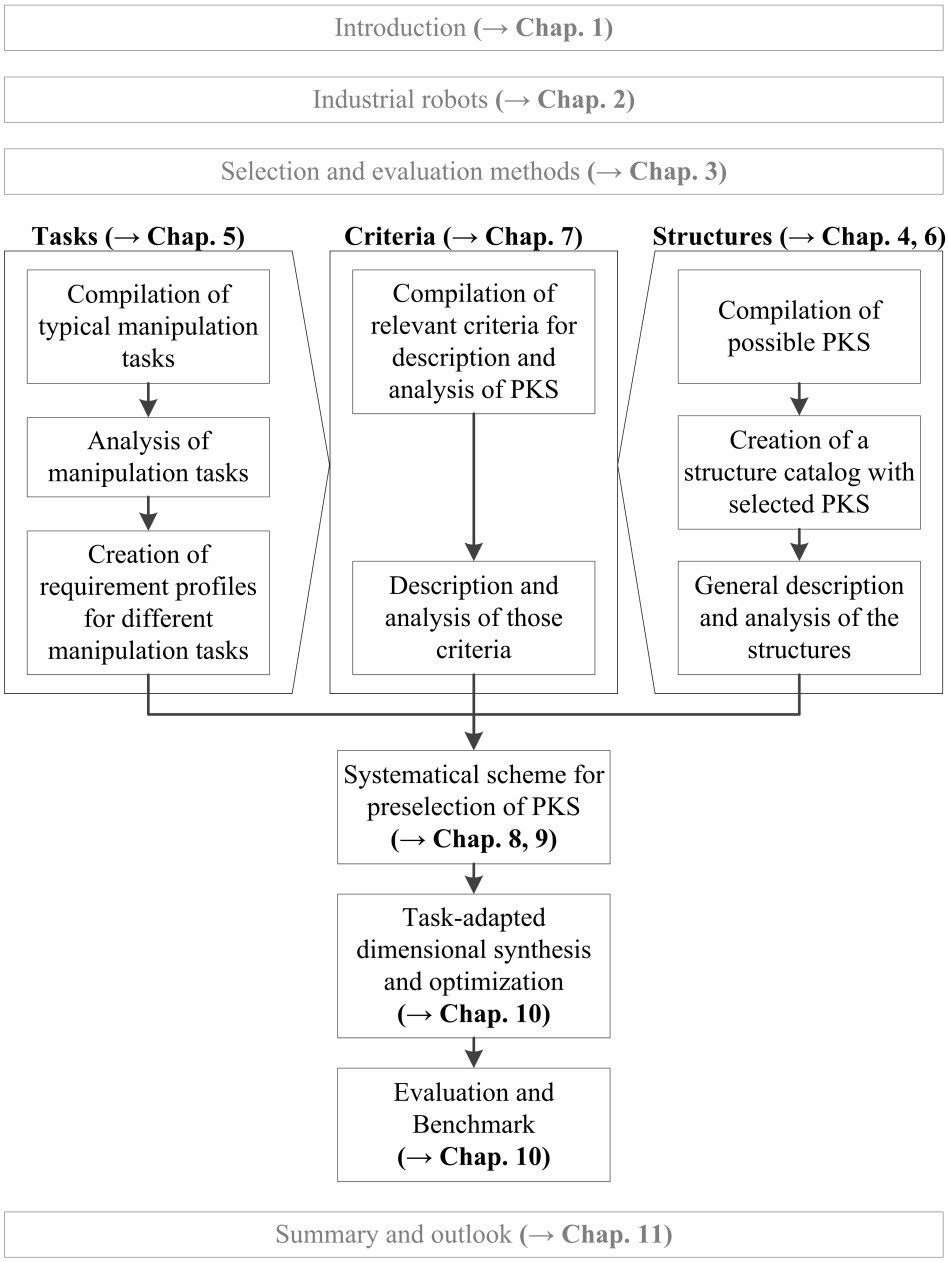

Fig. 1.2: Main structure of this thesis

2 Industrial robotics

According to DIN 8373 [DIN8373] a robot is an *"operated mechanism programmed in more than one axis with a certain degree of autonomy that moves within its environment to perform given manipulation tasks"*. Also the definition of a manipulator or handling device can be found in the same norm: *"Machine, of which the mechanism consists of a sequence of components connected by joints or displaceable to each other with the purpose to grasp and/or move objects (workpieces or tools) usually with several DoF"*. To perform very different tasks in the industrial environment, various types of robots are used. These include not only serial, but also parallel kinematic robots.

2.1 Serial robots in industry

The following paragraph describes the properties of the most frequently used serial structures in industry. Examples of serial robots are the vertical as well as horizontal jointed-arm robot and the portal structures (Cartesian robot). They are characterized by an open kinematic chain. This means that multiple links lined in series are connected together by (revolute) joints. On the one hand advantages of serial structures are their large workspace and their easier control. However, on the other hand disadvantages are high mass inertia due to carried actuators, lower stiffness, as well as the accumulation of drive errors on the end-effector in contrast to parallel kinematic structures [Neu06; Tsa99].

The vertical jointed-arm robots with DoF from three to six are an important representative of this group (cf. Fig. 2.1). Such robots consist of a regional structure and a local structure, each with three DoF. The latter is responsible for positioning, the regional structure for orientation of the object. The bandwidth of this robot type is listed in Tab. 2.1. Examples are: the Neuronics Katana 450 6M180 [Neu14] allowing a "*harmless collaboration with people*" with a payload capacity up to 0.4 kg and a weight of only 5.2 kg due to its lightweight design, as well as the KUKA KR1000 titan – which is (according to the manufacturer [KUK14]) the "*strongest and biggest 6-axis robot, which is available on the market*". With a weight of almost 5000 kg, this robot can handle a load of up to 1000 kg. Applications of this type are found in the automotive, foundry and construction material industry, where large and heavy work pieces must be handled.

		self weight [kg]	payload [kg]	accuracy [mm]	range [mm]
vertical jointed-arm robot	min	5.2	0.4	0.01	500
	max	5000	1000	0.5	3300
horizontal jointed-arm robot (SCARA)	min	2.7	0.5	0.01	250
	max	2710	300	0.2	2350
Cartesian robot	min	25	4	0.01	2500
	max	2500	6000	1	50000

Tab. 2.1: Properties of serial robots (extrema)

The scope of vertical jointed-arm robots is highly diversified, because they are available in any size and performance class. Due to their universal design with six DoF, vertical jointed-arm robots are suitable in many areas for a variety of different tasks. These robots are integrated in production processes starting from material application (e.g. spraying, coating, painting), and inserting or removing of work pieces of tool machines, stoves, bathes (e.g. put cast parts in quench bath) or the conveyor belt up to simulation of motion (e.g. stress testing of car seats). Requirements imposed on automation technology are high accuracy, short cycle times and high speed as well as a most compact design so that the installation space can be kept as low as possible [KUK14; Stä14].

A horizontal jointed-arm robot, called SCARA robot, has up to four DoF (translational motion in all Cartesian directions and rotation about the vertical axis of the end-effector). For this type there exists a wide range of payloads as well. The IX-NNN2515 [IAI14] should be mentioned here as an example. The robot has a weight of 17 kg with a maximum lifting capacity of 3 kg (see Fig. 2.1). Applications are pick & place or even packaging tasks in the food industry, just to name a few. In contrast, the Reis RH300 [Rei14] has a payload capacity of 300 kg with a self-weight of approximately 2700 kg.

Portal systems may provide 1-6 DoF and consist of several linear axes. Due to variable motion capabilities and adaptable size, many different applications are possible.

To sum up and to give an overview of the characteristics of the different systems, the

Fig. 2.1: Serial robots in industry - vertical jointed-arm [KUK14] (left), horizontal jointed-arm [Mit14] (middle), portal system [Yam] (right)

	DoF	self weight [kg]	payload [kg]	accuracy [mm]	range [mm]
vertical jointed-arm robot	3-6	127	10	0.05	1400
horizontal jointed-arm robot (SCARA)	4	40	5.5	0.02	600
Cartesian robot	1-6	-	-	0.1	5500

Tab. 2.2: Properties of serial robots (median values)

median values of the SCARA robot, the vertical jointed-arm robots, as well as the Cartesian systems are listed in Tab. 2.2. The data is based on information provided by robot suppliers (cf. supplier websites).

2.2 Parallel robots in industry

Among the types of parallel robots, the DELTA robot is the robot used most often for pick & place tasks in the industrial environment (cf. Fig. 2.2, right). By means of hygienic design (often even clean room suitability) in food industry, any kind of cold cuts, meat or sweets coming from a conveyor belt can be placed into the corresponding boxes. Due to specially developed grippers, also several products can be handled at the same time (a compilation is made in [Ruc13]). But also in the electrical and solar technology or in areas of general mechanical engineering DELTA robots are used for pick & place or assembly tasks.

Moreover, the DELTA robot exists in a smaller version. The company Asyril/Frei-Technik [Asy14] has focused on its development. The company's portfolio includes three different types: the PocketDELTA, the DesktopDELTA and the PowerDELTA (cf. Fig. 2.2, left). These structures are used specifically for tasks where the payloads are negligible - the

Fig. 2.2: DELTA robots - PocketDELTA [Asy14] (left), Adept Quattro [Ade14] (middle), ABB Flex Picker [ABB14] (right)

Fig. 2.3: Parallel robots in industry - Hexapod [PI14] (left), Festo Tripod [Fes14] (middle), Tricept [Tri14] (right)

majority of energy is needed for the movement of the structure itself. Tasks include, for example, precise assembly of micro parts as well as fast movement of those parts.

A further development of the DELTA robot is the Adept Quattro (see Fig. 2.2, middle) [Ade14]. This robot has basically the same structure as a DELTA robot, but with four legs. The robot is designed for high speed applications in the packaging and solar industries. Also payloads of 15 kg can be handled with high precision.

The Hexapod is a parallel kinematic robot with six actuated limbs and therefore, it possesses six DoF. The structure of a Hexapod is shown in Fig. 2.3, left. A rotation of 360° of the end-effector can be realized by special design (cf. [Mik14]). Not only Hexapods, but also other parallel kinematic robots are characterized by the following features and advantages in contrast to their serial counterparts:

- low moving masses of the end-effector,
- high stiffness,
- handling and positioning of high payloads (especially the Hexapod),
- high resonance frequency,
- no dragged cables,
- low installation space.

Different application fields can be derived on the basis of these characteristics. In electronics or in machine tools micro- or even nano-positioning systems are needed [PI14] for precise control.

Furthermore, for example, telescopes require positioning systems for high loads. Thanks to its six DoF, a Hexapod is able to perform simulation tasks: as a flight simulator or in the field of biomechanics for the simulation of joint movement or as an earthquake simulator [Qua14]. In contrast, the F-200iB Fanuc is used for tasks, when high forces are needed [Fan14]. These do not only include machining, deburring or cutting, but also drilling or welding tasks. The latter is combined with a special end-effector. The Hexapods of Moog

		self weight [kg]	payload [kg]	accuracy [mm]	height workspace [mm]	range [mm]
DELTA	min	3.3	0.02	0.002	150	150
	max	160	20	0.2	1600	
Hexapod	min	8	5	0.0002	7	13
	max	550	15000	0.1	508	1200
Tripod	min	0.4	0.5	0.01	10	20
	max	3400	2000	0.2	700	3000

Tab. 2.3: Properties of parallel robots (extrema)

	DoF	self weight [kg]	payload [kg]	accuracy [mm]	height workspace [mm]	range [mm]
DELTA	3-4	115	3	0.1	300	1130
Hexapod	6	190	95	0.002	54	101
Tripod	3-5	-	-	0.035	200	1200

Tab. 2.4: Properties of parallel robots (median values)

CSA Engineering [Moo14] are specialized, among others, on vibration insulation. In this context the Hexapod is used for camera stabilization or to protect fragile goods during transport.

A parallel kinematic robot with three legs is called Tripod. However, the structure is not thereby defined. An example is the ABB FlexPLP Tripod [ABB14], characterized by a high degree of stiffness and by handling of large loads (30 kg). Therefore, applications for these robots are the positioning of large, heavy objects (e.g. car) in floor or ceiling mounting for both, packaging and palletizing tasks. The Festo Tripod has a different design (Fig. 2.3, middle) [Fes14]. It works similar to the DELTA robots for pick & place tasks, for adhesive application or also for palletizing and sorting tasks. This structure has a maximum working load of 5 kg.

Another parallel manipulator with three legs is the Tricept (see Fig. 2.3, right). This robot achieves five or six DoF by an additional end-effector. Its structure is adapted to the requirements of the handling of different geometries in combination with a high degree of stiffness. Especially for tasks that require high forces in the direction of gravity, the use of the Tricept has advantages. This is the case, for example, for friction stir welding, in which the tool must be kept against the material or for deburring, which requires high cutting forces without reduced accuracy [Tri14].

To sum up, the median and extremal values of the industrially used parallel robots are listed in Tab. 2.3 and 2.4 so that an overview of their characteristics is given. The data is based on information provided by robot suppliers (cf. supplier websites).

2.3 Comparison of serial and parallel robots in the industrial environment

Some comparisons regarding the properties of the above-mentioned structures should be made. Thereto, different available data sheets of the robots are taken into account. The maximum possible payload is plotted against the respective self-weight of different industrial robots in Fig. 2.4. Both, serial (vertical + horizontal jointed-arm robots) and parallel kinematic robots (DELTA robots, Hexapods) are considered. For better clarity a logarithmic scale on the axes is selected.

Especially vertical jointed-arm robots and Hexapods have a relatively high self-weight, but they can also carry high payloads. Hexapods can achieve payload/self-weight ratios even greater than 1, which is primarily due to their structural design. While Hexapods in average have a relatively high payload capacity of 95 kg, the payload of vertical jointed-arm robots varies, depending on the application, between 0.4 and 1000 kg and is 10 kg on average.

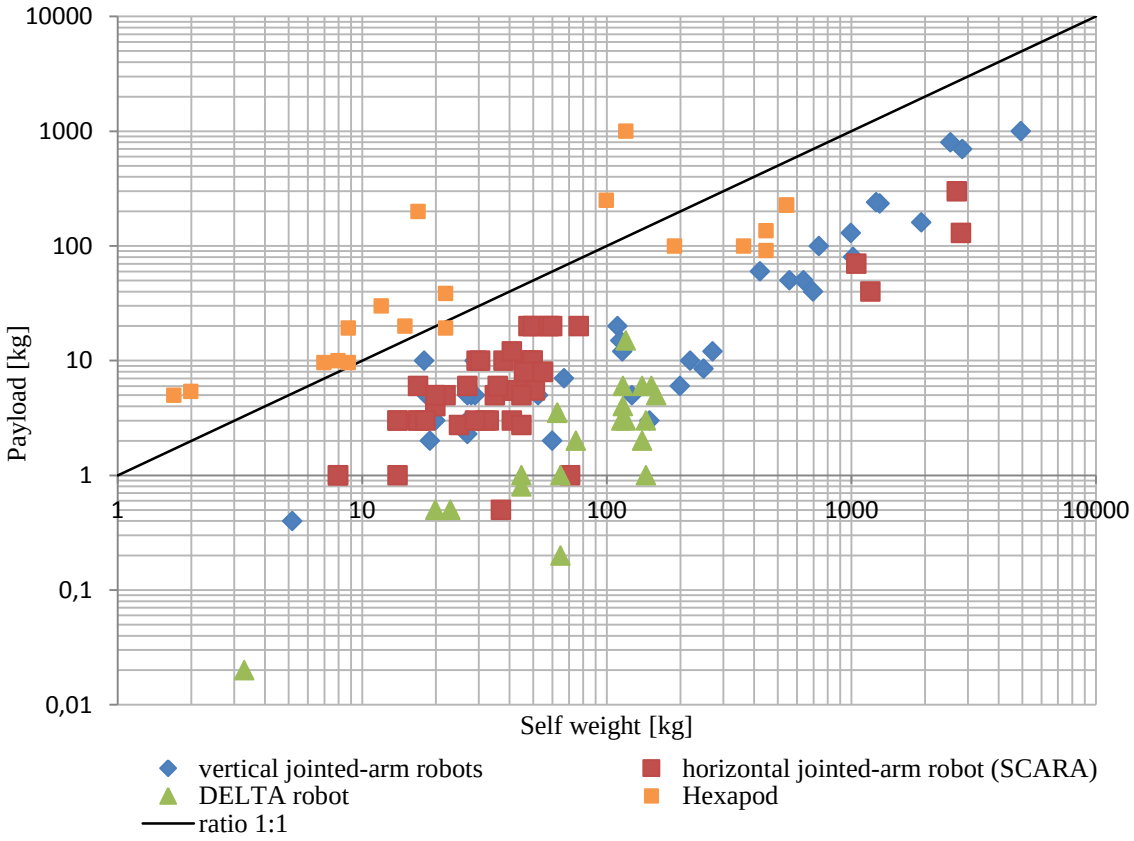

Fig. 2.4: Overview of self-weight/payload ratio of industrial robots

A more accurate comparison between serial and parallel robots can be made between the SCARA robot and the DELTA robot, since both types are used for pick & place tasks. With the same payload capacity DELTA robots tend to be somewhat heavier (median: 115 kg) than SCARA robots (median: 40 kg), because for DELTA robots the actuators are mounted on the fixed frame and do not have to move with it – such as for the SCARA robot. So the actuators may also be correspondingly heavier. The medial payload of the SCARA robots is at 5.5 kg, while for the DELTA robots it is at 3 kg only. A detailed technical and economic evaluation between a SCARA and a DELTA robot is performed in [Sch13]. The results show that the differences between the two robots are marginal – the performance of a SCARA is comparable with that of a DELTA.

2.4 Available software for dimensioning and design of robots

Available software can be divided into software for dimensioning and path planning, software for simulation and factory planning and software for control and programming. A representative of the first group is the software Cymex® [Wit14b]. It is a software for the dimensioning and analysis of complete power-trains, where common applications are already predefined. When choosing the required components the product catalog of Wittenstein AG is assessed. With the help of the software, the user receives more confidence in dimensioning by making him aware of performance potential and, where appropriate, he can reduce the cost by selecting smaller gears.

Software for simulation and factory planning is provided by almost every robot supplier. For example, ABB's software [ABB14] tends to improve processes and to optimize productivity. Furthermore, software for KUKA robots [KUK14] is used for implementation and application. The software includes, for the most common handling tasks, tools to simulate, plan and optimize production processes. EASY-Rob™ [Eas14] is a tool for the simulation of robots. It mainly serves the planning of production and manufacturing processes to check accessibilities, to detect and avoid collisions in advance and to reduce the implementation time. The software CIROS [CIR14] of Festo and the Technical University of Dortmund shall enable inexperienced users the entry into the automation technology. Mechatronic systems are shown in a virtual environment. To save costs new processes can be simulated and analyzed. The planned processes and motion trajectories can be transferred to the real controllers after successful and safe simulation.

With control and programming software, production processes can be simulated and thereafter transferred to the robotic system (for example [Fan14; Fes14; Stä14]).

In collaboration with CAE Electronics Ltd., the Robotic Institute of the University of Laval (Québec, Canada) has developed a software for the design, analysis, and visualization of flight simulators (Hexapod). The user can interactively change the geometric parameters (such as distance of the legs to each other, max. stroke length, etc.) while at the same time, the change of workspace, singular positions or other properties of the robot are graphically shown. In addition, the modification of mass and inertia properties is possible. Thus, the user receives a feeling for the properties of the robotic structure. Furthermore, trajectories can be implemented by which the movement of the robot can be simulated. At the same time the required actuator forces are calculated. The software is not only limited to the Gough platform with six DoF, but also contains analysis capabilities for a planar parallel manipulator with three DoF, as well as a serial structure.

Matlab codes can be found on the website of [Bon14], which deal with parallel manipulators. Scripts for calculation and displaying singularities can be downloaded for symmetrical parallel manipulators with three DoF, for simulation of the planar 3-RRR and the simulation of spatial 6-PUS parallel manipulators.

QSpider [QSp16] is a software for modeling of mechanical systems (e.g. parallel manipulators). The program's main function is the parameterization of models. Currently, only the motion of two types of robots is possible: of a Tripod and a serial kinematic structure. A variation of parameters is possible (e.g. changing limb lengths, masses) and the robot can be moved by using the pan function. Achieving the boundary conditions (e.g. maximum stroke length) will be displayed to the user by coloring the respective components.

In conclusion, a large part of available software is highly specialized for industrial applications and implementations. The software solutions aim for raising cost awareness, performance potential or reduced implementation time amongst the users. They tend to facilitate even unexperienced users the access to robotic and automation systems. But the examples show that since most of the software is driven by industry, it is limited to industrial available robots. Only a few attempts by academia focus on the design and analysis of different robotic systems, including parallel robots. But a comprehensive software tool for analyzing and comparing different PKS and selecting a suitable design is missing.

3 Selection and evaluation methods

In principle an evaluation is possible after each step within a design and development process. It serves to develop only the most promising solutions. There are various evaluation methods that can be applied depending on the technical maturity and complexity of the present solutions. These methods are divided into four groups (cf. Fig. 3.1) according to the affordable time and effort (low, middle, higher, very high). Methods allowing weighting of different criteria are included in the following descriptions.

For the **argumentative balance sheet** arguments (for every individual variant to be evaluated) are sorted in a table according to advantages and disadvantages [PBG07; BK97]. It is a quick procedure that can be performed in less than an hour. The advantage of this method is characterized by the fact that the criteria are not quantitatively described, nor weighted or adjusted. This evaluation is, however, less accurate compared to other methods. It is also not suited for assessing complex variants.

The **selection list** is based on the recommendation of [PBG07]. Only those solutions will be developed, which

- are compatible with each other and/or with the task (A),
- fulfill the list of requirements (B),
- are realizable (C), and
- can expect an acceptable effort (D).

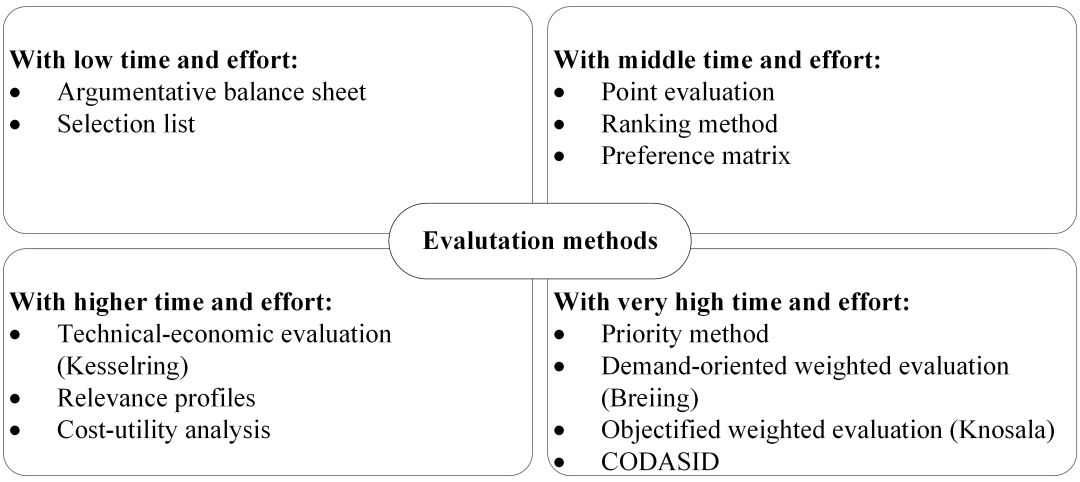

Fig. 3.1: Evaluation methods with regard to time and effort

The solutions to be evaluated are listed and are evaluated one by one with the above mentioned criteria. If the first two criteria (A, B) are not fulfilled, the solution is directly eliminated. For the assessment of criteria C and D the scope of discretion is quite high, so the following two criteria can be used in addition:

- direct security technology or good ergonomic conditions are feasible (E),
- a variant appears more feasible (e.g. by well-known expertise, known materials or work procedures) (F).

Especially if from many solutions a selection should be made for further development or more accurate assessment, the selection list is a suitable and quick procedure. Only those solutions are considered as worth prosecuting, which meet all criteria.

The **point evaluation** is not only suitable for technical, but also for economic evaluation. However, it must be noted that the criteria are not divided into groups and no cleanup of the criteria is carried out. The point evaluation takes about a day and can be used for evaluating solutions of medium complexity. Each variant is evaluated based on each criterion by points, which are summed up afterwards. The choice of scale is arbitrary. A point distribution from 0 to 4 is recommended according to VDI 2225 [VDI2225] or from 0 to 10 based on the cost-utility analysis. The maximum number of points is the best rating, i.e. the best possible compliance with a criterion. If the criteria should be weighted differently, their point values can be multiplied with the respective weighting factors.

The **ranking method according** to Wenzel, Müller and Gutsch [BK97; PBG07] is especially suitable for fast determination of weighting factors and thus the assessment of variants of low complexity within the concept phase. It should be pointed out that no absolute significance can be determined. The criteria (of similar extent) are compared pairwise in a table. The comparison takes place via blanket judgments and by the mark “+”, “-” and “o”. The weighting factor is determined by the frequency of the judgments:

$$w_i = \frac{100\%}{\sum w_+} \cdot \sum +_i. \tag{3.1}$$

Then, the previously determined points (e.g. with the help of scoring) are weighted with the respective weighting factors.

The **preference matrix** is suitable as ranking method especially for variants of low complexity and for weighting of criteria. A pairwise comparison of the criteria is carried out, where only the marks “+” and “-” are used; “equally important” does not exist. A

weighting factor is determined by the frequency of positive evaluation. The respective frequencies are divided by the largest frequency. Here as well, the combined use of preference matrix (for determining the weighting factors) and scoring takes place for the assessment of solutions.

The **technical-economic evaluation** according to Kesselring is described in VDI 2225 [VDI2225]. The criteria are divided into a technical and an economic group; the procedure is not suitable for other forms. The technical-economic evaluation is suitable for simple and medium complex solutions. Already within a day, a statement can be made using this procedure. However, it should be noted that no measures against subjective weighting are taken. The solutions are compared with a fictitious ideal solution and are rated by points from 0 to 4. Generally, all criteria are equally weighted, but weighting is possible if necessary. While the technical criteria are further subdivided, only the evaluation of manufacturing cost K is recommended as economic criterion. The so-called technical value x is calculated as follows:

$$x = \frac{1}{n \cdot p_{max}} \cdot \sum_{i=1}^{n} p_i \tag{3.2}$$

with n = number of technical criteria, p_{max} = maximum points for each criterion, p_i = points for criterion i. If the individual criteria are subject of weighting, consequently, the weighted mean x_g is calculated [VDI2225]. The benchmark of the costs is based on ideal costs K_{ideal}, which can be determined by market analysis. The economic value y is:

$$y = \frac{K_{ideal}}{K}. \tag{3.3}$$

The results are displayed on a strength chart by plotting the economic value y against the technical value x. The strength s is determined either by the straight line method (arithmetic mean: $s = \frac{x+y}{2}$) or by using the hyperbola approaches (geometric mean: $s = \sqrt{x \cdot y}$).

Relevance profiles are created by a survey of customers or users of a technical system. Therefore, the effort is relatively high. The criteria that are expressed through linguistic terms or that are neutrally described, are arranged in a list in any order. Next to each criterion, a scale of $-xx$ up to 0 up to $+xx$, which includes the recognition values, can be found. Each respondent must specify the fulfillment of each criterion to subjective feeling. The relevance profile is presented by connecting the individual points of each respondent or of all by averaging.

The **cost-utility analysis** is suitable for problems of low to medium amount of investment. First, the target system is set up by arranging the criteria on a tree hierarchy.

Thus, coherent criteria can easily be weighted and assessed. For weighting, for example, a dominance matrix (similar to the preference matrix) can be used. Generally, the target system at the second level of the tree hierarchy includes the criteria costs and benefits, which can then be subdivided. In a target matrix the real values of the variants for each criterion are retained. The scoring is done by evaluation boards and is documented in another matrix, the target value matrix. Subsequently, the so-called utility value matrix can be determined by weighting the target values. The results are presented in a table or as a profile. With the latter a weak-point analysis can be performed. The cost-utility analysis is similar to the technical-economic evaluation by Kesselring. However, it is more complicated due to weighting and several steps.

With the **priority method** according to Saaty (also analytic hierarchy process) [Saa08], variants from different areas and of varying degrees of complexity can be assessed. In a first step, the goal must be formulated. Subsequently, criteria are defined and possible solutions or alternatives that can be represented in a tree hierarchy are listed. To determine the significance of each criterion, first, the criteria are compared pairwise in a matrix. From this matrix the eigenvector is calculated to indicate the priorities of the individual criteria (eigenvector of significances).

The method emphasizes objectivity of the results. In particular, this plays a major role for subjectively assessed criteria. To objectify the assessment of the variants, again a pairwise comparison – here of two variants – for each criterion is carried out (in a decision matrix). This matrix should be as consistent as possible. This means that the transitivity rule must be respected: "*if the entity* e_1 *is equivalent to the entity* e_2 *and it is as equivalent to the entity* e_3*, then the entity* e_2 *must be equivalent to the entity* e_3" [BK97]. Twelve further rules can be derived regarding the dependencies.

Subjective sensations are not limited in advance; first, the decision matrix is free of any constraints. The closeness to consistency is checked by calculating the ratio of consistency:

$$C.R. = \frac{C.I.}{R.I.}, \tag{3.4}$$

with $R.I.$ as random index (cf. table in [BK97], page 68) and $C.I.$ as consistency index:

$$C.I. = \frac{\lambda_{max} - n}{n - 1}, \tag{3.5}$$

with λ_{max} = maximum eigenvalue and n = number of pairwise compared entities e_i. The matrix is absolutely consistent, if the index (C.R.) is equal to 0. If the matrix is not

consistent, i.e. $C.R. \geq 0.2$ a compensation calculation must be performed or the matrix cannot be used.

The individual significance vectors are summarized in a matrix (row = variant, column = criterion, ij = significance), which is then multiplied by the eigenvector of significances. The resulting vector gives the solution of the decision problem with the final order of the variants.

The costs will be included at the end of this method: the variants are compared in the context of a cost-utility analysis. The results are represented in tables. The implementation of the priority method is very expensive and takes about one week to complete.

The **demand-oriented weighted evaluation**, also called method of Breiing [BK97], works with absolutely consistent evaluation parameters. The procedure is applicable in the same way for simple and complex solution variants. At the beginning, a group of independent raters defines the evaluation criteria. These can be derived from the task or solutions and can be divided into a technical, economic, psychological, qualitative and quantitative group. The criteria are cleaned up with a relation advisory matrix. Weighting of the individual criteria is carried out by a consistent decision matrix. The scoring is implemented also with a consistent decision matrix, value functions or review boards. Then, weighting factors are determined between the groups of criteria to calculate the group rank. Then, the total value can be derived. The effort for this review is considered as relatively high.

The **objectified weighted evaluation** is also called procedure after Knosala [BK97]. The type of assessment is very profound. For assessing, a rater group consisting of five persons is established, which consists of a leading expert, an engineer, a manufacturer, a technician and a user. The opinion of the individual group members can be weighted. First, the criteria, which can be cleaned up by the relation advisory matrix, are listed. The weighting of the criteria is done by freely predicted decision matrices. Thus, the matrices can be inconsistent, so that in this case compensation calculations must be performed (see priority method according to Saaty). The same applies to the eigenvector of the scoring matrix since the evaluation is based on clearly identifiable, fuzzy and probabilistic usually inconsistent assessment parameters. The effort for this method is very high, but the objectivity of the assessment is higher than for the method of Breiing.

CODASID is the acronym for “concordance and discordance analyses by similarity to ideal designs” or “concordance and discordance analysis regarding the similarity to ideal solution” and was developed by Sen and Yang [SY98]. During evaluation it is determined to what extent the properties of individual variants correspond to the properties of the ideal solution, so whether they are concordant or not (discordant). The procedure is

suitable for complex variants and a large number of alternatives and should be performed if high investments are looming. The effort is very high; the method takes at least one week – in addition, one week is required for training. For more information about this method relevant literature should be considered, e.g. [SY98].

Finally, the evaluation methods and their applicability are summarized in Tab. 3.1. To determine weighting factors in case of an unequally weighting of criteria, the presented methods are reduced to four. Possible methods include the ranking method, the preference matrix, the priority method and the demand-oriented weighted evaluation as well.

For the selection of PKS for the structure catalog most of the presented methods are not applicable, because for this development step insufficient information and quantifiable criteria are known and available. Therefore, only the argumentative balance sheet or the selection list can be taken into account.

Tab. 3.1: Evaluation methods and applicability

Evaluation methods	**Applicable for...**			
	...determination of weighting factors[1]	**...selection for structure catalog**	**...structure preselection**	**...final structure selection**
Argumentative balance sheet	-	(+)	-[2]	-[2]
Selection list	-	+	-[2]	-[2]
Point evaluation	-	-[3]	+	+
Ranking method	+	-	-	-
Preference matrix	+	-	-	-
Technical-economic evaluation (Kesselring, [VDI2225])	-	-[3]	(+)[8]	(-)[8]
Relevance profiles[4]	-	-	-	-
Cost-utility analysis	-	-[3]	+	+
Priority method	+	-[6]	+	+
Demand-oriented weighted evaluation	+	-[6]	+	+
Objectified weighted evaluation[5]	-	-	-	-
CODASID[7]	-	-[6]	(+)	+

Legend: + applicable, - not applicable, () maybe applicable

[1] process-related selection
[2] cannot be fully automated due to verbal evaluation and weighting
[3] too little quantifiable criteria
[4] customer survey not possible
[5] cannot be fully automated, too complex, no rater groups available
[6] too little information on individual structures available
[7] too complex, possible for final selection because more information are available
[8] economic evaluation is too complex and too difficult for not industrially implemented PKS, only technical consideration is possible

Almost the same methods are applicable for structure preselection or final selection comprising point evaluation, cost-utility analysis, priority method, demand-oriented weighted evaluation and CODASID. As an economic evaluation is too complex and too difficult for PKS that are not implemented by industry, for the evaluation according to [VDI2225] only costs for components can be considered. Due to the necessary high effort for the priority method, the demand-oriented weighted evaluation or CODASID, these methods are excluded from further considerations. Hence, the applied method (cf. following chapters) is a combination of point evaluation, technical-economic evaluation and the cost-utility analysis.

4 Structure selection

4.1 Structural synthesis methods

In recent years, several structural, respectively type synthesis, methods were developed based in general on the algebraic set theory. However, following difficulties were and are underlying the methods [HL01; HL02; JY04; KG07]:

- How can the DoF of a PKS be determined clearly and correctly? A good and comprehensive overview of formulas for calculating the DoF based on the developments of the last 150 years is given by [Gog05].
- How can the properties of mechanisms with DoF ≤ 6 be described, so that, for example, it can be defined whether revolute or prismatic joints within the PKS are needed?
- How can different limb structures be combined in order that the mechanism gets the desired DoF and properties?

Basically, two different approaches can be distinguished [YLP11]: type synthesis based on constraints (constraint-synthesis approach) [HL01; HL02; HL03; KG04d; KG04a; KG07] and type synthesis based on kinematic relations (kinematic synthesis approach) (see Fig. 4.1). The latter may be further classified in structure synthesis theory based on the single-opened-chain [CL09; JY04; STY00; SYM05] and the displacement group theory [HS91; Her99; LHH04; MLL07]. These methods should be discussed in detail below. Besides, a comparison of different methods for type synthesis is carried out by [YLL09a] and [YLL09b].

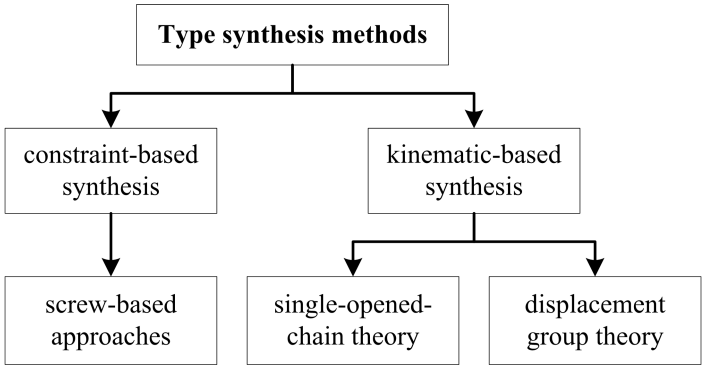

Fig. 4.1: Methods for type synthesis

Based on synthesized, parallel kinematic structures with desired DoF a further difficulty is to determine the actuated joints. It should be noted that they cannot be selected randomly. Approaches for choosing driven joints are based on the displacement group theory (cf. [LHH04]), on the screw theory (cf. [HL03; KG04b; KG04a; KG04e]), and are described in particular in [KG06] with respect to the virtual chain approach, and in [JY04] within the framework of the single-opened-chain method. The aim is to find all combinations allowing the overall actuation of the mechanism.

4.1.1 Screw-based approaches

This method of structure synthesis is based on the screw theory. In particular, the reciprocal screw theory is considered [FT04; HL02; HL03; ZFD06]. The core idea is that the DoF of the moving platform (DoF < 6) is determined by the constraints imposed by the limbs [HL03]. Therefore, it can be distinguish between the constraint system of the moving platform and the constraint system of the limbs. The geometric conditions for the latter should be investigated [HL02]. A screw is defined as a vector, consisting of two components:

$$\$ = \begin{bmatrix} S \\ S_0 \end{bmatrix} = \begin{bmatrix} S \\ r \times S + hS \end{bmatrix}. \tag{4.1}$$

The first component S is a unit vector along the screw axis, r is the position vector to any point on the axis of the screw and h is the pitch of the screw. Thus, $r \times S$ describes the moment of the screw axis about the origin of the reference coordinate system. A screw is called *twist* (ξ), if it reflects the current motion (rotation (ξ_0) or shift (ξ_∞)) of a rigid body. The first component of the screw vector is the vector of angular velocities; the second component of the vector designates the linear velocities. A screw is referred to as *wrench* (ζ), if it describes a force (ζ_0) or coaxial moment (ζ_∞) acting on the rigid body. The first component of the *wrench* describes the resulting forces; the second component composes the resultant moments about the origin of the reference coordinate system. These forces and moments are also called constraints. Thus, different joints and external loads can be depicted as unit screws. This is called a screw system. For a prismatic joint (P) (pitch $h = \infty$) or a moment the unit screw is:

$$\$ = \begin{bmatrix} 0 \\ S \end{bmatrix}. \tag{4.2}$$

For a revolute joint (R) (pitch $h = 0$) or an applied force it is:

$$\$ = \begin{bmatrix} S \\ r \times S \end{bmatrix}. \tag{4.3}$$

Other joints such as cylindrical, universal or spherical joints are a combination of the mentioned basic joints. A cylindrical joint, for example, is composed of a P- and a R-joint; a spherical joint contains three revolute joints whose axes intersect in one common point.

A screw $\$_r = \begin{bmatrix} S_r^T & S_{0r}^T \end{bmatrix}^T$ and a screw set $\$_1, \$_2, \ldots, \$_n$ are reciprocal to each other if the following condition is complied:

$$\$_j \circ \$_r = S_j * S_{0r} + S_r * S_{0j} = 0 \qquad \text{with} \qquad j = 1, 2, \ldots, n. \tag{4.4}$$

"$\circ$" is the short version for the reciprocal product and $\$_j$ is the j^{th} screw of the screw set.

If a screw set reflects the joint *twists* of a parallel manipulator's limb, $\$_r$ and the joint *twists* are reciprocal to each other. $\$_r$ is referred to as the *wrench* of the constraints imposed on the moving platform in order to restrict its motion possibilities. Eq. (4.4) shows that the virtual power developed by a *wrench* (ζ) along the *twists* (ξ) is equal to 0. In other words for a given *wrench* the reciprocal *twist* spans a space with motion possibilities, where the *wrench* imposes no forces. It follows:

$$\zeta_\infty \circ \xi_0 = 0 \quad \text{if axes are perpendicular;} \quad \zeta_0 \circ \xi_\infty = 0 \quad \text{if axes are coplanar.} \tag{4.5}$$

The mobility of the moving platform is fully determined by combining all constraint *wrenches* of the limbs. If a mobility of six is required no reciprocal screw system exists. For DoF less than six there are 6-c reciprocal screws (c = number of unwanted DoF).

At the beginning of the structure synthesis, the required *twist*-system of the entire mechanism is determined. The basis of a screw system for three rotations and three translations presents itself in the following way; the *twists* have to be selected according to the desired DoF [HL02]:

Rotations:	Translations:
$\$_1 = (100; 000)$	$\$_4 = (000; 100)$
$\$_2 = (010; 000)$	$\$_5 = (000; 010)$
$\$_3 = (001; 000)$	$\$_6 = (000; 001)$

This results in the *constraint/wrench*-system which is reciprocal to the *twist*-system. By using this constraint system the constraint systems of the limbs (6-n systems) are formed, from which the limb *twist*-systems (n-systems) can be determined. The limb *twist*-systems are the basis for the development of the kinematic chains of the limbs and are linear combinations of the *twists* of the standard base.

Kong and Gosselin [KG07] describe compositional units for serial kinematic chains with special characteristics with respect to their motion possibilities (*twist*-systems). Thus, their *wrench*-system has a certain number of independent *wrenches* with zero or infinity pitch. In a final step the developed kinematic chains for the limbs between frame and moving platform are arranged, so that the combination of all constraint systems corresponds to the desired constraint system of the mechanism. The *twist*- (T) and the *wrench*-system (W) of the manipulator with m limbs [KG07] are as follows:

$$T = \bigcap_{i=1}^{m} T^i \qquad \text{with} \qquad T^i = \sum_{j=1}^{f^i} T^i_j, \tag{4.6}$$

(T^i_j = *twist*-system of the j^{th} joint of limb i, f_i = DoF of limb i),

$$W = \sum_{i=1}^{m} W^i \qquad \text{with} \qquad W^i = \bigcap_{j=1}^{f^i} W^i_j, \tag{4.7}$$

(W^i_j = *wrench*-system of the j^{th} joint of limb i, f_i = DoF of limb i).

The virtual chain approach is a further development and improvement of the previously described method [KG04a; KG04e; KG06; KG07]. The simplest kinematic chain (serial or parallel) representing a certain motion pattern is called a virtual chain. If a virtual chain is added to a structure, the motion pattern of the mechanism does not change (the *wrench*-system of the parallel kinematic chain corresponds to the one of the virtual chain). Therefore, each limb as well as the virtual chain generates an open kinematic chain corresponding to the desired DoF. The type synthesis according to the virtual chain approach follows three steps [KG07]:

1. Determination of the *wrench*-system of the parallel kinematic chain/of the manipulator and derivation of all possible limb *wrench*-systems (the *wrench*-system is a linear combination of all limb *wrench*-systems in a general position)
2. Type synthesis of the limbs
   a) Type synthesis of simple, closed kinematic chains with x DoF and a desired limb *wrench*-system

b) Removal of virtual chain and thus creation of possible limb structures (it is important to ensure that the joint *twists* (except that of the virtual chain) are linearly independent ⇒ no redundancy)

3. Assembly of the manipulator with the previously synthesized limb structures

Examples for a 3-DoF parallel manipulator are described in [KG04e] and for a 4-DoF parallel manipulator in [KG04a]. Advantages of this method are that in contrast to the reciprocal screw theory less derivations are needed. Thus the understanding is facilitated. In addition, more types of parallel mechanisms can be synthesized compared to the synthesis using the displacement group theory or single-opened-chain theory [KG06]. A disadvantage of the method, however, is that the motion of the synthesized structures is only instantaneous. Therefore, it must be checked whether full mobility can be guaranteed [LHH04].

4.1.2 Displacement group theory

The displacement group theory introduced by Hervé [HS91; Her99] (also called lie group theory) is based on the algebraic properties of a lie group of displacement in Euclidean space. The relative motion of a joint creates a lie subgroup of the displacement. For example, $\{\mathbf{R}(N, \mathbf{u})\}$ describes the lie subgroup of a revolute joint which corresponds to a rotation about a fixed axis $(N, \mathbf{u})$. The axis passes a fixed point N. $\mathbf{u}$ is the unit vector parallel to the axis of rotation. A revolute joint is called a mechanical generator of $\{\mathbf{R}(N, \mathbf{u})\}$. Hervé [Her77] represents 12 types of so-called displacement subgroups. The displacement group including all movements in the Euclidean space is called $\{D\}$. Generally, Li et al. [LHH04] and Meng et al. [MLL07] extend the method of displacement group theory. $\{M\}$ expresses the set of all possible movements of a kinematic chain. The individual motions of rigid bodies are represented as subgroups. $\{M\}$ is a subgroup of $\{D\}$. For example, $\{M\}$ contains for a kinematic chain consisting of a revolute, a prismatic and a spherical joint (RPS), the following three subgroups $\{\mathbf{R}(N, \mathbf{u})\} * \{\mathbf{T}(\mathbf{w})\} * \{\mathbf{S}(N)\}$. The reason for this is the fact that according to the set theory a product of two elements of a subgroup is part of this group [HS91]. This subgroup $\{M\}$ is called the kinematic bond; the kinematic chain is the generator of this bond. For the analysis of the parallel manipulator, the motion possibilities of the overall system arise from the intersection of movements which are possible through the individual limbs [LHH04].

The procedure of structure synthesis using the displacement group theory is divided into four steps. First of all, the displacement subgroup $\{M\} \subseteq \{D\}$ of the complete structure is determined based on the desired DoF of the moving platform. Then, the subgroups of the limbs must be determined and the geometrical conditions have to be found so, that:

$\{M\} = \cap_{i=1}^{n}\{L_i\}$ ($\{L_i\}$ is the kinematic bond of the i^{th} limb). This is the greatest difficulty within the synthesis process, because there are different combinations of displacement subgroups for generating a predetermined motion [LHH04].

In the third step, the mechanical generators of the kinematic bonds are determined. Out of these, the limbs of the parallel manipulator can be designed by a serial sequence of joints. Unsymmetrical structures can be created, because one mechanical generator is sufficient to obtain the desired kinematic bond. The other limbs can be mechanical generators of the displacement group $\{D\}$ with six DoF. Nevertheless, a symmetrical design is preferred.

An advantage of this method is that the developed structures are completely movable; an additional verification is not necessary in contrast to the constraint-based synthesis. However, the mechanism must be based on a lie subgroup structure. Thus, not all mechanisms can be covered with this method (e.g. Bennett mechanism) [LHH04; YLL09a].

4.1.3 Single-opened-chain theory

The single-opened-chain method for type synthesis is based on the assumption that any (parallel kinematic) linkage with ν closed-loop kinematic chains can be always split into $\nu + 1$ simple, open kinematic chains (SOC = single-opened-chain) [STY00]. For a given DoF, in the first step, the so-called 3×2 position and orientation matrix (POC-matrix) of the entire structure must be determined. The first row of this matrix specifies the Cartesian coordinates of the moving coordinate system in coordinates of the base coordinate system; in the second row there are the three Euler angles of the moving coordinate system relative to the base coordinate system.

After the POC matrix for the entire structure has been specified, the POC matrices for the limbs are set, so that the intersection of the limb POC matrices results in the POC matrix of the entire structure. Then, the structural synthesis for the limbs is performed. Only five types of joints are used: these include revolute (R-joint, DoF = 1), prismatic (P-joint, DoF = 1), cylindrical (C-joint, DoF = 2), universal (U-joint, DoF = 2) and ball joints (S-joint, DoF = 3), where the last three are generated by combination of revolute and prismatic joints. With these joints open kinematic chains, so-called single-opened-chains (SOC) or even hybrid-single-opened-chains (HSOC), for the limbs are designed. Then, the minimum number of SOC required to design the desired parallel manipulator is determined [JY04]. The SOC are arranged in parallel between the moving platform and the frame. The challenge is to find all possible configurations of the SOC generating the desired motion [STY00]. Limbs do not have to be all identical, i.e. unsymmetrical structures can be designed as well [YLL09a]. However, the prismatic joints should be replaced whenever possible.

After actuator selection, the coupling degree k for the structure can be calculated in a further step. The coupling degree states about the decoupling of the inputs and resulting output motion. If $k = 0$, the kinematic and dynamic equations of various closed kinematic chains can be solved separately. If $k > 0$, different kinematic chains must be combined, however, to get a system of equations, which can then be solved in its entirety. Therefore, a small value of k [CL09; JY04; SYM05] is aimed for. The mechanisms created by using this method are completely movable, but not all types of mechanisms can be covered (e.g. the Bennett mechanism) [YLL09a].

4.1.4 Structural synthesis based on Gogu

Gogu [Gog08] has proposed a new methodology for the synthesis of PKS. It is called "*evolutionary morphology approach*" and is based on new formulae for mobility (number of independent joint parameters), connectivity (number of relative independent DoF between two links), structural redundancy (difference between mobility and connectivity) and overconstraint (difference of number of kinematic constraints in opened and closed loops). The required formulae are derived in [Gog08] and are not further investigated in the context of this work. Many examples of newly synthesized robots using the evolutionary morphology approach can be found in Gogu's books, especially for 3-DoF PKS in [Gog09].

4.1.5 Structural synthesis based on the DoF

The structural synthesis described in [Tsa01] is based on Grübler's formula for the calculation of the DoF (F):

$$F = \lambda(n - j - 1) + \sum_{i=1}^{j} f_i, \tag{4.8}$$

with n = number of links, j = number of joints, f_i = DoF of joint i, λ= motion parameter ($\lambda = 3$ for planar mechanisms, $\lambda = 6$ for spatial structures).
With the Euler equation

$$L = j - n + 1, \tag{4.9}$$

the following loop mobility criterion can be derived

$$\sum_{i=1}^{j} f_i = F + \lambda L. \tag{4.10}$$

Tsai assumes that the number of limbs (m) is equal to the DoF (F). Hence, each limb has one actuator. It is

$$F = m = L + 1, \tag{4.11}$$

i.e. the number of limbs (m) is greater by one than the number of independent loops (L).

Furthermore, Tsai introduces the connectivity (C_k) of limb k as the sum of all joint DoF within the limb. Hence, it yields for the entire PKS:

$$\sum_{k=1}^{m} C_k = \sum_{i=1}^{j} f_i. \tag{4.12}$$

To control the mobility of the end-effector, the connectivity of one limb should neither exceed the value of the motion parameter λ nor be smaller than the DoF of the end-effector:

$$\lambda \geq C_k \geq F. \tag{4.13}$$

This yields, for spatial structures with λ equal to six, to the following equation:

$$\sum_{k=1}^{m} C_k = 7F - 6. \tag{4.14}$$

If Eq. 4.14 is solved for positive values of C_k according to the DoF F of the entire structure, all possible limb connectivities are determined. In this case, the value of the limb connectivity cannot exceed six. The calculation results are listed in Tab. 4.1.

The structural synthesis approach described in [Neu06] is similar to that in [Tsa01]. Based

Tab. 4.1: Limb-connectivities with respect to the desired DoF

DoF (F)	$\sum_{i=1}^{j} f_i$	C_k **for** $k = 1, ..., m$
2	8	4,4 5,3 6,2
3	15	5,5,5 6,5,4 6,6,3
4	22	6,6,5,5 6,6,6,4
5	29	6,6,6,6,5
6	36	6,6,6,6,6,6

on the sum of all joint DoF, Neugebauer [Neu06] distributes this sum evenly on the respective kinematic chains (limbs) and lists possible arrangements of joints with respective DoF. For example, if the sum of all joint DoF is equal to 15, each limb has five DoF. For three joints within this limb the distribution of the DoF on the joints is as follows: two joints with DoF = 1 and one joint with DoF = 3 or one joint with DoF = 1 and two joints with DoF = 2.

4.2 Selection scheme

Section 4.1 shows that with the presented methods a huge number of possible PKS can be synthesized. The scope of this thesis is not to analyze all of them but at least a part, so that a selection has to be made. Therefore, in this paragraph, a selection scheme is presented step by step to reduce the number of possible PKS being considered. The procedure is related to the method of selection list, recommended by Pahl et al. [PBG07] and described in Chapter 3. The basis is the structural synthesis explained in [KG07].

Often, not all six degrees of freedom (DoF) in space are required for handling tasks in modern industrial applications, so that the development of parallel robots with given motion characteristics and less than six DoF is of great interest [FT02; FT04; HL02; HL03; JY04; KG04d; KG04a]. These PKS possess, in addition to the reduced number of required components, lower manufacturing and process costs and easier kinematic models [HL01; TJ01]. Therefore, the DoF is considered as a first selection criteria.

① Degree of Freedom

The DoF determines the desired motion behavior of the PKS and it is defined by the task. For various tasks three DoF are sufficient. Many mechanisms with this number of DoF have already been developed: structures with pure translational (3T) or pure rotational (3R) motion, as well as structures with one translational and two rotational DoF (1T2R) [CP03a; HL01; HL03]. So the second selection criteria is the kind of motion of the end-effector.

② Kind of motion of the end-effector

This thesis focuses on PKS with three translational DoF, because these PKS are able to perform, inter alia, drilling, turning or milling tasks in the context of manufacturing processes [Mer06] or pick & place tasks. Especially the DELTA or Tsai's UPU are well known examples for this group of PKS.

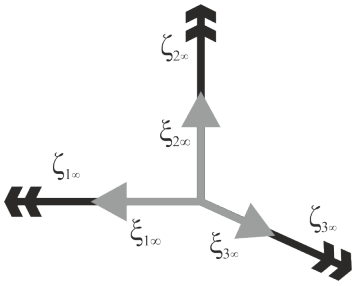

Fig. 4.2: *Twist (ξ)/wrench (ζ)*-system of PKS with three translational DoF [KG04c]

According to [KG07] there are two conditions that have to be fulfilled for a parallel kinematic chain in order for the PKS to have three translational DoF:

I Each limb of the PKS has an open kinematic chain with three DoF, i.e. each limb has at least three simple joints (prismatic or revolute joints).

II The *wrench*-system of the PKS corresponds to the one of the virtual chain (for explanation cf. 4.1.1) in any position.

The structural synthesis approach of PKS with three translational DoF is divided according to [KG07] in four steps:

1. The *wrench*-system is decomposed for the entire PKS. Because the *twist*-system for a PKS with three translational DoF is a 3-ξ_∞ system, a 3-ζ_∞ system results for the *wrench*-system (cf. Fig. 4.2).

2. The type synthesis for the limbs of the PKS is performed. The foregoing condition (I) must be fulfilled. Due to the fact that the *wrench*-system of the PKS is a linear combination of the *wrench*-systems of all limbs (cf. Eq. (4.7)), the *wrench* of a limb is either a 3-ζ_∞, a 2-ζ_∞ or a 1-ζ_∞ system.

3. At least two or more limbs are assembled to a PKS. The above-mentioned condition (II) must be fulfilled. Here, the *wrench*-system is a 3-ζ_∞ system. If the *wrench*-systems of the limbs with regard to the frame or the moving platform are invariable, the linear combination of these generally forms a 3-ζ_∞ system. If the *wrench*-systems of the limbs with regard to the frame or the moving platform are variable, certain geometric conditions (on the frame or on the moving platform) must be complied, so that it is guaranteed that the linear combination of the *wrench*-systems of the limbs results in a 3-ζ_∞ system.

4. The actuated joints are selected.

This procedure results in two more selection criteria:

③ Number of limbs

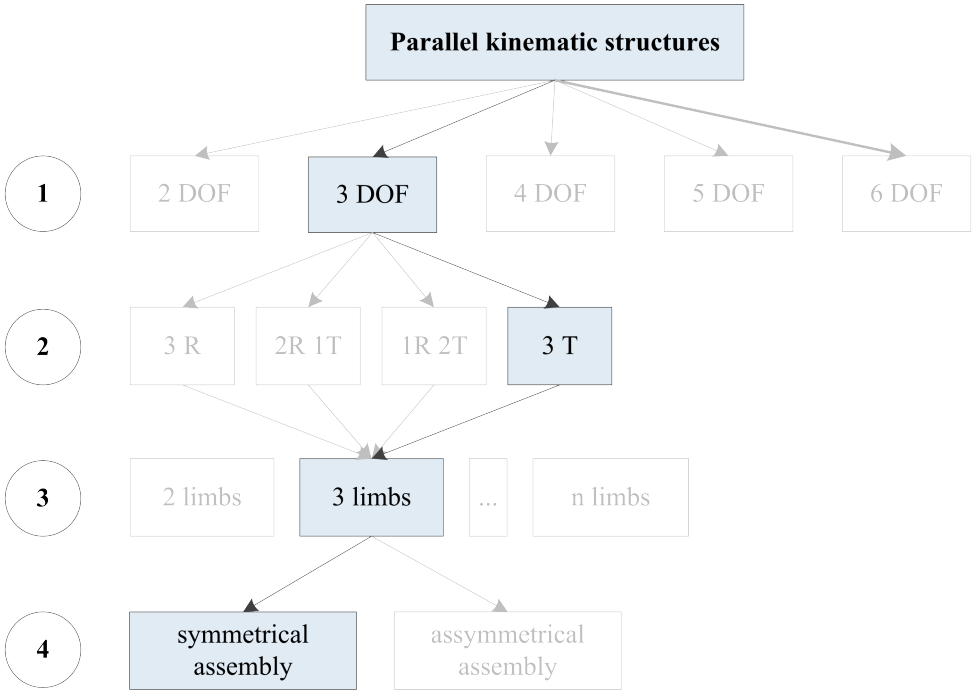

Fig. 4.3: Selection scheme (1)

④ Kind of assembly

To perform a 3-DoF motion at least three actuators are necessary. Those are preferably fixed close to the frame to reduce inertia. Therefore, only PKS with three limbs are considered in this thesis, allowing a frame side arrangement of the three actuators. Furthermore, the assembly should be symmetrical. Reasons for this are, amongst others, easier calculation and analysis procedures; the latter due to symmetrical performance properties within the workspace. Furthermore, this leads to reduced design and manufacturing costs [Neu06]. To summarize, the first part of the selection scheme is shown in Fig. 4.3.

The next step is to define the kinematic structure of the limbs for PKS with three translational DoF, three limbs and symmetrical assembly resulting from the presented selection scheme. First, it is assumed that only rotational (R) and prismatic (P) joints are used. The maximum number of joints is limited to five; at least three joints are necessary (cf. condition (I), p. 32). This is due to the fact that within a symmetrical assembly with three limbs one joint blocks at least one DoF of each limb [KG07, p. 90]. In total, the three rotational DoF have to be blocked. Thus, there are the following structure groups:

- 3 joints: 3P
- 4 joints: 3R-1P, 2R-2P, 1R-3P
- 5 joints: 5R, 4R-1P, 3R-2P, 2R-3P

Consequently, the fifth and sixth selection criteria can be derived:

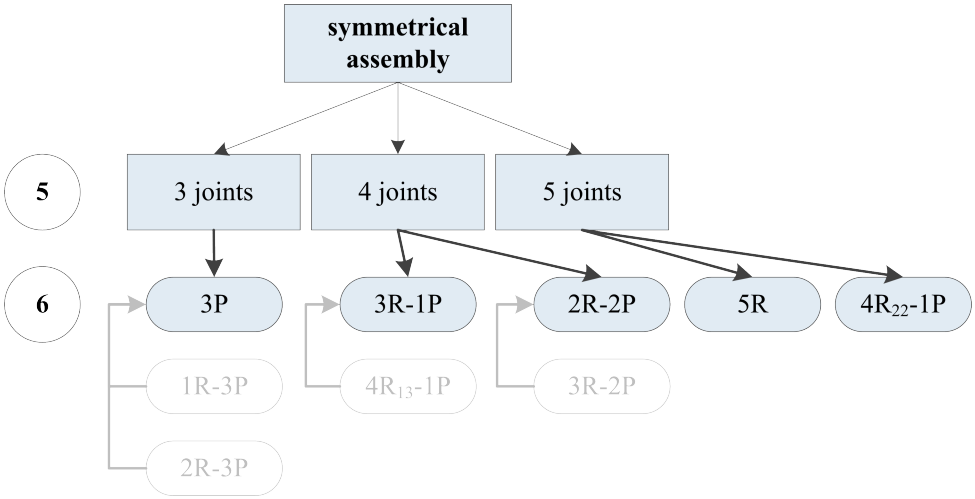

Fig. 4.4: Selection scheme (2)

⑤ Number of joints within each limb

⑥ Kind of joints

The limbs of the structure groups 1R-3P, 3R-2P, 2R-3P and part of 4R-1P contain inactive joints. According to [KG07] an inactive joint is a joint within the kinematic chain that cannot move due to the constraints imposed by the other joints. If an inactive joint is blocked, the relative motion characteristics within the kinematic chain will not change. The inactive joint for group 1R-3P is always the R joint and for group 3R-2P and 4R-1P it is the R joint whose axis is not parallel to the axes of the two (three) other R joints within the kinematic chain [KG07]. Finally, for 2R-3P both R joints are inactive joints. Hence, by blocking or removing of inactive joints the groups 1R-3P and 2R-3P can be reduced – with regard to the motion characteristic of the kinematic chain – to the group 3P; the group 4R-1P with three parallel aligned revolute joints to the group 3R-1P and the group 3R-2P to the group 2R-2P. For further consideration only five groups remain (cf. Fig. 4.4).

The joints within each limb cannot be aligned arbitrarily. [KG07] develop several conditions that must be fulfilled. Tab. 3, p. 220 summarizes these conditions for the remaining groups. Additionally, further geometrical conditions are given for the assembly of PKS with three identical limbs and for the case that the first joint of each limb is actuated.

To calculate the number of possible joint arrangements the formula for permutations with repetition is considered. If identical objects occur (here: joints with identical axes' alignment), the number of permutations is determined with the multinomial coefficient

Tab. 4.2: Number of possible configurations

joints per limb	kind of joints	possible permutations (1st level)	considered permutations
3	3P	$\frac{3!}{3!} = 1$	1
4	3R-1P	$\frac{4!}{(3!\cdot 1!} = 4$	4
	2R-2P	$\frac{4!}{(2!\cdot 2!)} = 6$	6
5	5R	$\frac{5!}{(2!\cdot 3!)} = 10$	$5^{(1)}$
	4R-1P	$\frac{5!}{(2!\cdot 2!\cdot 1!)} = 30$	$10^{(2)}$
total		51	26

Comments:
(1) Three revolute joint axes are parallel whereas the other two revolute joint axes are parallel as well. In general 10 joint combinations are possible. Five of them have to be discarded because they are not valid. This is due to the fact that either the group of the three or of the two parallel revolute joints have to be kept together [KG07]. So the number of permutations reduces to five.
(2) Two revolute joints have parallel axes. With one prismatic joint 30 permutations result. Though, only the prismatic joint and one revolute joint can be arranged in any order, i.e. two revolute joints with parallel rotational axes are always in series. Thus, this yields only 12 possible permutations. However, nevertheless identical kinematic chains occur in the sense of permutation. Therefore, the possible number decreases to nine. But by inserting a prismatic joint between two revolute joints with parallel axes, the orientation of those does not change, so that one further possible joint combination has to be added. Finally, the number of permutations used is 10.

(n = number of objects, here: number of joints; k_i = number of identical objects i):

$$\binom{n}{k_1, k_2, ..., k_m} := \frac{n!}{k_1! \cdot k_2! \cdot ... \cdot k_m!}. \tag{4.15}$$

Tab. 4.2 summarizes the number of considered permutations. Additionally, the various R- and P-joint alignments for each group are presented in the annex, p. 189.

4.2.1 Selection based on Tsai and Neugebauer

With respect to the selection criteria introduced in Section 4.2 that only parallel manipulators with identical limbs should be synthesized and the DoF corresponds to three, the possible combinations of limb-connectivities listed in Tab. 4.1 are reduced to one, i.e. 5,5,5. This means that the sum of joint mobilities of each limb is equal to five. Therefore, each limb is assembled with max. five joints. The minimum number is three. Revolute, prismatic, cylindrical, universal and spherical joints are available. The configurations synthesized by Tsai [Tsa01] are listed in Tab. 4.3. The first number in the column “Type”

Tab. 4.3: Synthesized structures by Tsai [Tsa01]

Type	limb-configurations
120	PUU, UPU, RUU, ~~URU~~, ~~UUR~~, ~~UUP~~
201	~~RRS~~, ~~RSR~~, ~~RPS~~, ~~PRS~~, ~~RSP~~, ~~PSR~~, ~~SPR~~, ~~PPS~~, ~~PSP~~, ~~SPP~~, ~~SRR~~, ~~SRP~~
310	RRRU, RRPU, RPRU, PRRU, RPPU, PRPU, PPRU, RRUR, RRUP, RPUR, PRUR, RPUP, PRUP, PPUR, RURR, RURP, RUPR, PURR, RUPP, PURP, PUPR, ~~UPRR~~, ~~UPRP~~, ~~UPPR~~, ~~URRR~~, ~~URRP~~, ~~URPR~~, ~~URPP~~
500	RRRRR, RRRRP, RRRPR, RRPRR, RPRRR, PRRRR, RRRPP, RRPPR, RPPRR, PPRRR, PRPRR, PRRPR, PRRRP, RPRPR, RPRRP, RRPRP

describes the number of joints with DoF = 1, the second number the number of joints with DoF = 2, and the third number the number of joints with DoF = 3.

Additionally, Tsai [Tsa01] makes some assumptions to reduce the number of structures. First of all, a revolute or prismatic joint fixed to the frame or a prismatic joint in the middle of the limb is preferable for actuation. So all structures with an universal joint as first joint are excluded. Furthermore, the condition that leads to translational motion has to be fulfilled. Theoretically, each limb should impose a rotational constraint on the end-effector to completely block the rotational DoF. All constraints imposed by the limbs should be independent from each other. As a spherical joint cannot impose any rotational constraint on a rigid body, all type 201 configurations are removed from the selection.

For parallel kinematic structures with three DoF and with regard to the possible structure configurations developed by [Neu06], the number reduces as well due to the following (same) reasons: (1) if a spherical joint occurs in the kinematic chain, the rotation of the end-effector is not blocked, i.e. the DoF of one joint should be less than three. (2) If the DoF of the limb is equal to six, no DoF of the end-effector is blocked. (3) Not all joint distributions are possible for three translational DoF regarding the criteria described in [KG07]. Hence, only five distributions remain. They are listed in Tab. 4.4 and a reference to the structure groups of [KG07] is given. Neugebauer [Neu06] introduces further criteria to synthesize feasible structures. The next paragraph applies these criteria to the described structure groups.

4.3 Considered structures

In order to further reduce the structures within the identified groups, the method of selection list is applied again. Exclusion criteria according to [Neu06] are considered. These contain:

1. Max. three prismatic joints within one limb

Tab. 4.4: Joint distributions by Neugebauer [Neu06]

DoF of the limb	Number of joints	Distribution of DoF to joints	Relation to structure groups [KG07]
5	5	1+1+1+1+1	5R, 2R-3P, 3R-2P, 4R-1P
	4	1+1+1+2	with C- or U-joint
	3	1+2+2	with C- or U-joint
4	4	1+1+1+1	3R-1P, 2R-2P, 1R-3P
	3	1+1+2	with C- or U-joint
3	3	1+1+1	PPP

2. Arrangement of the actuators close to the frame
3. Identical limbs
4. Joints with DoF < 4

The mentioned criteria are all valid for the proposed structures. There is no group with structures containing more than three prismatic joints. An actuator arrangement close to the frame to reduce inertia is possible (cf. [KG07]). Criteria 3 is already included in the starting assumptions. At this point, only R- and P-joints, i.e. joints with DoF equal to one, are assembled. Therefore, criteria 4 is fulfilled. Due to various drawbacks of prismatic joints such as clamping, a fifth criterion is introduced:

5. If passive joints, then revolute joints

To comply with criterion 5, the PPP limb kinematic chain should be excluded. Also the 2R-2P group with two prismatic joints must be considered under special aspects.

The sixth criterion leads to further reduction:

6. Max. three joints within one limb

One limb should not have more than three joints because otherwise stiffness properties decrease significantly and tolerance errors due to serial design of the kinematic chains increase [Neu06]. In order to comply with this criteria, the simple R- and P-joints within the limbs have to be combined. Two R-joints whose axes are perpendicular to each other form a universal joint. If the axis of a P-joint is parallel to the axis of a revolute joint and the distance between both joints is zero, then it is called a cylindrical joint. For all these joints the DoF is smaller than three. Because the rotations are blocked for 3-DoF translational motion, no spherical joints are used. Only hybrid limbs, such as for the DELTA, also contain spherical joints.

By combining the R- and P-joints, the number of PKS is reduced further. The remaining structures are presented in Tab. 4.5 and in the annex, Fig. 1-4, pp. 189-190.

Tab. 4.5: Reduced number of structures

3P	**3R-1P**	**2R-2P**	**5R**	**4R$_{22}$ -1P**
~~PPP~~	RRC*	RCP*	(URU)	(UUP)*
	RCR*	RPC*	(UUR)	(URC)
	(CRR)	(CPR*)	RUU	(UCR*)
		(CRP*)		(UPU)
		PRC*		RCU*
		PCR*		(CRU)
				PUU
				RUC
				(CUR)

* with passive prismatic joint

Another criterion follows:

7. Actuation only at joints with DoF = 1

This is also mentioned by [Tsa10] in such a way that preferably a revolute or prismatic joint at the frame or a prismatic joint in the middle of the kinematic chain of the limb is actuated. As a result, the number of possible structures is restricted further. All structures where Cardan or cylindrical joints would have to be driven are put into parentheses. But in general, for a cylindrical joint linear actuation is realizable.

To analyze the properties of different structural configurations, all structures are treated first regardless of whether an actuation of a universal joint is possible or not. Furthermore, structures with one passive prismatic joint are not excluded. In total, 21 PKS remain for further investigations.

4.4 Frame configurations

To design the structures, various frame configurations are possible. These configurations are schematically shown in Fig. 4.5 and abbreviated in the further part of this thesis with the following symbols.

Δ = *triangular configuration (tr)*
The actuation axes are all parallel to one plane, but not parallel to each other.

$\perp$ = *orthogonal configuration (or)*
The actuation axes are perpendicular to each other.

$\parallel$ = *parallel configuration (pa)*
The actuation axes are parallel to each other.

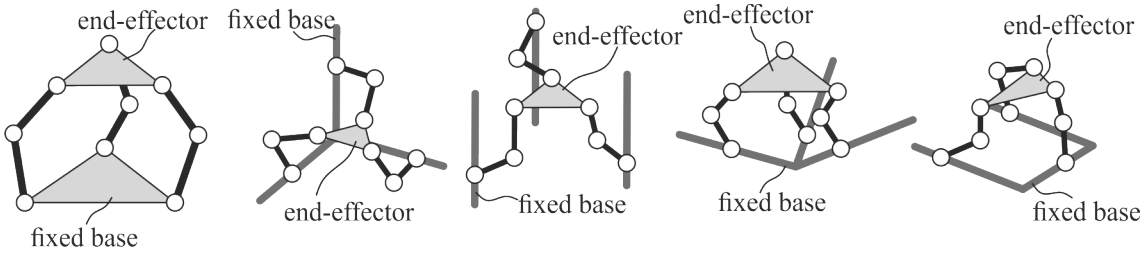

Fig. 4.5: Frame configurations (Δ, $\perp$, $\parallel$, $\star$, $\cup/\mathsf{T}$)

$\star$ = *star-shaped configuration (st)*
The actuation axes intersect in one common point.

$\cup^1$ = *U-shaped configuration (us)*
The actuation axes form a U-shape.

T^1 = *T-shaped configuration (ts)*
The actuation axes form a T-shape.

It should be mentioned that the orthogonal configuration is a special case of the star-shaped configuration. Each frame configuration is not appropriate for all structure types. For example, the star-shaped and the parallel frame configurations are only realizable for such structures, which have a prismatic joint as first articulated in each limb. For structures with a revolute joint as first joint of the kinematic chain $\star$ and $\perp$ can be reduced to the triangle configuration. The groups 3R-1P, 2R-2P, 5R and 4R-1P are now considered separately to highlight the possible frame configurations of each structure. All results are summarized in Tab. 4.6.

4.4.1 3R-1P

For the structures RRC and RCR, the frame configurations $\star$ and $\parallel$ are omitted, because the first joints of the kinematic chains are not prismatic joints. The assembly rule that has to be fulfilled according to [KG04c; KG07] is that all rotational joint axes within one limb must be parallel to each other. However, all rotational axes of the entire structure should not be parallel. The frame configurations $\perp$, Δ and $\cup/\mathsf{T}$ comply with this rule. For both structures, only an actuation via a revolute joint is useful, as for the RRC the prismatic joint is located at the end-effector and for the RCR in the middle of the kinematic chain. But for the latter, the prismatic joint rotates around the first revolute joint. This is nevertheless not recommended from a design and dynamic perspective (cf. Section 4.3, criterion 5). Therefore, the structure is completely omitted. For RRC, the lengths of the prismatic motion axes are limited by the size of the end-effector.

[1] This frame configuration is listed for the sake of completeness, although it does not allow full-symmetrical design.

Tab. 4.6: Possible frame configurations for the selected PKS

		Frame configurations						Actuation	
		Δ	$\perp$	$\parallel$	$\star$	$\cup$	T	R	P
3R-1P	RRC	✓	✓	-[1]	-[1]	✓	✓	✓	-
	RCR[5]	-	-	-	-	-	-	-	-
	CRR	✓[2]	✓	✓[2]	✓	✓[2]	✓[2]	-[4]	✓
2R-2P	RCP[5]	-	-	-	-	-	-	-	-
	RPC	✓	✓	-[1]	-[1]	✓	✓	✓	✓
	CPR	✓[2]	✓	-[2,5]	✓	✓	✓	-[4]	✓
	CRP[5]	-	-	-	-	-	-	-	-
	PRC	-[5]	✓	✓	✓	✓	✓	-	✓
	PCR[5]	-	-	-	-	-	-	-	-
4R-1P	UUP	✓	✓	-[1]	-[1]	✓	✓	(✓)	-
	URC	✓	✓	-[1]	-[1]	✓	✓	(✓)	-
	UCR	✓	✓	-[1]	-[1]	✓	✓	(✓)	-
	UPU	✓	✓	-[1]	-[1]	✓	✓	-	✓
	RCU[5]	-	-	-	-	-	-	-	-
	CRU	✓	✓	-[2,5]	✓	✓	✓	-[4]	✓
	PUU	✓	✓	✓	✓	✓	✓	-	✓
	RUC	✓[3]	✓	-[1]	-[1]	✓	✓	✓	-
	CUR	✓[3]	✓	✓[2]	✓	✓[3]	✓[3]	-[4]	✓
5R	URU	✓	✓	-[1]	-[1]	✓	✓	(✓)	-
	UUR	✓	✓	-[1]	-[1]	✓	✓	(✓)	-
	RUU	✓	✓	-[1]	-[1]	✓	✓	✓	-

[1] no P- or C-joint respectively as first joint
[2] prismatic and revolute joint axes are not parallel (inclination angle δ)
[3] revolute joint axes at the end-effector are inclined
[4] only linear actuation for C-joint
[5] unfavorable design

CRR is based on the basic structure PRRR or RPRR. In case the prismatic joint is the first joint of the kinematic chain, the rotational joint axes of all revolute joints may not be parallel to a plane. Thus, the frame configurations Δ, $\cup/\mathsf{T}$ and $\parallel$ are omitted. With regard to the basic structure PRRR, however, and the specification that the rotational joint axes within a limb are neither parallel to the respective prismatic joint axis nor orthogonal to it, the mentioned frame configurations are applicable (here inclination angle δ). A rotational actuation would be possible, but then, the actuator would move during motion, greatly increasing the inertia of mass. Therefore, this actuator option is excluded (cf. Section 4.3). In summary, RRC with rotational actuation and CRR with prismatic actuation are considered.

4.4.2 2R-2P

For the basic structure RRPP, i.e. also for the resulting structure RCP, the following assembly rule is valid: "*Three axes that are perpendicular to the axis of the non-actuated*

prismatic joints within a limb, are not parallel to a plane“ [KG07]. Regardless of the actuated joints, the revolute joint axes may not all be parallel [KG04c].

Since both, RCP and RPC, have revolute joints as first articulated within each kinematic chain, a $\star$-shaped frame configuration does not make sense. Also the $\parallel$ frame configuration is omitted for both structures. For RPC the actuation is not only possible about the first revolute joints, but also about the second prismatic joints. Thus, the structure has limbs with variable lengths. The maximum length of the cylindrical joint axes will be determined by the size of the end-effector. In case of RCP the cylindrical joint axes would rotate about the first revolute joint axes which is the same as for CRR. Therefore, this structure is omitted from a design point of view.

All frame configurations except of the Δ and $\parallel$ configuration are possible for the CPR without breaking any assembly rule. It is assumed that the cylindrical joints attached to the frame are linearly actuated. Similar to the CRR with fixed cylindrical joint axes, the revolute joint should not be actuated to avoid high inertia. A Δ or $\parallel$ frame configuration is possible if, and only if, the basic structure PRPR is taken into account and the prismatic joint axis of the first joint is not parallel to the revolute joint axis (inclination angle δ).

The same applies to the structure CRP with the basic structure PRRP. The question, however is, whether this structure is useful. The prismatic joints attached to the end-effector, significantly increasing the installation space, are problematic. Therefore, the CRP structure is not considered any further.

Only a linear actuation can be provided for the structures PRC as well as PCR, because otherwise not the first joint of each kinematic chain is driven. All frame configurations are feasible. Due to the rotating cylindrical joint axes, the structure PCR has an unfavorable design. For the PRC only the Δ configuration is waived, assuming that the P and C axes are perpendicular to one another. To conclude, only three structures of this group remain: RPC, CPR and PRC.

4.4.3 4R-1P

For the group 4R-1P the frame configurations $\star$ and $\parallel$ are not possible for a total of six structures, since the first joints of their kinematic chains are not prismatic joints. These include UUP, URC, UCR, UPU, RCU and RUC. The necessary assembly rule includes that three axes perpendicular to the axes of rotation within a limb should not be parallel to a plane [KG04c; KG07]. Thus, the frame configurations $\perp$, Δ and $\cup/\mathsf{T}$ are possible for all structures in the same way.

For UPU and PUU the prismatic joint is actuated, whereas for RUC it is the first revolute joint within each kinematic chain. Again, rotating cylindrical joint axes occur for RCU, so that this structure is excluded. Because the structures UUP, URC and UCR have a universal joint as first joint within the limbs, they are reduced to the basic structures if necessary. That means that the universal joint is replaced by two revolute joints with an additional link in between them. To simplify the calculations for these structures, however, they are ideally calculated, i.e. the distance between these two revolute joints is set to zero. Even if UCR has a rotating cylindrical joint axis, the structure is not excluded for the first analysis. A linear actuation is used for CRU and CUR. Both structures require for a $\parallel$ frame configuration that first prismatic and revolute joint axes of the cylindrical joint are not parallel. Furthermore, the design of a Δ-CUR is improved by inclining the revolute joint axes attached to the end-effector.

4.4.4 5R

There are no further rules for the assembly of the structures URU, UUR, and RUU. However, two or three revolute joints in series within a limb must be parallel, while the axes of the other revolute joints are also parallel [KG04c; KG07]. Because the 5R structures only have revolute joints, no linear actuation is possible, i.e. the frame configurations $\star$ and $\parallel$ can be omitted. In principle, as already mentioned before, the actuation of a universal joint is difficult, but a design solution can be found (e.g. splitting-up of the first universal joint), so that the structures URU and UUR are also further investigated.

4.5 Summary and final selection

In this chapter different type synthesis methods were presented. Based on the constraint-synthesis approach and synthesized PKS (cf. [KG07]), a selection scheme was executed. It allows reducing the high number of possible PKS. The selection criteria were described in detail. Five structure groups were specified with regard to the kind of joints (R- and P-joints). Each group possesses other geometrical conditions (cf. annex, Tab. 3, p. 220) for the joint alignment within each limb and for the entire structure. Due to this fact not all PKS are useful from a design point of view.

Finally, 16 PKS are considered for further analysis (cf. Tab. 4.7). With the applied frame configurations Δ, $\star$ and $\parallel$, for in total 25 structures calculation procedures (e.g. inverse kinematics, Jacobian matrix, inverse dynamics, etc.) have to be derived to allow an optimization of the geometrical parameters and a comparison of the characteristic properties.

For better understanding of the composition of each structure, Tab. 4 and 5, p. 221 show CAD drawings.

Tab. 4.7: Final selection

		RRC	CRR	RPC	CPR	PRC	UUP	URC	UCR	UPU	CRU	PUU	RUC	CUR	URU	UUR	RUU
Frame	Δ	✓	✓[1]	✓	✓[1]	-	✓	✓	✓	✓	✓	✓	✓	✓[2]	✓	✓	✓
	$\parallel$	-	✓[1]	-	-	✓	-	-	-	-	-	✓	-	✓[1]	-	-	-
	$\star$	-	✓	-	✓	✓	-	-	-	-	✓	✓	-	✓	-	-	-
Act.	R	✓	-	✓	-	-	(✓)	(✓)	(✓)	-	-	-	✓	-	(✓)	(✓)	✓
	P	-	✓	✓	✓	✓	-	-	-	✓	✓	✓	-	✓	-	-	-

[1] prismatic and revolute joint axes are not parallel
[2] revolute joint axes at the end-effector are inclined

5 Study on typical manipulation tasks

Within this chapter first general aspects on requirements for manipulation tasks are presented. Thereafter, tasks for serial and parallel robots are summarized in order to provide an overview of realistic manipulation task for PKS with three translational DoF. For further analysis, selected manipulation tasks are described in detail. Furthermore, relevant requirements defining those tasks are specified and comparable reference structures from industry with their specific properties are selected and listed.

5.1 General requirements

Requirements for robots can be derived from application scenarios and areas. First of all, different types of demands and classification methods are explained.

So-called **requirement families** for the individual needs can be classified according to [BK97]. These comprise the functional requirements first, which "*include all requirements that ensure the required function of a technical system; so they are required only to comply with function*" [BK97]. In general, these are stress or motion data, details of the required DoF and functional boundary conditions, including e.g. maximum weight. Operational requirements form a further requirement family [BK97] including "*all requirements, which maintain the required function of a technical system from launch of operation until decommissioning; so they are only required for operating performance*". Yet, many of the operational requirements cannot be considered at this stage of development. Reasons for this are:

- They are considered only in the context of fine design (such as manageability, security, portability).
- They depend on the choice of additional components, such as engines, transmissions (including usability, maintenance, maintainability, reliability).
- They depend on specific tasks (including life, operating time, duration of use).

Requirements of the family design, manufacturing or environmental issues are not considered in the further course, because no relevant criteria can be derived for the considered structure selection and the level of development.

The individual requirements within each requirement family can be divided into three **requirement categories** (cf. Fig. 5.1). These include technical requirements, economic needs and psychological requirements. Mainly the technical requirements are considered in the context of this work. Here, the economic requirements only cover the costs, including simply the material costs, i.e. the cost of joints, limbs, and drives. Psychological requirements are irrelevant within this thesis.

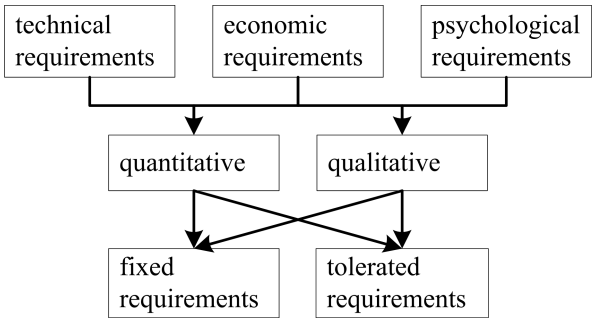

Fig. 5.1: Classifying of requirements [BK97]

In addition, there are two **types of requirements**, quantitative and qualitative, that are either fixed or tolerated. Pahl and Beitz [PBG07] classify these further. Fixed requirements are not only basic, but in addition technical custom requirements. Tolerated requirements are also known as attractiveness requirements or desires. In contrast to the fixed requirements, their fulfillment is not a must. Additionally, requirements are presented explicitly, i.e. directly, or only implicitly. This means that they have to be derived from boundary conditions and scientific laws. Therefore, their fulfillment is presupposed.

Technical individual requirements playing a role in the development of robots are discussed in the following paragraphs. Whether they are quantifiable or just qualitative requirements, depends on the task to be carried out, and is therefore not relevant. The assignment of the type of requirement (fixed or tolerated) is specific to the task as well.

For the compilation of relevant individual requirements, please refer to enumerations and sample lists in the relevant literature [BK97; VDI2222; VDI2225]. Only the list of main features according to [PBG07] should be mentioned at this point. However, not all listed main features are relevant within this thesis. Tab. 5.1 gives an overview of the considered main features.

The **workspace** is one criterion covered by the main feature geometry. It is defined as the space that contains all geometrical locations, in which the end-effector (or rather the tool center point (TCP)) of the handling device can operate. Mathematically, it is the number of permissible output vectors (position vectors of the end-effector or TCP, respectively) [Neu06]. The size of the workspace depends on the kinematic dimensions of the handling

Further considered	Not relevant within this thesis
• Geometry • Kinematics • *Dynamics** • Forces • Energy supply • *Accuracy** • Assembly • Costs	• Material • Signal • Safety • Ergonomics • Manufacturing • Testing • Maintenance • Recycling

*not in primary list, but added due to relevance

Tab. 5.1: Further considered and not relevant main features according to [PBG07]

device or PKS, respectively, and the mechanical design. [VDI2861] gives a more detailed definition.

It can still be distinguished between:

- **(Prescribed) workspace**
  The prescribed workspace is the workspace that has to be reached with regard to the tasks by the TCP of a handling device.
- **Reachable workspace or dexterous workspace**
  The reachable workspace describes the workspace which contains all reachable points by the TCP (min. one orientation is possible). In contrast, the dexterous workspace is the workspace where the end-effector can be orientated arbitrarily, i.e. the orientation is still chosen freely. The dexterous workspace is very small for most structures and is therefore not necessarily useful. Also, it is completely needed only in the rarest cases because for most applications not all full rotations are necessary [GG97]. All considered structures within this thesis have three translational DoF. Therefore, there is no difference between the reachable and the dexterous workspace.
- **Usable workspace**
  The usable workspace is the workspace the TCP, the end-effector or handling device achieve without passing through a singular position [LWK06].

The workspace can be classified according to different criteria. First of all, the volume can be calculated. However, still no statement is made regarding its appearance. Therefore, the form of the workspace should be considered as well. Parallel structures have complex workspaces depending on many parameters. Because these cannot be described universally, it is advisable to consider the distribution of the working volume in Cartesian space [GRN95]. For some applications only the size of the workspace in one direction is relevant. Therefore, the **working range** is important for the main feature geometry

as well. Finally, some tasks require a prescribed quality of the workspace. For example the workspace should be singularity-free or the force or velocity transmission shall be homogeneous.

The **motion or operating space** is the entire space, which can theoretically be passed through during motion of the handling device [Sch87]. After [Neu06] this is equal to the danger zone from a safety point of view. The structure forms the boundaries of the motion space in the positions when the outer points of the workspace are reached.

In addition to the motion space, the **installation space** should be considered. According to well-known standards and guidelines, no clear definition for the installation space of a handling device can be found. According to [Pok04] the installation space can be defined as pack size, i.e. the taken volume of the entire robot in retracted state, hence in the closest possible position. A larger pack size requires more space and a larger footprint and therefore, it costs more. A smaller pack size offers more flexibility.

Finally, the **geometric structure** should be considered. That means depending on the requirements the number of links and the number and type of joints is important.

The kinematics include the **motion type and direction**, i.e. the DoF. Depending on the task, not always all six spatial DoF are required. In the framework of this thesis, the DoF is equal to three for all considered structures. The **movability** within the workspace is limited by joint angles, stroke lengths, as well as actuator limits. As a result, the flexibility is restricted. For example, tasks during body-in-white production or orbital welding require high movability and thus flexibility. A crucial requirement is also the **output velocity**, i.e. the velocity of the end-effector. For many tasks, short cycle times, i.e. high speeds are required. This is the case, for example, for loading and unloading of machines or pick & place tasks. Fast start-up, i.e. good **acceleration properties**, is necessary in spot welding [Sch87].

Not only **weight forces** are among the feature forces, but also **static and dynamic process forces** occurring during motion. First, the payload is mentioned. Depending on the payload, five areas can be distinguished (cf. [KUK14; Stä14]):

- $<$ 0.5 kg: small robotics
- 0.5-10 kg: low payload
- 10-80 kg: middle payload
- 80-300 kg: high payload
- $>$ 300 kg: heavy load

In addition, the maximum forces in joints and friction forces must be observed. The dynamic process forces include, for example, mass inertia or changing loads.

External forces cause a displacement of the end-effector as a result of occurring compliance of the actuators, the structure, or even the joints. The **stiffness** has direct influence on the positioning accuracy. It depends on the size and the material of the limbs, the transmission mechanisms and the type of drives. The influence of the stiffness on the motion behavior of the robot can be depicted within a stiffness model.

Energy supply includes the **transmission behavior** of the structure and hence its **efficiency**. The maximum possible payload acting on the end-effector or the maximum possible speed of the TCP highly depend on the required **actuator limits** regarding velocity, force and power.

The accuracy of a parallel manipulator describes the **positioning or orientation error** of the end-effector from the desired position as a result of actuator-related inaccuracies [DIN9283]. In addition to this pose accuracy the term of **repeatability** exists: "*The pose repeatability specifies the accuracy of matches between the positions after n repeated attempts to the same target pose in the same direction*" [DIN9283]. Tolerances on kinematic dimensions, as well as joint errors by backlash can adversely affect the accuracy and repeatability. But high precision is required in many areas. Examples are the production of fuel cells, orbital welding or the transport of samples. The latter requires a reproducible process, i.e. a good repeatability.

If a high **degree of flexibility** is required, different mounting options can be provided. This is aimed at varied frame configurations (cf. Chapter 4.4) or at reconfiguration possibilities of the system. For further information please consider the corresponding chapters.

Costs are considered as the only feature reflecting economic aspects. As mentioned before, only the material costs are relevant within this work. These include the costs for the joints, limbs, as well as for the drives. Production, external service, operation, or also follow-up costs cannot be quantified at this stage of development.

Consequently, the requirements to define in advance are as follows:

- Required workspace (volume, range, distribution)
- Motion space and available installation space
- Actuator and joint boundaries
- Max. velocity of end-effector or TCP respectively
- Max. acceleration of end-effector or TCP respectively
- Max. payload and process forces
- Required accuracy and repeatability
- Necessary flexibility (reconfiguration, frame variation)
- Max. costs

5.2 General manipulation tasks

Robots are used in different areas: from foundry industry, which requires handling of large and heavy parts to food industry, for which clean room suitability of the robot is important up to the use in machine tools, such as in machining involving high precision and good repeatability (cf. Fig. 5.2). The three examples show that there are different handling and manufacturing processes. Accordingly, the diversity of the tasks is very large placing different demands on the automation process. General manipulation tasks are divided into several areas provided by [Han10] and information on websites of robot suppliers. In all areas the manipulation of both, workpieces or tools, is possible in the same way. This contains amongst others:

- Handling
- Surface treatment
- Positioning
- Machining

Handling includes, besides the assembly of workpieces (e.g. vibration-free handling of wafers [KUK14]), also loading and unloading of machines. In packaging industry not only packaging is carried out automatically, but robots take over palletizing tasks in many places. Examples can be found in the production of puzzle and game boxes of different sizes or in the handling of packaged beverages, which have to be stacked (cf. Fig. 5.3, right). Pick & place is another task in the field of handling. Using high speed robots goods from the conveyor are taken and inserted in packages (e.g. production of meat and sausages, Fig. 5.2, middle).

In the field of **surface treatment** it comes to clean parts, to paint or to coat (e.g. in automotive industry). Just for the uniform and optimal material application and where dangerous mist occurs, the use of precise spray robots is suitable (Fig. 5.3).

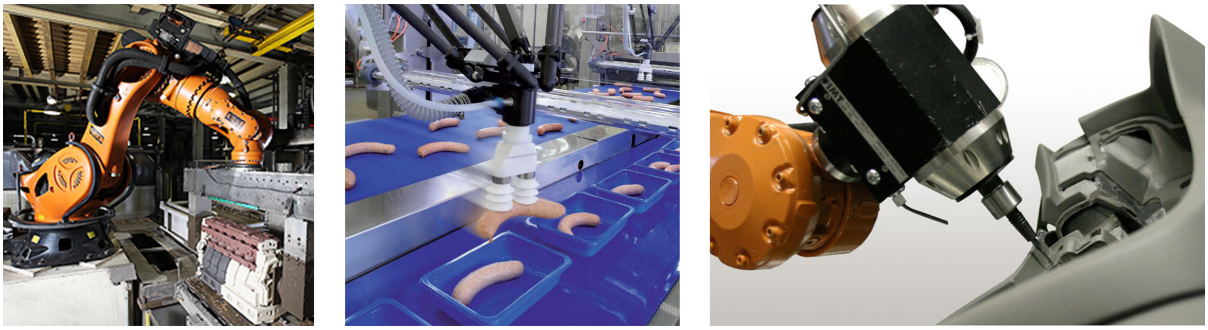

Fig. 5.2: Manipulation tasks in different areas (from left to right: handling of heavy cast parts [KUK14], packaging of sausages [Ben08], milling task [car14])

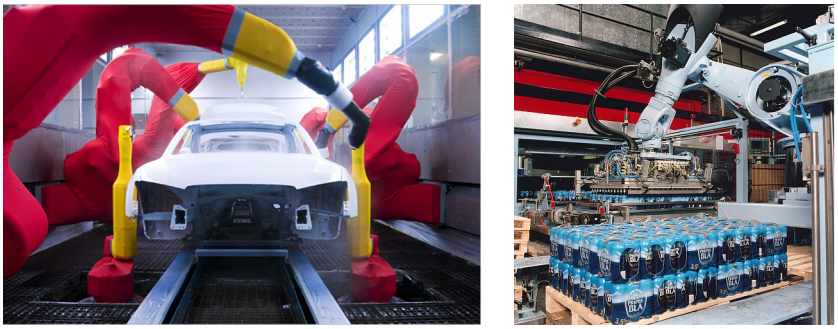

Fig. 5.3: Spray robot in automotive industry [Aud14] and palletizing of beverages [KUK14]

Fig. 5.4: left: stringer positioning [www15], right: positioning system [Moo14]

Positioning takes place in the macro-, micro, as well as in the nano-range. For example, telescopes must be guided to previously defined positions and then held in a certain position. But also the surface testing requires precise positioning of the components. An example for the positioning of stringers in aircraft industry and a positioning system based on a Hexapod structure is shown in Fig. 5.4. **Machine processing** includes drilling, deburring, milling (cf. Fig. 5.2, right), sawing, grinding, cutting, or welding of workpieces. Some of these tasks can be found, for example, in the field of fettling. **Other handling tasks** include the simulation of movements, amongst others for specific products or components (e.g. stress testing of car seats [KUK14], handset positioner [HEA14], Fig. 5.5), material testing with high accuracy by precise insertion and positioning of the material to be tested and assembly or disassembly, respectively (e.g. production of flanges for electrical steering of motor vehicles [KUK14]).

Tab. 5.2 summarizes the mentioned manipulation tasks and the industrial robots employed. It is clear that the 6-axis vertical jointed-arm robot is very versatile. Therefore, it can be used in almost all areas. In the following paragraph typical manipulation tasks are described in detail with their specific requirements. For the fields pick & place, quasistatic positioning and mold guidance for 3D fiber injection an example is presented.

	Task	Parallel robots				Serial robots		
		Hexapod	Tripod	Tricept	Delta	Scara	Joint-arm	Cartesian
Handling	(un)loading						x	x
	complex inserting				x			
	packing		x		x	x	x	x
	palletizing		x		x	x	x	x
	pick & place		x		x	x		
Surface treatment	coating						x	
	adhesive bonding		x		x		x	
	painting						x	
	polishing						x	
Positioning	macro	x					x	
	micro/nano	x	x					
Machine processing	drilling	x						
	burring	x		x			x	
	milling	x					x	
	sawing						x	
	sanding						x	
	cutting	x		x			x	
	welding	x		x			x	x
	machining	x	x				x	
Others	simulate motion	x					x	
	measuring	x					x	
	assembling			x	x	x	x	x
	isolate vibrations	x						

Tab. 5.2: Manipulation tasks ([Han10] and information on websites of robot suppliers)

Fig. 5.5: Stress testing of car seats [KUK14], head positioner [HEA14]

5.3 Description of selected manipulation tasks

Since in this work only PKS are considered, this section focuses especially on manipulation tasks for these systems. In the following, a pick & place, a positioning and a guidance task are described.

5.3.1 Handling (pick & place)

In a pick & place process an object with a mass of, e.g., 5 kg is handled. It is picked at the one end of the desired trajectory and placed at the other end. Such a trajectory is exemplary shown in Fig. 5.6. Here, the motion is placed in the xz-plane. In x-direction the trajectory reaches the boundaries of the prescribed workspace. The cycle time is set to $t = 0.4375$ s with a time step of 0.0005 s. Hence, 875 points along the trajectory are considered described by position vectors in the global reference frame. Additionally, velocity and acceleration vectors are specified. The value of the maximum velocity is 6.85 m/s, the value of the maximal acceleration is 49.86 m/s^2. This trajectory is an example for a pick & place task performed by a DELTA robot. It is also described in [Kie14; Sch13].

5.3.2 Positioning (quasistatic positioning)

Quasistatic positioning tasks can be found, for example, in aircraft assembly. Existing positioning systems consist of multiple manipulators with Cartesian or serial architecture, which act simultaneously to handle aircraft components [Ble03; Gog08; HL01; Mer06]. The manipulators pick up the aircraft component at defined grasping points and manipulate it in six DoF. The challenge for these assembly systems consists in the proper handling of large components with high payloads and extremely narrow tolerances in terms of absolute positioning accuracy and repeatability [Mer06]. Due to better stiffness and precision

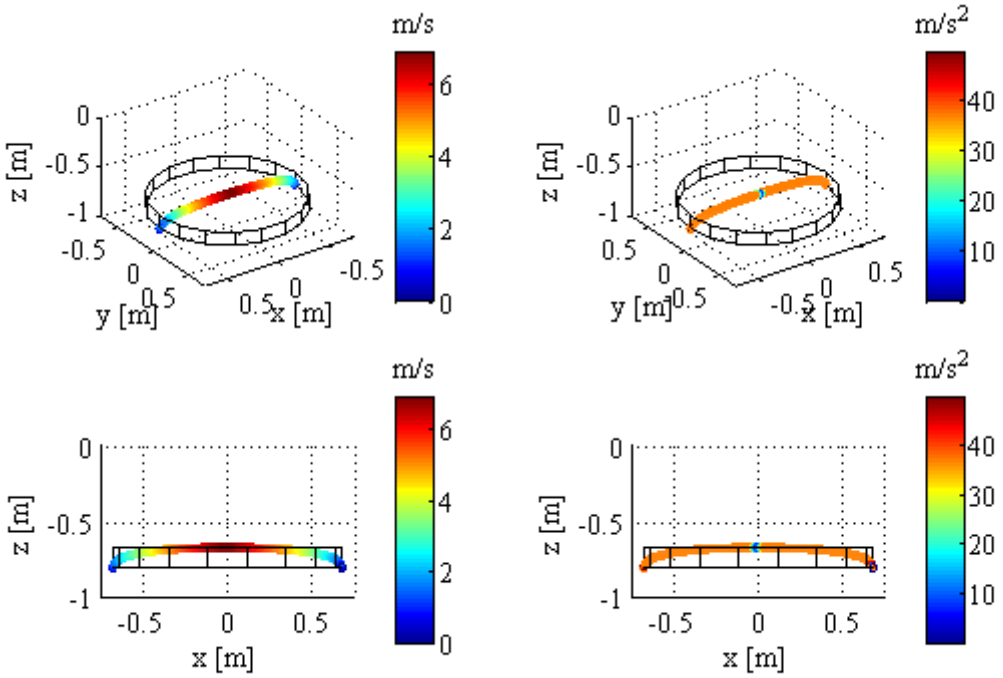

Fig. 5.6: pick & place trajectory, velocity (left) and acceleration (right) distribution

properties, parallel kinematic manipulators predestine the use in robot assisted aircraft structural assembly. Fig. 5.7 shows an exemplary positioning system for the handling of shell panels (S), which consists of two positioning units (Pos 1 and Pos 2). Each positioning unit comprises a parallel manipulator (PM) with three DoF and two bipod structures (B) with two DoF [PMC14].

The component to position has a mass of 1500 kg. An exemplary trajectory runs diagonally through the maximum workspace (e.g. cuboid). The maximum positioning velocity is 0.2 mm/s. The accelerations are negligibly small with a maximum of 0.01 m/s^2. [Kie14; Sch13; PMC14] describe this task in detail.

5.3.3 Guidance (3D fiber injection plant)

A method developed at the Institute of Plastic Processing (IKV) (3D fiber injection) allows directly manufacturing of near-net shape, three-dimensional preforms with local mechanical properties. This concerns fiber orientation, length and thickness. Basic material are thermoplastic hybrid rovings. Good component properties are achieved by a defined, near-net shape fiber placement on a permeable mold dictating the shape of the bottom or inside of the component.

The entire structure of the 3D fiber injection plant is shown in Fig. 5.8. The supply of semi-manufactured hybrid roving is located on the roof. The hybrid roving is directed

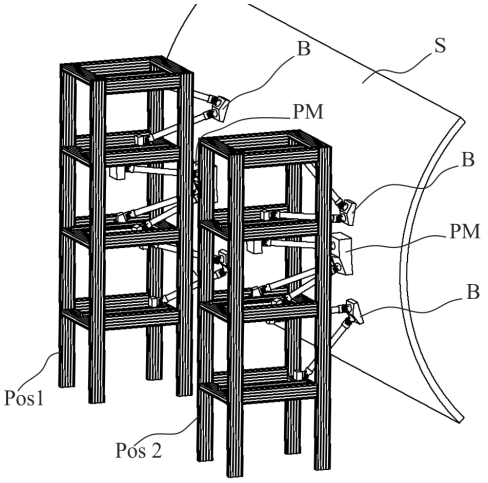

Fig. 5.7: Positioning system, PM = parallel manipulator, B = Bipod, S = shell, Pos = positioning unit

from there by a thread guide into the yarn take-off. Then, using airflow, venturi nozzles direct the roving in the cutter, where it is cut by a coated carbide knife. Airflow conveys the fibers to the fiber control unit, which determines the orientation of the fibers due to its funnel shape.

The fibers pass the opening of the fiber control unit and are "injected" and placed in specified trajectories on the permeable mold (forming tool). A 6-axis jointed-arm robot (RV30 26 of the company Reis GmbH & co. KG Maschinenfabrik [Rei14]) moves the forming tool on trajectories between the fixed fiber control unit and the either fixed or mobile extraction of air device (Fig. 5.8).

The extraction fixes the fibers in short term on the metal grid of the fiber forming tool and compresses them by the created vacuum. Two heaters symmetrically arranged on the fiber control unit melt the thermoplastic filaments. The glass fibers are fixed by the molten thermoplastic fibers and a robust preform is created.

The current design of the system has some disadvantages, which lead to poor quality of the preforms. These include:

- Deflection of the form grid from horizontal position (unilateral fixation, no suitable amount of extraction of air)
- No optimal motion of the forming tool (limited workspace)
- Limited movability of the robot (limitation through cell and robot size)
- Inertia of components (robot takes certain time to reach required speeds, time delays are possible)

A detailed analysis of the process and of the problems is carried out in [Ben14]. Other kinematic concepts for the manipulation of the forming tool under the fiber control unit

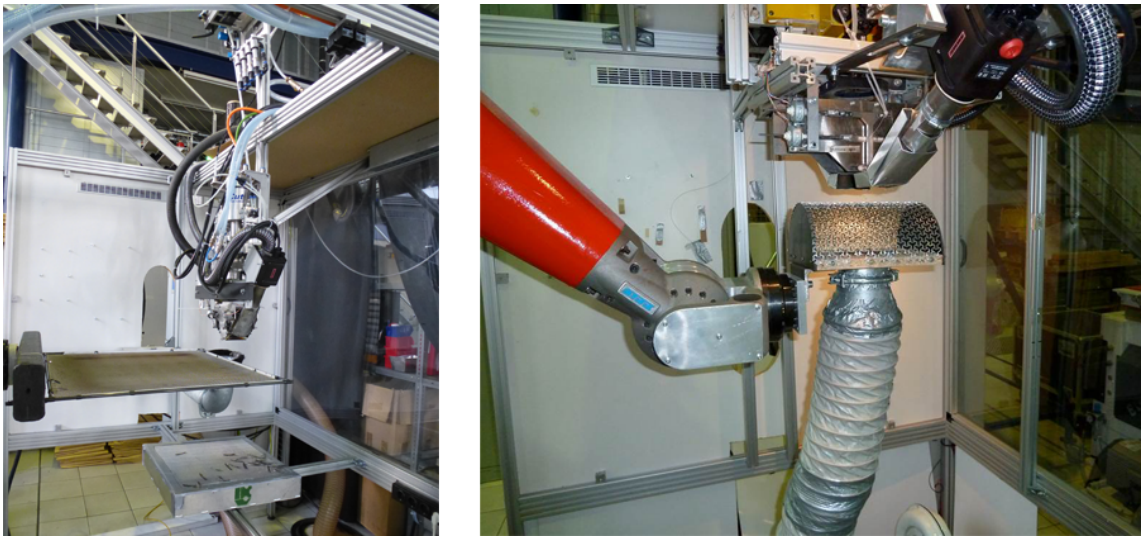

Fig. 5.8: Basic structure of the 3D fiber injection plant (left) [Ben14] and system with mobile and global air extraction (right) [Wer11]

are taken into consideration to counteract the problems mentioned above. These include, for example:

(1) Parallelkinematic manipulator with six DoF

(2) Parallelkinematic manipulator with three DoF and spherical wrist as end-effector

(3) Parallelkinematic manipulator with three translational DoF and additional spherical mechanism (spatial separation of translational and rotational DoF)

(4) PARAGRIP (cf. [Rie13])

Only concept (3) that decouples not only functionally, but also spatially the required translational and rotational DoF is relevant within this thesis. It is conceivable that the forming tool moves only translationally, while the fiber control unit performs the rotational motion using a spherical mechanism. For the translational motion one of the kinematic structures listed in Tab. 4 or 5, annexe, can be taken.

The requirements for the new kinematic concept are as follows: The desired workspace has the shape of a cuboid (0.6 m x 0.8 m x 0.33 m). At the same time the drop height must be selected small, about 0.03-0.1 m, to achieve a high degree of fiber orientation. To avoid collisions with the fiber control unit, all moving parts of the kinematic unit should be located “under” the mobile platform. The installation space is also limited because the extraction of air shall be integrated in the forming tool. To put all fibers on a horizontal surface, a stabilization of the mold should be included. This can be done e.g. through an integration of the forming tool in the kinematic structure. In order to meet future demands on trajectories the manipulator should reach speeds up to 0.6 m/s. The payload

through the forming tool and the preform is approximately 5 kg. The task requires a repeatability of the manipulator up to ±0.08 mm. To enhance the dynamic performance low inertia are advantageous. [Ben14]

5.4 Reference structures from industry

In order to provide a comparison between the synthesized PKS and industrial applications, some robotic examples are selected. With regard to the group of serial robots, PKS with three translational DoF are only able to compete against the SCARA robot. Neither vertical jointed-arm robots nor Cartesian robots have properties that 3-DoF PKS could fulfill in an appropriate manner: for example, the wide range of Cartesian robots or the dexterity of vertical jointed-arm robots due to their six DoF (cf. Chapter 2).

For further consideration, the Adept Cobra s600 [Ade14] is taken as a representative of this group because its characteristics are close to the median values determined in Tab. 2.2. With these properties the Adept Cobra s600 executes handling (pick & place, palletizing) or assembly tasks (see also Fig. 5.9, left). Besides, the Festo Tripod EXPT 120 and the Autonox24 Delta IP65 RL4 1200 are industrial examples for parallel robots (Fig. 5.9 middle left, middle right). They have similar properties, provide four DoF – three translational and one rotational at the end-effector – and are both used for handling tasks.

The Hexapod structure is not comparable to 3-DoF structures with regard to pick & place tasks because this kind of robot provides six DoF and therefore, it has a limited range of motion (Fig. 5.9, right). Though, Hexapods accomplish positioning tasks for high payloads. Nevertheless, the data given for positioning accuracy and range of motion for the translational degrees of freedom can only be taken as a rough reference target, since special designed robots (without rotational DoF) should be more precise.

Fig. 5.9: Adept Cobra s600, Festo Tripod EXPT 120, Autonox24 Delta IP65 RL4 1200, PI M-850 Hexapod (from left to right)

The properties of the chosen robots and the selected tasks (cf. Section 5.3) are listed in Tab. 5.3.

		DoF [-]	range [m]	height workspace [m]	required workspace [m^3]	installation space [m^3]	self weight [kg]	payload [kg]	process forces [N]	repeatability [mm]	accuracy [mm]	cycle/min $[\frac{1}{min}]$	max. end-effector velocity $[\frac{m}{s}]$	max. end-effector acceleration $[\frac{m}{s^2}]$
Robots	Adept Cobra s600	4	0.6	0.21	-	-	41	5.5	-	xy ±0.017, z ±0.003	n/a	143	(1.1)	n/a
	Festo Tripod EXPT 120	4	1.2	0.1	-	-	n/a	5	-	±0.1	±0.5	150	7	110
	Autonox24 Delta IP65 RL4 1200	4	1.2	0.25	-	-	n/a	6	-	0.1	n/a	60	n/a	n/a
	PI M-850 Hexapod	6	-	-	0.1	±0.025	17	250	-	±0.001	n/a	-	$5 \cdot 10^{-4}$	
Tasks	Handling (Pick & Place)	3	1.35	0.13	-	2x1.9x1.6	-	5	-	n/a	±0.5	137	6.85	49.86
	Positioning (quasistatic)	3	-	-	0.1x0.4x0.2	0.8x1.3x1.05	-	1500	-	±0.05	±0.1	-	$2{\cdot}10^{-4}$	0.01
	Others (3D fiber injection)	3	-	-	0.6x0.8x0.33	1.63x1.63x1.14	-	5	-	±0.08	n/a	-	0.6	n/a

Tab. 5.3: Properties of chosen robots and selected tasks

6 Derivation and implementation of calculation methods

To analyze the selected PKS, different calculation methods are necessary. First, relevant geometrical parameters are described. Afterwards, this section gives an overview of relevant algorithms and methods used in this work. Since 25 PKS are considered, all necessary derivations and equations can be found in the annex, pp. 229–283. Furthermore, Tab. 6.1 summarizes relevant literature related to the considered PKS with regard to calculations and analysis methods.

6.1 Definition of parameters

With regard to the dimensional synthesis and the illustration of the analysis methods, two reference frames are introduced: $R_0(O, x, y, z)$ describes the reference frame attached to the fixed base and $R_P(O_P, x_P, y_P, z_P)$ designates the reference frame attached to the end-effector. All axes of R_P are parallel to those belonging to R_0 because the end-effector is supposed to perform only translational motions (cf. Fig. 6.1, Fig. 6.2).

The three limbs are assembled symmetrically for all configurations. Therefore, the geometric parameters α and β are equal to 120° (Eq. (6.1), Eq. (6.2)). Additionally, for the $\star$-shaped configuration, the angle ψ is introduced. It designates the inclination of the actuation axes with respect to the xy-plane. The size of the end-effector is determined by the radius r_B, which defines a circle and hence, the location of the end-effector side joints B_i and the vector $\mathbf{b}_i$. For Δ and $\parallel$ frame configurations, the positions of the base joints A_i are defined by the frame radius r_A and the vector $\mathbf{a}_i$:

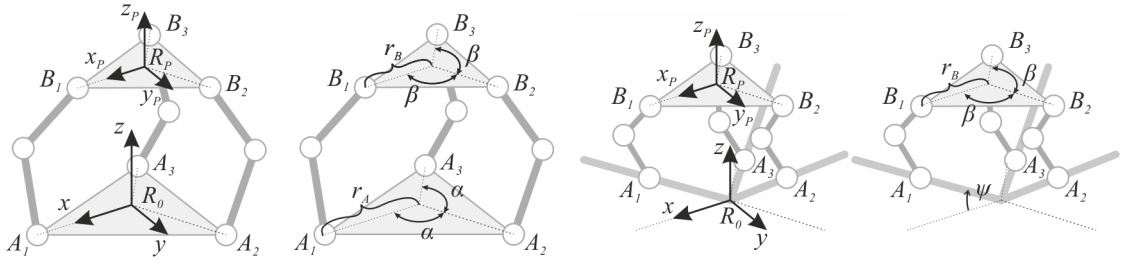

Fig. 6.1: Reference frames and parameter definition (Δ and $\star$-shaped)

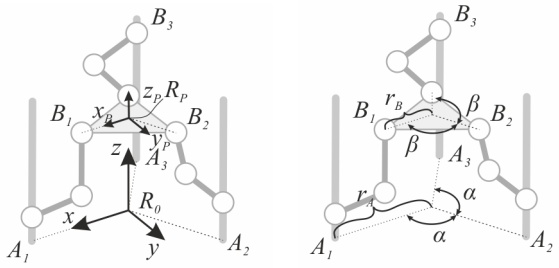

Fig. 6.2: Reference frames and parameter definition (‖-shaped)

$$\mathbf{a}_i = r_A \cdot \begin{pmatrix} \cos\alpha_i \\ \sin\alpha_i \\ 0 \end{pmatrix}, \tag{6.1}$$

$$\mathbf{b}_i = r_B \cdot \begin{pmatrix} \cos\beta_i \\ \sin\beta_i \\ 0 \end{pmatrix}. \tag{6.2}$$

Furthermore, rotation matrices are introduced to describe the reference frames attached to the base joints. The rotation matrix for rotation about the z-axis of R_0 is:

$$\mathbf{R}_{zi} = \begin{pmatrix} \cos\varphi_i & -\sin\varphi_i & 0 \\ \sin\varphi_i & \cos\varphi_i & 0 \\ 0 & 0 & 1 \end{pmatrix}. \tag{6.3}$$

For an inclination angle ψ the new reference frame is rotated again about the new x-axis:

$$\mathbf{R}_{xi} = \begin{pmatrix} 1 & 0 & 0 \\ 0 & \cos\psi & -\sin\psi \\ 0 & \sin\psi & \cos\psi \end{pmatrix}. \tag{6.4}$$

In general, each link is described by a vector $\mathbf{l}_i$. This vector is composed of a length, l_i, and the unit vector $\mathbf{l}_{0i}$. Velocity or acceleration vectors for the revolute joints are (with $\mathbf{e}_i$ = rotational axis):

$$\boldsymbol{\omega}_i = \omega_i \mathbf{e}_i \quad \text{and} \quad \dot{\boldsymbol{\omega}}_i = \dot{\omega}_i \mathbf{e}_i, \quad \text{with} \quad \omega_i = \dot{\Theta}_i, \tag{6.5}$$

and the velocity or acceleration vectors for the prismatic or cylindrical joints, respectively, are:

$$\dot{\mathbf{d}}_i = \dot{d}_i \mathbf{d}_{i0} \quad \text{and} \quad \ddot{\mathbf{d}}_i = \ddot{d}_i \mathbf{d}_{i0} \quad \text{resp.} \quad \dot{\mathbf{s}}_i = \dot{s}_i \mathbf{s}_{i0} \quad \text{and} \quad \ddot{\mathbf{s}}_i = \ddot{s}_i \mathbf{s}_{i0}. \tag{6.6}$$

6.2 Calculation methods and models

6.2.1 Kinematics

The kinematics describe the movement of elements, such as points, planes, or bodies, i.e. the temporal change of their position in space without taking into account masses or the causal forces [CBB04; Neu06]. The kinematic description is a prerequisite, for example, for the subsequent dynamic analysis, for which the acting forces on the system are considered. The aim of the kinematics is the representation of the relationship between input and output coordinates based on active coordinate transformations. This means that the motion of an object with respect to a fixed coordinate system is described.

For the **forward kinematics** (direct kinematics), the position and orientation of the end-effector is specified according to given coordinates of the actuator. The number of variables corresponds to the number of DoF of the structure. The direct kinematic problem is clearly analytically solvable for serial structures, but there are several solutions for parallel structures.

In contrast to the forward kinematics, the actuator quantities (such as angles, stroke lengths) in the **inverse kinematics** are calculated by backward transformation of the coordinates of the end-effector. For parallel structures, often only the inverse kinematic problem is analytically solvable; serial structures require a numerical approach. A desired trajectory defines the coordinates of the end-effector. Different approaches exist to solve the inverse kinematic problem: closed-form, numerical or meta-heuristic algorithms [Tab01]. In this work, the closed-form algorithm based on vector loop equations is chosen (cf. annex, pp. 229–283).

6.2.2 Jacobian matrix

The Jacobian is a descriptive structure matrix, which elements specify the translation and transmission ratios of the respective structure of their input to their output quantities. The Jacobian depends on the geometric parameters of the robot and its current position (cf. Eq. (7.1) and Eq. (7.2)). The Jacobian has various benefits. First of all it indicates the actuators to be selected in terms of power and speed. The Jacobian is known as a matrix of stability as well as a matrix of sensitivity [CBB04], as it is used to determine the singularities of a robot. There are different methods to calculate the Jacobian (see [Ang14; Spo05]). In this work, the Jacobian is determined by deriving analytical geometric expressions (here: vector loop equations).

6.2.3 Stiffness model

A stiffness model represents the influences of the stiffness on the motion behavior of the robot. Three main approaches are known to derive the stiffness matrix of a mechanical structure: The Finite Elements Analysis (FEA) [EF99; BPC11; BPB12; Cam12], the Virtual Joint Method (VJM) [Zha00; BPC11; PKC11] and the Matrix Structure Analysis (MSA) [BPC11; GC09].

Well-known is the FEA, which divides the structure into a large number of finite elements. These elements are connected elastically. The method is based on a numerical calculation approach, which serves to solve partial differential equations. An advantage of the FEA is that it is very accurate, depending only on the level of discretization [BPB12; BPC11; PKC11]. But in contrast, this requires high computational costs, not only for calculating the system of equations but also for re-meshing the model in each configuration.

The VJM, also known as "lumped modeling", is based on the work of Salisbury and Gosselin [Sal80; Gos90a], where the stiffness of a structure is derived considering only the actuator stiffnesses. The method reduces the compliance of every element in a structure to the compliance of the actuators by means of virtual compliant joints [TAL12] (for joints and for links). In comparison to the FEA, the VJM gives accurate results with much lower computational effort [BPB12; EF99].

The MSA is based on the FEA: the mechanical structure is modeled as a combination of beams connected by nodes. The stiffness properties of every beam element are represented in a stiffness matrix [GC09]. The displacement of every node is calculated analytically from the overall stiffness matrix. Initially introduced only for structures with relatively simple elements, it can be extended to integrate more complex effects (e.g. joint stiffness [DHM06]). Compared to the FEA, the MSA is less computational expensive [BPB12; BPC11; PKC11; AAS11] and results are in a good balance between computational costs and accuracy [PCW09]. Therefore, this method is used in this work to analyze the stiffness characteristics of the PKS. Translational and rotational deformations of the PKS at the end-effector resulting from stiffness properties of the links, the joints and the actuators are calculated. Details of the method and the modeling can be found in [Seb14; DC16].

6.2.4 Dynamics

The **forward dynamics** calculate the resulting system response due to provided actuation torques or forces. This serves amongst others as simulation of closed loop control. But since control strategies are not considered in this work, the forward dynamics are not derived for the selected PKS. In contrast, the **inverse dynamics** describe methods

for the calculation of forces and/or torques, which are based on the motion of bodies and their inertia characteristics. A desired motion of the end-effector is provided, e.g. in the form of a trajectory, and the required actuation torques or forces are calculated. Three approaches for the inverse dynamics calculation are common: the principle of virtual work, the Lagrangian equations of 2$^{\text{nd}}$ order and the Newton/Euler approach [CBB04]. Here, the last approach is chosen, because it allows calculating the internal forces or torques which are important for the design of actuators or joints in future work. For this approach, the motion state of all components must be known. The required velocities are calculated by using the Jacobian, the accelerations are determined by differentiating the vector loop equations twice. For the inverse dynamics the following equation is introduced:

$$\mathbf{F}_{int} = \mathbf{J}_p^{-1}\mathbf{F}_{ext}. \tag{6.7}$$

It describes the relation between the external forces (acting on the end-effector) and the internal forces. Thus, the matrix $\mathbf{J}_p$ is called the matrix of force transmission.

Since inertia properties are taken into consideration, the total inertia tensor $\mathbf{I}_{tot,i}$ of a limb i in the global reference frame R_0 has to be calculated. It is based on the local inertia tensor $\mathbf{I}_i$ in the link reference frame R_i (see PKS figures in annex for definition) and is transferred with the rotational matrix $\mathbf{R}_i$ into R_0 in the following way:

$$\mathbf{I}_{tot,i} = \mathbf{R}_i \cdot \mathbf{I}_i \cdot \mathbf{R}_i^T. \tag{6.8}$$

For a prismatic joint as limb it consists of two parts, the inertia tensor of the stator ($\mathbf{I}_{1i}$) and the one of the slider ($\mathbf{I}_{2i}$).

6.2.5 Multi-body simulation model

Mechanical components and their kinematic properties can be simulated with special multi-body simulation software. All derived analytic models (inverse kinematics, Jacobian matrix, accelerations, etc.) are validated by using MATLAB SimMechanics©. Especially for the stiffness analysis it should be pointed out that the results obtained by MATLAB SimMechanics© are based on a nonlinear model. Therefore, displacements do not match for very high payloads compared to the analytic model. For lower payloads and thus for smaller displacements, the consistency of the two models is ensured.

To model the stiffness properties, a custom joint is assembled in the middle of each link, which enables the specification of the link stiffness in each direction according to Eq. (10.5), p. 121. It is possible to model other stiffness properties of the PKS in the same way.

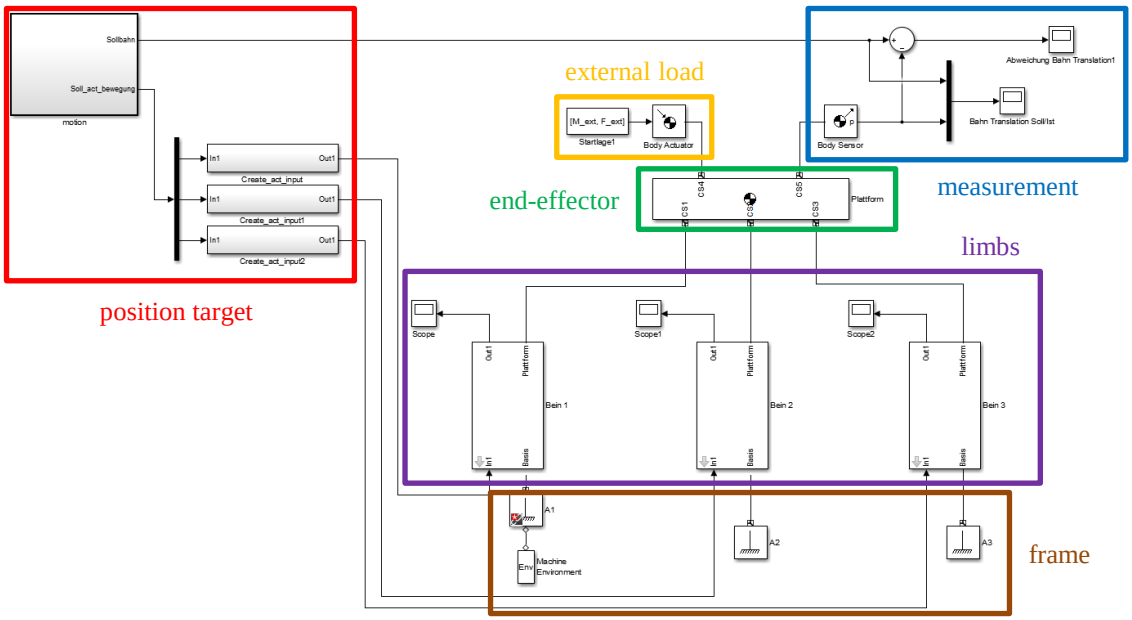

Fig. 6.3: Graphical interface of a MATLAB SimMechanics© model

More details about the built multi-body simulation models can be found in [Seb14; DC16; PMC14]. Furthermore, Fig. 6.3 gives an idea of the implementation. The models consist of a frame, limb substructures, an end-effector and blocks for defining the external load and the motion or position target. Final measurements can be made by using sensor blocks.

structure		kinematics inv.	dynamics inv.	Jacobian	analysis general	stiffness	singularities
3R-1P	RRC	[LZL10; DHZ12; SLT09]	-	-	[DHZ12; Tsa97]	-	-
	CRR	[KG02; GMD07; YHT13; KT03]	[YHT13; GMD07]	[GMD07; YHT13; KT03]	[KG02; YHT13]	[TH11; GMD07; QG11]	[KG02; KT03]
2R-2P	RPC	[RR11; CT03; YQ05b; GGZ10]	[GGZ10]	[GGZ10]	[RR11; RDP13]	-	[CT03]
	PRC	[YQ05b; LX06b; XL07; XL07]	[YQ07]	-	[LX06b; XL07; YQ05b]	[XL07]	[LX06b; XL07; YQ05b]
4R-1P	URC	[Di 04; KG05; Di 06]	-	-	-	-	-
	UPU	[TJ00; TJ01; TJ02; CHG99; CWH01; DP99; Gol02; Tsa96; WH11; YO10]	[CWH01; XYH07]	-	[TJ00; TJ01; TJ02; BMM02; BW10; CHG99; Che11; CP13; JT03; LJL04]	[Gol02]	[DP99; DiG04; HKK02; RAF02; WSP02; YO09; YO10]
	CRU	[CCC13]	-	-	[CCC13]	-	[CCC13]
	PUU	[TJ01; TJ02; ZBM04; YQ05c; LX06a; LXS11; YQ05a]	[YQ05a]	[LX06a]	[TJ01; TJ02; LX06a; XL06a]	[PCW08; PCW09; LX08; QY06; XL06c; XL06a; XL06b]	-
	CUR	[Rug08; CP03a; SNC08; LMZ07; ZHL06]	-	-	[Rug08; DP98; ZHL06]	-	[Rug08; CP03a; DP98; SNC08]
5R	RUU	[TJ02; ZBM04; WW11; WLF05; Di 01]	-	[TJ02]	[TTH08; WW11; YWS12; TJ01; WLF05; Di 01]	-	[TTH08; WW11]
	general	[CP03b; SCZ06; SZ05]	-	[TTH08]	[LH04; QZ03; SZ05; TT10]	-	[TTH08]

Tab. 6.1: Available research on considered structures and related work

7 Analysis and evaluation criteria

Based on the type synthesis (cf. Chapter 4) and the requirements for the manipulation task (cf. Chapter 5), the considered PKS can be analyzed and evaluated further. To perform a benchmark study, different criteria are applied. The first part of this chapter (Section 7.1) gives a brief review on the state of the art of relevant criteria in the context of robotics. The second part (Section 7.2) describes the final selection of the criteria for further analysis.

7.1 Compilation of relevant criteria

Relevant criteria found in literature are related to five groups. These contain:

- robotic structure
- kinematic model
- Jacobian matrix
- stiffness model
- dynamic model

With respect to the different groups, the criteria are listed and described in the next paragraphs. These criteria, also called performance indices, are used to:

- measure and quantify the performance properties,
- study, evaluate and optimize the design,
- compare different architectures

of (parallel) kinematic structures [PS14]. The performance indices can be either minimized or maximized to get an optimal result.

7.1.1 Criteria based on the robotic structure

The robotic structure comprises only the appearance based on different joints and links. Therefore, the **number of joints** and links can be treated as a first evaluation criteria. By increasing the number of joints (and thereby of links), for example, the stiffness of the entire PKS is reduced [Neu06]. In addition, the **kind of links** (e.g. hollow cylinder, square profile) influences the stiffness properties. Due to different accuracy and compliance

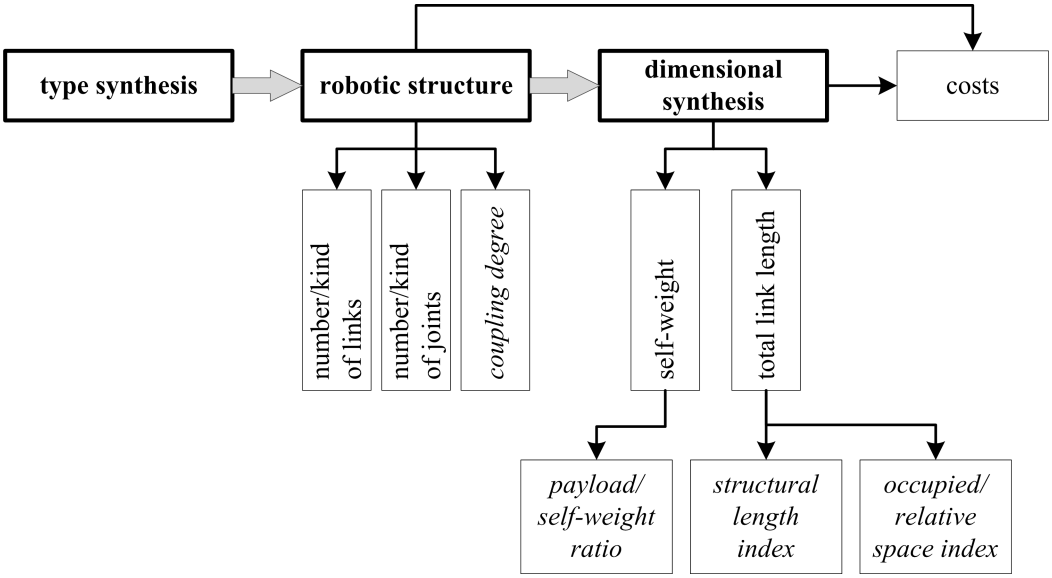

Fig. 7.1: Criteria based on the robotic structure

properties, the **kind of joints** within a PKS can highly affect the properties of the entire structure. To describe the decoupling of input and resulting output motion, the **coupling degree** (cf. Section 4.1.3) is taken into account by [CL09; JY04; SYM05]. Further properties of the PKS are revealed by performing a dimensional synthesis based on kinematic, dynamic and stiffness models. With known dimensions of the links, the size of the end-effector and material properties, the **self-weight** of the entire structure can be calculated. Thereafter, it is possible to calculate the **payload to self-weight ratio** (cf. Fig. 2.4, p. 12).

By considering the total link length of a (serial) robotic structure, three indices are introduced: the **occupied space index**, the **relative space index** and the **structural length index**. Please refer to [TTE95; KB06] for further information about the last mentioned indices.

Fig. 7.1 summarizes the mentioned criteria concerning the robotic structure.

7.1.2 Criteria based on the kinematic model

The kinematic model describes the relation between the position of the end-effector and the drive positions (cf. Section 6.2.1). By solving the inverse and/or forward kinematic problem, the reachable workspace of the PKS is calculated. With regard to a larger predefined space, the workspace index can be determined. Moreover, evaluation criteria for the reachable workspace contain on the one hand the **volume** and the **shape** [Sch87]. On the other hand the **distribution of the working volume** in Cartesian space can be analyzed. This is done by plotting the area of the workspace with respect to a variable

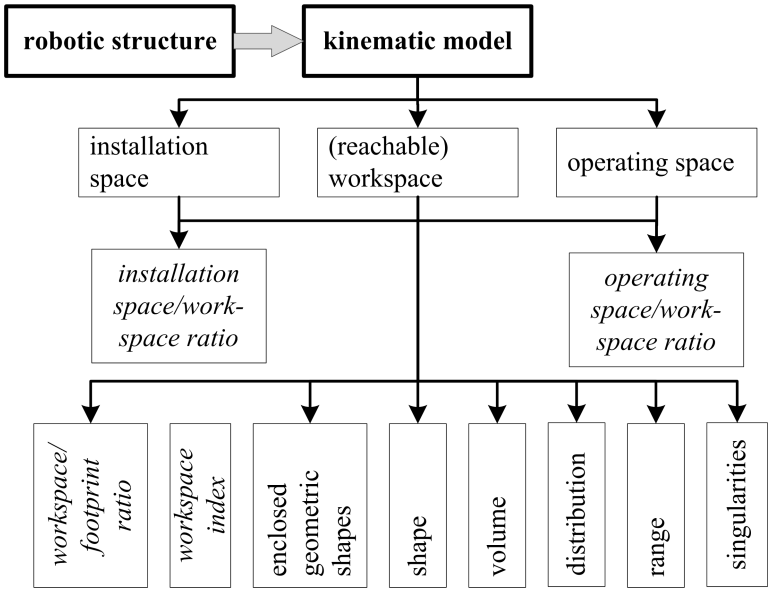

Fig. 7.2: Criteria based on the kinematic model

coordinate (e.g. z-direction) [GRN95]. As the **working range** can be one requirement, it is an evaluation criterion as well.

Another method to describe the properties of the workspace is to define and to calculate the size of **geometric objects** that can be enclosed by the reachable workspace. Such objects are, e.g. a sphere, a cylinder or a cube. A similar procedure for 2-DoF structures is presented in [LWP06]. Here, the biggest circle is calculated that fits into the reachable workspace. Frindt et al. [FKH11] develop a method to calculate the maximum cuboid inside the reachable workspace of a parallel robot. In all mentioned cases the reachable workspace should be free of singularities.

Two further criteria are the **volume of the installation space** and the **motion / operational space**. Both criteria have already been described in Section 5.1. Relating the volume of installation or motion space to the reachable or prescribed workspace results in the **installation space to workspace** and the **operating space to workspace ratio**. Both ratios should be minimized. Gosselin et al. [GMD07] proposes the vice-versa ratio. Frindt et al. [FKH11] suggest the (prescribed) workspace to footprint ratio as a performance criterion.

The criteria related to the kinematic model are presented in Fig. 7.2.

7.1.3 Criteria based on the Jacobian matrix

In general, the criteria based on the Jacobian matrix belong to the kinematic model, because it is related to the kinetostatic behavior of the manipulator. The **condition**

number is an indicator for the transmission quality of matrices. Since the Jacobian matrix describes the ratio between drive $\dot{\mathbf{q}}$ to output $\dot{\mathbf{p}}$ velocities and the inverse transposed Jacobian the ratio between drive torques or forces $\boldsymbol{\tau}$ to output forces or torques $\mathbf{F}$,

$$\dot{\mathbf{q}} = \mathbf{J} \cdot \dot{\mathbf{p}}, \tag{7.1}$$

$$\boldsymbol{\tau} = \mathbf{J}^{-T} \cdot \mathbf{F}, \tag{7.2}$$

the condition number of the Jacobian matrix is used to describe the **transmission quality** of PKS. In the best case the condition number is 1 which is equivalent to an isotropic and thus a uniform transmission behavior. As the Jacobian matrix depends on the position of the end-effector, the condition number is a local property of the robot. The condition number of a matrix is generally defined as (here: Euclidean norm, 2-norm) [DR06; Fri01; WWW10]:

$$\kappa(\mathbf{J}) = \kappa_{\|\cdot\|}(\mathbf{J}) := \|\mathbf{J}^{-1}\|\|\mathbf{J}\| = \frac{\sigma_{max}(\mathbf{J})}{\sigma_{min}(\mathbf{J})} = \frac{\sqrt{\lambda_{max}(\mathbf{J}^T\mathbf{J})}}{\sqrt{\lambda_{min}(\mathbf{J}^T\mathbf{J})}}. \tag{7.3}$$

As the condition number can reach values between 1 and ∞, the reciprocal of the condition number is often used. This is called **local conditioning index** [KB06; LWP06], **local dexterity index** [ZSZ10] or simply **dexterity index** [FKH11]:

$$\nu = \frac{1}{\kappa}. \tag{7.4}$$

Frindt [FKH11] uses the index of **kinematic condition** which was proposed by [AL92]. It is defined as follows ($min[\kappa(\mathbf{J})]$ is the minimum condition number of the entire workspace):

$$\kappa_c(J) = \frac{100}{min[\kappa(\mathbf{J})]}. \tag{7.5}$$

Gosselin [Gos90b] introduces the **new dexterity index**. It is based on the condition number of the Jacobian matrix $\mathbf{J}'$, composed by normalizing the Jacobian $\mathbf{J}$. This means that now all entries have the same physical units (length). The homogenization is done by eliminating the angular velocity of the end-effector [Gos90b].

To counteract the problem of inhomogeneous Jacobian matrix regarding different dimensions due to rotational and prismatic actuation, Ma et al. [MA91] and Chablat et al. [CCU10] use a **characteristic link length** (L). This characteristic natural (link) length is determined by Angeles [Ang92] so that it minimizes the condition number of the new

Jacobian matrix $\mathbf{J}_h$ which is calculated as follows:

$$\mathbf{J}_h := \mathbf{J} \cdot diag\left(\tfrac{1}{L}, \tfrac{1}{L}, \tfrac{1}{L}, 1, 1, 1\right). \tag{7.6}$$

Otherwise, in case of mixed actuator configurations, the Jacobian matrix has no physical meaning [SBS02]. Another possibility to address this problem is to divide the Jacobian matrix in two sub matrices, i.e. in a translational and a rotational part describing the transmission behavior (amongst others in [FKH11]). It should be noted that homogenization of the Jacobian should be treated carefully because the proposed methods are often arbitrarily chosen and suffer from lack of physical meaning [PS14; SBS02].

Schönherr [Sch97] and Neugebauer [Neu06] use the transmission quality Ü to describe the behavior between input to output quantities. It is similar to the conditioning index, however, in this case the Jacobian matrix is multiplied by a weighting matrix. Hence, for example, the actuation quantities can be weighted among each other (including conversion to quantities with same units, e.g. [SBS02]).

To include tolerance influences with respect to links besides the velocity and force or torque transmission in the description of the transmission quality, Schönherr [Sch97] introduces the following equation:

$$\ddot{\mathrm{U}}(\mathbf{J}, \mathbf{J}_d) = \frac{1}{2}(\|\mathbf{J}\|\|\mathbf{J}^{-1}\| + \|\mathbf{J}_d\|\|\mathbf{J}_d^{-1}\|). \tag{7.7}$$

The transmission quality is averaged about the sum of the condition numbers of the Jacobian of force transmission ($\mathbf{J}$) and of the Jacobian ($\mathbf{J}_d$), which is derived according to the tolerance effects. By minimizing Eq. (7.7), both a uniform load transmission and a uniform tolerance influence are achieved.

By integrating the local values (here the conditioning index) about the entire prescribed or reachable workspace W, the **global dexterity or conditioning index** is calculated [GLG95; GG97; GA91; KB06; LWP06; WWW10]:

$$\eta = \frac{\int_W (\xi) \mathrm{d}w}{\mathrm{d}w} = \frac{\int_W \left(\frac{1}{\kappa}\right) d\mathrm{d}w}{\mathrm{d}w}. \tag{7.8}$$

By globalization, a kind of average value is calculated, e. g. the arithmetic mean or the median representing the properties of the manipulator within the considered workspace. The following problem arises with one single value, because important information get lost: if only one high value of local property occurs, the average value is directly biased. Therefore, it is not useful to consider a globalized value, since local properties are more

important regarding the motion behavior of a robot [PS14]. Examples that show the disadvantages of globalization are presented in [Kie14].

If in one point both, the minimal and maximal singular values of the Jacobian matrix are high (i.e. $\sigma_{max} = \sigma_{min} \to \infty$) or very small (i.e. $\sigma_{max} = \sigma_{min} \to 0$) the manipulator is close to a singular configuration. The conditioning index does not cover this local phenomenon. Therefore, the **singularity index** is proposed in [SKC14]. It is best when close to 1.

$$s = min\left(\sigma_{min}, \frac{1}{\sigma_{max}}\right). \tag{7.9}$$

Based on the eigenvectors and eigenvalues of $\mathbf{J}^{-1}\mathbf{G}\mathbf{J}^{-T}$, the **manipulability ellipsoid** is determined. The matrix $\mathbf{G}$ is a diagonal weighting matrix representing the performance properties of the actuators. Please refer to Eq. (7.1) for the definition of the Jacobian matrix ($\mathbf{J}$). The major axis of the manipulability ellipsoid indicates the direction (eigenvector) with the highest velocity (square root of highest eigenvalue), the minor axis the direction with the lowest. If the calculation of the manipulability ellipsoid is based on $\mathbf{J}^T$, the major axis indicates the direction with the highest force, the minor axis the direction with the lowest force respectively. The manipulability ellipsoid of velocities is reciprocal to the manipulability ellipsoid of forces. This means that in the direction with high potential velocities, the mechanism can move with the least effort, whereas in the direction of the lowest force the manipulator is stiffest. Only minimum forces of the actuators are required to resist external forces [KPK00]. There exists a duality between task and articulation space. So it is possible to transform a sphere in the articulation space into an ellipsoid in the task space and vice versa.

Under the assumption of unit drive quantities, i.e. velocity $= 1\frac{m}{s}$ and force $= 1N$ or velocity $= 1\frac{1}{s}$ and torque $= 1Nm$ respectively, [CWM03; GG97; GLG98; LWP06; WWW10] present the calculation of the **velocity and payload index**. The maximal and minimal linear and angular velocity indices (force or torque indices) are determined about the square roots of maximal and minimal eigenvalue of the matrix $\mathbf{J}^{-1}\mathbf{G}\mathbf{J}^{-T}$ ($\mathbf{J}^T\mathbf{G}\mathbf{J}$). In this case $\mathbf{G}$ is equal to the identity matrix. It should be noted at this point that the Jacobian matrix is divided into a rotational and a translational part as soon as there are both kind of actuators, rotational and translational. Consequently, maximum and minimum velocity amplification (force amplification) in the direction of the main axes are:

$$\|v_{max}\| = \sqrt{\lambda_{vmax}}; \quad \|\omega_{max}\| = \sqrt{\lambda_{\omega_{max}}}, \tag{7.10}$$

$$\|F_{max}\| = \sqrt{\lambda_{Fmax}}; \quad \|\tau_{max}\| = \sqrt{\lambda_{\tau_{max}}}, \tag{7.11}$$

The velocity performance (payload capability) is better when the minimum velocity

(forces) increases. Also these two indices can be globalized by integration over the workspace.

[LWL10] derive based on an inverse dynamic model the **velocity and external payload capability**. In this case, the average of the maximal actuator velocity (force or torque) is calculated if a unit velocity (force) vector acts on the end-effector. This means they use the inverse ratio of the velocity and force transmission: input to output. If the value is small, the manipulator can withstand higher external forces with the same actuators. Translational and rotational parts of the Jacobian are separated in this calculation as well; globalization is also possible.

Already in 1985 the **manipulability measure** w is introduced by [Yos85] which is based on the determinant of the Jacobian (here over the ratio of output to drive velocities). It applies to redundant or non-redundant manipulators:

$$w(\mathbf{J}^{-1}) = \sqrt{\det(\mathbf{J}^{-1}(q)\mathbf{J}^{-T}(q))} \quad \text{resp.} \quad w(\mathbf{J}^{-1}) = |\det \mathbf{J}^{-1}(q)|. \tag{7.12}$$

If the determinant is non-zero, the system of equations is uniquely solvable and $\mathbf{J}^{-1}$ is invertible. w is proportional to the volume of the parallelepiped which is spanned by the vectors by $\mathbf{J}^{-1}$. At the same time $\det(\mathbf{J}^{-1})$ describes (with exception of a constant value) the volume of the manipulability ellipsoid generated by transformation of the unit sphere by means of $\mathbf{J}^{-1}$. In [Mer06] the manipulability measure is also called **manipulability index**. Zhang et al. proposed in [ZDC00] the following ratio as manipulability index where $\det(\mathbf{J}_m\mathbf{J}_m^T)$ is the maximum value:

$$\lambda = \sqrt{\frac{\det(\mathbf{J}\mathbf{J}^T)}{\det(\mathbf{J}_m\mathbf{J}_m^T)}} \quad \text{resp.} \quad \lambda = \frac{|\det(\mathbf{J})|}{|\det(\mathbf{J}_m)|}. \tag{7.13}$$

Another possibility to measure the isotropic behavior within the prescribed workspace is the calculation of the (local) **isotropy index**. It is defined as ratio of the manipulability index and the arithmetic mean of the eigenvalues. The upper bound is 1. The higher the isotropic index, the more isotropic is the manipulability ellipsoid. Thus, the isotropy index is better to evaluate the isotropic performance than the volume of the manipulability ellipsoid.

Another index based on the Jacobian matrix can be calculated, presented in [GG97]: the (global) **error index**. It describes the influence of position errors of drives $\delta\mathbf{q}$ as well as limb length tolerances $\delta\mathbf{e}_D$ on the position accuracy of the end-effector $\delta\mathbf{p}_{tot}$. It applies:

$$\delta\mathbf{p}_{tot} = \delta\mathbf{p} + \delta\mathbf{e}. \tag{7.14}$$

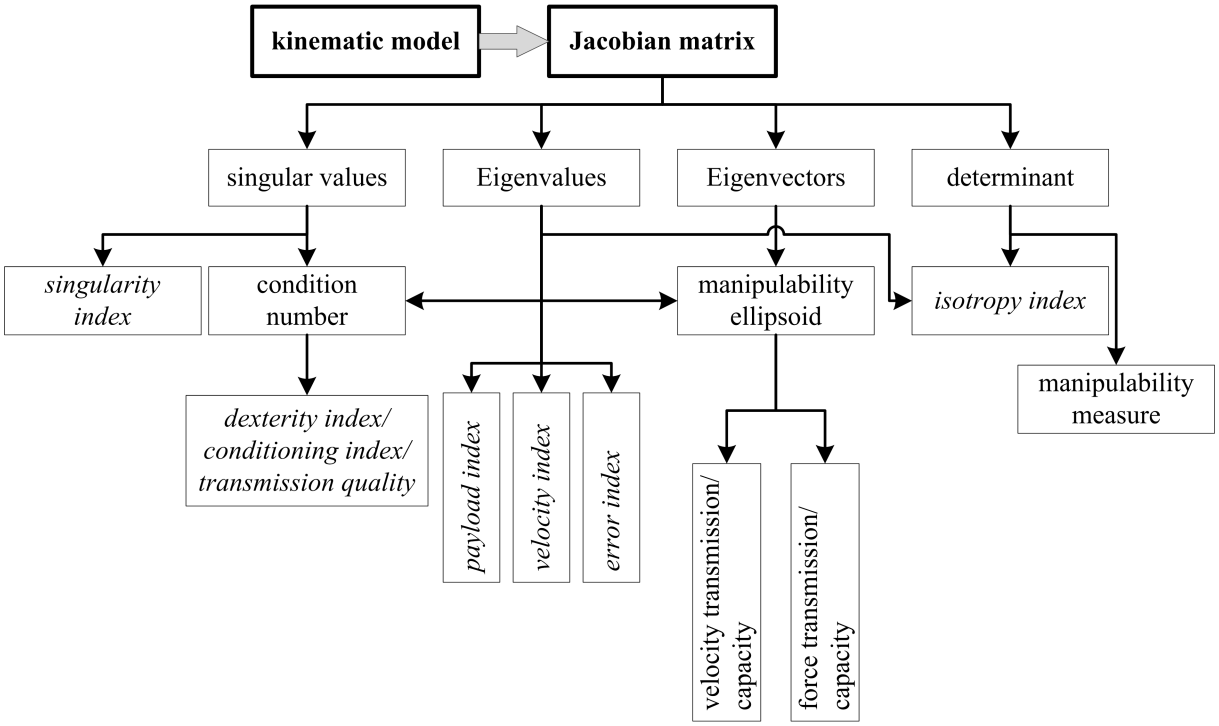

Fig. 7.3: Criteria based on the Jacobian matrix

If the end-effector has both, rotational and translation DoF, a separation between position and orientation errors should be made. The position errors $\delta\mathbf{p}$ of the end-effector are linked via Eq. (7.1) with the position errors of the drives $\delta\mathbf{q}$ allowing for the same indices as for the velocity index (cf. Eq. (7.10)). To determine the transmission of tolerance errors $\delta\mathbf{e}_D$ to position errors $\delta\mathbf{e}$ of the end-effector the matrix $\mathbf{J}_D$, describing the error transformation, has to be derived:

$$\delta\mathbf{e} = \mathbf{J}_D \delta\mathbf{e}_D. \tag{7.15}$$

The square roots of the maximum and minimum eigenvalues of $\mathbf{J}_D^T\mathbf{J}_D$ give information about the behavior of the structure. A note for determining $\mathbf{J}_D$ is omitted in [GG97]. But similar considerations are carried out by Binaud et al. in [BCW11] for a planar 3-DoF parallel manipulator. Binaud et al. specify an index describing the overall sensitivity of the end-effector due to variation of geometrical parameters as well as drive errors (**sensitivity index**). If the index is small, the sensitivity of the end-effector is low. For calculating this index, a new Jacobian has to be determined as already mentioned in [GG97]. This Jacobian is derived regarding changes in the joint positions. Fig. 7.3 summarizes the mentioned criteria related to the Jacobian matrix.

7.1.4 Criteria based on the stiffness model

Positioning errors of the end-effector can also be caused by the stiffness properties of the limbs, joints and the actuators. If the stiffness matrix $\mathbf{K}$ includes all actuator stiffnesses (diagonal matrix), the following relationship between drive forces or torques $\boldsymbol{\tau}$ and the displacement or twist $\Delta\mathbf{q}$ of the drive yields [GGG97; WWW10]:

$$\boldsymbol{\tau} = \mathbf{K} \cdot \Delta\mathbf{q} \tag{7.16}$$

Furthermore, positioning errors $\Delta\mathbf{p}$ of the end-effector and positioning errors $\Delta\mathbf{q}$ of the drives are related:

$$\begin{aligned} \Delta\mathbf{p} &= \mathbf{J}^{-1} \cdot \Delta\mathbf{q} \\ &= \mathbf{J}^{-1}\mathbf{K}^{-1}\mathbf{J}^{-T}\mathbf{F} \\ &= \mathbf{C} \cdot \boldsymbol{\tau}, \end{aligned} \tag{7.17}$$

where $\mathbf{C}$ is the compliance matrix and $\mathbf{f}_{EE}$ the applied force vector acting on the end-effector.

The so called **deformation or stiffness index** is calculated by the square roots of the maximal and minimal eigenvalues of $\mathbf{C}^T\mathbf{C}$. Here as well the geometric representation is an ellipsoid, in [KPK00] labeled as **compliance ellipsoid**. If an external load is applied

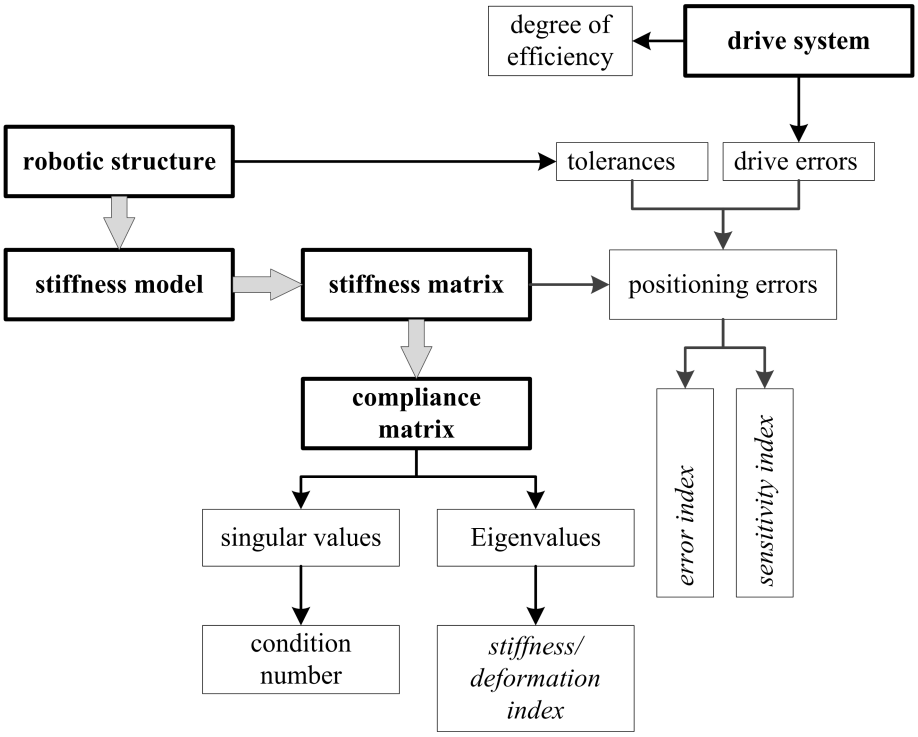

Fig. 7.4: Criteria based on the stiffness model

on the end-effector, this ellipsoid indicates the directions in which the displacements of the end-effector are the largest or the smallest. Thus, conclusions can be made on the stiffness behavior. The stiffness properties of the manipulator are better when the value of the highest deformation is as small as possible.

The condition of the matrix $\mathbf{C}$ can be calculated and thereby the conditioning index [LWP06]. However, it should be noted that the compliance matrix $\mathbf{C}$ depends on the Jacobian matrix. Therefore, $\mathbf{J}$ influences the condition number of $\mathbf{C}$.

The criteria based on the stiffness model are represented in Fig. 7.4.

7.1.5 Criteria based on the dynamic model

Performance indices based on the dynamic model highly depend on the inertia properties of the manipulator. With respect to the inverse dynamics different indices can be determined describing the dynamical behavior of the PKS. Analog to the manipulability measure the **dynamic manipulability measure** of redundant or non-redundant robots is introduced by [Asa83; Yos85]:

$$w_d = \sqrt{\det(\mathbf{J}^{-1}(\mathbf{M}^T\mathbf{M})^{-1}\mathbf{J}^{-T})} \quad \text{resp.} \quad w_d = \frac{|\det(\mathbf{J}^{-1})|}{|\det(\mathbf{M})|}. \tag{7.18}$$

where $\mathbf{M}$ is the inertia matrix. The value w_d is proportional to the volume of the **dynamic manipulability ellipsoid**. If unit forces or torques, respectively, are applied at the actuators, the dynamic manipulability ellipsoid designates the directions in which position or orientation changes of the end-effector are the easiest. Reworded, the manipulability ellipsoid indicates the directions in which changes of position and/or orientation of the end-effector require low (or high) forces.

Gregori et al. [GP02] take up the concept of dynamic manipulability. In an isotropic configuration, i.e. when the ellipsoid degrades to a sphere, the inertia forces are independent of motion changes. Li et al. [LWL10] and Gregori et al. [GP02] calculate an index for the local, translational **dynamic isotropy** which depends on the determinant and the trace of the inertia matrix.

Li et al. [LWL10] define two indices based on the inertia matrix: **acceleration capability** and **swiftness**. The acceleration capability with regard to actuator forces k_{At} is (i = number of limbs, $\bar{\mathbf{M}}_{ti}$ = submatrix of $\bar{\mathbf{M}}$, $\bar{\mathbf{M}} = \mathbf{JM}$):

$$k_{At} = \frac{1}{3}\sum_{i=1}^{3}\sqrt{\bar{\mathbf{M}}_{ti}\bar{\mathbf{M}}_{ti}^T}, \tag{7.19}$$

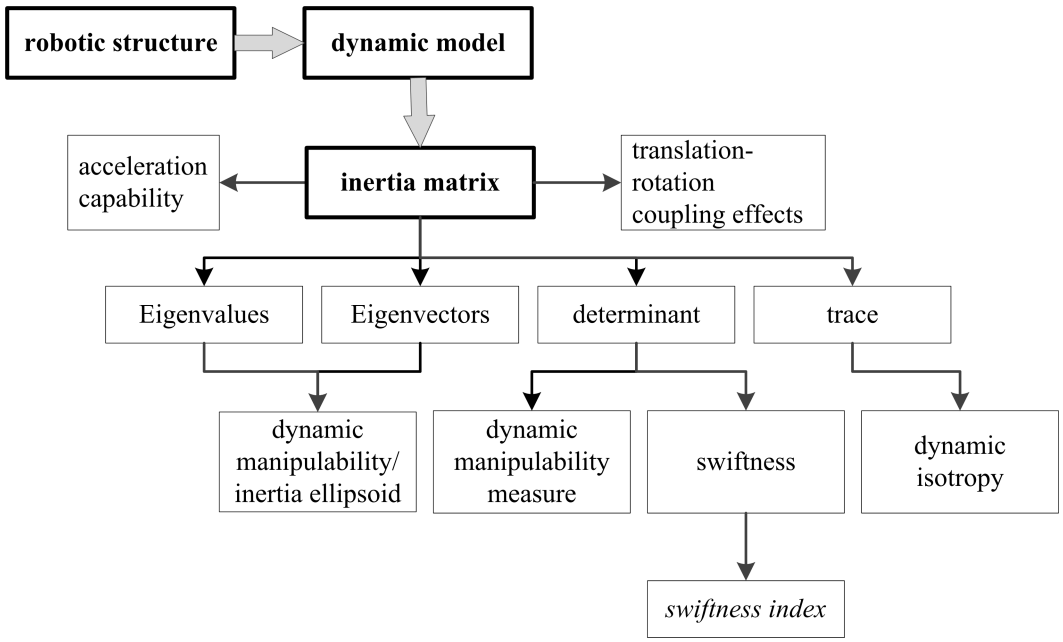

Fig. 7.5: Criteria based on the dynamic model

It is the average value of the maximal required actuator forces to produce unit acceleration of the end-effector. If the robotic structure has rotational degrees of freedom, the inertia matrix is divided into two parts and the rotational acceleration capability is considered separately. According to Eq. (7.8), the index can be globalized. If the global index is small, (here) the linear acceleration is better, i.e. the index describes the ability of the robot to accelerate the end-effector for the same variation of actuator forces or torques respectively. This is limited by the weakest acceleration that can be achieved in one direction [BK00].

The **swiftness** k_s is calculated as the reciprocal of the determinant of the inertia matrix [LWL10]:

$$k_s = \frac{1}{\det(\mathbf{M})}. \tag{7.20}$$

The greater the value, the easier high accelerations can be performed. $\det(\mathbf{M})$ describes (except of a constant factor) the volume of the dynamic manipulability ellipsoid resulting by transformation of the unit sphere by means of $\mathbf{M}$. Gregori et al. [GP02] define the swiftness slightly different compared to Eq. (7.20):

$$k_s = \frac{3}{tr(\mathbf{M})}. \tag{7.21}$$

The higher the arithmetic mean of the eigenvectors of the matrix $\mathbf{M}$ related to a position, the smaller are the accelerations the end-effector can reach from this point. This means that k_s must be minimized in this case. To calculate the swiftness index the values are

globalized about the workspace. The index only depends on the inertia and geometrical parameters of the manipulator and thus, it can be used to compare different architectures. It is recommended to consider the rotational swiftness separately if the robot has rotational DoF. Fig. 7.5 summarizes the mentioned criteria due to dynamic considerations.

7.2 Final selection for further analysis

For further analysis of the PKS, described in detail in Chapter 4 and annex, pp. 229–283, some of the mentioned criteria are selected. Concerning the robotic structure, only the kind of joints and the costs are relevant. Here, costs cover only the cost for links, joints and actuators. The PKS have to be described kinematically and dynamically anyway, so that the coupling degree cannot be used as an exclusion criterion. Furthermore, the number of joints is equal to three for each limb; the number of links varies between zero and two. Occupied space, relative space and structural length index are only applicable for serial structures and thus they are not relevant for the 3-DoF PKS. The payload to self-weight ratio can be taken into account to classify different kind of structures, already shown in Fig. 2.4, p. 12.

With regard to the kinematic model, the reachable workspace is an important design criterion. Since the shape or the volume are only less expressive, the size of the largest enclosed geometric object within the reachable (singularity-free) workspace is considered. The distribution of the reachable workspace is a good possibility for comparison. Since installation space to workspace ratio and operating space to workspace ratio are similar, for further optimization and/or evaluation only the operating space to prescribed workspace ratio is treated.

As structure describing matrix, the Jacobian matrix is important for a rash of optimization and evaluation criteria. For further analysis the conditioning index is taken into account. But to avoid singular configurations, for every point within the prescribed workspace the singularity index is interpreted. Moreover, by calculating the determinant of the Jacobian matrix (manipulability index) statements about its invertibility and thus the existence of singularities can be made.

To graphically show the transmission behavior, the manipulability ellipsoid is determined and based on it the minimum velocity and minimum payload index. The performance of the manipulator is the best when those indices are higher. This is related to the minimum singular value which is a better indicator of closeness to singularities than the condition number or the manipulability index [PS14]. Instead of calculating the volume of the

manipulability ellipsoid, the isotropy index is considered to evaluate the isotropic behavior of the manipulator.

Since local performance indices are more important than global indices, for comparison always the distribution within the prescribed workspace is plotted (e.g. by using box plots). All considered PKS have either only rotational or translational actuators and no rotational DoF, so that the problem of inhomogeneous Jacobians does not occur.

For a quick stiffness evaluation the concept of stiffness index can be chosen. The stiffness matrix [GRN95; HA86; TJ01] is used for comparison of different structures, which depends on the configuration and thus varies over the workspace. If an external force is applied, the resulting displacement at a particular position (e.g. at the TCP) can be calculated. As in this case only actuator stiffness properties are taken into account, for extended comparison a more detailed stiffness model, including link and joint stiffnesses, is developed (cf. Section 6.2.3).

All listed dynamic criteria depend on the mass matrix. So if dynamic properties should be considered, this matrix has to be derived. Alternatively, by calculating the required actuation forces or torques based on a dynamic model, inertia and accelerations properties can be taken into account.

8 First analysis and comparison of selected structures

To demonstrate the differences between the considered structures, a first optimization of the geometric parameters followed by a kinetostatic analysis for two load cases is performed. The procedure is similar to the approach presented in [Cha13; PCC14]. For the dimensional synthesis, the selected PKS have to be described according to their kinematic and kinetostatic properties. For that purpose, the inverse kinematics and the Jacobian matrix are derived analytically (cf. annex, pp. 229–283).

8.1 General assumptions

The aim is to minimize the actuator forces or torques respectively for two given external load cases at the end-effector within a prescribed workspace W_{pre}. W_{pre} is in the first case a cuboid with side lengths (x_S, y_S) of 0.2 m and a height z_S of 0.1 m and for the second case a cylinder with the radius $r_s = 0.25$ m and height z_s of 0.15 m (cf. Fig. 8.1). The coordinates of their midpoints M_S are shifted with z_{MS} only along the positive z-axis of the reference frame R_0. In this case z_{MS} is a variable parameter and hence the first optimization parameter. Due to complexity reasons and according to Eq. (8.1) only three points in each Cartesian direction of the prescribed workspace (here cuboid) are considered during optimization (hence, in total 27 points (cf. gray points in Fig. 8.1, left)). For the cylinder, the considered points are marked in Fig. 8.1 as well and the vector components are summarized in Eq. (8.2). Here, in total, 30 points are considered.

$$\begin{aligned} \mathbf{x}_{vec} &= \begin{pmatrix} 0.5x_S & 0 & -0.5x_S \end{pmatrix}^T \\ \mathbf{y}_{vec} &= \begin{pmatrix} 0.5y_S & 0 & -0.5y_S \end{pmatrix}^T \\ \mathbf{z}_{vec} &= \begin{pmatrix} z_{MS} + 0.5z_S & z_{MS} & z_{MS} - 0.5z_S \end{pmatrix}^T \end{aligned} \tag{8.1}$$

$$\begin{aligned}
\mathbf{r}_{vec} &= \begin{pmatrix} \frac{r_s}{2} & r_S \end{pmatrix}^T \\
\mathbf{z}_{vec} &= \begin{pmatrix} 0 & \frac{z_s}{2} & z_s \end{pmatrix}^T \\
\boldsymbol{\epsilon}_{vec} &= \begin{pmatrix} 0 & \frac{2}{5}\pi & \frac{4}{5}\pi & \frac{6}{5}\pi & \frac{8}{5}\pi \end{pmatrix}^T
\end{aligned} \tag{8.2}$$

Additionally, two different external force/velocity vectors/matrices ($\mathbf{f}_{EE}, \mathbf{v}_{EE}$) are assumed for further calculations:

$$\begin{aligned}
\text{Case 1:} \quad & \mathbf{f}_{EE} = \begin{pmatrix} 2 & 2 & -10 \end{pmatrix}^T N; \quad (1)\ \mathbf{v}_{EE} = \begin{pmatrix} 1 & 0 & 0 \end{pmatrix}^T \frac{m}{s}, \\
& (2)\ \mathbf{v}_{EE} = \begin{pmatrix} 0 & 1 & 0 \end{pmatrix}^T \frac{m}{s}, \quad (3)\ \mathbf{v}_{EE} = \begin{pmatrix} 0 & 0 & 1 \end{pmatrix}^T \frac{m}{s}
\end{aligned} \tag{8.3}$$

$$\text{Case 2:} \quad \mathbf{f}_{EE} = \begin{pmatrix} 180 & 180 & 85 \end{pmatrix}^T N; \quad \mathbf{v}_{EE} = \begin{pmatrix} 5 & 5 & 2 \end{pmatrix}^T \frac{m}{s} \tag{8.4}$$

The first case is only a simple scenario without directly considering a specific application. Besides low forces in x- and y-direction, the force acting on the end-effector in z-direction is higher (for example due to gravity considerations). Furthermore, the end-effector should move with at least 1 $\frac{m}{s}$ in every Cartesian direction.

Case 2 is related to the pick & place task described in Section 5.3.1. With a handling mass of 5 kg, the external force is calculated with respect to the desired acceleration properties. In general, accelerations in x- and y-direction are higher (here 36 $\frac{m}{s^2}$, cf. Fig. 5.6, p. 54), whereas the acceleration in z-direction is less than 1**g** (here 7 $\frac{m}{s^2}$). The external force vector (Eq. (8.4)) is calculated with these assumptions. The applied velocity vector is derived from the handling task described in Section 5.3.1 as well. Only the diameter of the prescribed workspace (cylinder) is smaller than presented in Fig. 5.6 (here: = 0.5 m).

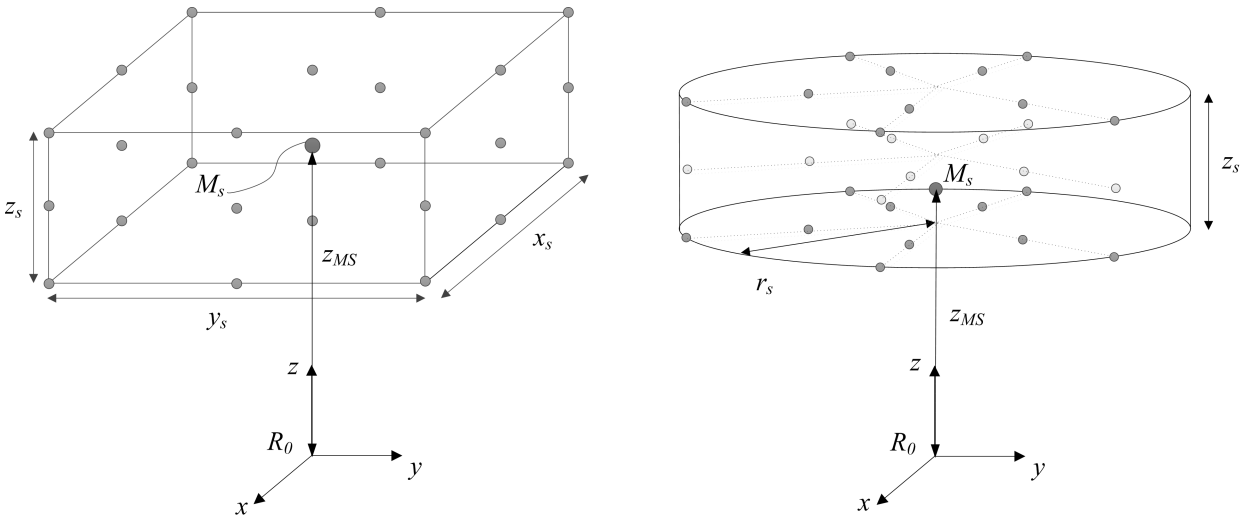

Fig. 8.1: Prescribed workspaces and considered points

Both, the reachable and the prescribed workspace of the PKS are obtained by discretization of a sufficiently large space. For every point of this space (cf. Eq. (8.1)), the actuator positions and internal joint parameters are calculated by means of the inverse kinematic model (*InvKin*) and the Jacobian matrix. The actuator forces (f_q) and torques (τ_q) respectively are considered separately for each limb for the given payload. Thereby, the objective functions are written as follows for linear and rotational drives:

$$\min f_{q,max}(\mathbf{Optpar}) = \min(\max|f_{q,i}(\mathbf{f}_{EE})|) \tag{8.5}$$

$$\min \tau_{q,max}(\mathbf{Optpar}) = \min(\max|\tau_{q,i}(\mathbf{f}_{EE})|) \tag{8.6}$$

with **Optpar** as vector of all parameters to be optimized. So the aim is to minimize the required actuator forces or torques respectively. Thereby, for every point within W_{pre} only the maximum of all three actuator forces or torques is considered.

Each structure and frame configuration has maximum five variable parameters that can be optimized (see as well annex, pp. 229–283). These include:

- Distance between base reference frame R_0 and R_p (z_{MS})
- Size of end-effector (r_B)
- Frame size (r_A) (only for Δ and $\|$ frame configuration)
- Inclination angle (ψ) (only for $\star$-shaped frame configuration)
- Link lengths (l_1, l_2)
- Revolute joint inclination angle (δ) (only for CRR$^{\Delta}$, CRR$^{\|}$, CPR$^{\Delta}$, CUR$^{\Delta}$, CUR$^{\|}$)

For all these optimization parameters lower (l_b) and upper (u_b) bounds are defined, summarized in Tab. 8.1.

Furthermore, several boundary conditions (BC_i) have to be applied to assure that the calculated values are feasible. These boundary conditions are explained in more detail in the following.

Tab. 8.1: Bounds of optimization parameters

		Case 1	**Case 2**
r_A	[m]	0.2 - 0.6	0.2 - 0.6
r_B	[m]	0.1 - 0.5	0.1 - 0.5
ψ	[°]	5 - 30	5 - 30
l_1	[m]	0.1 - 0.5	0.2 - 0.7
l_2	[m]	0.1 - 0.5	0.2 - 0.9
z_{MS}	[m]	0.15 - 0.85	0.15 - 0.95
δ	[°]	5 - 80	5 - 80

8.2 Optimization method

For every point within the discretized space it is checked if the joint parameters are real for the desired position $\mathbf{p}$ of the end-effector:

$$BC_1(\mathbf{p}) = \begin{cases} 1, & \text{if } img(InvKin) = 0 \\ 0, & else \end{cases}. \tag{8.7}$$

Then, the calculated actuator positions $\mathbf{q}(\mathbf{p})$ are compared to the admissible maximum and minimum joint limits (q_{max}, q_{min}) (given by the stroke length and angular boundaries respectively):

$$BC_2(\mathbf{p}) = \begin{cases} 1, & \text{if } max(\mathbf{q}(\mathbf{p})) \leq q_{max} \wedge min(\mathbf{q}(\mathbf{p})) \geq q_{min} \\ 0, & else \end{cases}. \tag{8.8}$$

If the two boundary conditions BC_1 and BC_2 are fulfilled, the considered point P (defined by $\mathbf{p}$) is a valid point for the PKS and hence, a point of its reachable workspace.

Furthermore, to evaluate the quality for every valid point of the end-effector, the singularity index is taken into consideration for case 2 optimization (cf. Eq. (7.9), p. 74):

$$BC_3(\mathbf{p}) = \begin{cases} 1, & \text{if } s \geq 0.1 \\ 0, & else \end{cases}. \tag{8.9}$$

It should be mentioned at this point, that the presented approach is only one possibility to find valid points. For sure, there are other approaches, for example, [NRC07] analyzes the singularity positions of the PKS in order to get feasible boundaries of the workspace and hence, valid points.

The definition of additional boundary conditions is required with regard to the optimization and the prescribed workspace. Since the actuator velocities generally increase when minimizing the actuator forces, in particular, the maximum of the actuator velocities $\dot{\mathbf{q}}(\mathbf{p})$ should not exceed a certain limit ($\dot{q}_{max}$, $\dot{q}_{min}$) (Eq. (8.10)). The minimum actuator velocity is equal to zero.

$$BC_4(\mathbf{p}) = \begin{cases} 1, & \text{if } max(\dot{\mathbf{q}}(\mathbf{p})) \leq \dot{q}_{max} \\ 0, & \text{if } max(\dot{\mathbf{q}}(\mathbf{p})) > \dot{q}_{max} \vee min(\dot{\mathbf{q}}(\mathbf{p})) < \dot{q}_{min} \end{cases} \tag{8.10}$$

Tab. 8.2: Further limits

		Case 1	**Case 2**
Max. $\sum$ of link lengths (l_{max})	[m]	1	1.3
Max. stroke length	[m]	0.4	0.6
Max. velocity (linear)	$[\frac{m}{s}]$	2.5	7.5
Max. velocity (rotational)	$[\frac{rad}{s}]$	5.19π	10.38π
Max. angular range	[°]	180	

Furthermore, the radius of the end-effector r_B should be smaller than the radius of the frame r_A (Eq. (8.11)). This condition can only be applied for the triangular and parallel frame configuration. In case of the star-shaped frame configuration, the parameter r_A does not occur.

$$BC_5(\mathbf{Optpar}) = \begin{cases} 1, & \text{if } r_A > r_B \\ 0, & \text{else} \end{cases}. \tag{8.11}$$

At last, the sum of all link lengths ($\sum l_i$) and the displacements of the prismatic or cylindrical joints ($\mathbf{q}_S$) not attached to the frame should not exceed the value l_{max} (here equal to 1):

$$BC_6(\mathbf{p}) = \begin{cases} 1, & \text{if } \sum l_i + max(|\mathbf{q}_S(\mathbf{p})|) < 1 \\ 0, & \text{else} \end{cases}. \tag{8.12}$$

The minimization problem is solved by using the genetic algorithm of the MATLAB Optimization Toolbox [The14]. Based on the evolution, there are randomly generated solution candidates for the above mentioned minimization problem. The objective function value improves and ideally achieves the optimum by changing the solution candidates according to different rules [Wei02]. The initialization of the algorithm randomly creates a population (here size of 250) describing the number of solution candidates (individuals). Within this population, individuals are further changed by varying the individual parameters (mutation) and evaluated by the fitness function (fi). As Eq. (8.5) describes a minimization problem, individuals with lesser fitness are selected (selection) and used as starting values for new generations [GKK04]. The maximum number of iterations is set to 1000 for case 1 and 100 for case 2. The fitness function contains the boundary conditions described in Section 8.2. Let g_h be the function value of a tested boundary condition h. The boundary conditions are distinguished between inequalities with an upper bound ub and with a lower bound lb respectively:

$$g_h < ub_h; \quad g_h > lb_h.$$

If an individual satisfies a boundary condition, its fitness remains constant. If an individual does not comply with a constraint it is not eliminated, but punished instead by adding a penalty value. This value indicates how to adjust the following individuals and thus affects the efficiency of the algorithm. The penalty values consist of a constant value C_1 ($> 10^7$) and a linear term. The linear term is the difference between the test value g_h and the upper or lower bound (ub_h, lb_h) respectively and it is multiplied by a constant C_2 ($> 10^7$). If a boundary condition is violated by an upper bound, the fitness fi is

$$fi = fi + (g_h - ub_h) \cdot C_2 + C_1, \tag{8.13}$$

and in case of the lower bound:

$$fi = fi + (lb_h - g_h) \cdot C_2 + C_1. \tag{8.14}$$

If, however, all tested boundary conditions are complied, the resulting fitness corresponds to the computed objective function value (cf. Eq. (8.5)).

8.3 Analysis procedure

The analysis of the optimized PKS is based on different criteria with regard to the prescribed workspace W_{pre} (cf. Fig. 8.1). The applied load case is the same as for the optimization in section 8.1 (cf. Eq. (8.3) and Eq. (8.4)). The workspace is discretized with a step size of 0.01 m. Consequently, the performance of each structure is analyzed at 4851 points within the prescribed workspace for case 1. For case 2 7920 points are considered, i.e. the step size for the radius is 0.025 m, the step size for the height is 0.015 m and the step size for ϵ is $\frac{\pi}{36}$.

For the given end-effector velocities the necessary drive velocities are calculated using Eq. (7.1). For each point within the prescribed workspace the maximum of all velocities is stored for further analysis. When an external load $\mathbf{f}_{EE}$ is applied at the end-effector, the necessary actuator forces and torques $\boldsymbol{\tau}$ can be calculated by the following equations [Gos90a]:

$$\boldsymbol{\tau} = \begin{pmatrix} f_{q1} \\ f_{q2} \\ f_{q3} \end{pmatrix} = \mathbf{J}^{-T} \cdot \mathbf{f}_{EE}; \quad \boldsymbol{\tau} = \begin{pmatrix} \tau_{q1} \\ \tau_{q2} \\ \tau_{q3} \end{pmatrix} = \mathbf{J}^{-T} \cdot \mathbf{f}_{EE}. \tag{8.15}$$

Based on Eq. (7.1) and Eq. (8.15), the required power of the actuators $\mathbf{pw}_q$ can be expressed as:

$$\mathbf{pw}_q = \boldsymbol{\tau}_q \cdot \dot{\mathbf{q}}. \tag{8.16}$$

Furthermore, for this first analysis stiffness properties of the actuators are taken into account. With the compliance matrix $\mathbf{C}_q$ of the actuators the displacement of the end-effector $\Delta\mathbf{p}$ due to an applied external force $\mathbf{f}_{EE}$ can be calculated (see Eq. (7.17)). All links and joints are treated as ideally rigid (cf. Eq. (7.17), p. 77). Tab. 8.3 summarizes the compliance c_{qi} (diagonal entries of the compliance matrix) of the linear and rotational actuators respectively.

The positioning error $\delta\mathbf{p}$ measures the maximum deviation of the position of the end-effector from the target position in relation to the inaccuracies of the actuators $\delta\mathbf{q}$. Thus, it is a measure of the positioning accuracy [Nef10], Eq. (7.14):

$$\|\delta\mathbf{p}\| = max(\|\|\mathbf{J}^{-1}|\delta\mathbf{q}\|\|). \tag{8.17}$$

The inaccuracies of the actuators $\delta\mathbf{q}$ depend on the direction of the inaccuracy. As all of the analyzed PKS come with three actuators, eight possible combinations of directions are considered (Eq. (8.18)):

$$\delta\mathbf{q} = \begin{bmatrix} \delta q_1 & 0 & 0 \\ 0 & \delta q_2 & 0 \\ 0 & 0 & \delta q_3 \end{bmatrix} \cdot \begin{bmatrix} 1 & 1 & 1 & -1 & 1 & -1 & -1 & 1 \\ 1 & 1 & -1 & 1 & -1 & -1 & 1 & -1 \\ 1 & -1 & 1 & 1 & -1 & 1 & -1 & -1 \end{bmatrix}. \tag{8.18}$$

δq_i is the positioning error of the actuator of limb i. $\delta\mathbf{q}$ is a 3x8-matrix with a 3x1 vector in each column. Finally, $\delta\mathbf{p}$ describes the displacement of the end-effector in x-, y-, and z-direction for the respective direction of motion. Here, only the maximum of the norm of each column of $\delta\mathbf{p}$ is considered. The values for the positioning error of linear and rotational actuators are listed in Tab. 8.3. To evaluate the transmission quality of the workspace, the local dexterity index is calculated for every point within W_{pre} (cf. Eq. (7.5)). For the analysis and comparison only the maximum value of the current criteria – except for the local dexterity index the minimum – at the considered point is taken into account.

Tab. 8.3: Actuator properties [Wit14a; Hiw13]

	linear actuator	**rotational actuator**
position accuracy	$0.52 \cdot 10^{-3}$[m]	$\frac{\pi}{10800}$[rad]
compliance	$\frac{1}{150} \cdot 10^{-6}[\frac{m}{N}]$	$\frac{\pi}{10800 \cdot 43}\left[\frac{rad}{Nm}\right]$

8.4 Results

The optimized parameters for all PKS for load case 1 and 2 are listed in Tab. 8.4. In the following, the PKS are compared regarding geometrical parameters, workspace and performance.

8.4.1 Geometrical parameters

Fig. 8.2a shows the relation between l_1 and l_2 and Fig. 8.2b between r_A and r_B respectively. In general, link lengths for case 2 are longer than for case 1. This is due to the fact, that

Tab. 8.4: Dimensions resulting from first analysis

	Case 1							Case 2						
PKS	z_{MS} [m]	r_A [m]	r_B [m]	l_1 [m]	l_2 [m]	ψ [°]	δ [°]	z_{MS} [m]	r_A [m]	r_B [m]	l_1 [m]	l_2 [m]	ψ [°]	δ [°]
$\underline{\text{R}}\text{RC}^{\Delta}$	0.43	0.43	0.16	0.19	0.49	-	-	0.62	0.6	0.15	0.35	0.78	-	-
$\underline{\text{C}}\text{RR}^{\Delta}$	0.18	0.52	0.5	0.21	0.27	-	60	0.51	0.53	0.44	0.31	0.43	-	15
$\underline{\text{C}}\text{RR}^{\parallel}$	0.58	0.55	0.11	0.45	0.46	-	51	0.64	0.59	0.12	0.46	0.46	-	52
$\underline{\text{C}}\text{RR}^{\star}$	0.39	-	0.1	0.31	0.31	25	-	0.59	-	0.16	0.36	0.37	13	-
$\text{R}\underline{\text{P}}\text{C}^{\Delta}$	0.57	0.56	0.18	-	-	-	-	0.64	0.6	0.14	-	-	-	-
$\underline{\text{R}}\text{PC}^{\Delta}$	0.22	0.6	0.1	-	-	-	-	0.64	0.6	0.15	-	-	-	-
$\underline{\text{C}}\text{PR}^{\Delta}$	0.37	0.5	0.5	-	-	-	37	0.68	0.27	0.27	-	-	-	13
$\underline{\text{C}}\text{PR}^{\star}$	0.54	-	0.1	-	-	17	-	0.76	-	0.2	-	-	10	-
$\underline{\text{P}}\text{RC}^{\parallel}$	0.55	0.59	0.27	0.5	-	-	-	0.80	0.54	0.23	0.7	-	-	-
$\underline{\text{P}}\text{RC}^{\star}$	0.46	-	0.42	0.5	-	10	-	0.32	-	0.5	0.35	-	30	-
$\underline{\text{U}}\text{UP}^{\Delta}$	0.15	0.59	0.35	0.5	-	-	-	x	x	x	x	-	-	-
$\underline{\text{U}}\text{RC}^{\Delta}$	0.24	0.5	0.35	0.38	0.15	-	-	0.36	0.3	0.28	0.53	0.2	-	-
$\underline{\text{U}}\text{CR}^{\Delta}$	0.53	0.44	0.44	0.44	-	-	-	0.81	0.27	0.27	0.7	-	-	-
$\text{U}\underline{\text{P}}\text{U}^{\Delta}$	0.56	0.51	0.14	-	-	-	-	0.62	0.6	0.1	-	-	-	-
$\underline{\text{C}}\text{RU}^{\Delta}$	0.84	0.26	0.12	0.5	0.5	-	-	0.87	0.59	0.3	0.52	0.9	-	-
$\underline{\text{C}}\text{RU}^{\star}$	0.37	-	0.4	0.1	0.39	28	-	x	-	x	x	x	x	-
$\underline{\text{P}}\text{UU}^{\Delta}$	0.38	0.38	0.38	0.5	-	-	-	0.4	0.52	0.5	0.7	-	-	-
$\underline{\text{P}}\text{UU}^{\parallel}$	0.54	0.6	0.27	0.5	-	-	-	0.68	0.28	0.15	0.49	-	-	-
$\underline{\text{P}}\text{UU}^{\star}$	0.34	-	0.15	0.49	-	5	-	0.15	-	0.36	0.7	-	5	-
$\underline{\text{R}}\text{UC}^{\Delta}$	0.53	0.54	0.26	0.26	0.5	-	48	0.92	0.35	0.45	0.6	0.65	-	9
$\underline{\text{C}}\text{UR}^{\Delta}$	0.78	0.55	0.23	0.5	0.5	-	52	0.86	0.58	0.34	0.7	0.6	-	82
$\underline{\text{C}}\text{UR}^{\parallel}$	0.53	0.5	0.5	0.25	0.43	-	77	0.95	0.33	0.3	0.35	0.6	-	40
$\underline{\text{C}}\text{UR}^{\star}$	0.65	-	0.27	0.33	0.35	14	-	0.8	-	0.26	0.53	0.34	26	-
$\underline{\text{U}}\text{RU}^{\Delta}$	0.56	0.6	0.1	0.4	0.48	-	-	0.83	0.5	0.2	0.46	0.6	-	-
$\underline{\text{U}}\text{UR}^{\Delta}$	0.47	0.39	0.18	0.2	0.5	-	-	0.6	0.6	0.11	0.36	0.8	-	-
$\underline{\text{R}}\text{UU}^{\Delta}$	0.6	0.45	0.33	0.23	0.5	-	-	0.91	0.51	0.29	0.41	0.73	-	-

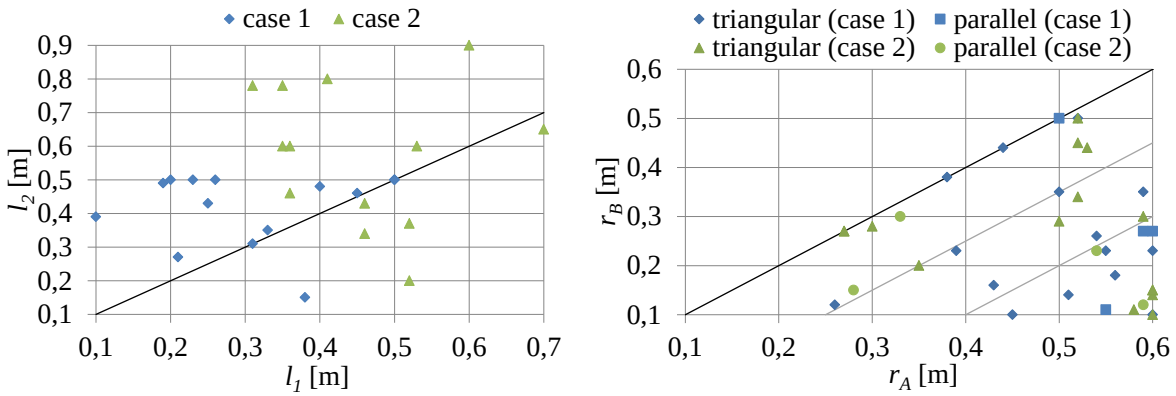

(a) l_2 over l_1 **(b)** r_B over r_A

Fig. 8.2: Relations of geometrical parameters for all PKS

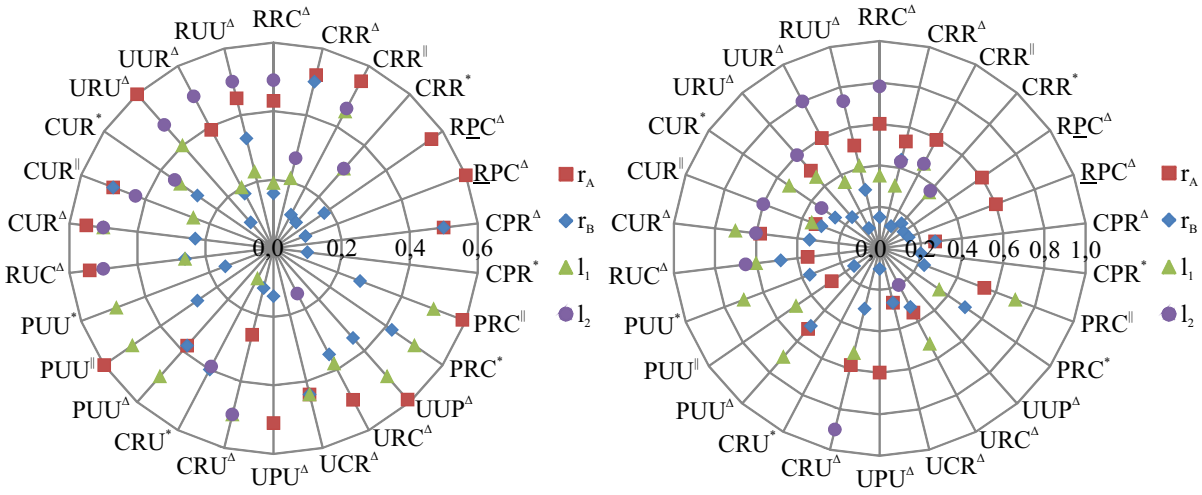

(a) Case 1 **(b)** Case 2

Fig. 8.3: Optimized parameters

the considered workspace and hence the boundaries for the optimization parameters are larger. For case 1 optimization, the length of link 2 is close to the boundary of 0.5 m. Not only for case 1 but also for case 2, l_2 is longer than l_1. There are PKS with a link length ratio of 1, especially for both optimization cases $\underline{\text{C}}\text{RR}^{\parallel}$ and $\underline{\text{C}}\text{RR}^{\star}$. Furthermore, some PKS have the same link length ratio for case 1 and case 2. These are: $\underline{\text{R}}\text{RC}^{\Delta}$, $\underline{\text{C}}\text{RR}^{\Delta,\parallel,\star}$, $\underline{\text{U}}\text{RC}^{\Delta}$, $\underline{\text{C}}\text{UR}^{\Delta,\parallel}$, $\underline{\text{U}}\text{RU}^{\Delta}$ and $\underline{\text{U}}\text{UR}^{\Delta}$. For PKS with only one link within each limb, the length l_1 is close to the maximum possible value.

If the values for r_A are compared, for case 2 r_A is longer than 0.5 m for 70 % of the PKS. Especially parallel frame configurations require a large frame radius. The results presented in Fig. 8.2b show that the ratio of frame and end-effector radius is either 1, or the end-effector radius depends approximately on the frame radius in the following

ways:

$$r_B = r_A - 0.25, \qquad r_B = r_A - 0.3, \qquad r_B = r_A - 0.5.$$

The following PKS have the same radii ratio for case 1 and case 2: $\underline{\mathrm{C}}\mathrm{RR}^{\parallel}$, $\underline{\mathrm{C}}\mathrm{PR}^{\Delta}$, $\underline{\mathrm{P}}\mathrm{RC}^{\parallel}$, $\underline{\mathrm{U}}\mathrm{CR}^{\Delta}$, $\underline{\mathrm{P}}\mathrm{UU}^{\Delta}$ and $\underline{\mathrm{C}}\mathrm{UR}^{\parallel}$. $\star$-shaped configurations tend to have a small end-effector radius r_B.

To summarize, Fig. 8.3 presents the obtained geometrical parameters for case 1 and case 2 in spider charts for all PKS.

8.4.2 Workspace

The workspaces for all PKS for case 1 and case 2 optimization are plotted in annex, Tab. 7, p. 224, Tab. 8 and Tab. 9, p. 226, Tab. 10, p. 227.

For case 1 optimization, the following PKS have relatively large workspaces: $\underline{\mathrm{U}}\mathrm{CR}^{\Delta}$, $\underline{\mathrm{C}}\mathrm{PR}^{\Delta}$, $\underline{\mathrm{P}}\mathrm{UU}^{\Delta}$, $\underline{\mathrm{C}}\mathrm{UR}^{\Delta}$. Those contain especially PKS with triangular frame configuration and cylindrical joint as first joint of each limb. In contrast, the workspaces of $\underline{\mathrm{R}}\mathrm{RC}^{\Delta}$, $\underline{\mathrm{R}}\mathrm{PC}^{\Delta}$, $\underline{\mathrm{U}}\mathrm{RU}^{\Delta}$, $\underline{\mathrm{U}}\mathrm{UR}^{\Delta}$, $\underline{\mathrm{C}}\mathrm{RR}^{\star}$, $\underline{\mathrm{P}}\mathrm{RC}^{\parallel}$, $\underline{\mathrm{C}}\mathrm{RP}^{\star}$ and $\underline{\mathrm{P}}\mathrm{UU}^{\parallel}$ are very compact, i.e. they cover the prescribed workspace perfectly. The workspaces of $\underline{\mathrm{U}}\mathrm{UP}^{\Delta}$, $\underline{\mathrm{U}}\mathrm{RC}^{\Delta}$ and $\underline{\mathrm{C}}\mathrm{RR}^{\Delta}$ are located close to the xy-plane.

For case 2 optimization, the already mentioned PKS have large workspaces, but moreover $\mathrm{U}\underline{\mathrm{P}}\mathrm{U}^{\Delta}$ and $\underline{\mathrm{R}}\mathrm{UU}^{\Delta}$ as well. PKS with relatively compact workspaces are: $\underline{\mathrm{P}}\mathrm{RC}^{\parallel}$, $\underline{\mathrm{C}}\mathrm{PR}^{\star}$, $\underline{\mathrm{C}}\mathrm{RR}^{\parallel}$, $\underline{\mathrm{U}}\mathrm{UR}^{\Delta}$, $\underline{\mathrm{R}}\mathrm{RC}^{\Delta}$ and both configurations of RPC^{Δ}. Again, the workspaces of $\underline{\mathrm{C}}\mathrm{RR}^{\Delta}$ and $\underline{\mathrm{U}}\mathrm{RC}^{\Delta}$ are located close to the xy-plane, as well as those of $\underline{\mathrm{P}}\mathrm{UU}^{\star}$ and $\underline{\mathrm{P}}\mathrm{RC}^{\star}$.

8.4.3 Performance

The analysis results are displayed graphically in Fig. 8.4 and Fig. 8.5 and annex, Fig. 5, p. 191 to Fig. 14, p. 194 using box plots. Thus, a reliable statement can be made on the absolute values with respect to each criterion and their distribution within the prescribed workspace. The box plots show the median as a line, the two quartiles as a rectangle, and the two extremes as a horizontal line (whiskers). If the whisker exceeds 1.5 times the corresponding interquartile range, the values are marked by a cross as an outlier [PCC14].

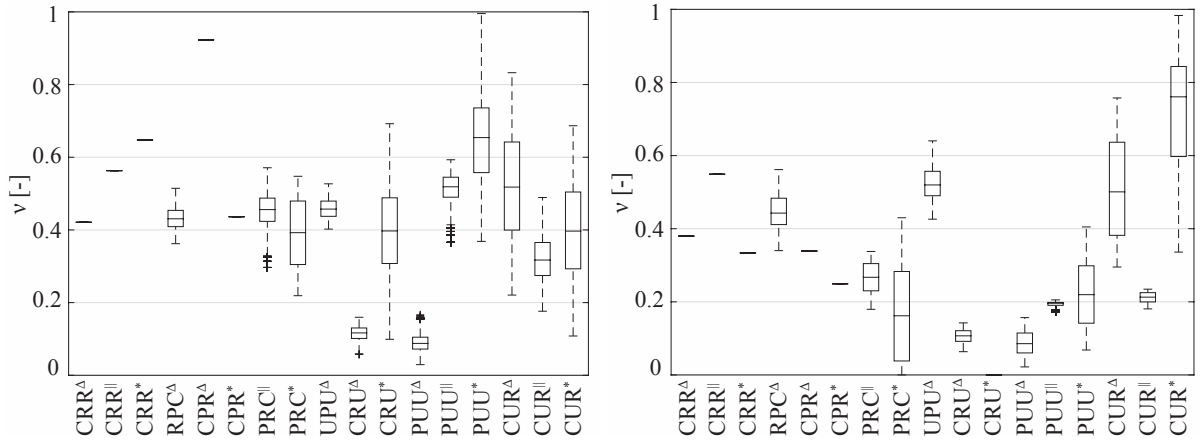

(a) Case 1 **(b)** Case 2

Fig. 8.4: Min. local dexterity index distribution - prismatic actuation

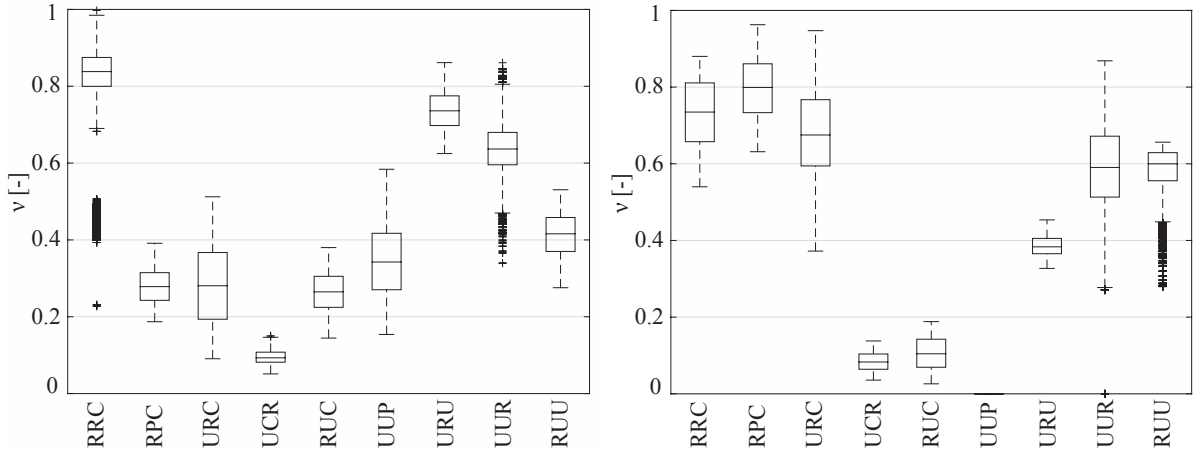

(a) Case 1 **(b)** Case 2

Fig. 8.5: Min. local dexterity index distribution - rotational actuation

The presented results show that $\underline{\mathrm{U}}\mathrm{CR}^{\Delta}$, $\underline{\mathrm{P}}\mathrm{UU}^{\Delta}$ and $\underline{\mathrm{C}}\mathrm{RU}^{\Delta}$ have bad performance characteristics – despite their large workspace. For case 2 optimization, no parameter configuration is obtained for $\underline{\mathrm{U}}\mathrm{UP}^{\Delta}$ and $\underline{\mathrm{C}}\mathrm{UR}^{\star}$. For case 1 optimization the drive velocities are small for RPC^{Δ}, $\underline{\mathrm{U}}\mathrm{RU}^{\Delta}$, $\underline{\mathrm{C}}\mathrm{RR}^{\star}$ and $\underline{\mathrm{C}}\mathrm{PR}^{\star}$. But in contrast, the required actuator forces or torques, respectively, are higher. Therefore, the power can be considered additionally. It is higher for $\underline{\mathrm{C}}\mathrm{RR}^{\star}$, $\underline{\mathrm{C}}\mathrm{PR}^{\star}$, $\underline{\mathrm{C}}\mathrm{RU}^{\Delta}$, $\underline{\mathrm{P}}\mathrm{UU}^{\Delta}$ and $\underline{\mathrm{U}}\mathrm{CR}^{\Delta}$.

For the PKS $\underline{\mathrm{C}}\mathrm{UR}^{\star}$, $\underline{\mathrm{C}}\mathrm{UR}^{\|}$ and $\underline{\mathrm{C}}\mathrm{RU}^{\star}$ the stiffness properties are worse for case 1 compared to the other PKS. $\underline{\mathrm{C}}\mathrm{UR}^{\|}$ and $\underline{\mathrm{C}}\mathrm{UR}^{\star}$ show bad accuracy for case 1, for case 2 it is $\underline{\mathrm{P}}\mathrm{UU}^{\star}$. Especially PKS with $\star$-shaped configuration are less suitable for the larger cylindrical workspace.

In general, the local dexterity index (Fig. 8.4 and Fig. 8.5) represents well the overall performance based on static properties and can be taken for a quick evaluation. It is for case 1 optimization equal or better compared to the results of case 2 optimization (for

linear actuation, except $\underline{\mathrm{C}}\mathrm{UR}^{\star}$). Especially the performance decreases for $\star$-shaped frame configurations when the prescribed workspace increases. Similar observations can be made for the $\parallel$ frame configuration. Large ranges of quartiles can be observed for the $\star$-shaped frame configurations, if the Jacobian depends on the position of the end-effector.

Although the applied forces at the end-effector for case 2 are 90 times higher (in x/y-direction), the required actuator forces are only 50 times higher approximately. The required torques are even only 25 times higher. For the actuator velocity a similar result can be assumed: the applied velocities for case 2 are five times higher, whereas the required actuator velocities are only three times higher. Consequently, the relation between applied and required forces or torques, respectively, and velocities is not proportional.

8.5 Conclusion and summary

In this chapter a first optimization, analysis and comparison of the selected structures was performed. For this purpose, the inverse kinematics and the Jacobian matrix were derived analytically. The geometrical parameters were optimized with respect to two load cases using a genetic algorithm. The objective function consisted of minimizing the maximum required actuator torques or forces respectively.

To demonstrate the differences between the considered structures, various criteria were applied and analyzed. Based on the performed analysis, five PKS with rather bad results are excluded from further consideration. Those structures are:

- $\underline{\mathrm{C}}\mathrm{RU}^{\Delta,\star}$
- $\underline{\mathrm{P}}\mathrm{UU}^{\Delta}$
- $\underline{\mathrm{U}}\mathrm{CR}^{\Delta}$
- $\underline{\mathrm{R}}\mathrm{UC}^{\Delta}$

Bad performance results for case 2 optimization show $\underline{\mathrm{P}}\mathrm{RC}^{\star}$ and $\underline{\mathrm{P}}\mathrm{UU}^{\star}$ as well, but since the $\star$-shaped frame configuration should not be considered as best for larger workspaces with limited structural dimensions, those two structures are not excluded from further comparison. No optimization results could be found for case 2 for $\underline{\mathrm{U}}\mathrm{UP}^{\Delta}$. Here as well the structural limitations and the structure itself restrict the workspace.

Furthermore, general statements regarding the results can be made:

- l_2 should be longer than l_1
- $\underline{\mathrm{C}}\mathrm{RR}^{\parallel}$ and $\underline{\mathrm{C}}\mathrm{RR}^{\star}$ should have a link length ratio of 1
- there are PKS with a fixed link length ratio regardless of the task
- l_1 should be close to the maximum if only one link per limb exists

- $\|$-shaped frame configurations require a large frame radius r_A
- $\star$-shaped frame configurations require a small end-effector radius r_B
- r_B is a linear function of r_A
- if the Jacobian depends on the position of the end-effector, the transmission behavior for $\star$-shaped frame configurations is very inhomogeneous over W_{pre}
- $\star$-shaped frame configurations are less suitable for larger workspaces

9 General research study of selected structures

In this chapter a general research study of the selected structures is performed. Since the performance highly depends on the selected parameter configuration, different dimensions for the PKS are considered and analyzed. Based on a prescribed workspace inside the reachable workspace various criteria are applied. The results are graphically presented, followed by an evaluation step.

9.1 Methodology

In order to compare and evaluate the performance of different PKS, a general analysis is executed. The different steps are shown in Fig. 9.1. The PKS can be divided into four groups based on the number of geometrical parameters (see Tab. 9.1). Group 1 has two parameters, r_A and r_B resp. ψ (for $\underline{\mathrm{C}}\mathrm{PR}^{\star}$). Most of the PKS of group 2 depend on r_A, r_B and one link length (l_1). $\underline{\mathrm{C}}\mathrm{PR}^{\Delta}$ and $\underline{\mathrm{P}}\mathrm{RC}^{\star}$ have no link, but the inclination angle δ resp. ψ are additional parameters. $\underline{\mathrm{P}}\mathrm{UU}^{\star}$ is described by r_B, l_1 and ψ. The parameters of group 3 are either r_A, r_B, l_1 and l_2 or r_B, l_1, l_2 and ψ. The inclination angle δ of the revolute joint is additionally to r_A, r_B, l_1, l_2 the fifth parameter for the PKS of group 4.

First, a parameter configuration is chosen. The minimum and maximum values for each geometrical parameter and the step size are listed in Tab. 9.2. The joint limits are the

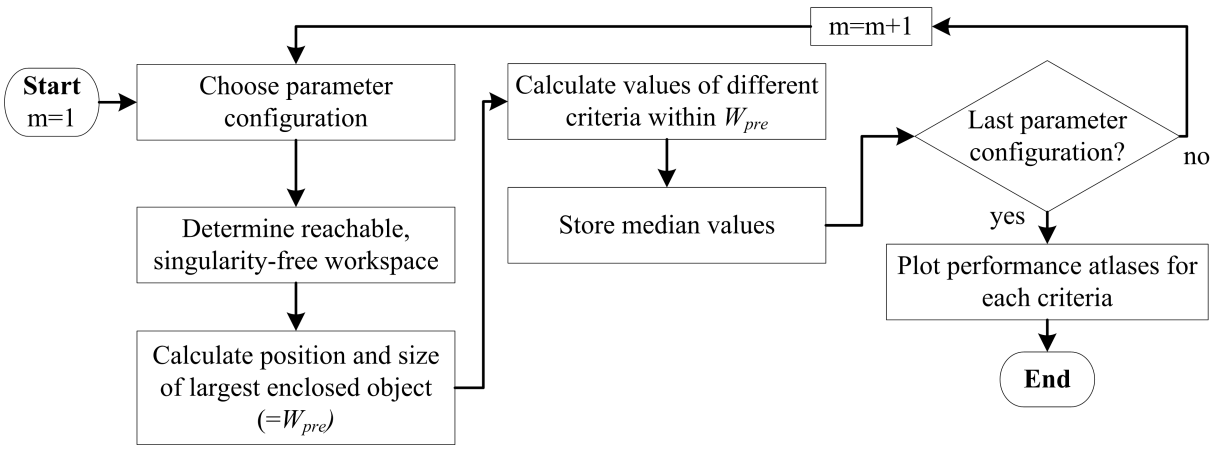

Fig. 9.1: Applied analysis steps

Tab. 9.1: Different groups based on number of geometrical parameters

Group 1	Group 2	Group 3	Group 4
R$\underline{\text{P}}$C$^{\Delta}$	$\underline{\text{C}}$PR$^{\Delta}$	$\underline{\text{R}}$RC$^{\Delta}$	$\underline{\text{C}}$RR$^{\Delta}$
$\underline{\text{R}}$PC$^{\Delta}$	$\underline{\text{P}}$RC$^{\parallel}$	$\underline{\text{C}}$RR*	$\underline{\text{C}}$RR$^{\parallel}$
$\underline{\text{C}}$PR*	$\underline{\text{P}}$RC*	$\underline{\text{U}}$RC$^{\Delta}$	$\underline{\text{C}}$UR$^{\Delta}$
U$\underline{\text{P}}$U$^{\Delta}$	$\underline{\text{U}}$UP$^{\Delta}$	$\underline{\text{C}}$UR*	$\underline{\text{C}}$UR$^{\parallel}$
	$\underline{\text{P}}$UU$^{\parallel}$	$\underline{\text{U}}$RU$^{\Delta}$	
	$\underline{\text{P}}$UU*	$\underline{\text{U}}$UR$^{\Delta}$	
		$\underline{\text{R}}$UU$^{\Delta}$	

Tab. 9.2: Bounds of parameters and step size

		Lower/upper bound	Step size
r_A	[m]	0.2 - 1	0.1
r_B	[m]	0.1 - 0.9	0.1
ψ	[°]	5 - 30	5
l_1	[m]	0.1 - 1	0.1
l_2	[m]	0.1 - 1	0.1
δ	[°]	5 - 80	15

same as for case 1 optimization, described in Section 8.2. The contour and hence the volume of the reachable workspace are calculated for each parameter configuration, since its size is one important criterion for benchmark studies (cf. Section 5.1).

There are different possibilities to determine the workspace of PKS. The methods are based, amongst others, on algebraic, numerical or geometrical considerations. As for PKS the inverse kinematics problem is analytically solvable, valid workspace points can be directly determined by using discretization or random samplings. In case of forward kinematics, additionally numerical solution strategies have to be applied. Geometrical methods allow workspace representation as well. Here, the joint limits and their motion space are analyzed based on geometrical objects. Finally, their intersection results in the workspace [Arr12].

In [Com15] different methods are applied to determine the workspace of the RPC-PKS. These include:

- Discretization using inverse kinematics
- Random samplings using Monte Carlo method and inverse kinematics
- Bisection method using inverse kinematics
- Analysis of joint motion spaces using forward kinematics
- Analysis of joint motion spaces using set theory

The methods are compared regarding object time and accuracy. Some of the obtained results are summarized in this paragraph.

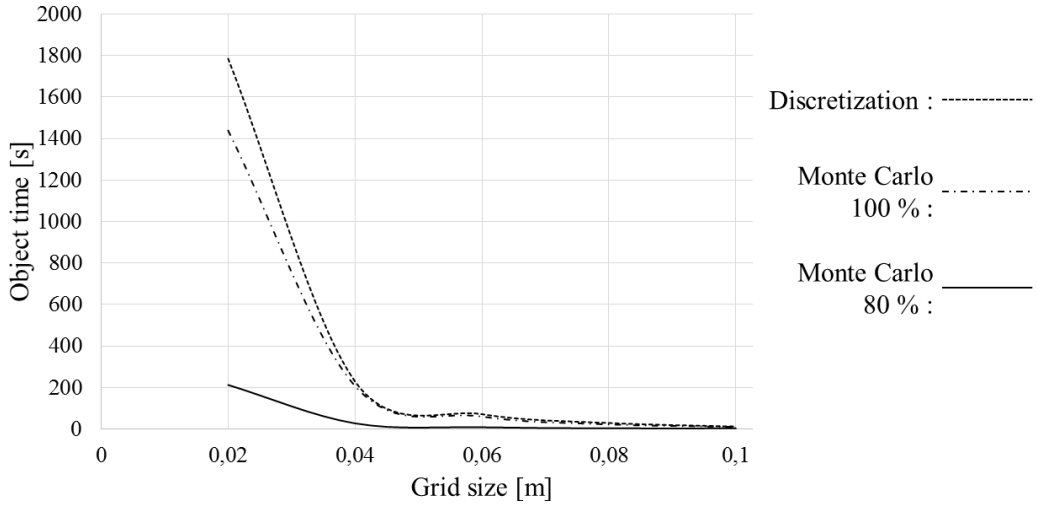

Fig. 9.2: Object time for different methods calculating the workspace of RPC [Com15]

In general, for discretization or for the Monte Carlo method the grid size has the highest influence on object time. Furthermore, for random samplings the object time depends on the number of loop cycles. The user should be aware that if the number of loop cycles is too small, too few workspace points are found, so that the workspace cannot be properly presented. Results in [Com15] show that the Monte Carlo method offers time savings compared to normal discretization (cf. Fig. 9.2). The time savings can be further increased, if, for example, only 90 % of the maximum selectable workspace points are determined with a grid size of 0.1 m. The determination would be still faster or as fast as the workspace determination using discretization with a grid size of 0.2 m, which detects all points. So the user can choose between a 90 % covered workspace with grid size of 0.1 m or a completely covered workspace with grid size of 0.2 m.

To conclude, with both methods, the workspace of PKS can be represented effectively, so that accurate statements about the volume, as well as the quality of the workspace can be made. The accuracy of both methods can be increased by refining the grid size. But for this analysis only the contour of the workspace is crucial. Therefore, the bisection method is introduced in the next section.

9.1.1 Bisection method

The bisection method provides a procedure to detect the workspace boundaries of PKS without time-consuming discretization. As a result, a quick statement about the workspace volume and its shape with variable parameters can be made for new or for improving existing structures. In addition, only the points of the workspace boundaries are stored when applying the bisection method. This significantly reduces the amount of data. A major drawback of the bisection method is that singularities within the workspace cannot

be determined. The calculated volume by using the bisection method is close to the exact volume of the workspace calculated with discretization and small grid size (cf. [Com15]).

To apply the bisection method, first, a coordinate system is generated. Then a straight line is created by defining a starting (P_{start}, inside the workspace) and end point (P_{end}, outside the workspace, see Fig. 9.3). A further point P_{z1} is defined which is located on the half of the distance of the starting and end point. An algorithm checks the position of this point by solving the inverse kinematics and returns a Boolean variable. If the validated point is within the workspace, the algorithm returns 1, otherwise the Boolean variable is 0. Is the validation of the point negative, the point is declared as new endpoint of the algorithm and a second point is calculated. This (second) point P_{z2} is located on the half of the distance between P_{start} and P_{z1}. Again the algorithm checks the validity of this second point. The workspace boundary is calculated until r_{diff} is smaller than the preset value r_{min}. The border-crossing point is stored and a new straight line with different orientation is generated. Along this straight line the end and starting points are redefined.

Three methods can be identified using the bisection method:

- Bisection method along z-axis of R_0
- Bisection method using polar coordinates (start point is either lower or upper intersection point of workspace with z-axis)
- Bisection method using normals of the sphere (start points are points on sphere)

The bisection method along the z-axis of R_0 does not completely cover the bottom of the workspace, e.g. cavities. In this case, the bisection method using polar coordinates provides better results, since the shape of the workspace can be better involved (cf. [Com15]). But the bisection method using normals of the sphere most accurately replicates the workspace boundaries. The boundaries in the upper area of the workspace as well as the workspace boundaries at the bottom are included. The accuracy of the procedure depends mainly on the values $\delta\phi$, $\delta\theta$ and r_{min} (cf. Fig. 9.3 and Fig. 9.4).

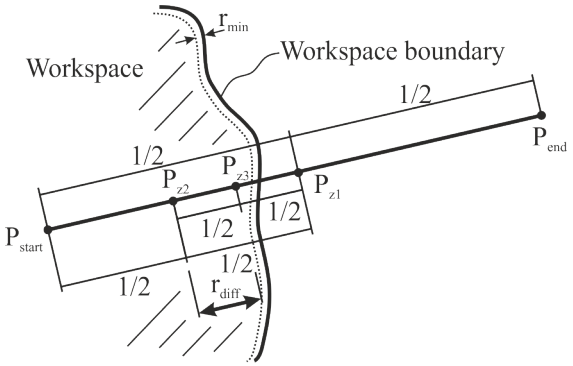

Fig. 9.3: Fundamentals of the bisection method

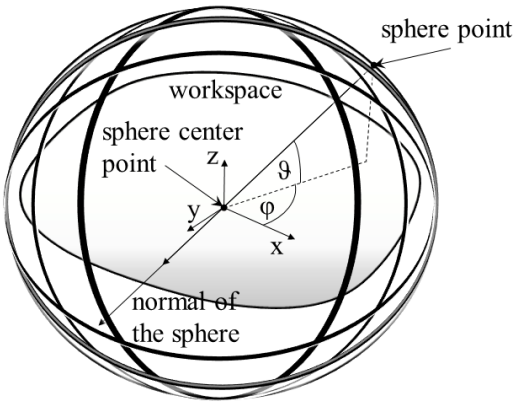

Fig. 9.4: Implementation of the bisection method using normals of the sphere [Com15]

The basic idea of this method is to create a sphere that spans the expected workspace of the PKS. Then, straight lines are defined that run through the sphere with pitch of the normal of the sphere. Along these straight lines, the bisection procedure is applied and the determined points of the workspace boundaries are stored. Polar coordinates are used to define the sphere points; the radius is roughly estimated. The center of the sphere is located in the approximate center of the expected workspace. By applying the bisection method with normals of the sphere, the shape of the workspace can be traced better because the workspace surface is considered from different directions. The approach of this method is shown in Fig. 9.4 and in the activity plan (annex, Fig. 15, p. 195).

9.1.2 Largest enclosed object

Fig. 9.5 compares the necessary object time to determine the largest enclosed sphere according to different methods for workspace determination. The figure shows that the object time is shorter if the bisection method using polar coordinates or normals of the sphere is applied. It is the longest when workspace points are determined through discretization. The longer program runtime to determine the largest object from a point cloud is based on the fact that the calculation of the radius is more complex as it is for the bisection method. A disadvantage of this procedure is that singularities are not included in the object definition.

The largest sphere inside the calculated boundaries is defined as prescribed workspace W_{pre}. This sphere is determined based on the results of the workspace analysis through bisection method. Here, the advantage is used that only the contour of the reachable workspace was calculated. Since all PKS are symmetrical, the center point of the largest sphere must lie on the z-axis of R_0. A predefined section of this axis with valid workspace points is discretized and at each point the distance to the nearest neighbor of the outer

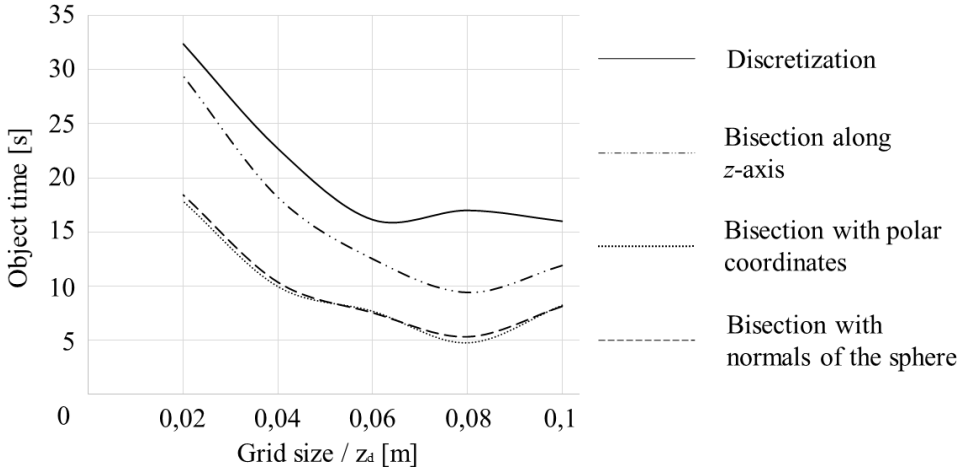

Fig. 9.5: Object time for different methods [Com15]

boundaries is calculated using the MATLAB© function *knnsearch.m*. This distance is the radius of the largest sphere that fits into the workspace at that point. Finally, the point on the z-axis with the max. distance is determined and hence the radius and location of the largest sphere. Within W_{pre} the performance of the PKS can be analyzed. Fig. 9.6 shows as an example the workspace of the RPC-PKS determined by discretization (blue), the workspace boundaries found by the bisection method with normals of the sphere (black dots) and the largest enclosed sphere within the workspace (red).

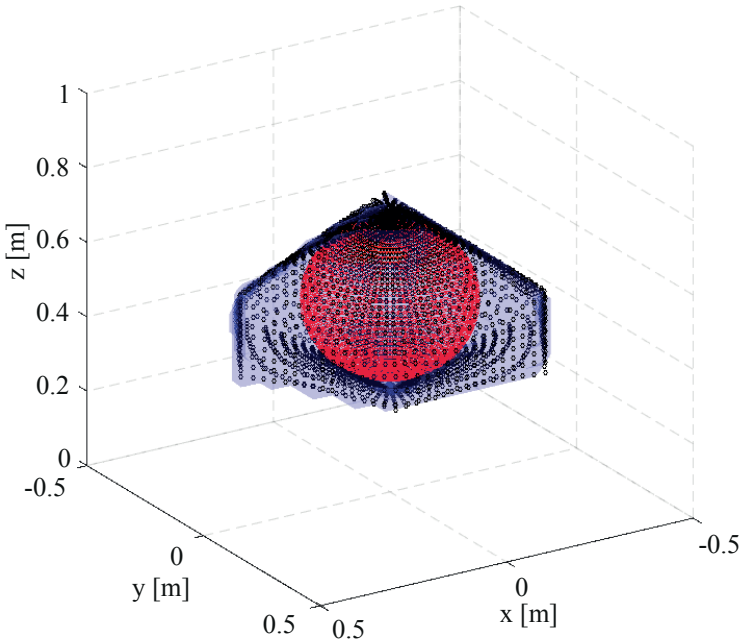

Fig. 9.6: Workspace and largest enclosed sphere of RPC-PKS

9.1.3 Singularities

Singularities are one of the main limitations of the workspace. In a singular configuration, the position of the robot is kinematically not clearly defined. The DoF of the robot changes so that the robot can take multiple poses without any motion of the drives. Depending on the type of singularity the DoF of the PKS either increases or decreases [Bie06]. Singularities can be determined through the analysis of the Jacobian. The motion capability is unique, when an inversion of the Jacobian in the relevant range of motion is possible. For this context the theorem of implicit functions can be used [HKS97]. By using the theorem of implicit functions, it is clear that the Jacobian matrix is invertible, if its determinant is non-zero (cf. manipulability index, Eq. (7.12)). Consequently, positions for which the Jacobian matrix is not invertible, are singular positions and the Jacobian matrix has no full rank. Therefore, the determination of the number of singularities requires to examine the rank of the Jacobian matrix [HKS97]. Another possibility to identify singular positions is to analyze the condition number ($\kappa \rightarrow 0$), the examination of the singular values (singularity index, Eq. (7.9)) or the calculation of the eigenvalues of the Jacobian. In addition, the determinant condition can be used (Eq. (7.12)).

Determining the rank of the Jacobian matrix via the singular value decomposition offers the most accurate results [The15; DR06]. In positions where the Jacobian loses its rank, the determinant is according to MATLAB© approximately 10^{-17}, so close to zero. Therefore, the examination with the determinant condition and the eigenvalue condition is less stable than checking the rank condition.

9.1.4 Applied criteria

For this analysis only these criteria are applied which do not depend on a specific load case or material properties. With reference to Chapter 7 these contain:

- Local conditioning index (cf. Eq. (7.4))
- Singularity index (cf. Eq. (7.9))
- Velocity index (cf. Eq. (7.10))
- Payload index (cf. Eq. (7.11))
- Normalized manipulability index (cf. Eq. (7.12))
- Isotropy index (cf. Section 7.1.3)

For each parameter configuration the median and minimum value of the criteria within W_{pre} are calculated. A global value is not calculated due to the mentioned drawbacks (see Section 7.1.3). The evaluation of the minimum value allows evaluating singularity

configurations, since the value of the criteria is set to 0 if the Jacobian matrix looses its rank.

Furthermore, for the analysis, the following assumptions are made:

- δ is not a variable parameter if the PKS has four length parameters
- r_B should be smaller than r_A
- r_B should be smaller than l_1 for $\underline{\mathrm{P}}\mathrm{UU}^{\star}$ and $\underline{\mathrm{P}}\mathrm{RC}^{\star}$
- the z-components of the unit vectors of the links are positive at all points

To avoid analyzing the workspace boundaries with bad performance characteristics, only 90 % of the radius of the largest sphere is taken into consideration. Hence, the radius is discretized from 0 to 90 % of the maximum radius with step size 0.01 m. For both, the rotation about the z-axis and the rotation about the x-axis, the step size is set to 4° (cf. Fig. 9.4).

9.2 Results and evaluation

The results are presented using performance charts. Since each group has a different number of geometrical parameters, different graphical methods are applied:

- for two parameters: contour plot
- for three parameters: contour plot in different planes, slice model
- for three lengths and one angle: contour plot in different planes, slice model with fixed angle ψ
- for four lengths: contour plot in different planes, slice model with fixed length r_B

Fig. 9.7 and Fig. 9.8 show as an example the performance charts of the $\underline{\mathrm{R}}\mathrm{PC}^{\Delta}$ and $\underline{\mathrm{P}}\mathrm{RC}^{\star}$-PKS. The results for the other structures (median values) can be found in the annex, Fig. 16 – Fig. 34, p. 196 – p. 214.

Based on the performance charts the properties of the PKS for different parameter configurations can be examined. With respect to the volume of the largest sphere, lengths ranges can be identified offering good transmission results. Especially the opposed behavior of payload and velocity index can be observed easily.

In order to facilitate the assessment of the PKS and to select a suitable parameter configuration, a possible benchmark approach is briefly described which consists of the following steps:

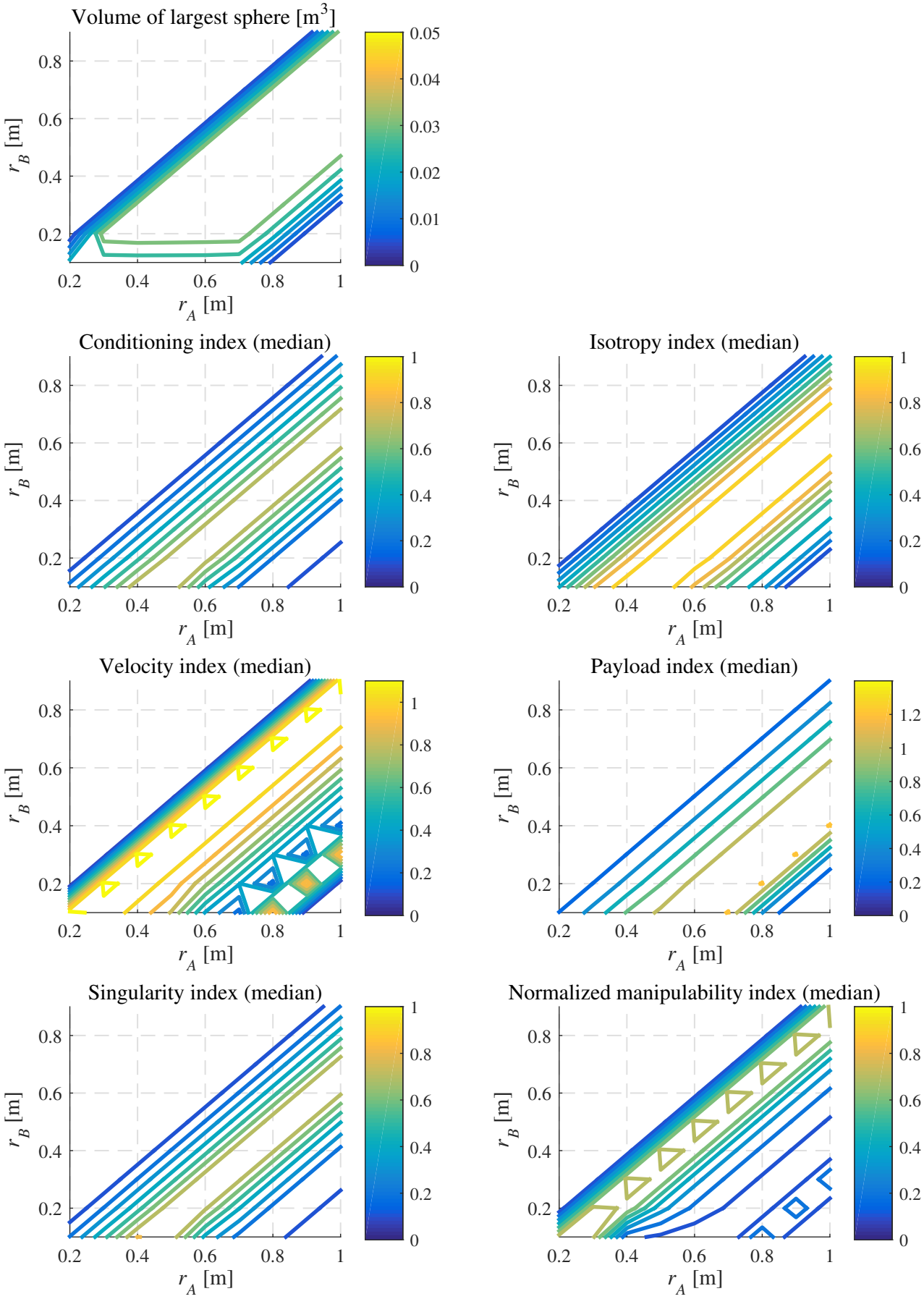

Fig. 9.7: RPC median values

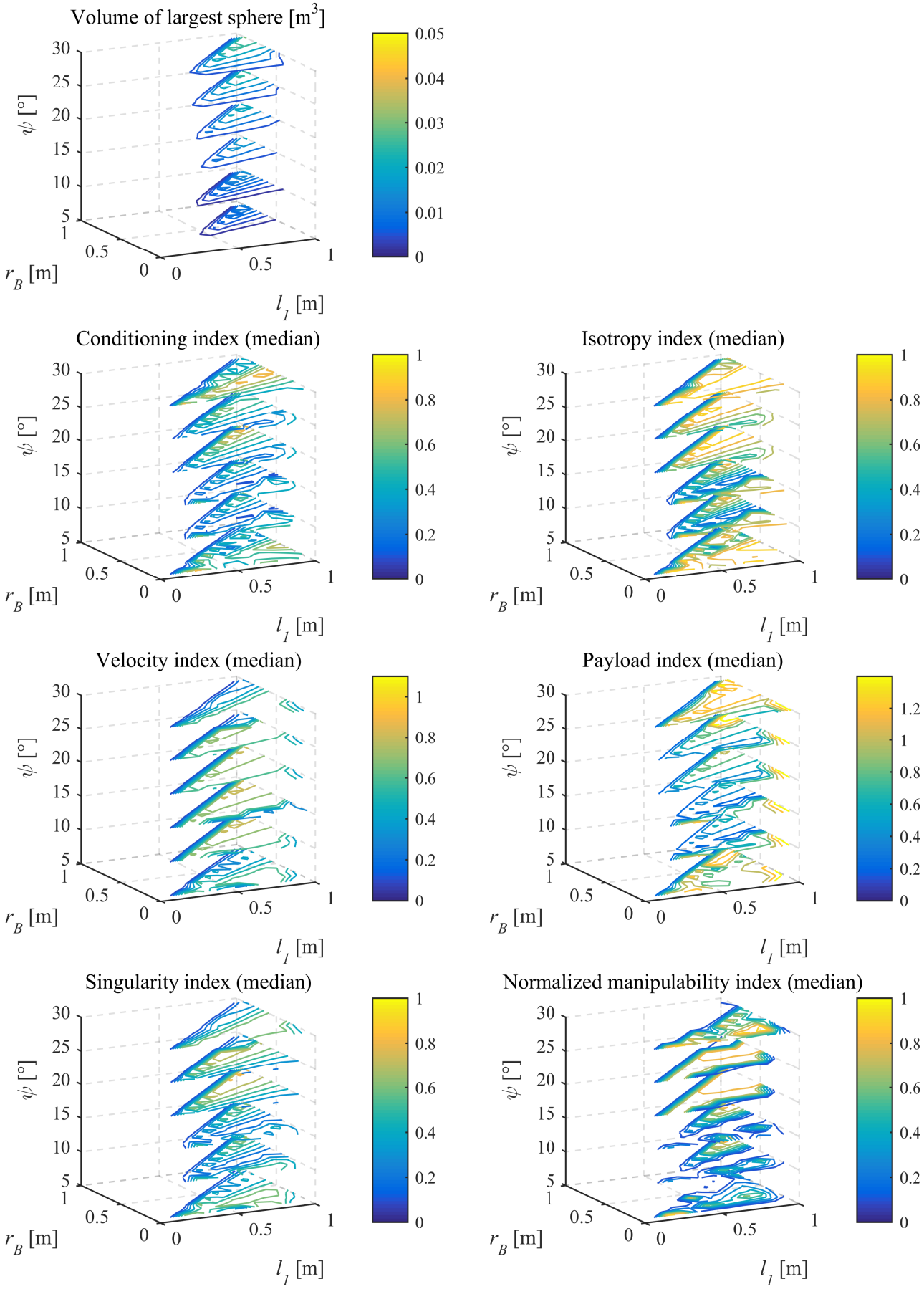

Fig. 9.8: PRC* median values

1. Selection of the criteria
2. Weighting of the criteria
3. Definition of a rating scale
4. Calculation of the target values for each criterion
5. Calculation of the overall results
6. Plot of the results

Within the first step, three criteria are selected as examples: radius of maximum enclosed sphere (r_{max}), conditioning (ν) and singularity index (s). In general, it is important to ensure that the criteria are independent of each other. It is not directly the case for the selected criteria because both, conditioning and singularity index depend on the Jacobian matrix. But since the conditioning index describes the overall transmission behavior and the singularity index provides information about the closeness to singularities (better than the condition number or the manipulability index [PS14]), they are selected in this case.

Then, the criteria can be weighted, for example, with the preference matrix (see Section 3). Here, a uniform distribution is assumed, so that 1/3 is the weighting factor for all three criteria. The rating scale is defined according to the cost-utility analysis with points from 0 to 10. To generate indicators based on the analysis results different ways are possible. For example, the value ranges of the individual indices can be divided in a predefined number of subranges. Each subsection receives a score that indicates how good or bad that property is represented through this value range. The ranges can have either all the same size or they are of different size. The latter is especially recommended if the values to be compared are very unevenly scattered over the total range. Thereby, a finer distinction in subranges is possible, where the values are close together [Kie14].

Eleven ranges are generated for each criterion which are scored with points from 0 to 10. The higher the score, the better is the performance of the structure. Because the conditioning index can take only values between 0 and 1, the points are distributed evenly over the spectrum, i.e. $\nu = 0.1 \rightarrow r(\nu) = 1$ point, $\nu = 0.5 \rightarrow r(\nu) = 5$ points, etc. The same applies to the singularity index $r(s)$. For the evaluation of the radius of the largest sphere, the largest radius of all parameter configurations is rated with 10, the smallest with 0. The other subranges are evenly distributed between those values.

The overall result is achieved by summing up the weighted target values for each criterion. Here it is:

$$X = \frac{1}{3}r(\nu) + \frac{1}{3}r(s) + \frac{1}{3}r(r_{max}). \tag{9.1}$$

Then, the value X is plotted to visualize the benchmark metric (Tab. 9.4 and Tab. 9.5).

Finally, based on the performance charts and the benchmark metrics, the parameter ranges offering good properties (median values) of the PKS within the largest sphere are highlighted in Tab. 9.3. The results prove the statements made in Section 8.5. For most PKS with two links the length of link 2 should be longer than the length of link 1. Furthermore, a fixed link length ratio can be observed for the already mentioned PKS $\underline{\mathrm{R}}\mathrm{RC}^{\Delta}$, $\underline{\mathrm{C}}\mathrm{RR}^{\Delta,\parallel}$, $\underline{\mathrm{C}}\mathrm{UR}^{\parallel}$ and $\underline{\mathrm{U}}\mathrm{RU}^{\Delta}$. Especially the preferred link length ratio of 1 for $\underline{\mathrm{C}}\mathrm{RR}^{\parallel}$ is shown in its benchmark metric. Statement four (if only one link, this link should be as long as possible) is pointed out with regard to $\underline{\mathrm{P}}\mathrm{RC}^{\parallel,\star}$, $\underline{\mathrm{U}}\mathrm{UP}^{\Delta}$, $\underline{\mathrm{U}}\mathrm{RC}^{\Delta}$, and $\underline{\mathrm{P}}\mathrm{UU}^{\parallel,\star}$. Here, the link length should be longer than 0.5 m. For parallel frame configurations the radius of the frame, r_A, tends to be longer: at least longer than 0.4 m. Moreover, the assumption that in some cases r_B is a linear function of r_A, is presented in the benchmark metrics of $\underline{\mathrm{R}}\mathrm{PC}^{\Delta}$, $\mathrm{R}\underline{\mathrm{P}}\mathrm{C}^{\Delta}$, $\underline{\mathrm{C}}\mathrm{PR}^{\Delta}$, $\underline{\mathrm{P}}\mathrm{RC}^{\parallel}$, $\underline{\mathrm{U}}\mathrm{UP}^{\Delta}$, $\mathrm{U}\underline{\mathrm{P}}\mathrm{U}^{\Delta}$, and $\underline{\mathrm{P}}\mathrm{UU}^{\parallel}$.

Tab. 9.3: Parameter ranges

PKS	r_A [m]	r_B [m]	l_1 [m]	l_2 [m]	ψ [°]	δ [°]
$\underline{\mathrm{R}}\mathrm{RC}^{\Delta}$	any	any		$l_2 \geq l_1$	-	-
$\underline{\mathrm{C}}\mathrm{RR}^{\Delta}$	any	any		$l_1 \geq l_2$	-	fixed (30)
$\underline{\mathrm{C}}\mathrm{RR}^{\parallel}$	> 0.4	any		$l_1 \approx l_2$	-	fixed (50)
$\underline{\mathrm{C}}\mathrm{RR}^{\star}$	-	< 0.3		$l_1 \approx l_2$	> 10	-
$\mathrm{R}\underline{\mathrm{P}}\mathrm{C}^{\Delta}$	> 0.3	$\approx r_A - 0.4$	-	-	-	-
$\underline{\mathrm{R}}\mathrm{PC}^{\Delta}$	> 0.3	$\approx r_A - 0.4$	-	-	-	-
$\underline{\mathrm{C}}\mathrm{PR}^{\Delta}$	> 0.2	$\approx r_A - 0.25$	-	-	-	any
$\underline{\mathrm{C}}\mathrm{PR}^{\star}$	-	< 0.3	-	-	5-20	-
$\underline{\mathrm{P}}\mathrm{RC}^{\parallel}$	> 0.4	$\approx r_A - 0.4$	> 0.5	-	-	-
$\underline{\mathrm{P}}\mathrm{RC}^{\star}$	-	any	> 0.5	-	any	-
$\underline{\mathrm{U}}\mathrm{UP}^{\Delta}$	any	$\approx r_A - 0.2$	> 0.5	-	-	-
$\underline{\mathrm{U}}\mathrm{RC}^{\Delta}$	any	any	> 0.5	any	-	
$\mathrm{U}\underline{\mathrm{P}}\mathrm{U}^{\Delta}$	> 0.4	$\approx r_A - 0.5$	-	-	-	-
$\underline{\mathrm{P}}\mathrm{UU}^{\parallel}$	> 0.4	$\approx r_A - 0.4$	> 0.5	-	-	-
$\underline{\mathrm{P}}\mathrm{UU}^{\star}$	-	$\approx l_1 - 0.3$	> 0.5	-	5, 15	-
$\underline{\mathrm{C}}\mathrm{UR}^{\Delta}$	> 0.3	any	> 0.3	> 0.3, $l_2 \geq l_1$	-	fixed (50)
$\underline{\mathrm{C}}\mathrm{UR}^{\parallel}$	any	any	any	$\approx 1.4 - l_1$	-	fixed (50)
$\underline{\mathrm{C}}\mathrm{UR}^{\star}$	-	> 0.3	any	$l_2 \approx 0.9 - l_1$	> 10	-
$\underline{\mathrm{U}}\mathrm{RU}^{\Delta}$	> 0.3	any		$l_2 \approx 1.4 - l_1$	-	-
$\underline{\mathrm{U}}\mathrm{UR}^{\Delta}$		$r_B = r_A - 0.1$		$l_2 > l_1$	-	-
$\underline{\mathrm{R}}\mathrm{UU}^{\Delta}$	any	any		$l_2 > l_1$	-	-

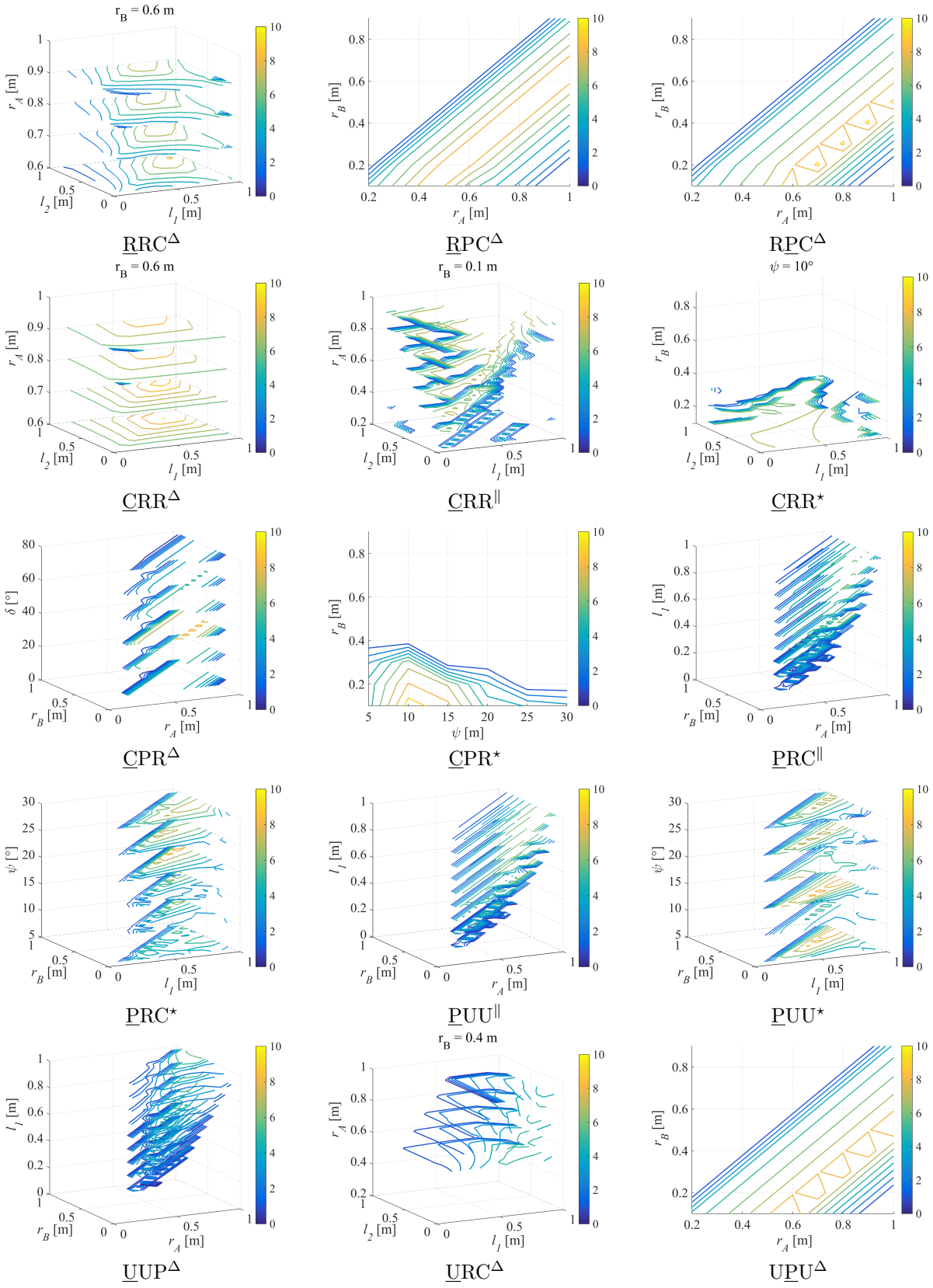

Tab. 9.4: Benchmark metrics (I)

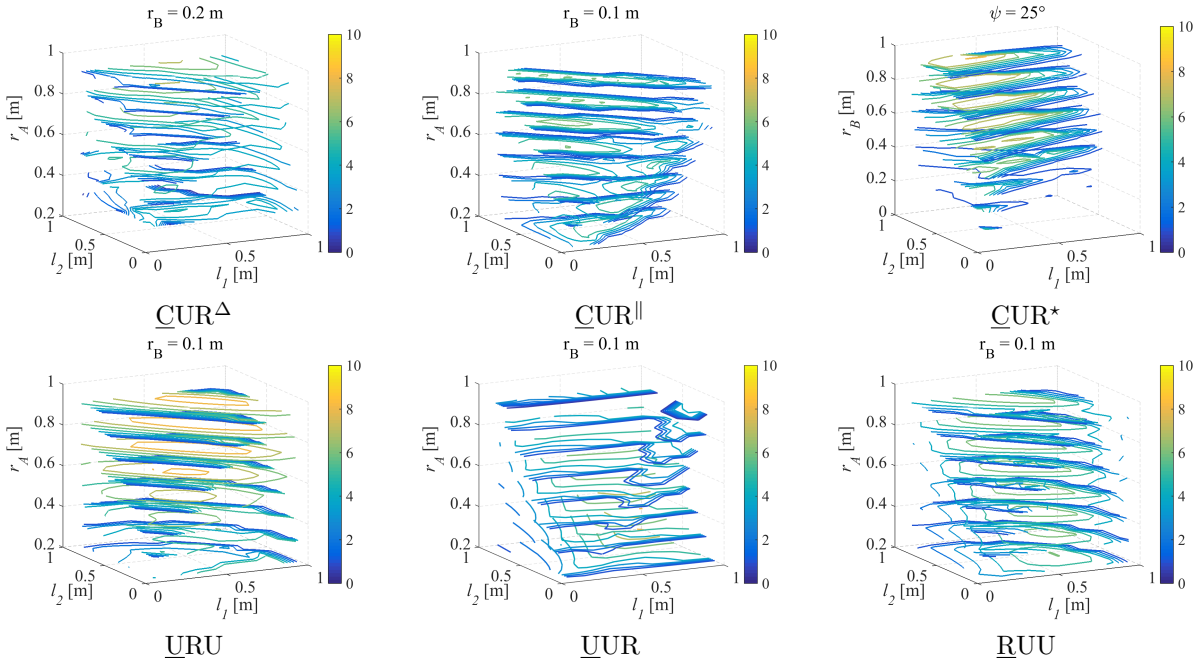

Tab. 9.5: Benchmark metrics (II)

9.3 Discussion

The first three steps of the evaluation method described in the previous section offer room for discussion.

As mentioned before, different criteria can be selected. Instead of using the radius of the largest sphere within the reachable workspace, the volume of that sphere could be considered as well. The workspace volume scales with the third power of the radius, so that results might be different. To analyze this influence the same evaluation is performed with the sphere volume instead of the radius. Hence, the sensitivity of the score distribution is analyzed. In this case it can be observed that the general statement of the benchmark metrics (Tab. 9.4 and Tab. 9.5) remains the same. That means that higher rated parameter combinations are still higher rated, whereas less appropriate parameter combinations show still a bad overall result. Nevertheless, especially variations for the lower rated regions in the benchmark metrics can be observed, e.g. overall results are around 0 instead of around 1. As a consequence, using the volume of the largest sphere instead of the radius as one of the selected criteria enhances the result of less appropriate parameter combinations.

Furthermore, for the evaluation equal weighting factors were assumed. Since this is not a necessary requirement, the sensitivity of changing weighting factors can be analyzed according to the following procedure:

1. Increase (decrease) one weighing factor by 20 %

	Weighting factor r_{max}		**Weighting factor** ν		**Weighting factor** s	
	+20%	-20%	+20%	-20%	+20%	-20%
general	-10%-8%	-8%-10%	-10%-9%	-9%-10%	-10%-20%	-20%-10%
specific	-10%-15%	-15%-10%	-10%-1%	-1%-10%	0%-20%	-20%-1%
	$\underline{U}RU^{\Delta}$, $\underline{U}UR^{\Delta}$, $\underline{R}UU^{\Delta}$ $\underline{U}UP^{\Delta}$, $\underline{U}RC^{\Delta}$, $\underline{R}RC^{\Delta}$		$R\underline{P}C^{\Delta}$, $\underline{R}PC^{\Delta}$, $U\underline{P}U^{\Delta}$		$R\underline{P}C^{\Delta}$, $\underline{R}PC^{\Delta}$, $U\underline{P}U^{\Delta}$	

Tab. 9.6: Sensitivity of weighting factors

2. Divide this added (subtracted) value by two and subtract (add) it equally to the other weighting factors
3. Calculate the new overall result
4. Calculate the percentage deviation of the new value (uneven weighting factors) from the origin value

Regarding 2) the new weighing factors are (1) for +20 %: 0.4, $\frac{3}{10}$, $\frac{3}{10}$ and (2) for -20 %: $\frac{4}{15}$, $\frac{11}{30}$, $\frac{11}{30}$.

Regarding 4) the newly obtained results are summarized in Tab. 9.6. As can be seen, the variation of the overall results is less than the increase/decrease of the weighting factor (for the criteria radius and conditioning index). In contrast, the overall result is more sensitive if the weighting factor of the singularity index changes. Furthermore, specific structures are highlighted that show higher changes of the overall results when the weighting factors are unequal. Again, it can be observed that variations are higher for less appropriate parameter combinations. Especially $U\underline{P}U^{\Delta}$ is the PKS the less sensitive regarding changing weighting factors.

9.4 Conclusion and summary

In this chapter a general research study of the selected PKS has been performed. Different dimensions were considered and analyzed in order to evaluate the performance characteristics. To do so, a method has been proposed to determine the largest sphere inside the reachable workspace. First, the contour of the reachable workspace was determined based on the bisection method. Then, the largest sphere was calculated using a nearest neighbor search algorithm. Finally, various criteria were calculated for every point within this sphere for each parameter configuration. The results have been presented graphically using performance charts. A short discussion highlighted the sensitivity of the evaluation regarding changes in weighting factors and score distribution.

Adapted from the obtained results, further restrictions can be made regarding the PKS. Especially all frame configurations of $\underline{\mathrm{C}}\mathrm{UR}$ and $\underline{\mathrm{U}}\mathrm{RC}^{\Delta}$ have singular positions within the prescribed workspace (= sphere) for each parameter setting. This can be seen if the minimum value of each criteria is evaluated. Furthermore, the benchmark study for $\underline{\mathrm{U}}\mathrm{UP}^{\Delta}$ shows bad results for most of the parameter combinations. Therefore, these five PKS are excluded from further considerations.

10 Task adapted dimensional synthesis

As already pointed out in the previous chapters, the greatest challenge in robotic development is to determine the optimal kinematic dimensions, i.e. to perform a dimensional synthesis [GGZ96; Mer97; LW07; LWK06]. To fulfill all requirements imposed on the mechanism, a parameter configuration (including link lengths) must be selected in such a way, that the structure has good properties with regard to various criteria over a wide range (e.g. workspace) [TTE95] or along a prescribed trajectory. Whereas the results in Chapter 8 and 9 show the performance characteristics of different PKS within a prescribed workspace for several parameter configurations and arbitrary use cases, here, the aim is to analyze the suitability of each PKS for a specified task. Thus, a task adapted dimensional synthesis is performed. The procedure is divided into several steps, explained in detail in the next paragraphs.

10.1 Preliminary studies

Some preliminary steps are necessary to perform a task-adapted optimization. This includes first:

① Task definition

It is obvious that without a specific task the dimensions of the PKS cannot be adapted to a desired trajectory. Hence, three tasks are selected including a pick & place (cf. Section 5.3.1), a positioning (cf. Section 5.3.2) and a guidance task (cf. Section 5.3.3). For the pick & place task the PKS are mounted at the ceiling, for the positioning task sideways (pos 1) (cf. Fig. 5.7, p. 55) and additionally on the ground (pos 2). For the guidance task the PKS are placed on the ground as well. The demands for each task are summarized in Tab. 5.3. So the second step is:

② Requirement determination

The selected tasks are highly diversified so that they place differing demands on the PKS. These differences are summarized in Tab. 10.1 according to Section 5.1. In general, a small installation space, low self-weight and good transmission quality are requirements for all mentioned tasks. Furthermore, the costs should be as low as possible. In the next step PKS have to be selected that could fulfill the defined tasks:

Tab. 10.1: Task-dependent demands

Demand	Tasks		
	pick & place	**positioning**	**guidance**
workspace	large	small	large
velocities	high	low	middle
accelerations	high	low	middle
payload	low	low-high	low
accuracy	high	high	middle
stiffness	high	high	middle
flexibility	low	low	middle

Tab. 10.2: Selected PKS for final optimization and analysis

	RRC	**CRR**			**RPC**		**CPR**		**PRC**		**UPU**	**PUU**		**RUU**
	Δ	Δ	$\parallel$	$\star$	P	R	Δ	$\star$	$\parallel$	$\star$	Δ	$\parallel$	$\star$	Δ
pick & place	✓	✓	✓	✓	✓	✓	✓	✓	✓	✓	✓	✓	✓	✓
positioning	✓	✓	✓		✓	✓	✓		✓		✓	✓		✓
guidance	✓	✓			✓	✓	✓				✓			✓

③ Structure selection

PKS with general bad performance characteristics were systematically excluded in previous selection steps. Moreover, the last two PKS with universal joints as actuated joints, UUR$^{\Delta}$ and URU$^{\Delta}$, are discarded as well (cf. 7$^{\text{th}}$ criteria, p. 38). Consequently, the remaining PKS, listed in Tab. 10.2, are considered for optimization. For all these PKS the inverse dynamics according to the Newton/Euler approach are derived (cf. annexe, pp. 229–283). Furthermore, a stiffness model is established based on the MSA (cf. Section 6.2.3).

Tab. 10.2 shows that not all frame configurations are suitable for the mentioned tasks. For instance, due to the limited space and the installation options, only PKS with triangular frame configuration are selected for the guidance task. In case of the positioning task, PKS with star-shaped frames are excluded. According to the assembly shown in Fig. 5.7, p. 55, those with parallel-shaped frames are preferred for this task.

To assess the suitability of a PKS for a task, specific performance characteristics must be determined and evaluated, i.e.

④ Criteria selection

These criteria can be deduced from the requirements (cf. Tab. 10.1). Since every point of the trajectory should be reachable by the end-effector, it has to be part of the reachable workspace. Besides, possible criteria include:

- Homogeneous transmission quality
- Low actuator forces/torques
- High stiffness

Tab. 10.3: Preference matrix and respective weighting factors

	pick & place					**positioning**					**guidance**				
	Hom. transmission quality	Low actuation forces/torques	High stiffness	High positioning accuracy	High acceleration capability	Hom. transmission quality	Low actuation forces/torques	High stiffness	High positioning accuracy	High acceleration capability	Hom. transmission quality	Low actuation forces/torques	High stiffness	High positioning accuracy	High acceleration capability
Hom. transmission quality		0	0	1	0		1	0	0	1		0	1	0	0
Low actuation forces/torques	1		0	1	0	0		0	0	1	1		1	0	0
High stiffness	1	1		1	0	1	1		1	1	0	0		0	0
High positioning accuracy	0	0	0		0	1	1	0		1	1	1	1		1
High acceleration capability	1	1	1	1		0	0	0	0		1	1	1	0	
	0.1	0.2	0.3	0	0.4	0.2	0.1	0.4	0.3	0	0.1	0.2	0	0.4	0.3

- High positioning accuracy
- High acceleration capability

Since not all criteria are equally important, they should be weighted, so the next step is:

⑤ Weighting

Methods for weighting of criteria are summarized in Tab. 3.1, p. 20. Here, the preference matrix is selected due to its easy and quick implementation. The results, i.e. the different weighting factors, are presented in Tab. 10.3.

10.2 Components and stiffness modeling

The following remarks regarding important components of PKS are based on [Riv88; SK08; van06; Neu06].

Joints

The compilation of the mechanical parts of a PKS, e.g. the joints, leads to a source of structural compliance. The resulting deformations on the joints or bearings respectively reduce the preload of the bearing. This causes bearing clearance and therefore, the accuracy of the PKS decreases. Hence, four different kind of joints are modeled with regard to their stiffness properties: revolute, prismatic, cylindrical and universal joints.

Because planar rotational motions are a typical application in mechanical engineering, conventional bearings with low friction can be used to design **revolute joints**. Good stiffness properties can be achieved if the bearings are preloaded. High bending and torsional stiffness properties are important, so that the following types of radial bearings are possible: angular contact ball bearings (double-row), radial deep groove ball bearings and cylindrical roller bearings [Jac12]. The design of the bearing is standardized for each size. Therefore, also the permitted loads depend less on the manufacturer [KK14].

Models to calculate the bearing stiffness can be divided into two groups: linear and nonlinear models. The following remarks are mainly based on [LDJ09] and [Sch14]. The linear model provides reasonably accurate results in case of low load fluctuations with low computational costs. However, a linear behavior of the bearing under load is assumed. This assumption greatly differs from the real operation of the bearing, especially at low speeds and loads.

If the distortions of the displacement are not tolerated, fixed characteristic curves in axial and radial direction of the bearing are used. To determine these characteristic curves, two methods are possible. On the one hand, the characteristic curves can be determined based on measurement data or databases provided by the manufacturer. On the other hand different operating points can be defined and thereby, the appropriate displacements in these points can be determined using BEARINX® – a tool for calculating properties of bearings (cf. [FAG15], details concerning the software and the calculation are described in [Seb14]). The calculated values are linearly interpolated in MATLAB©, so that for different forces the displacements can be determined.

Since double bearing is more convenient, two ball bearings with distance l_b in between are used within a revolute joint. The stiffness matrix is derived from the axial (k_{axial}) and radial (k_{radial}) stiffness of a single ball bearing. The torsional stiffness of a single ball bearing is not considered. But for resistance against tilt mathematical expressions are used which are derived from the axial and radial stiffness and the distance l_b. The force dependent stiffness properties are determined for a set of ball bearings using BEARINX®. The values are extracted from a look up table in the database by linear interpolation. The y-axis (here = $\mathbf{e}_{iy}$) is defined as axis of rotation with a rotational stiffness equal to zero. For the MSA model only diagonal stiffness matrices are considered. Coupling terms are neglected. Hence, the resulting local stiffness matrix for a double bearing is [Seb14]:

$$\mathbf{K}_{i,rev} = \begin{pmatrix} \sum_{i=1}^{2} k_{i,rad} & 0 & 0 & 0 & 0 & 0 \\ 0 & \sum_{i=1}^{2} k_{i,ax} & 0 & 0 & 0 & 0 \\ 0 & 0 & \sum_{i=1}^{2} k_{i,rad} & 0 & 0 & 0 \\ 0 & 0 & 0 & \frac{\sum_{i=1}^{2} k_{i,rad} \cdot l_b^2}{4} & 0 & 0 \\ 0 & 0 & 0 & 0 & 0 & 0 \\ 0 & 0 & 0 & 0 & 0 & \frac{\sum_{i=1}^{2} k_{i,rad} \cdot l_b^2}{4} \end{pmatrix}. \tag{10.1}$$

In this work, radial deep groove ball bearings are used to model the stiffness properties of revolute, universal and cylindrical joints. The necessary characteristics of the bearings are calculated using the BEARINX® program. Forces acting on the bearing positions are calculated by means of the MSA and can be absorbed by radial deep groove ball bearings. Here, the radial deep groove ball bearing FAG 6202-C-2Z (10 €/piece) [Sch15] is selected. More details about the selection can be found in [Seb14].

There are two general types of **prismatic joints**: single-stage and telescopic joints. A single-stage joint consists of a movable and a fixed part. The benefits of single-stage prismatic joints include simple design and high rigidity. Telescopic joints consist of multiple nested, single joints and are characterized by a high ratio between retracted and extended state.

In general, linear ball or linear roller bearings and ball or roller bearing guideway assemblies can be used as prismatic joints in robotic applications, especially for short stroke lengths. Advantages of linear bearing guideways are low speed-independent friction, small size, high repeatability and a simple process of lubrication. Also, a slight preload of these linear units leads to the elimination of bearing clearance and consequently, it increases the stiffness. Within a robotic structure during manipulation, the magnitude and direction of forces continuously change. Therefore, high stiffness properties are required. In particular, the possibility of internal preload of ball bearing guideways ensures increased stiffness properties in all directions. Ball bearing guideways have higher stiffness properties compared to roller bearing guideways with the same size. Furthermore, they offer sufficient payload and high accuracy for robotic applications.

The manufacturer ROLLON [ROL15] indicates the force displacement curves under vertical and lateral load for various types of ball bearing guideways. For a linear bearing, the stiffness matrix is derived from the translational stiffness k_x and k_z. The rotational stiffness k_{rot} is approximated from the translational stiffness based on the geometry of the bearings [Mie13]. For a set of linear bearings these force dependent stiffness properties

are provided by the manufacturer (e.g. [SKF04; ROL01]). The values are extracted from a look up table in the database by linear interpolation. The y-axis (here = $\mathbf{e}_{iy}$) is defined as axis of translation with a translational stiffness equal to zero. Again, non diagonal coupling terms are not considered:

$$\mathbf{K}_{i,pris} = \begin{pmatrix} k_{i,x} & 0 & 0 & 0 & 0 & 0 \\ 0 & 0 & 0 & 0 & 0 & 0 \\ 0 & 0 & k_{i,z} & 0 & 0 & 0 \\ 0 & 0 & 0 & k_{i,rotx} & 0 & 0 \\ 0 & 0 & 0 & 0 & k_{i,roty} & 0 \\ 0 & 0 & 0 & 0 & 0 & k_{i,rotz} \end{pmatrix}. \tag{10.2}$$

Here, for all passive prismatic joints, the ball bearing guideway ROLLON MRS25W (slider 50 €, guideway 100 €/m) is selected. More details about the selection can be found in [Seb14]. Finally, **cylindrical joints** are kinematically described by serial arrangement of a revolute and a prismatic joint.

Universal joints consist of two revolute joints in series with perpendicular joint axes. Universal joints are standardized according to DIN 808 [DIN808]. Therefore, the variety is severely restricted. The joints have a maximum deflection angle of ±45°. A greater angle is possible only by using two revolute joints in series. Concrete values for permissible torques are dependent on the diameter of the shaft (see DIN 808). In addition, the maximum torques reduce with increased speed and deflection angle. According to Neugebauer [Neu06] conventional universal joints "*are less suitable to transmit high push or pull forces due to their design*". Therefore, some manufacturers offer joints that are tailored to the needs of PKS: e.g. by the use of angular contact needle bearings higher load capacities can be achieved [Dür99].

Further information about the development of novel joint concepts especially for PKS can be found in [POI11].

Actuators

Analogous to the requirements in machine tools, high-force drives with high accuracy are needed for the application in PKS [Neu06]. A distinction is made between rotary and linear actuators. However, it is important to note that for linear actuators in most cases a rotary motion is transmitted to a linear motion.

Requirements that **rotary actuators** have to fulfill when used in PKS are high stiffness, positioning capability and high power density. Hence, eligible types of motors are synchronous motors, stepping motors, torque motors and synchronous servomotors.

Servo motors are able to move to preset positions or angles with high precision [Ger12]. In synchronous machines, the rotor follows the adjacent magnetic field to the stator. This will ensure the positioning. Furthermore, in contrast to asynchronous motors, stall torques – a necessary condition for the use in PKS – can be generated. There are synchronous servo motors with and without gear. Due to the wide range of engines and gearboxes, synchronous servo motors can cover relatively high torques or can allow high rotational speeds.

If high torques at low speeds are required, direct motors, so-called torque motors can be used. The advantage of such motors is that they do not need additional modules such as gears, belts or couplings. Since the inertia is low, the dynamic properties are high. The torque curve is constant within the low rotational speed range. So the maximum torque is available already at low speeds which can be an advantage for the use in PKS. More details concerning different types of motors can be found in [KK14].

For a rotary drive the stiffness matrix is based on catalog values provided by the manufacturer. Servo drives used for robotic applications are usually combined with a planetary drive. Hence, directly the rotational stiffness k_{rot} and the resistance against tilt k_{tilt} are given. The translational stiffness is assumed to be ideal (k_{id}), i.e. very high. The y-axis is defined as axis of rotation with a rotational stiffness k_{rot}. The resulting local stiffness matrix is:

$$\mathbf{K}_{i,rot} = \begin{pmatrix} k_{id} & 0 & 0 & 0 & 0 & 0 \\ 0 & k_{id} & 0 & 0 & 0 & 0 \\ 0 & 0 & k_{id} & 0 & 0 & 0 \\ 0 & 0 & 0 & k_{i,tilt} & 0 & 0 \\ 0 & 0 & 0 & 0 & k_{i,rot} & 0 \\ 0 & 0 & 0 & 0 & 0 & k_{i,tilt} \end{pmatrix}. \tag{10.3}$$

For **linear actuators** different types are available as well. Important within this work are linear actuators with sliders and cylindrical linear actuators. Linear actuators with sliders are designed for planar applications and can only be used in PKS when the sliding axes are stationary.

There are several possibilities for driving: geared belt drives, rack-and-pinion drives, spindle drives with driven nut or driven spindle, planetary screw drives and direct drives. All mentioned drives, except the direct drives, convert the rotational motion of an electric motor to the translational motion of the slider.

Tooth belt drives have good stiffness properties and high power transmission with high precision [GF11]. To achieve higher precision and zero backlash, they can be preloaded.

Spindle drives possess high mechanical efficiency, no slip-stick effect and offer high positioning accuracy and repeatability due to zero backlash [GF11; Riv88]. Though, the actuation speeds are quite low compared to other linear actuators.

For the use of linear actuators in spatial movements, it is necessary that the sliding axes do not require an additional mounting. Thus, the motion and guidance axes are integrated in the housing. The disadvantage is that the minimum length in the retracted state (i.e. the length of the stator) cannot be smaller than the maximum stroke length. As for linear actuators with slides, spindle drives provide high axial forces and low transfer speeds.

The basic principle for the determination of stiffness properties for spindle drives can be found in DIN ISO 3408-4 [DIN3408-4]. The axial stiffness of a spindle drive results from the axial stiffness of the spindle (depending on the kind of support and when indicated on the unsupported length), the axial stiffness of the nut, the axial stiffness of the support bearing (in general very stiff) and the nut supporting housing. More details about the stiffness properties of spindle drives and the formula for calculating the stiffness matrix entries are described in [Seb14].

For the selection of the actuators with regard to the requirements for each task, catalogs of different manufacturers are considered. Tab. 10.4 gives an overview of the selected components. Furthermore, actuator limits (force or torque, velocity, acceleration) are listed in the table as well. Further information provided by the manufacturers about the selected actuators can be found in Tab. 11, annex, p. 228. The required stiffness properties for the linear actuators are based on assumptions made in [Seb14]. To summarize, the sixth necessary step during the optimization procedure is:

⑥ Selection of components and limitations set-up

Links

The links are modeled as hollow cylinders with mean diameter d, outer diameter d_{ex}, inner diameter d_{in}, length l and wall thickness t with the following second moments of area:

$$I_T = \frac{\pi}{32}\left(d_{ex}^4 - d_{in}^4\right) \simeq \frac{\pi}{4} \cdot d^3 \cdot t,$$
$$I_B = \frac{\pi}{64}\left(d_{ex}^4 - d_{in}^4\right) \simeq \frac{\pi}{8} \cdot d^3 \cdot t. \tag{10.4}$$

Due to the reference frame in the middle of the link ($R_i(O_i, x_i, y_i, z_i)$ shifted by $\frac{l_i}{2}$ in direction of the x-axis), forces effective at the origin O_i generate no torque and hence no rotational deformation and vice versa. Using the Euler beam theory, this results in the diagonal compliance matrix for link j of limb i [GHS11]:

		pick & place/guidance	positioning
rotary drive	type	synchronous motor (incl. gear)	torque motor
	model	B&R, 8LSA55.EB030D000-1 with 8GP60-070hh032klmm	B&R, 8LTJC4.ee005ffgg-0
	max. torque	1324 Nm (max.), 371 Nm (nom.)	703 Nm (max.), 318 Nm (nom.)
	max. velocity	29.45 $\frac{1}{s}$ (max.), 9.81 $\frac{1}{s}$ (nom.)	73.3 $\frac{1}{s}$ (max.), 52.36 $\frac{1}{s}$ (nom.)
	max. acceleration	n/a	n/a
	positioning accuracy	$\frac{5\pi}{10800}\ rad$	no backlash $\left(\frac{0.5\pi}{10800}\ rad\right)$
	compliance	$4.15555{\cdot}10^{-5}\ \frac{rad}{Nm}$	$\sim 1.5555{\cdot}10^{-6}\ \frac{rad}{Nm}$
	torsional stiffness	7 $\frac{Nm}{arcmin}$	187 $\frac{Nm}{arcmin}$
	tilting stiffness	0 $\frac{Nm}{arcmin}$	n/a
	costs	1155 €	5380 €
linear actuator	type	linear actuator with slide	
	model	Nadella, Double-Line AXDL 240-Z	Nadella, Double-Line AXDL 160-S
	max. force	5000 N	9500 N
	max. velocity	10 $\frac{m}{s}$	2 $\frac{m}{s}$
	max. acceleration	n/a	n/a
	positioning accuracy	$0.05 \cdot 10^{-3} m$	$0.03 \cdot 10^{-3} m$
	compliance	n/a	n/a
	max. stroke length	user-defined	user-defined
	costs	3242 €	3419 €
linear actuator	type	cylindrical linear actuator	
	model	Bosch Rexroth, EMC-40-16x16	RK Rose + Krieger, LZ 70 PL
	max. force/torque	2000 N/5.7 Nm	5000 N/15 Nm
	max. velocity	1.23 $\frac{m}{s}$	0.5 $\frac{m}{s}$
	max. acceleration	50 $\frac{m}{s^2}$	10 $\frac{m}{s^2}$
	positioning accuracy	$0.02 \cdot 10^{-3} m$	$0.05 \cdot 10^{-3} m$
	compliance	n/a	n/a
	max. stroke length	0.75	0.6
	costs	1839 €	4500 €

Tab. 10.4: Properties of selected actuators

$$\mathbf{N}_{ji} = \begin{pmatrix} \frac{l}{EA} & 0 & 0 & 0 & 0 & 0 \\ 0 & \frac{l^3}{12EI_B} + \frac{l}{GA} & 0 & 0 & 0 & 0 \\ 0 & 0 & \frac{l^3}{12EI_B} + \frac{l}{GA} & 0 & 0 & 0 \\ 0 & 0 & 0 & \frac{l}{GI_T} & 0 & 0 \\ 0 & 0 & 0 & 0 & \frac{l}{EI_B} & 0 \\ 0 & 0 & 0 & 0 & 0 & \frac{l}{EI_B} \end{pmatrix} \tag{10.5}$$

with E = Young's Modulus, G = shear modulus, A = cross-sectional area of the link and l = link length.

Finally, the stiffness values can be determined by inverting the matrix $\mathbf{N}_{ji}$:

$$\mathbf{K}_{ji} = \mathbf{N}_{ji}^{-1}. \tag{10.6}$$

The mass of each link (or stator/slider) is calculated with the following formula:

$$m_i = \rho \cdot V = \rho \cdot \frac{\pi}{4} \left(d_{ex,i} - d_{in,i} \right). \tag{10.7}$$

This leads to the definition of the material properties:

⑦ Definition of material properties

In case of the pick & place and guidance task for all links and the end-effector aluminum is chosen as material with density $\rho = 2.7 g/cm^3$, Young's modulus $E = 70000 N/mm^2$ and shear modulus $G = 25500 N/mm^2$ (assumption 3 €/kg). For the positioning task it is steel with density $\rho = 7.85 g/cm^3$, Young's modulus $E = 210000 N/mm^2$ and shear modulus $G = 79300 N/mm^2$ (assumption 2 €/kg).

It is assumed that the end-effector has a triangular shape. Hence, its mass is:

$$m_p = \rho \cdot V = \rho \cdot 3 \cdot \sqrt{3} \cdot r_B^2 \cdot t_p, \tag{10.8}$$

with t_p = thickness of the end-effector. The thickness is set to 5 mm for all PKS in case of the pick & place and the guidance task and 10 mm for the positioning task respectively.

10.3 Optimization concept

In order to optimize the PKS according to the mentioned tasks, a flexible objective function is defined:

⑧ Flexible objective function

It can be adapted to the specific task by proper determination of the weighting factors. The flexible objective function is called performance index (PI) and consists of the following elements:

$$\begin{aligned} PI = & w_1 \cdot (1 - \nu) + w_2 \cdot \frac{max(|\boldsymbol{\tau}|)}{\tau_{max}} + w_3 \cdot \left(\frac{max(|\Delta \mathbf{p}_{trans}|)}{\Delta p_{trans,max}} + \frac{max(|\Delta \mathbf{p}_{rot}|)}{\Delta p_{rot,max}} \right) + \dots \\ & w_4 \cdot \frac{\|\delta \mathbf{p}\|}{\delta p_{max}} + w_5 \cdot \frac{max(|\Delta \boldsymbol{\tau}_{0 \to 1\mathbf{g}}|)}{\tau_{max}}. \end{aligned} \tag{10.9}$$

To assess the overall quality along the trajectory, the conditioning index ν can be taken into consideration. Eq. (10.9) includes the term (1-ν) because the PI should be minimized. For the velocity/force amplification, the velocity/payload index is one criterion. But more convenient to evaluate the required actuator forces/torques ($\boldsymbol{\tau}$) is the dynamic model, because it includes the accelerations, the applied external forces and the inertia

properties. In addition, the stiffness model allows calculating the translational $\Delta\mathbf{p}_{trans}$ and rotational deformations $\Delta\mathbf{p}_{rot}$ at the end-effector. Here, only the limb stiffnesses are taken into consideration because they are influenced by the diameters of the hollow cylinders (see optimization parameters). If the influence of inaccuracies of the actuators should be considered, Eq. (8.17) is applied. Finally, the acceleration capability can be expressed as changes in actuator torques/forces if the end-effector is accelerated from 0 to 1**g** ($\Delta\boldsymbol{\tau}_{0\rightarrow 1\mathbf{g}}$). All quantities (except the conditioning index) are divided by the maximum allowed value, here, the maximum actuator force/torque (τ_{max}), the maximum acceptable displacement/deformation of the end-effector ($\Delta p_{trans,max}$, $\Delta p_{rot,max}$) or the desired accuracy (δp_{max}) respectively. Thus, the PI is unit-less.

The PI must be minimized and contains all variable requirements, the fixed requirements are summarized in the boundary conditions (cf. Chapter 8): the solution of the inverse kinematic problem should not contain imaginary parts (BC_1), the joints should not exceed the defined limits (BC_2, BC_4) and the radius of the end-effector r_B should be smaller than the radius of the frame r_A (BC_5). Again, the singularity index is applied to evaluate the closeness to a singular configuration. It should be greater than 0.1 (BC_3). Furthermore, the outer diameter $d_{ex,i}$ of link i must not exceed the inner diameter $d_{in,i}$, i.e.:

$$BC_7(\mathbf{Optpar}) = \begin{cases} 1, & \text{if } d_{in,i} < d_{ex,i} \\ 0, & \text{else} \end{cases}. \tag{10.10}$$

All these boundary conditions are checked first: if an individual does not comply with a boundary condition, it is punished by a penalty value, added to the PI. It is the same procedure as described in Section 8.2. If all tested boundary conditions are complied, the resulting performance index corresponds to the flexible objective function value. In general, its value is between 0 and 1 if the limits for actuation forces/torques, accuracy and displacement/deformation are not exceeded. But for better optimization capacities, the PI is multiplied by factor 1000 during optimization.

The vector **Optpar** contains all geometrical parameters. So step nine is to define all relevant parameters of the PKS that can be optimized:

⑨ Definition of relevant parameters

The number of parameters is structure dependent; it varies from 5 to 10. Therefore, the relevant optimization parameters for the PKS are given in the following:

Tab. 10.5: Bounds of optimization parameters

		pick & place, positioning	guidance
r_A	[m]	0.2 - 0.7	0.4 - 1
r_B	[m]	0.1 - 0.5	0.2 - 0.6
ψ	[°]	5 - 30	5 - 30
l_1	[m]	0.1 - 1	0.1 - 1
l_2	[m]	0.1 - 1.5	0.1 - 1.5
z_{MS}	[m]	0.15 - 0.85	0.15 - 0.85
δ	[°]	5 - 80	5 - 80
d_{ex}	[m]	0.015 - 0.15	0.015 - 0.15
d_{in}	[m]	0.01 - 0.145	0.01 - 0.145

- $\underline{\mathrm{R}}\mathrm{PC}^{\Delta}$, $\mathrm{R}\underline{\mathrm{P}}\mathrm{C}^{\Delta}$, $\mathrm{U}\underline{\mathrm{P}}\mathrm{U}^{\Delta}$: r_A, r_B, $d_{ex,Stat}$, $d_{in,Stat}$, z_{MS}
- $\underline{\mathrm{C}}\mathrm{PR}^{\star}$: r_B, ψ, $d_{ex,Stat}$, $d_{in,Stat}$, z_{MS}
- $\underline{\mathrm{C}}\mathrm{PR}^{\Delta}$: r_A, r_B, δ, $d_{ex,Stat}$, $d_{in,Stat}$, z_{MS}
- $\underline{\mathrm{P}}\mathrm{RC}^{\parallel}$, $\underline{\mathrm{P}}\mathrm{UU}^{\parallel}$: r_A, r_B, l_1, d_{ex}, d_{in}, z_{MS}
- $\underline{\mathrm{P}}\mathrm{UU}^{\star}$, $\underline{\mathrm{P}}\mathrm{RC}^{\star}$: r_B, l_1, ψ, d_{ex}, d_{in}, z_{MS}
- $\underline{\mathrm{R}}\mathrm{RC}^{\Delta}$, $\underline{\mathrm{R}}\mathrm{UU}^{\Delta}$: r_A, r_B, l_1, l_2, d_{1ex}, d_{1in}, d_{2ex}, d_{2in}, z_{MS}
- $\underline{\mathrm{C}}\mathrm{RR}^{\star}$: r_B, l_1, l_2, ψ, d_{1ex}, d_{1in}, d_{2ex}, d_{2in}, z_{MS}
- $\underline{\mathrm{C}}\mathrm{RR}^{\Delta}$, $\underline{\mathrm{C}}\mathrm{RR}^{\parallel}$: r_A, r_B, l_1, l_2, δ, d_{1ex}, d_{1in}, d_{2ex}, d_{2in}, z_{MS}

The upper and lower bounds for the optimization parameters are listed in Tab. 10.5. The stroke length of the prismatic joints/actuators within a limb is set to 0.5 m. For PKS with $\star$- or $\parallel$-shaped frame configuration, the maximum length of the linear guidance axes is 0.8 m and 0.5 m respectively. The maximum lengths of the guidance axes for Δ-shaped frame or of the end-effector with attached cylindrical joints depend on the geometrical parameters r_A and r_B.

The gravity vector is $\mathbf{g} = \begin{pmatrix} 0 & 0 & -9.81 \end{pmatrix}^T \frac{m}{s^2}$.

Finally, the optimization can be performed:

⑩ Optimization

Again, a genetic algorithm is chosen with the following options in MATLAB©: 250 Populations, 1000 Generations, EliteCount = 5, CrossoverFraction = 0.8, MigrationInterval = 10, MigrationFraction = 0.1. Whereas for the guidance task the PI over a prescribed workspace (75 points) is optimized, it is minimized for the pick & place and positioning task along a trajectory (36 and 26 points respectively). Since the performance along such a trajectory depends on its position within the reachable workspace, the trajectory of the pick & place task is rotated twice, by 45° and 90° from its initial position.

10.4 Results

In this section the optimization results are presented according to the described manipulation tasks. The suitability of the optimized parameters is verified by using the implemented MATLAB SimMechanics© models. Hence, with all provided kinematic lengths and angles the motion tasks can be fulfilled.

10.4.1 Handling task (pick & place)

The optimized parameters are listed in Tab. 10.6. Furthermore, Fig. 10.1 shows the relations of the geometrical parameters. No parameter configuration could be found for R$\underline{\text{P}}$C$^{\Delta}$ and U$\underline{\text{P}}$U$^{\Delta}$, because amongst others the maximum allowed actuator velocity (1.23 $\frac{m}{s}$) of the cylindrical actuators is too low. This means, that boundary condition 4 (BC_4, Eq. (8.10), p. 86) is violated during optimization. For the other PKS again, some of the statements made in Chapter 8 can be checked: l_2 is longer than l_1, l_1 is close to the maximum if only one link per limb exists, the end-effector radius of $\star$-shaped frame configurations is small (and here for all other PKS as well) and the link length ratio of $\underline{\text{C}}$RR* and $\underline{\text{C}}$RR$^{\parallel}$ is almost 1. Moreover, the performance charts (cf. annex, pp. 196–214) can be recalled.

The inner and outer diameters of the links are illustrated in Fig. 10.1b. Only for $\underline{\text{R}}$RC$^{\Delta}$ and $\underline{\text{R}}$UU$^{\Delta}$ the links do not consist of a thin-walled hollow cylinder. Therefore, it can be

Tab. 10.6: Optimized parameters for pick & place task

PKS	z_{MS} [m]	r_A [m]	r_B [m]	l_1 [m]	l_2 [m]	ψ [°]	δ [°]	Θ_{traj} [°]
$\underline{\text{R}}$RC$^{\Delta}$	0.63	0.66	0.19	0.27	0.77	-	-	90
$\underline{\text{C}}$RR$^{\Delta}$	0.44	0.45	0.22	0.36	0.51	-	38	45
$\underline{\text{C}}$RR$^{\parallel}$	0.35	0.70	0.10	0.49	0.49	-	72	0
$\underline{\text{C}}$RR*	0.68	-	0.20	0.42	0.34	28	-	45
R$\underline{\text{P}}$C$^{\Delta}$	-	-	-	-	-	-	-	-
$\underline{\text{R}}$PC$^{\Delta}$	0.52	0.67	0.17	-	-	-	-	0
$\underline{\text{C}}$PR$^{\Delta}$	0.52	0.45	0.10	-	-	-	35	0
$\underline{\text{C}}$PR*	0.76	-	0.10	-	-	30	-	45
$\underline{\text{P}}$RC$^{\parallel}$	0.46	0.70	0.26	0.88	-	-	-	90
$\underline{\text{P}}$RC*	0.17	-	0.20	0.44	-	12	-	90
U$\underline{\text{P}}$U$^{\Delta}$	-	-	-	-	-	-	-	-
$\underline{\text{P}}$UU$^{\parallel}$	0.84	0.39	0.10	0.73	-	-	-	0
$\underline{\text{P}}$UU*	0.39	-	0.21	0.76	-	5	-	45
$\underline{\text{R}}$UU$^{\Delta}$	0.85	0.49	0.36	0.49	0.55	-	-	45

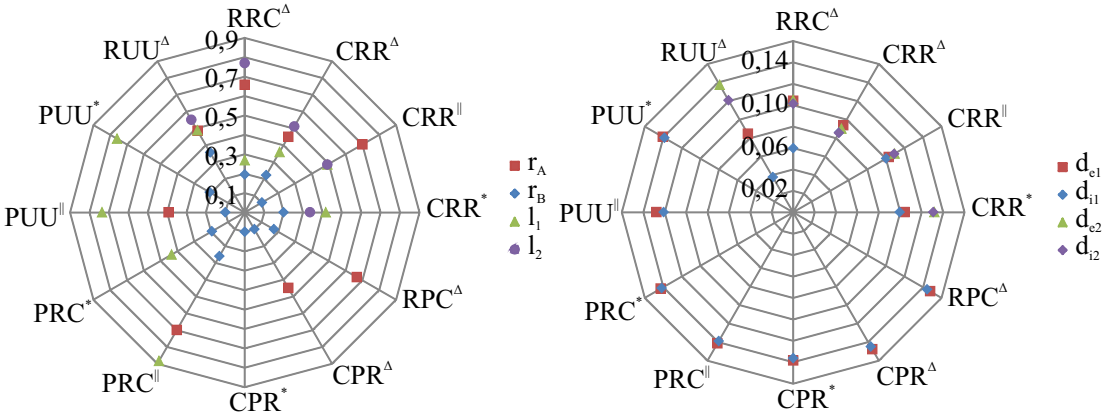

(a) Radii and link lengths **(b)** Inner and outer diameters

Fig. 10.1: Geometrical parameters for pick & place task

concluded that these PKS would suffer from structural compliance if hollow cylinders are assumed for the links.

To conclude, the bounds of the optimization parameters are suitable, because no trend of the optimized parameters to these boundaries can be observed. The only exception is the lower bound of r_B. But from a design point of view further reduction of the end-effector radius is challenging.

The performance index for all PKS, suitable for the pick & place task, is calculated along the entire trajectory (here 875 points) and plotted in Fig. 10.2. Additionally, the performance index of the DELTA robot is determined. This refers to a real structure available at the Department of Mechanism Theory and Dynamics of Machines and already optimized in advance for the described pick & place task. The DELTA robot has the following dimensions: size of frame $r_A = 0.204$ m, size of end-effector $r_B = 0.07$ m, length of upper arm $l_1 = 0.3445$ m and length of forearm $l_2 = 0.9$ m. Details about the mathematical description and relevant calculation methods can be found, amongst others, in [WC11] and [Sch13].

For easier comparison, the PI is plotted with a solid line for Δ-shaped frames, for $\star$-shaped frames with a dashed line and for $\|$-shaped frames with a dotted line. To highlight the characteristics of the DELTA robot, additionally, its line is plotted in blue. For all PKS the PI is lower than 1, so that the PKS fulfill the applied criteria/limits. Furthermore, the curves are similar to each other: the PI is worse at the beginning and at the end (high acceleration forces) and undergoes a lower peak in the middle of the trajectory ($x = y = 0$). At this point the velocity of the end-effector is highest of all points along the trajectory and hence, the acceleration is zero and no acceleration forces at the end-effector occur. Furthermore, the stiffness is highest due to the center position of the PKS (cf. Fig. 10.7e). The not fully symmetrical curves for the PI result from the orientation of the trajectory

with respect to the limb arrangement. Further peaks in the diagrams of the performance index, especially at the beginning and ending of the trajectory are due to positions of the PKS close to singularities (e.g. elongated limbs to reach the outer positions of the trajectory). Hence, high actuation torques or forces occur which affect the performance index.

The DELTA robot is the best compared to all PKS with rotational actuation, i.e. $\underline{\mathrm{R}}\mathrm{RC}^{\Delta}$

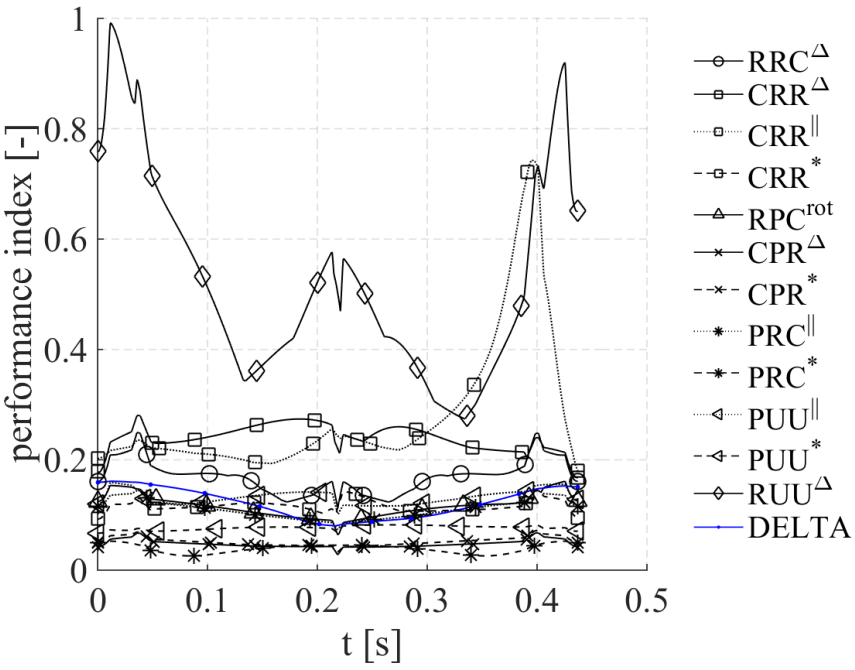

(a) Range 0-1

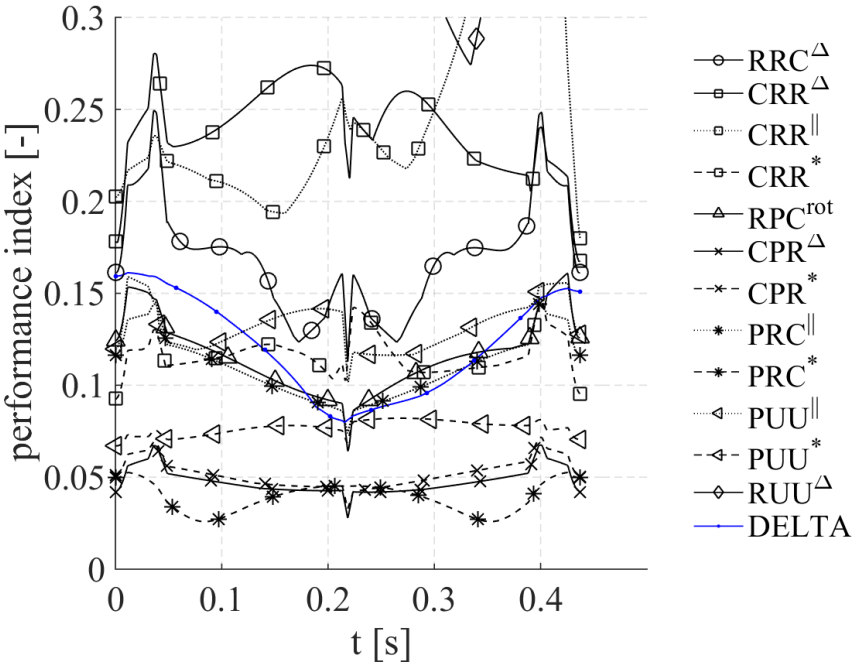

(b) Zoom, range 0-0.3

Fig. 10.2: Performance index for pick & place task

and $\underline{\mathrm{R}}\mathrm{UU}^{\Delta}$, and its PI is in the range of the other PKS with linear actuation. Especially the PI curve of the DELTA is similar to those of $\underline{\mathrm{R}}\mathrm{PC}^{\Delta}$ and $\underline{\mathrm{P}}\mathrm{RC}^{\parallel}$. Moreover, $\star$-shaped frame configurations show better performance compared to the other frame configurations. Besides, the PI of $\underline{\mathrm{C}}\mathrm{PR}$ is almost independent of the frame configuration. Moreover, $\underline{\mathrm{C}}\mathrm{RR}^{\parallel}$ and $\underline{\mathrm{R}}\mathrm{UU}^{\Delta}$ show the weakest performance characteristics for the pick & place task.

10.4.2 Positioning task (quasistatic positioning)

The optimized parameters for the positioning task for both mounting positions (pos 1 = sideways, pos 2 = ground) are summarized in Tab. 10.7. Furthermore, Fig. 10.3 shows the relation between r_A and r_B. All PKS with triangular frame configuration require a large frame radius, whereas it is shorter for parallel frame configurations. Generally, the end-effector radius tends to be smaller. But for the positioning task, this is not necessarily the case.

To facilitate the comparison of the geometrical parameters, they are presented in two spider charts (Fig. 10.4). The first spider chart, Fig. 10.4a, shows the end-effector and frame radii and the link lengths. The parameters are similar with regard to both load cases for each parameter configuration, especially for $\underline{\mathrm{R}}\mathrm{RC}^{\Delta}$, $\underline{\mathrm{R}}\mathrm{PC}^{\Delta}$ and $\mathrm{U}\underline{\mathrm{P}}\mathrm{U}^{\Delta}$. No optimization results were obtained for $\underline{\mathrm{R}}\mathrm{UU}^{\Delta}$. For this PKS, the motion ranges of the Cardan joints are too tight. As can be seen from Fig. 10.4b, the outer and inner diameters of the links are widely spaced. Hence, the assumption that the links consist of a thin-walled hollow cylinder is not permitted. This fact should be taken into account for the assessment of the

Tab. 10.7: Optimized parameters for positioning task

PKS	Positioning task 1							Positioning task 2						
	z_{MS} [m]	r_A [m]	r_B [m]	l_1 [m]	l_2 [m]	ψ [°]	δ [°]	z_{MS} [m]	r_A [m]	r_B [m]	l_1 [m]	l_2 [m]	ψ [°]	δ [°]
$\underline{\mathrm{R}}\mathrm{RC}^{\Delta}$	0.73	0.56	0.10	0.30	0.81	-	-	0.75	0.45	0.12	0.30	0.76	-	-
$\underline{\mathrm{C}}\mathrm{RR}^{\Delta}$	0.45	0.49	0.15	0.28	0.55	-	30	0.52	0.5	0.26	0.43	0.62	-	44
$\underline{\mathrm{C}}\mathrm{RR}^{\parallel}$	0.50	0.60	0.30	0.34	0.22	-	51	0.50	0.60	0.29	0.46	0.42	-	51
$\mathrm{R}\underline{\mathrm{P}}\mathrm{C}^{\Delta}$	0.47	0.70	0.10	-	-	-	-	0.50	0.66	0.15	-	-	-	-
$\underline{\mathrm{R}}\mathrm{PC}^{\Delta}$	0.58	0.70	0.27	-	-	-	-	0.42	0.70	0.12	-	-	-	-
$\underline{\mathrm{C}}\mathrm{PR}^{\Delta}$	0.63	0.66	0.38	-	-	-	24	0.63	0.57	0.46	-	-	-	31
$\underline{\mathrm{P}}\mathrm{RC}^{\parallel}$	0.73	0.51	0.33	0.54	-	-	-	0.81	0.45	0.20	0.62	-	-	-
$\mathrm{U}\underline{\mathrm{P}}\mathrm{U}^{\Delta}$	0.54	0.66	0.10	-	-	-	-	0.51	0.70	0.10	-	-	-	-
$\underline{\mathrm{P}}\mathrm{UU}^{\parallel}$	0.51	0.35	0.23	0.31	-	-	-	0.76	0.35	0.15	0.56	-	-	-
$\underline{\mathrm{R}}\mathrm{UU}^{\Delta}$	-	-	-	-	-	-	-	-	-	-	-	-	-	-

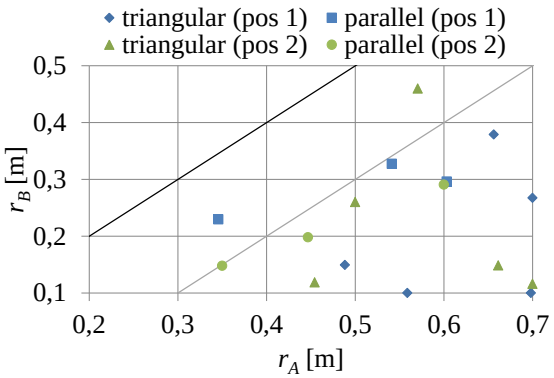

Fig. 10.3: r_B over r_A for positioning task; straight lines for $r_B = r_A$ and $r_B = r_A - 0.2m$

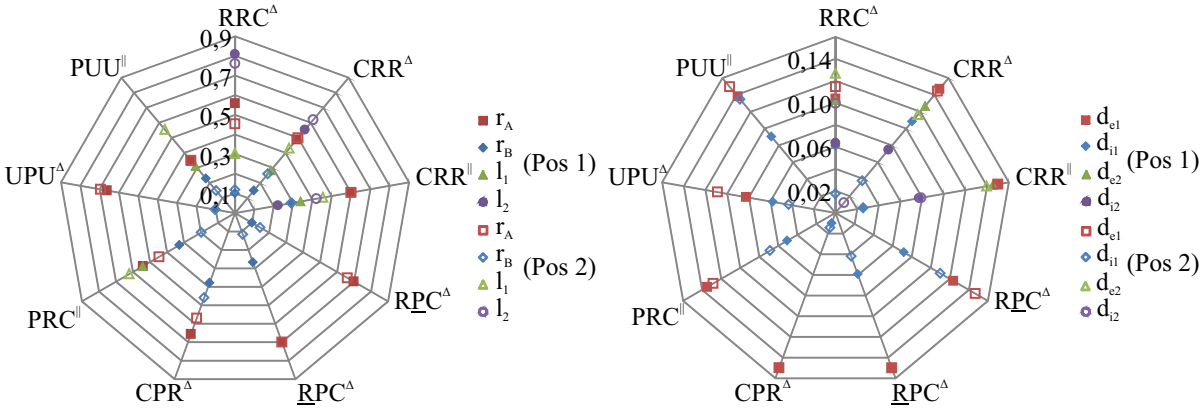

(a) Radii and link lengths **(b)** Inner and outer diameters

Fig. 10.4: Relations of geometrical parameters for positioning task

results for the displacement of the end-effector due to stiffness properties. So here, solid profiles are more appropriate.

The performance index is analyzed along the trajectory (225 points) for both mounting positions, see Fig. 10.5. It can be seen that the PI is homogeneous and lower than 4 for all PKS in bottom mounting compared to the sideways position. Especially the performance of $\underline{\text{C}}\text{RR}^{\Delta}$, $\underline{\text{P}}\text{RC}^{\|}$, $\text{U}\underline{\text{P}}\text{U}^{\Delta}$ and $\underline{\text{P}}\text{UU}^{\|}$ is better if the load is applied in z-direction. However, the PI remains about one for all PKS, so that they cannot comply the specific requirements of the motion task. Further analysis should focus on the reasons for this in greater detail.

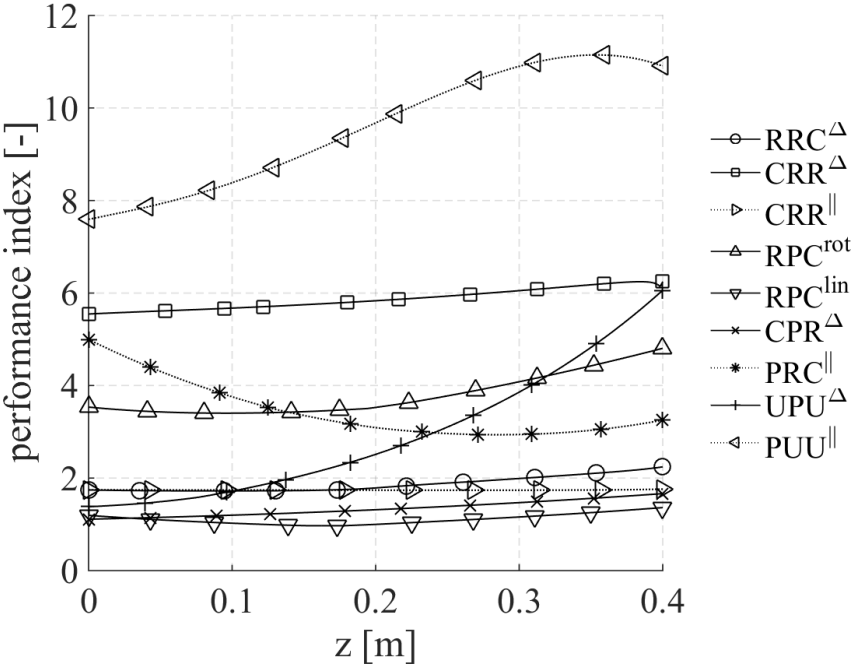

(a) Sideways mounting (pos 1)

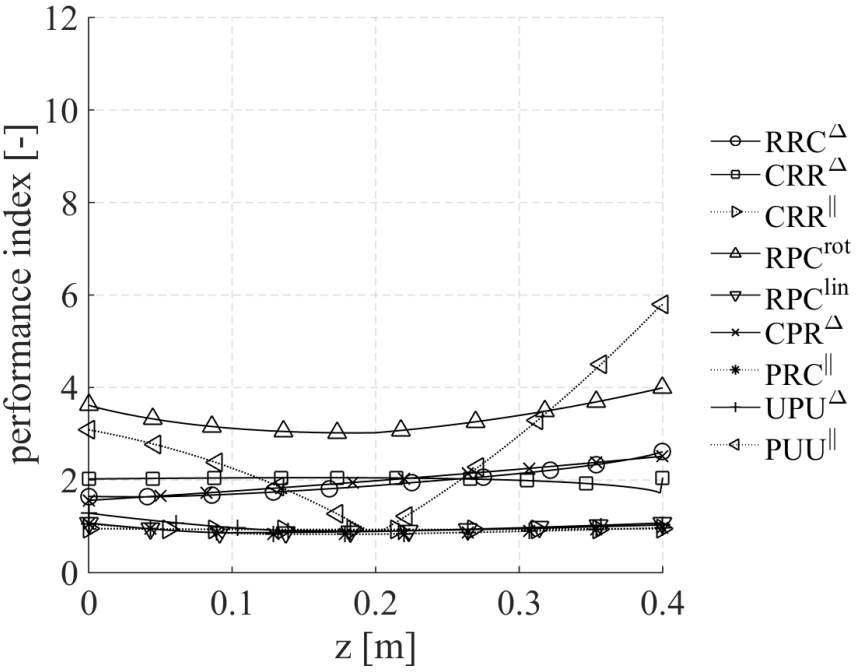

(b) Bottom mounting (pos 2)

Fig. 10.5: Performance index for positioning task

10.4.3 Guidance task (3D fiber injection plant)

No optimization results are obtained for the guidance task. This is due to the fact that the prescribed workspace is quite large and the actuator limits, especially for the linear actuators, are made very tight. Analysis results in [Ben14] already showed that the limits for the stroke lengths of the prismatic joints and linear actuators have to be selected

very largely (up to 1.3 m). From a design viewpoint this is not realizable for cylindrical prismatic actuators, i.e. in the middle of a limb. Hence, $\underline{\mathrm{R}}\mathrm{PC}^{\Delta}$, $\mathrm{R}\underline{\mathrm{P}}\mathrm{C}^{\Delta}$, $\underline{\mathrm{C}}\mathrm{PR}^{\Delta}$ and $\mathrm{U}\underline{\mathrm{P}}\mathrm{U}^{\Delta}$ are excluded from further analysis. For the remaining PKS suitable for this task, namely $\underline{\mathrm{R}}\mathrm{RC}^{\Delta}$, $\underline{\mathrm{C}}\mathrm{RR}^{\Delta}$ and $\underline{\mathrm{R}}\mathrm{UU}^{\Delta}$, the optimization is repeated with a slightly smaller workspace $(0.5\text{x}0.7\text{x}0.33)\mathrm{m}^3$.

The optimized geometrical parameters are listed in Tab. 10.8. For $\underline{\mathrm{R}}\mathrm{RC}^{\Delta}$ they fit perfectly to the "optimal" parameters obtained with respect to the largest sphere (cf. Fig. 11.3). For $\underline{\mathrm{C}}\mathrm{RR}^{\Delta}$ and $\underline{\mathrm{R}}\mathrm{UU}^{\Delta}$ the benchmark metric (Tab. 9.4) and the performance charts (Fig. 11.3, Fig. 11.3) emphasize the optimized parameter settings as well. Furthermore, the reachable and prescribed workspaces are shown in Fig. 10.6: here, as desired, the prescribed workspace is completely covered by the reachable workspace.

10.5 Evaluation

Based on the obtained results, an evaluation and benchmark study is performed. The PKS are analyzed depending on the task with regard to the following, already mentioned, criteria:

- Conditioning index
- Max. actuator torque/force
- Max. displacement/deformation of the end-effector (due to stiffness and drive errors)

Tab. 10.8: Optimized parameters for guidance task

PKS	z_{MS} [m]	r_A [m]	r_B [m]	l_1 [m]	l_2 [m]	ψ [°]	δ [°]
$\underline{\mathrm{R}}\mathrm{RC}^{\Delta}$	0.82	0.98	0.32	0.46	1.06	-	-
$\underline{\mathrm{C}}\mathrm{RR}^{\Delta}$	0.78	0.68	0.37	0.67	0.85	-	30
$\underline{\mathrm{R}}\mathrm{UU}^{\Delta}$	0.85	0.81	0.50	0.49	0.78	-	-

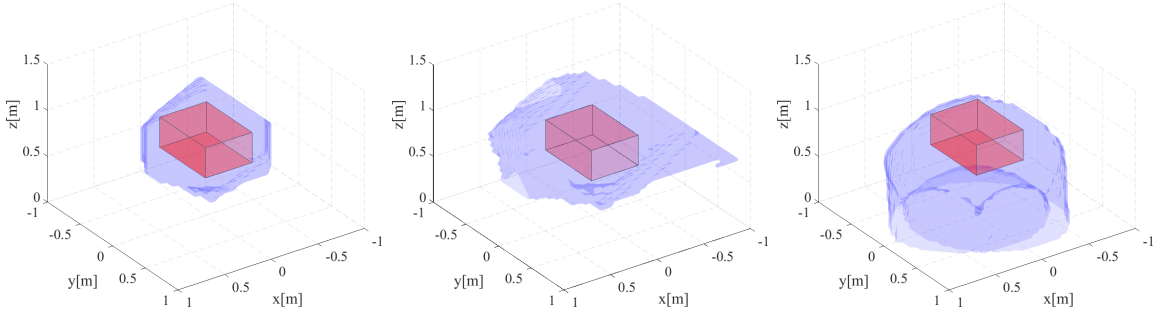

(a) $\underline{\mathrm{R}}\mathrm{RC}^{\Delta}$ **(b)** $\underline{\mathrm{C}}\mathrm{RR}^{\Delta}$ **(c)** $\underline{\mathrm{R}}\mathrm{UU}^{\Delta}$

Fig. 10.6: Reachable and prescribed workspace for guidance task

- Acceleration capability

Moreover, additional criteria are applied. These include:

- Singularity index
- Max. actuator velocity
- Max. power
- Installation space
- Distribution of the workspace volume
- Costs (estimated based on material, joints, actuators)

Especially with the performance index and the costs, a technical-economic evaluation according to Kesselring (cf. Chapter 3) can be performed.

10.5.1 Handling task (pick & place)

The analysis results are presented in Fig. 10.7 and in the annex, Fig. 35, p. 133. For all PKS the conditioning index is the best in the middle of the trajectory and its curve shows a symmetrical behavior in general. It is the highest for all PKS with position-independent Jacobian, such as $\underline{C}$RR-PKS (except $\underline{C}RR^{\parallel}$) and $\underline{C}$PR-PKS. As already pointed out with regard to the performance index, $\star$-shaped frame configurations tend to be more suitable for the pick & place task compared to $\parallel$-shaped frame configurations. Especially the conditioning index of the DELTA robot is not the best compared to the other PKS. The same applies to the singularity index. But with regard to the other criteria, such as actuation or acceleration torque and power the performance of the DELTA robot is better than for all other PKS. Very high acceleration and actuation torques occur for $\underline{R}UU^{\Delta}$, high acceleration and actuation forces for $\underline{C}RR^{\Delta}$. Hence, the poor transmission behavior and relatively high performance index of $\underline{R}UU^{\Delta}$ and $\underline{C}RR^{\Delta}$ are truly reflected in their analysis results (cf. required power). By means of the actuation torques and forces the peaks of the performance index can be explained. As mentioned before, high forces or torques respectively can occur if the PKS is in a configuration close to singularity. Due to the long trajectory of the pick & place task this is the case for some PKS.

The actuator velocities of the DELTA robot are higher compared to the other PKS with revolute joint actuation, but they are still in the range of the allowed values. Furthermore, the displacement of the end-effector due to structural stiffness properties is higher. Amongst others, this is due to the fact that for the stiffness model of the DELTA robot torsional and tilting stiffness of the gearbox unit are included.

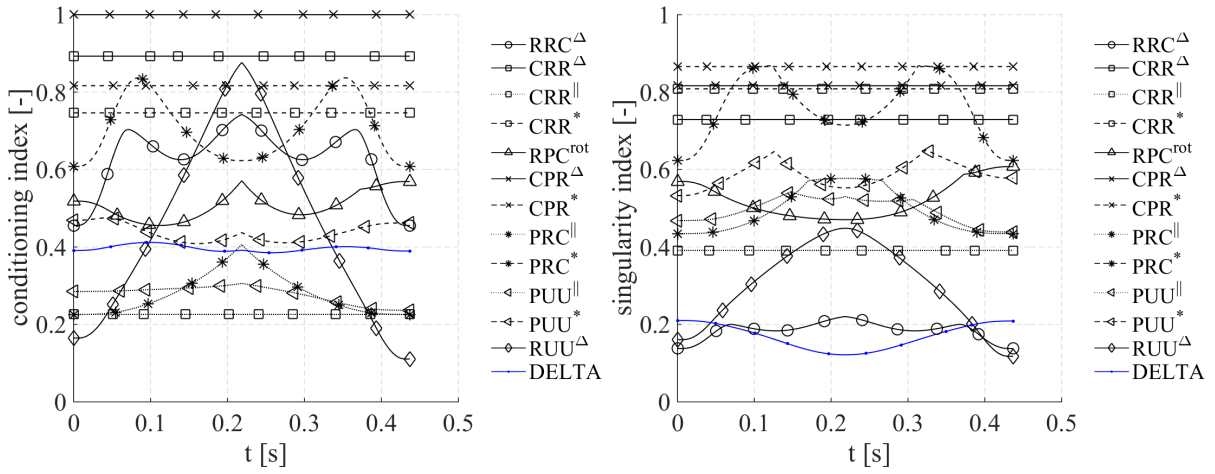

(a) Conditioning index

(b) Singularity index

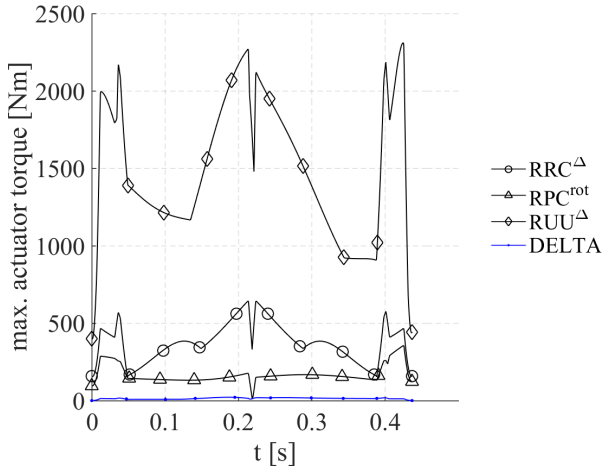

(c) Actuation torques

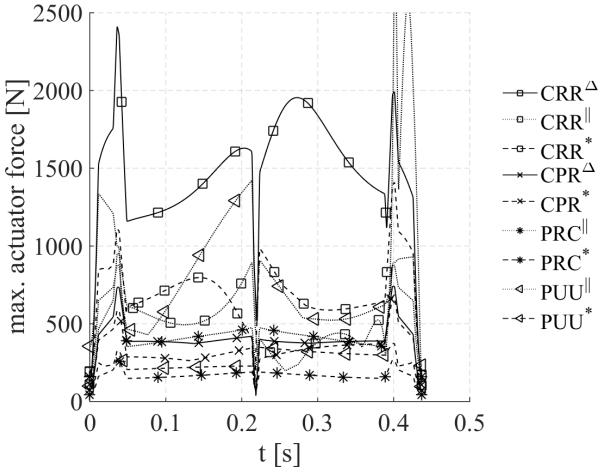

(d) Actuation forces

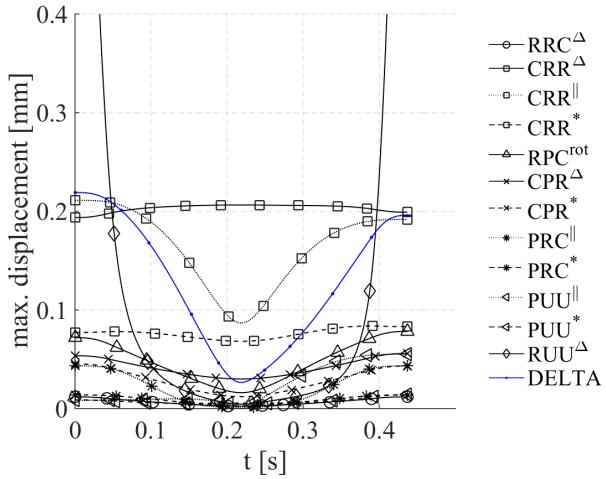

(e) Displacement of the end-effector

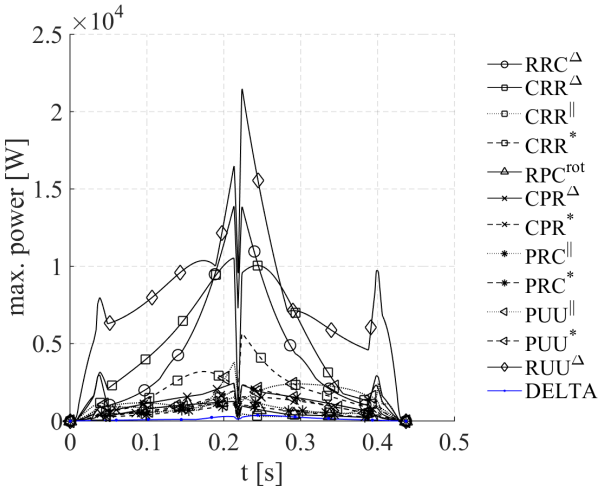

(f) Power

Fig. 10.7: Results pick & place task (I)

In general, the required velocity of the actuators along the trajectory increases till the center point ($x = y = 0$) is reached and decreases afterwards (similar as for applied velocity at the end-effector). Exceptions are the ‖-shaped frame configurations.

The positioning error is not part of the PI for the pick & place task ($w_4 = 0$), but it can be seen that it is higher for PKS with rotational actuation. So linear actuators are, in this case, more precise in positioning.

In conformity with the technical-economic evaluation according to Kesselring (cf. Chapter 3), a strength chart is generated for the pick & place task. The costs cover the costs for joints, links and actuators and are based on offers of suppliers (cf. Tab. 10.4). The ideal costs are set to 4000 €. Thus, the economic value y can be calculated according to Eq. (3.3).

However, the technical value x is not related to Eq. 3.2, but to the median value of the performance index along the trajectory. Since the evaluation is better if the PI is lower, x is calculated with the following formula:

$$x = 1 - med(PI). \tag{10.11}$$

The results are displayed graphically in Fig. 10.8. Due to the less expensive rotational actuators, the economic benchmark for $\underline{\text{R}}\text{RC}^{\Delta}$, $\underline{\text{R}}\text{UU}^{\Delta}$ and $\underline{\text{R}}\text{PC}^{\Delta}$ is better than for PKS with linear actuation. Furthermore, the results are independent of the frame configuration: for example, the position of $\underline{\text{C}}\text{PR}^{\Delta}$ and $\underline{\text{C}}\text{PR}^{\star}$ in the strength chart is similar.

10.5.2 Positioning task (quasistatic positioning)

For the positioning task the mentioned criteria are evaluated along the trajectory as well. Since the optimized parameters for most of the PKS are similar for sideways and bottom

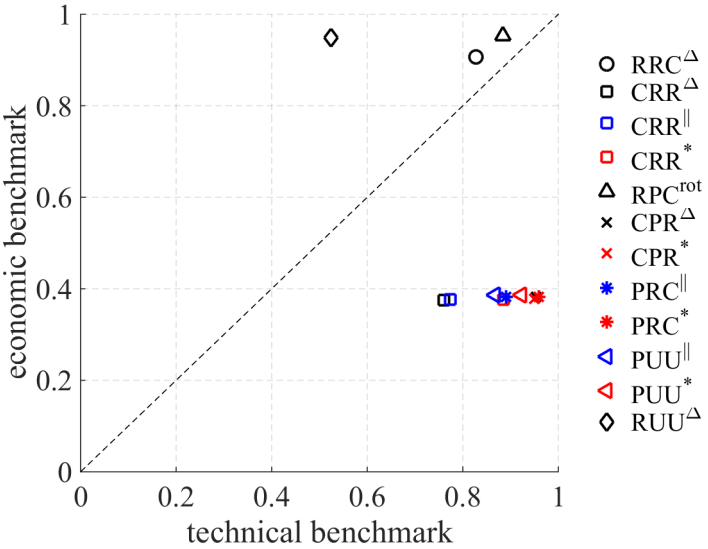

Fig. 10.8: Strength chart pick & place task

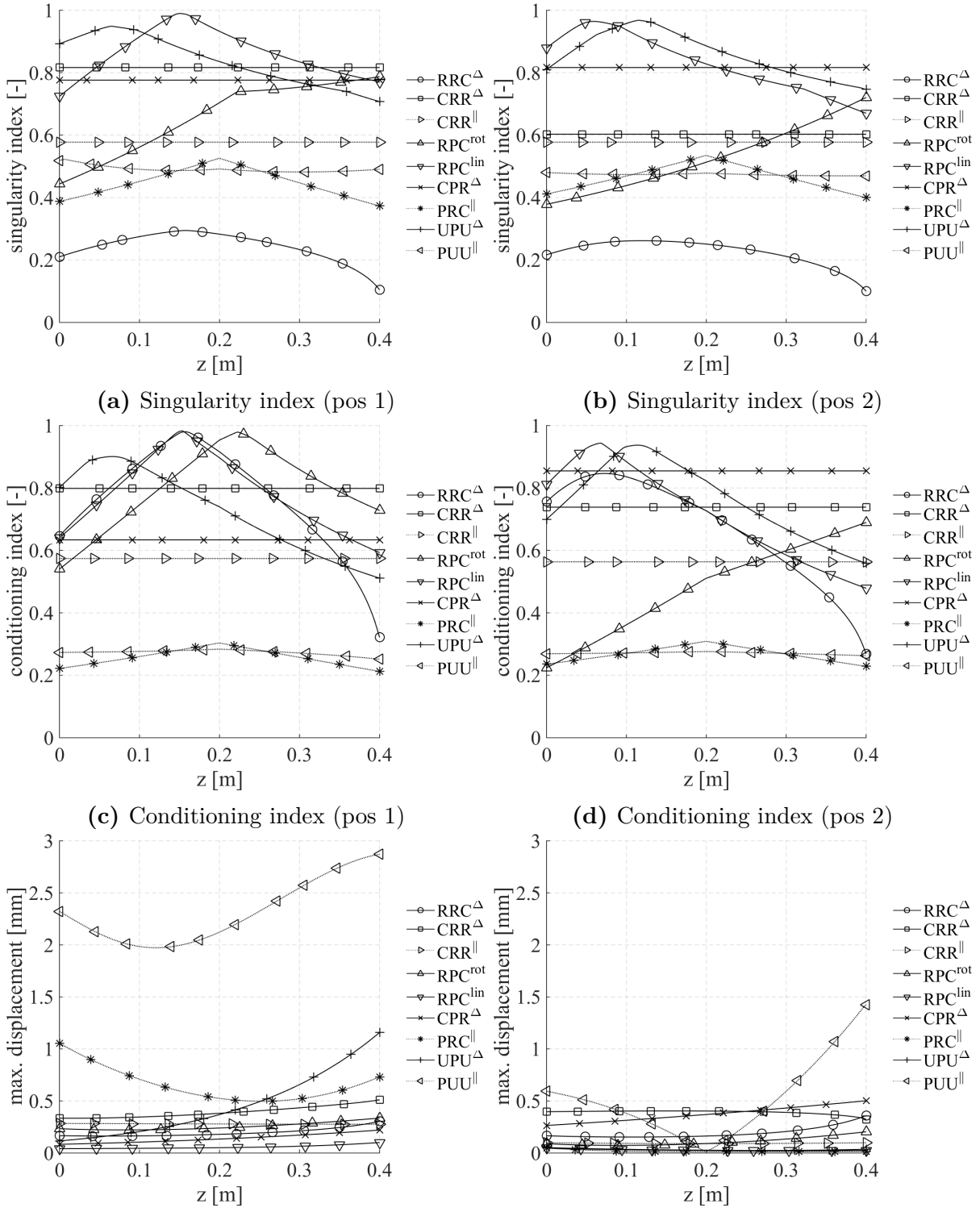

(a) Singularity index (pos 1)

(b) Singularity index (pos 2)

(c) Conditioning index (pos 1)

(d) Conditioning index (pos 2)

(e) Displacement of the end-effector (pos 1)

(f) Displacement of the end-effector (pos 2)

Fig. 10.9: Results positioning task (I)

mounting, the analysis results do not differ very much for all criteria which are independent of the load case: e.g. singularity index, conditioning index, actuator angular velocity and positioning error. In general, the values are worse for ∥-shaped frame configurations. Especially PKS with a prismatic joint in the middle of each link show good performance

characteristics, i.e. R$\underline{\text{P}}$C$^{\Delta}$, C$\underline{\text{P}}$R$^{\Delta}$, U$\underline{\text{P}}$U$^{\Delta}$.

Whereas the positioning error (Fig. 36e and Fig. 36f, p. 216) is lower than 0.1 mm for most PKS (max. 0.05 mm specified in the requirements), it is more than twice as high for $\underline{\text{R}}$RC$^{\Delta}$ and $\underline{\text{C}}$RR$^{\Delta}$. These are two of the three PKS that have two link lengths.

Because the end-effector velocity is very low for the positioning task, the required velocities for the actuators are insignificant (Fig. 36a–36d, p. 216). Hence, the required power is mainly influenced by the payload. It is up to 1 W lower in case of vertical load, because the force transmission in z-direction is better. In case of sideways mounting, $\|$-shaped frame configurations require higher actuation forces compared to the other PKS. Additionally, the selected motor for the rotary drives cannot supply the necessary torques. Here, another motor has to be selected. The same applies to the cylindrical linear actuator. The available force of 5000 N is not high enough to manipulate the end-effector with an external load of approximately 15 kN. Therefore, other actuation concepts, such as with hydraulic or pneumatic actuators, should be investigated. Solely the linear actuator with slide (F_{max} = 9.5 kN) can provide almost the required forces. Besides, for the sideways mounting the required forces are homogeneous along the trajectory, for the bottom mounting they can vary in a range of up to 10 kN.

The high actuation forces and torques together with the maximum displacement of the end-effector due to stiffness properties of the links are the main contributors to the value of the performance index above 1. There are no big differences between sideways and bottom mounting with regard to the maximum displacement (Fig. 10.9e and Fig. 10.9f). It is lower than 0.5 mm for all PKS except for $\underline{\text{P}}$UU$^{\|}$, $\underline{\text{P}}$RC$^{\|}$ and U$\underline{\text{P}}$U$^{\Delta}$. Only R$\underline{\text{P}}$C$^{\Delta}$ can fulfill the requirement of a maximum displacement of 0.1 mm for both mounting positions. Furthermore, U$\underline{\text{P}}$U$^{\Delta}$, $\underline{\text{P}}$RC$^{\|}$ and R$\underline{\text{P}}$C$^{\Delta}$ offer high stiffness properties in bottom mounting. Nevertheless, Fig. 10.4b showed that the assumption of a thin-walled hollow cylinder within the MSA model is not permitted. So stiffness properties increase in case of a solid profile and hence, the displacement of the end-effector would be lower. But in contrast, the weight increases and hence, the inertia forces or torques respectively.

There are no special remarks about the conditioning and singularity index. But for the positioning task an additional analysis is performed with regard to the distribution of the reachable workspace along the z-axis (Fig. 10.10). Mainly $\underline{\text{C}}$PR$^{\Delta}$, $\underline{\text{R}}$PC$^{\Delta}$ (pos 1) and $\underline{\text{P}}$RC* show unused workspace volume. In contrast, the shape of the workspace of $\underline{\text{R}}$RC$^{\Delta}$, $\underline{\text{P}}$UU$^{\|}$ (pos 1), $\underline{\text{C}}$RR$^{\|}$ and R$\underline{\text{P}}$C$^{\Delta}$ is more adapted to the trajectory of the positioning task.

Again, a strength chart is generated (Fig. 10.11). Here, the values for sideways mounting are marked with black symbols, those for bottom mounting with red symbols. Since the

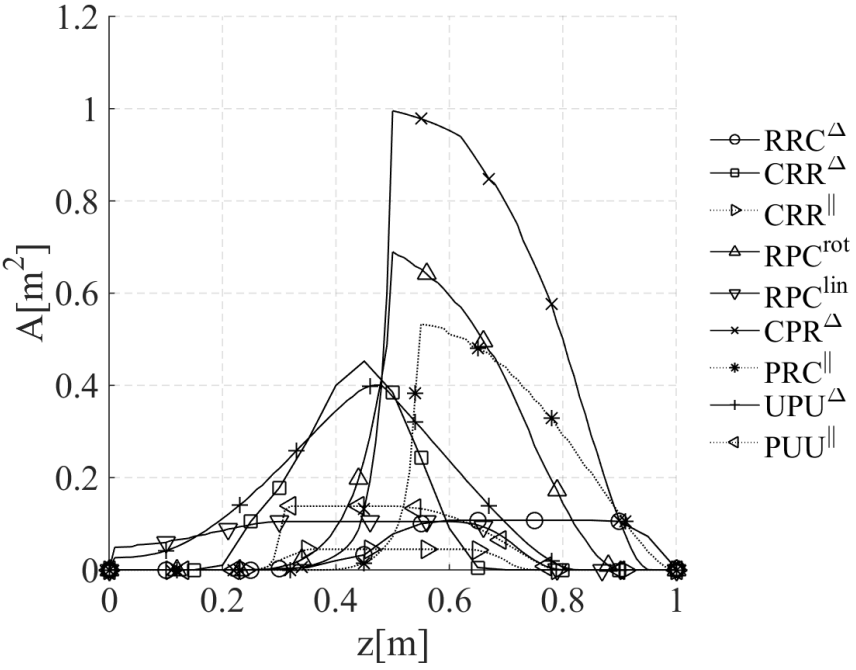

(a) Sideways mounting (pos 1)

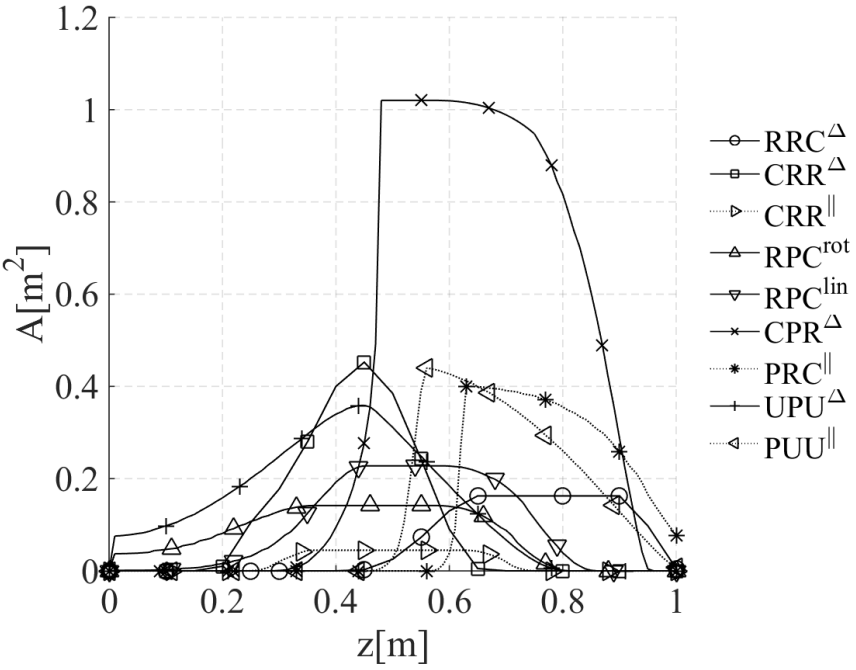

(b) Bottom mounting (pos 2)

Fig. 10.10: Distribution of reachable workspace with respect to z-axis

PI for most PKS is greater than one, the inverse of the median PI ($x = \frac{med(PI)}{2}$) is taken into consideration. Hence, the technical value for U$\underline{\text{P}}$U$^{\Delta}$, R$\underline{\text{P}}$CΔ and $\underline{\text{P}}$RC$^{\parallel}$ (pos 2) is greater than 1 because their PI is less than 1. In contrast to the pick & place task, the distribution about the technical benchmark is more spread out, whereas the range of the economic benchmark is very small. Here as well ideal costs of 4000 € are assumed. In general there are big differences between the mounting positions; exceptions are $\underline{\text{R}}$PC$^{\Delta}$,

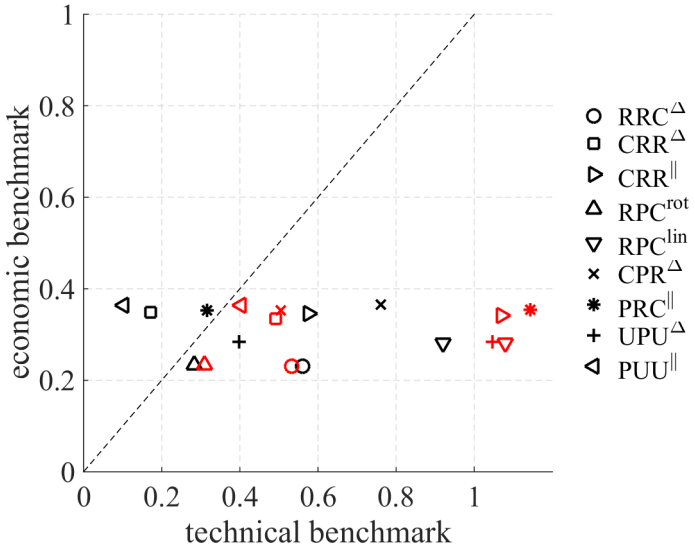

Fig. 10.11: Strength chart positioning task (black = pos 1, red = pos 2)

$\underline{\text{R}}\text{RC}^{\Delta}$ and $\text{R}\underline{\text{P}}\text{C}^{\Delta}$. A good balance between technical and economic benchmark show $\underline{\text{R}}\text{PC}^{\Delta}$, $\underline{\text{P}}\text{UU}^{\|}$ (pos 2) and $\underline{\text{P}}\text{RC}^{\|}$ (pos 1), but $\text{R}\underline{\text{P}}\text{C}^{\Delta}$, $\text{U}\underline{\text{P}}\text{U}^{\Delta}$ (pos 2), $\underline{\text{P}}\text{RC}^{\|}$ (pos 2) and $\underline{\text{C}}\text{RR}^{\|}$ (pos 2) possess the best technical benchmark.

10.5.3 Guidance task (3D fiber injection plant)

For the analysis 144 points within the prescribed workspace are considered. Since three PKS with different actuation concepts are compared, they are evaluated only with regard to the following criteria: performance index, conditioning index, maximum positioning error, maximum displacement of the end-effector and maximum power. The results are presented using box plots (Fig. 10.12). Because the Jacobian of $\underline{\text{C}}\text{RR}^{\Delta}$ does not depend on the position of the end-effector, the transmission behavior is homogeneous over the entire prescribed workspace. In contrast, $\underline{\text{R}}\text{RC}^{\Delta}$ and $\underline{\text{R}}\text{UU}^{\Delta}$ show a similar behavior for all criteria, except the power. Here, $\underline{\text{R}}\text{UU}^{\Delta}$ requires higher power due to higher actuation torques.

The presented PKS can fulfill the demands described in Tab. 5.3. Although not included in the performance index ($w_3 = 0$), the max. displacement is smaller than 0.1 mm (for $\underline{\text{R}}\text{RC}^{\Delta}$ and $\underline{\text{R}}\text{UU}^{\Delta}$) and smaller than 0.25 mm for $\underline{\text{C}}\text{RR}^{\Delta}$ for most points within W_{pre} and thus much smaller than the max. allowed displacement of 0.5 mm (cf. Tab. 10.4). However, it is worth noting that the assumption of a thin-walled cylinder as profile for the links has to be verified. Furthermore, the median of the max. actuator torque/force is lower than 1324 Nm/5000 N ($\tau_{med,RRC} = 507$ Nm, $\tau_{med,RUU} = 1101$ Nm, $f_{med,CRR} = 684$ N). The same applies to the required actuator velocities: the allowed limits are 29.45 $\frac{1}{s}$ and 10 $\frac{m}{s}$; the median values are: $\omega_{med,RRC} = 1.3\ \frac{1}{s}$, $\omega_{med,RUU} = 1.25\ \frac{1}{s}$, $v_{med,CRR} = 0.67\ \frac{m}{s}$.

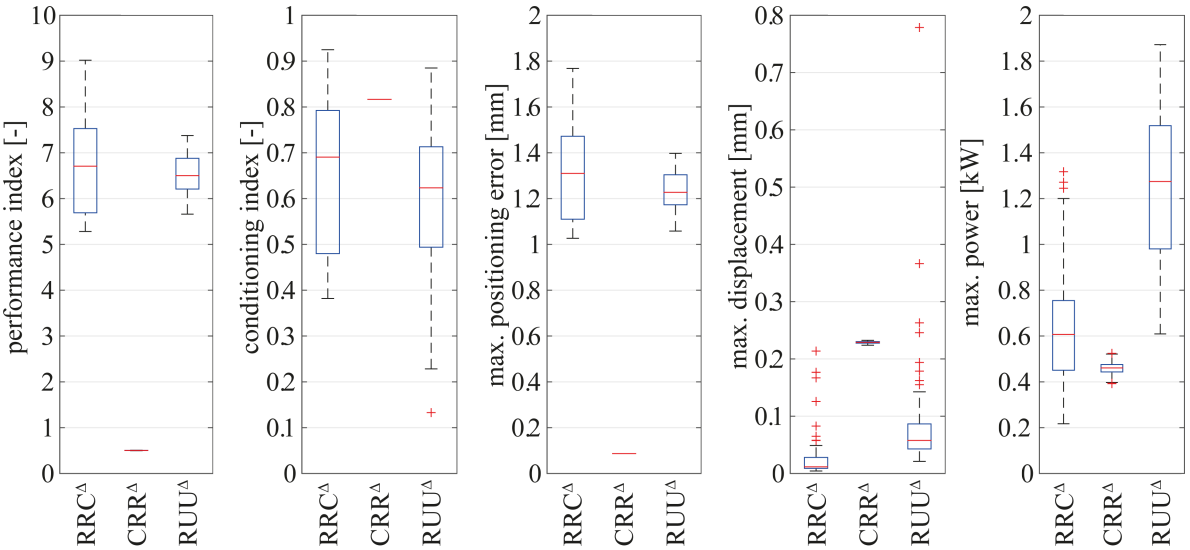

Fig. 10.12: Analysis results for guidance task

Only the positioning error is higher than the required repeatability (> 0.08 mm). So here, good control strategies and systems are necessary. Moreover, the PKS fit almost into the available installation space (r_A, Tab. 10.8) of (1.63x1.63x1.14)m^3. Here, only the footprint of $\underline{\text{R}}\text{RC}^{\Delta}$ is slightly larger. Since the position or distance respectively of the prescribed workspace with respect to the ground (z_{MS}, Tab. 10.8) in combination with half the length of the height of the cylinder is smaller than 1, the max. allowed installation space in z-direction is not exceeded.

Even if the external load increases to 15 kg, e.g. due to heavier cylindrical joint axes in case of $\underline{\text{R}}\text{RC}^{\Delta}$, the actuator limits are not exceeded ($\tau_{med,RRC} = 535$ Nm, $\tau_{med,RUU} = 1138$ Nm, $f_{med,CRR} = 741$ N). Only the displacement of the end-effector of $\underline{\text{C}}\text{RR}^{\Delta}$ increases significantly ($\delta p_{med,CRR} = 0.69$ mm). Hence, in conclusion, a parallel manipulator with tree translational DoF in combination with a spherical mechanism (spatially separated) is an alternative for the described guidance task (cf. Section 5.3.3).

10.6 Detailed stiffness modeling

For stiffness optimization tasks it is of interest which flexible element has the highest influence on the translational and rotational deflection of the end-effector. So finally, the impact of the elasticity contributors to the deflection of the end-effector are analyzed, i.e. link stiffness, actuator stiffness and bearing stiffness are considered separately. The stiffness model is based on the MSA (cf. Section 6.2.3) with the stiffness matrices introduced in Section 10.2. The analysis is performed according to the OFAT (One-Factor-At-a-Time) method. To proportionately determine the stiffness influence of each elasticity contributor

on the stiffness of the PKS, only one flexible element is considered in each step of the analysis. The stiffnesses of all not considered flexible elements are set to ideally rigid, e.g. $10^9 \frac{N}{m}$. To determine the percentage of each flexible element (par_k), the following formula is applied:

$$par_k = 100 \cdot \frac{|d_{dk} - d_{d0}|}{|d_{dlink} - d_{d0}| + |d_{djoint} - d_{d0}| + |d_{dact} - d_{d0}|}, \tag{10.12}$$

with d_{dk} = absolute deflection due to element k (k = link, joint, act) and d_{d0} = absolute deflection of rigid PKS.

As an example, $\underline{\mathrm{R}}\mathrm{RC}^{\Delta}$ is analyzed with regard to its elasticity contributors for the positioning and pick & place task. The results are presented in Fig. 10.13 and Fig. 10.14. In case of the positioning task, the translational deflection of the end-effector is influenced mainly by the compliance of the actuators – in contrast for the rotational deflection by the bearing stiffness. The elasticity contribution of the links – here modeled as solid rods – is negligible. Therefore, stiffness properties of $\underline{\mathrm{R}}\mathrm{RC}^{\Delta}$ can be improved by selecting stiffer bearings and/or actuators.

The same applies to the pick & place task: the main contributors for the translational deflection are the actuators, whereas the selected bearings influence the rotational deflection of the end-effector.

10.7 Conclusion and Summary

Within this chapter the suitability of PKS for three tasks, namely pick & place, positioning and guidance, has been analyzed. Thus, a task adapted dimensional synthesis was performed. The optimization procedure was divided into several steps, including task definition, requirement determination, structure and criteria selection, weighting, selection of components, limitations set-up and definition of material properties. Finally, the

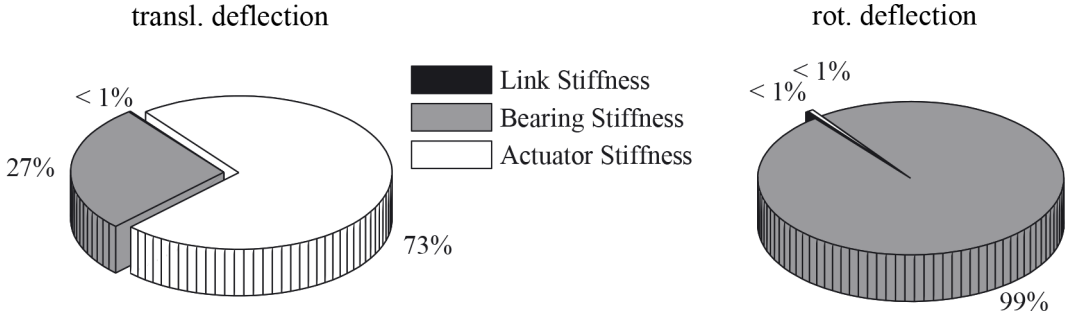

Fig. 10.13: Elasticity contributors for sideways mounting of positioning task

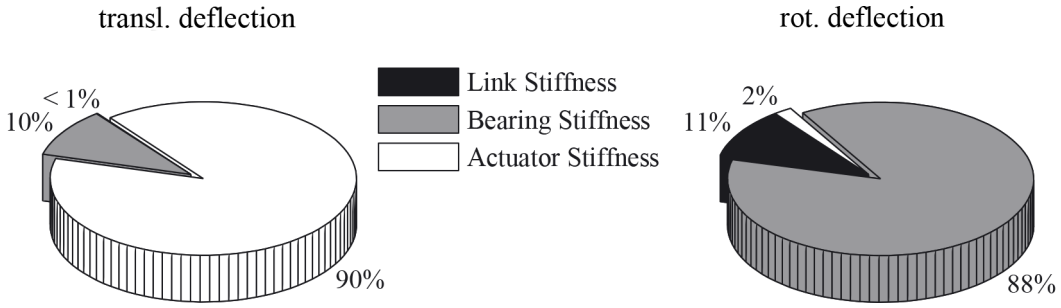

Fig. 10.14: Elasticity contributors for pick & place task

PKS were optimized by using a flexible objective function, which could be adapted by a task-based selection of the weighting factors.

In general, it is not possible to find a "best" PKS for the tasks. Each PKS possesses its own advantages and disadvantages. But nevertheless, the performed analysis gives new insights into the performance properties of different PKS. Compared to the DELTA robot used for pick & place tasks, the selected PKS do not offer higher potential. So the DELTA robot is not for nothing the most used parallel robot in industry. $\star$-shaped frame configurations tend to be more suitable for the pick & place task compared to $\|$-shaped frame configurations since the parallel frame arrangement limits the range of motion. Furthermore, a linear actuation is preferred. Especially PRC* and CPR* show very good results with regard to the applied criteria.

In case of the positioning task parameter configurations for the PKS can be found so that they can follow the prescribed trajectory. But since the applied force at the end-effector is quite high, the selection of suitable drives is challenging. Furthermore, in order to achieve the required accuracy and repeatability, good control systems and strategies are important prerequisites. Bottom mounting is preferred compared to sideways mounting since high loads can be better absorbed in this way. Here, $\|$-shaped frame configurations offer some advantages with regard to the performance index.

With respect to the described guidance task, in conclusion, a parallel manipulator with tree translational DoF is an alternative to the serial robot. But here, an additional spherical mechanism (spatially separated) is necessary and has to be designed. But the study has shown that the choice of suitable PKS for this task is very limited. Only PKS with Δ-shaped frame configuration are suitable.

The presented framework allows for good comparison of different PKS without going into detail of very specific components (e.g. bearings). A suitable PKS can be selected from a wide range and can be optimized afterwards. Weighting factors can be adapted according to specific needs and tasks.

11 Summary and outlook

11.1 Summary

Well known is Clavel's DELTA robot, but there are other parallel kinematic structures (PKS) with three translational degrees of freedom (DoF). They differ in the assembly and the limb structure (kinematic chain). For each kinematic chain a combination of revolute, prismatic, cylindrical and universal joints can be used. A broad range of PKS based on different joint and limb arrangements has been synthesized in the past years, but only a small number was further investigated in research.

Therefore, in this thesis, a structure catalog comprising different PKS with their respective characteristics was created. The selection was based on lists of previously synthesized PKS. To reduce the number of possible PKS for further analysis, the following assumptions were made:

- three translational DoF,
- three limbs,
- symmetrical limb arrangement,
- and three joints within each limb.

Additionally, further criteria reduced the number of possible PKS:

- arrangement of the actuators close to the frame,
- identical limbs,
- and each joint with DoF < 3.

Furthermore, different frame configurations were investigated: this included mainly the triangular, star- and parallel-shaped frame configuration.

For in total 25 different PKS the structure catalog has been expanded by mathematical descriptions, i.e. the inverse kinematics and the Jacobian matrix. Afterwards, a first analysis and comparison of the PKS was performed with regard to the following criteria: local dexterity index, required actuator forces or torques respectively, required actuator velocities and end-effector displacements due to compliance of the actuators and positioning errors. The kinematic dimensions were optimized with respect to two load cases: 1) rectangular workspace with low external forces and 2) cylindrical workspace with higher

external forces. The results showed that not all selected PKS possess good transmission qualities. Hence, some PKS were excluded from further analysis.

Then, a general research study of the selected structures was performed. Different dimensions for the PKS were considered and analyzed to identify the influence of selected parameter configurations. To do so, various criteria were applied within a prescribed workspace inside the reachable workspace. This prescribed workspace was based on the largest sphere that fits into the reachable workspace. It was determined by using a nearest neighbor search algorithm and the bisection method. The results have been presented graphically using performance charts. This analysis and the comparison afterwards resulted in further reduction of the PKS for the final task-adapted dimensional synthesis.

Thus, various manipulation tasks were presented and analyzed. Furthermore, dynamic and stiffness models were derived for the remaining PKS. Hence, it had to be identified which of the calculation procedures have already been derived and implemented for various structures and where gap filling was necessary.

Once the mathematical descriptions of the PKS have been completed, their kinematic dimensions were optimized for three tasks and trajectories respectively:

- pick & place
- positioning
- guidance

The optimization was based on a flexible objective function that allows adjusting the function value by including different criteria with adaptable weights. To select appropriate criteria, a compilation of criteria to measure, analyze and compare the performance of PKS has been presented. Consequently, the following criteria were included in the optimization: conditioning index, required actuator forces or torques respectively based on the dynamic model, acceleration capability and end-effector displacements due to compliance of the links and positioning errors of the actuators. The performance of the PKS along the trajectories or within the prescribed workspace was analyzed by using additional criteria such as required actuator velocities, required power or cost. The optimization and analysis results showed that some of the selected PKS can fulfill the described tasks and that no “best” PKS can be found.

11.2 Discussion

The work in hand presents a framework for the selection and analysis of parallel kinematic structures with three translational degrees of freedom. Detailed optimizations of

different parallel kinematic structures are possible since all required mathematical models have been derived. Mathematical descriptions, analysis methods and results can be used for further investigations. They offer high potential for in-depth and fundamental research studies in the field of parallel robots, e.g. comparison, dimensioning, optimization and control only to mention a few. Single PKS can be selected to prove new theories by simulation - the required basic calculation methods are implemented and can be applied directly. Hence, this work can be used as a database which provides fundamental information on different parallel kinematic structures. The use of the mathematical models saves time and accelerates the investigation of new concepts within the scope of parallel robots.

However, the impact of this work is not necessarily limited to an academic environment. Even industry-oriented research can benefit: it is possible to compare the properties of real industrial structures with potential concepts of new structures.

Nevertheless, some further points should be taken into account with regard to future work:

- Calculation and consideration of internal joint forces/torques and velocities
- Stiffness modeling of links and joints
- Design implementation and comparison with real structures
- Optimization method
- Evaluation method
- Singularity analysis
- Selection of criteria and sensitivity of weighting factors

The first two arguments are necessary to select and design appropriate components. An approach to calculate the occurring forces or torques and velocities gives the dynamic modeling according to Newton/Euler. Only quantifiable values allow the selection of joints (or bearings) and hence, their stiffness modeling can be improved. Moreover, the choice of a rectangular profile for the links offers further optimization potential, because the stiffness is higher but the mass remains equal compared to cylindrical profiles.

With regard to the design of the PKS it should be mentioned that all considerations are theoretical, i.e. design specific requirements such as physical separation of prismatic and revolute joint parts of cylindrical joints have not yet been considered in the analysis. This was done only for the DELTA structure that was taken as reference. Here, the intention was to use the dimensions of a real robot (available at the Department of Mechanism Theory and Dynamics of Machines). By showing the properties of this robot when analyzed according to the same criteria as the other PKS, valuable insights into possible potentials of these new structures can be highlighted. However, if a quantified statement should be

made on how much better the DELTA structure is, it has to be optimized in the same way as the other PKS.

In this thesis only one optimization method was applied: the genetic algorithm. However, for general optimization problems with an objective function it is not guaranteed that a solution will be found and no statements about: "how optimal is the solution?" can be made. In addition, objective functions are highly non-linear and the entire process is iterative and time consuming. One possibility to approach this problem is the interval analysis. With this method lower and upper bounds of a function with multiple unknowns can be determined, if the limits of the unknowns are known. Thus, the specific interval contains all solution candidates that can be generated with the possible values of the unknowns.

Besides, evaluation methods with very high time and effort can be applied to improve the selection and weighting of criteria and the benchmark study, e.g. priority method or demand-oriented weighted evaluation.

Detailed singularity analyses would be helpful to optimize the respective structures further (e.g. regarding lower actuation forces or torques) and to describe motion possibilities in a general way. Especially if the PKS should be used for more than one task or trajectory a singularity analysis and the definition of a singular-free workspace is highly recommended.

There is a wide scope regarding the selection of criteria. Different criteria can be applied in all stages of the selection and evaluation process that may lead to different results. For example, the use of the largest sphere inside the reachable workspace might not be the best criteria if the volume of the workspace should be considered. However, it is a useful measure to evaluate the largest possible, direction-independent workspace. Furthermore, the sensitivity of the selection of the weighting factors requires some attention. A first step in this direction has been done for the weighting factors used to generate the benchmark metrics. Moreover, a sensitivity analysis regarding the task-adapted weighting factors of the flexible objective function could give some insights into the general suitability of some PKS for specific tasks, independent of the weighting factors.

The method presented in this thesis could be applied for robotic architectures with different motion patterns as well since it is expected to be generally applicable, but criteria selection and usage at all stages of the process have to be adapted. A problem here could be mixed actuation (rotational and linear actuators) within the same structure.

In a further step, a graphical user interface could be implemented to facilitate the analysis and comparison of the PKS for other users. In this connection, not only the kinematic

and kinetostatic models are important but also the dynamic and stiffness models. An integration of the task-adapted optimization method is possible as well.

11.3 Conclusion

This thesis presented, analyzed and compared different PKS with three translational degrees of freedom with regard to various criteria and tasks. The presented research study was done in this way for the first time and offers insights into the characteristics and special properties of the considered PKS. A major part took the derivation of fundamental calculation models. To summarize the contribution of this thesis regarding mathematical models, Tab. 11.1 gives an overview of the selected PKS and the respective mathematical descriptions.

Various analysis steps were performed which are listed in Tab. 11.2 related to the PKS considered. There is no "best" PKS that is suitable for all tasks in the same way. The contrasted results represent very well the diversity of the tasks and hence, the differing suitability of the PKS.

For example, PKS that are suitable for the guidance task, are not suitable for the pick & place task. It is the same for PKS that show good results for the positioning task: they do not seem to be a good choice for the pick & place task. However, there are two exceptions: $\underline{C}PR^{\Delta}$ and $\underline{P}RC^{\parallel}$ show good performance for both, pick & place and guidance task.

Group 4R-1P offers a broad range of PKS, but most of the PKS cannot be rated as good configurations. Thus, it is more likely to find a suitable PKS in the groups 3R-1P and 2R-2P.

There is no preference regarding rotational or linear actuation, but all PKS with an universal joint as actuated joint were successively excluded from further analysis.

In conclusion, 16 different PKS were considered in this thesis - including three possible frame configurations this has led to a number of 25 PKS. However, only 13 PKS (52 %) were allowed for a task-adapted dimensional synthesis.

	PKS	frame	actuation	fwd. kinematics	inv. kinematics	Jacobian matrix	SimMechanics model	stiffness model (SimMech)	stiffness model (MSA)	inv. dynamics	accelerations	CAD model	in GUI
3R-1P	RRC	Δ	R	-	✓	✓	✓	✓	✓	✓	✓	✓	✓
		⋆		x	✓	✓	✓	✓	✓	✓	✓	✓	✓
	CRR	Δ (R≠ P)	P	-	✓	✓	✓	✓	✓	✓	✓	✓	✓
		∥ (R≠ P)		-	✓	✓	✓	✓	✓	✓	✓	✓	✓
2R-2P	RPC	Δ	R	-	✓	✓	✓	✓	✓	✓	✓	✓	✓
			P	-	✓	✓	✓	✓	✓	✓	✓	✓	✓
	CPR	Δ (R≠ P)	P	-	✓	✓	✓	✓	✓	✓	✓	✓	✓
		⋆		-	✓	✓	✓	✓	✓	✓	✓	✓	✓
	PRC	⋆	P	x	✓	✓	✓	✓	✓	✓	✓	✓	✓
		∥		-	✓	✓	✓	✓	✓	✓	✓	✓	✓
4R-1P	CUR	Δ (R≠ P)	P	-	✓	✓	✓	x	x	x	x	✓	✓
		⋆		-	✓	✓	✓	-	-	x	x	✓	✓
		∥ (R≠ P)		-	✓	✓	✓	x	x	x	x	✓	✓
	RUC	Δ	R	-	✓	✓	✓	x	x	-	-	✓	-
	UUP	Δ	R	-	✓	✓	✓	x	x	-	-	✓	✓
	UPU	Δ	P	x	✓	✓	✓	✓	✓	✓	✓	✓	✓
	PUU	Δ	P	-	✓	✓	✓	x	x	-	-	✓	-
		⋆		x	✓	✓	✓	✓	✓	✓	✓	✓	✓
		∥		-	✓	✓	✓	✓	✓	✓	✓	✓	✓
	URC	Δ	R	x	✓	✓	✓	x	x	-	-	✓	✓
	CRU	Δ	P	-	✓	✓	✓	x	x	-	-	✓	-
		⋆		-	✓	✓	✓	-	-	-	-	✓	-
	UCR	Δ	R	-	✓	✓	✓	-	-	-	-	✓	-
5R	URU	Δ	R	-	✓	✓	✓	x	x	x	x	✓	✓
	UUR	Δ	R	-	✓	✓	✓	x	x	x	x	✓	✓
	RUU	Δ	R	-	✓	✓	✓	✓	✓	✓	✓	✓	✓

✓ implemented
\- not implemented
x implemented but not further used

Tab. 11.1: Derived and implemented mathematical models within the framework of this thesis

	PKS	frame	actuation	first analysis	benchmark metrics	task-adapted: pick & place	task-adapted: positioning	task-adapted: guidance
3R-1P	RRC	Δ	R	✓	✓	↓	↑	↑
		$\star$		✓	✓	↑	-	-
	CRR	Δ (R$\neq$ P)	P	✓	✓	↓	↓	↑
		$\parallel$ (R$\neq$ P)		✓	✓	↓	↑	-
2R-2P	RPC	Δ	R	✓	✓	↑	↓	x
			P	✓	✓	x	↑	x
	CPR	Δ (R$\neq$ P)	P	✓	✓	↑	↑	x
		$\star$		✓	✓	↑	-	-
	PRC	$\star$	P	✓	✓	↑	-	-
		$\parallel$		✓	✓	↑	↑	-
4R-1P	CUR	Δ (R$\neq$ P)	P	✓	✓	-	-	-
		$\star$		✓	✓	-	-	-
		$\parallel$ (R$\neq$ P)		✓	✓	-	-	-
	RUC	Δ	R	✓	-	-	-	-
	UUP	Δ	R	✓	✓	-	-	-
	UPU	Δ	P	✓	✓	x	↑	x
	PUU	Δ	P	✓	-	-	-	-
		$\star$		✓	✓	↑	-	-
		$\parallel$		✓	✓	↑	↓	-
	URC	Δ	R	✓	✓	-	-	-
	CRU	Δ	P	✓	-	-	-	-
		$\star$		✓	-	-	-	-
	UCR	Δ	R	✓	-	-	-	-
5R	URU	Δ	R	✓	✓	-	-	-
	UUR	Δ	R	✓	✓	-	-	-
	RUU	Δ	R	✓	✓	↓	x	↑

↑	analyzed, more suitable
↓	analyzed, less suitable
✓	analyzed
x	no results found
-	not analyzed

Tab. 11.2: Analyses done within the framework of this thesis

Bibliography

[AAS11] Ahmad, A.; Anderson, K.; Sellgren, U.
An approach to stiffness analysis methodology for haptic devices
In: IEEE (ed.), 3rd International Congress on Ultra Modern Telecommunications and Control Systems and Workshops (ICUMT), Budapest, Hungary, 2011, pp. 1–8.

[ABB14] ABB
ABB Deutschland
http://new.abb.com/de (visited on 08/01/2014).

[Ade14] Adept
Adept Technology GmbH
http://www.adept.de (visited on 08/01/2014).

[AL92] Angeles, J.; Lopez-Cajun, C. S.
Kinematic Isotropy and the Conditioning Index of Serial Robotic Manipulators
In: The International Journal of Robotics Research, 11 (1992) 6, DOI 10.1177/027836499201100605, pp. 560–571.

[Ang14] Angeles, J.
Fundamentals of robotic mechanical systems, Theory, methods, and algorithms
Springer, 4. ed., 2014, ISBN 9783319018508.

[Ang92] Angeles, J.
The Design of Isotropic Manipulator Architectures in the Presence of Redundancies
In: The International Journal of Robotics Research, 11 (1992) 3, DOI 10.1177/027836499201100303, pp. 196–201.

[Arr12] Arrouk, K.
Techniques de conception assistée par ordinateur (CAO) pour la caractérisation de l'espace de travail de robots manipulateurs parallèles
Dissertation, Clermont-Ferrand: Université Blaise Pascal - Clermont-Ferrand II, 2012.

[Asa83] Asada, H.
A Geometrical Representation of Manipulator Dynamics and Its Application to Arm Design
In: Journal of Dynamic Systems, Measurement, and Control, 105 (1983) 3, DOI 10.1115/1.3140644, p. 131.

[Asy14] Asyril
asyril
http://www.asyril.ch/en (visited on 08/01/2014).

[Aud14] Audi
Audi Deutschland
http://www.audi.de/de/brand/de.html (visited on 08/11/2014).

[BCW11] Binaud, N.; Caro, S.; Wenger, P.
Comparison of 3-RPR planar parallel manipulators with regard to their kinetostatic performance and sensitivity to geometric uncertainties
In: Meccanica, 46 (2011) 1, DOI 10.1007/s11012-010-9390-0, pp. 75–88.

[Ben08] Bengtsson, K.
Flexibler Helfer - ABB präsentiert die zweite Generation des FlexPicker
In: ABB-Technik - Die technische Zeitschrift des ABB-Konzerns, 28 (2008) 4, pp. 29–33.

[Ben14] Bender, A.
Systematische Entwicklung von kinematischen Konzepten für Handhabungseinheiten beim 3D-Faserspritzen, (engl.: Systematically development of kinematic concepts for manipulation units for 3D fiber injection)
Master Thesis, Aachen: RWTH Aachen University, Department of Mechanism Theory and Dynamics of Machines, 2014.

[BG99] Boudreau, R.; Gosselin, C. M.
The Synthesis of Planar Parallel Manipulators with a Genetic Algorithm
In: Journal of Mechanical Design, 121 (1999) 4, DOI 10.1115/1.2829494, p. 533.

[Bie06] Bier, C. C.
Geometrische und physikalische Analyse von Singularitäten bei Parallelstrukturen
Essen: Vulkan-Verlag, 2006, ISBN 9783802786907.

[BK00] Bowling, A.; Khatib, O.
Robot acceleration capability: the actuation efficiency measure

In: IEEE (ed.), International Conference on Robotics and Automation, San Francisco, CA, 2000, pp. 3970–3975.

[BK97] Breiing, A.; Knosala, R.
Bewerten technischer Systeme
Berlin, Heidelberg: Springer Berlin Heidelberg, 1997, ISBN 978-3-642-63908-1.

[Ble03] Bleicher, F.
Parallelkinematische Werkzeugmaschinen
Wien: NWV Neuer Wissenschaftlicher Verlag, 2003, ISBN 9783708301181.

[BMM02] Badescu, M.; Morman, J.; Mavroidis, C.
Workspace optimization of 3-UPU parallel platforms with joint constraints
In: IEEE (ed.), International Conference on Robotics and Automation, Washington, DC, USA, 2002, pp. 3678–3683.

[Bon14] Bonev, I.
Software Related to Parallel Mechanisms
http://www.parallemic.org/Software.html (visited on 08/01/2014).

[BPB12] Bondarenko, D.; Pashkevich, A.; Briot, S.; Ritou, M.; Furet, B.
Elasto-Dynamic Model of Robotic Milling Process Considering Interaction Between Tool and Workpiece
In: ASME (ed.), 11th Biennial Conference on Engineering Systems Design and Analysis, Nantes, France, 2012, ISBN 0791844870, pp. 217–226.

[BPC11] Briot, S.; Pashkevich, A.; Chablat, D.
Reduced elastodynamic modelling of parallel robots for the computation of their natural frequencies
In: IFToMM (ed.), 13th World Congress in Mechanism and Machine Science, Guanajuato, Mexico, 2011.

[BW10] Bi, J.; Wen, R.
Errors Analysis of 3-UPU Parallel Manipulator Using Screw Theory
In: IEEE (ed.), International Conference on Measuring Technology and Mechatronics Automation (ICMTMA), Changsha City, China, 2010, pp. 137–140.

[Cam12] Cammarata, A.
On the Stiffness Analysis and Elastodynamics of Parallel Kinematic Machines
In: Kucuk, S. (ed.), Serial and Parallel Robot Manipulators - Kinematics,

Dynamics, Control and Optimization, InTech, 2012, ISBN 978-953-51-0437-7.

[car14] carat robotic innovation GmbH
FAMOS robotic® - HomePos
http://www.famos-robotic.de/index.php?id=homepos (visited on 08/11/2014).

[CBB04] Clavel, R.; Bleuler, H.; Bauer, D.; Bouri, M.; Breguet, J.-M.
Robotique, Microrobotique, pour la section de microtechnique
Lecture notes, Lausanne: Ecole Polytechnique Fédérale de Lausanne, Faculté sciences et techniques de l'ingénieur, 2004.

[CCC13] Chen, Q.; Chen, Z.; Chai, X.; Li, Q.
Kinematic Analysis of a 3-Axis Parallel Manipulator: The P3
In: Advances in Mechanical Engineering, 2013 (2013) 1, DOI 10.1155/2013/589156, pp. 1–10.

[CCU10] Chablat, D.; Caro, S.; Ur-Rehman, R.; Wenger, P.
Comparison of Planar Parallel Manipulator Architectures Based on a Multi-Objective Design Optimization Approach
In: ASME (ed.), International Design Engineering Technical Conferences and Computers and Information in Engineering Conference, Montreal, Quebec, Canada, 2010, pp. 861–870.

[Cha13] Charaf Eddine, S.
Herleitung und Implementierung unterschiedlicher Berechnungsverfahren für parallelkinematische Werkzeugmaschinen mit drei translatorischen Freiheitsgraden, (engl.: Derivation and implementation of different calculation methods for parallel kinematic machine tools with three translational degrees of freedom)
Master Thesis, Aachen: RWTH Aachen University, Department of Mechanism Theory and Dynamics of Machines, 2013.

[Che11] Chebbi, A. H.
The potential of the 3-UPU topology for translational parallel manipulators and a procedure to select the best architecture
Doctoral Thesis, Bologna: University of Bologna, Meccanica e Scienze Avanzate dell'Ingegneria Progetto n. 3 – Meccanica Applicata, 2011.

[CHG99] Cai, G. Q.; Hu, M.; Guo, C.; Li, B.; Wang, Q. M.
Development and Study of a New Kind of 3-DOF Tripod
In: CIRP Annals - Manufacturing Technology, 48 (1999) 1, DOI 10.1016/S0007-8506(07)63196-5, pp. 333–336.

[CIR14] CIROS
CIROS Engineering
http://www.ciros-engineering.com/home (visited on 08/01/2014).

[CL09] Chen, Y.; Li, B.
Topology synthesis and classification of a novel family of parallel manipulator with 3-dimension translation and 1-dimension rotation
In: IEEE (ed.), International Conference on Information and Automation (ICIA 2009), Zhuhai/Macau, China, 2009, pp. 212–217.

[Com15] Commatteo, A.
Implementierung, Analyse und Vergleich unterschiedlicher Verfahren zur Arbeitsraumdarstellung von Robotern, (engl.: Implementation, analysis and comparison of different methods for workspace representation of robots)
Bachelor Thesis, Aachen: RWTH Aachen University, Department of Mechanism Theory and Dynamics of Machines, 2015.

[CP03a] Carricato, M.; Parenti-Castelli, V.
A Family of 3-DOF Translational Parallel Manipulators
In: Journal of Mechanical Design, 125 (2003) 2, DOI 10.1115/1.1563635, p. 302.

[CP03b] Carricato, M.; Parenti-Castelli, V.
Position Analysis of a New Family of 3-DOF Translational Parallel Manipulators
In: Journal of Mechanical Design, 125 (2003) 2, DOI 10.1115/1.1564073, p. 316.

[CP13] Chebbi, A. H.; Parenti-Castelli, V.
The potential of the 3-UPU topology for translational parallel manipulators and a procedure to select the best architecture for a given task
In: Romanion Journal of Technical Sciences, 58 (2013) 1-2, pp. 5–30.

[CT03] Callegari, M.; Tarantini, M.
Kinematic analysis of a novel translational platform
In: Journal of Mechanical Design, 125 (2003) 2, pp. 308–315.

[CWH01] Cai, G. Q.; Wang, Q. M.; Hu, M.; Kang, M. C.; Kim, N. K.
A study on the kinematics and dynamics of a 3-DOF parallel machine tool
In: Journal of Materials Processing Technology, 111 (2001) 1-3, DOI 10.1016/S0924-0136(01)00532-5, pp. 269–272.

[CWM03] Chablat, D.; Wenger, P.; Merlet, J.-P.
A comparative study between two three-dof parallel kinematic machines using kinetostatic criteria and interval analysis
In: IFToMM (ed.), 11th World Congress in Mechanism and Machine Science, Tianjin, China, 2003.

[Dan13] Danino, M.
Herleitung und Implementierung unterschiedlicher Berechnungsverfahren für translatorische Parallelmanipulatoren mit vier Gelenken pro Bein, (engl.: Derivation and implementation of different calculation methods for translational parallel manipulators with four joints per leg)
Master Thesis, Aachen: RWTH Aachen University, Department of Mechanism Theory and Dynamics of Machines, 2013.

[DC16] Detert, T.; Corves, B.
Extended procedure for stiffness modeling based on the Matrix Structure Analysis
In: Corves, B. et al. (eds.), The Joint International Conference of the XII International Conference on Mechanisms and Mechanical Transmissions (MTM) and the XXIII International Conference on Robotics (Robotics'16), Aachen, Germany, 2016, pp. 299–310.

[Deo14] Deo, A.
Derivation and implementation of different calculation methods for parallel manipulators with three degrees of freedom
Mini-Thesis, Aachen: RWTH Aachen University, Department of Mechanism Theory and Dynamics of Machines, 2014.

[DHM06] Deblaise, D.; Hernot, X.; Maurine, P.
A systematic analytical method for PKM stiffness matrix calculation
In: IEEE (ed.), International Conference on Robotics and Automation (ICRA), Orlando, FL, USA, 2006, pp. 4213–4219.

[DHZ12] Du, N.; Hou, H.; Zhao, J.; Wang, H.
An upper limb rehabilitation robot based on 3-RRC parallel mechanism
In: IEEE (ed.), 2012 International Conference on Advanced Mechatronic Systems, Tokyo, Japan, 2012, ISBN 1467319627.

[Di 01] Di Gregorio, R.
A new parallel wrist using only revolute pairs: the 3-RUU wrist
In: Robotica, 19 (2001) 03, DOI 10.1017/S0263574700003192, pp. 305–309.

[Di 04] Di Gregorio, R.
Kinematics of the Translational 3-URC Mechanism
In: Journal of Mechanical Design, 126 (2004) 6, DOI 10.1115/1.1814390, p. 1113.

[Di 06] Di Gregorio, R.
Closure to "Discussion of 'Kinematics of the Translational 3-URC Mechanism' " (2006, ASME J. Mech. Des., 128, pp. 812–813)
In: Journal of Mechanical Design, 128 (2006) 4, DOI 10.1115/1.2205876, p. 814.

[DiG04] DiGregorio, R.
Statics and Singularity Loci of the 3-UPU Wrist
In: IEEE Transactions on Robotics, 20 (2004) 4, DOI 10.1109/TRO.2004.829475, pp. 630–635.

[DIN3408-4] DIN ISO 3408-4
Ball screws - Part 4: Static axial rigidity
Norm, German Institute for Standardization, Beuth Verlag GmbH, 2011-04-01.

[DIN808] DIN 808
DIN 808 - Machine tools; cardan joints; sizes, connecting dimensions, loading, installation
Norm, German Institute for Standardization, Beuth Verlag GmbH, 1984-08-01.

[DIN8373] DIN EN ISO 8373
Manipulating industrial robots - Vocabulary (ISO 8373:1994)
Norm, German Institute for Standardization, Beuth Verlag GmbH, 1996-08-01.

[DIN9283] DIN 9283
DIN EN ISO 9283 - Manipulating industrial robots - Performance criteria and related test methods
Norm, German Institute for Standardization, Beuth Verlag GmbH, 1999-05-01.

[DP98] Di Gregorio, R.; Parenti-Castelli, V.
A Translational 3-dof Parallel Manipulator
In: Lenarčič, J.; Husty, M. L. (eds.), Advances in Robot Kinematics: Analysis and Control, Dordrecht: Springer Netherlands, 1998, ISBN 978-90-481-5066-3, pp. 49–58.

[DP99] Di Gregorio, R.; Parenti-Castelli, V.
Mobility analysis of the 3-UPU parallel mechanism assembled for a pure translational motion
In: IEEE/ASME (ed.), International Conference on Advanced Intelligent Mechatronics, Atlanta, GA, USA, 1999, pp. 520–525.

[DR06] Dahmen, W.; Reusken, A.
Numerik für Ingenieure und Naturwissenschaftler, Mit 59 Tabellen
Berlin, Heidelberg, New York: Springer, 2006, ISBN 3540298835.

[Dür99] Dürschmied, F.
Baugruppen für parallele Kinematiken
In: Werkstatt und Betrieb, - (1999) 5, pp. 1–8.

[Eas14] Easy-Rob
EASY-ROB
http://www.easy-rob.com/easy-rob-intro.html (visited on 08/01/2014).

[EF99] El-Khasawneh, B. S.; Ferreira, P. M.
Computation of stiffness and stiffness bounds for parallel link manipulators
In: International Journal of Machine Tools and Manufacture, 39 (1999) 2, pp. 321–342.

[FAG15] FAG INA Schaeffler
BEARINX online Easy Friction
http://www.fag.de/content.fag.de/de/products_services/calculating/bearinx_online_easyfriction/bearinx_easyfriction.jsp (visited on 07/14/2015).

[Fan14] Fanuc
FANUC Robotics
http://www.fanucrobotics.de (visited on 08/01/2014).

[Fes14] Festo
Festo AG and Co. KG
https://www.festo.com/cms/de_de/index.htm (visited on 08/01/2014).

[FKH11] Frindt, M.; Krefft, M.; Hesselbach, J.
Structure and Type Synthesis of Parallel Manipulators
In: Siciliano, B.; Khatib, O.; Groen, F.; Schütz, D.; Wahl, F. M. (eds.), Robotic Systems for Handling and Assembly, Berlin, Heidelberg: Springer Berlin Heidelberg, 2011, ISBN 978-3-642-16784-3, pp. 17–37.

[Fon14] Fontán, G.
Derivation and implementation of the inverse kinematic and the Jacobean matrix for symmetrical 3-DOF parallel manipulators with 5 DOF per leg followed by comparison of these structures
Master Thesis, Aachen: RWTH Aachen University, Department of Mechanism Theory and Dynamics of Machines, 2014.

[Fri01] Frindt, M.
Modulbasierte Synthese von Parallelstrukturen für Maschinen in der Produktionstechnik
Essen: Vulkan-Verl., 2001, ISBN 9783802786594.

[FT02] Fang, Y.; Tsai, L.-W.
Structure Synthesis of a Class of 4-DoF and 5-DoF Parallel Manipulators with Identical Limb Structures
In: The International Journal of Robotics Research, 21 (2002) 9, DOI 10.1177/027836490202100931 4, pp. 799–810.

[FT04] Fang, Y.; Tsai, L.-W.
Structure Synthesis of a Class of 3-DOF Rotational Parallel Manipulators
In: IEEE Transactions on Robotics and Automation, 20 (2004) 1, DOI 10.1109/TRA.2003.819597, pp. 117–121.

[GA91] Gosselin, C.; Angeles, J.
A Global Performance Index for the Kinematic Optimization of Robotic Manipulators
In: Journal of Mechanical Design, 113 (1991) 3, DOI 10.1115/1.2912772, p. 220.

[GC09] Goncalves, R.,S.; Carvalho, J.,C.,M.
Stiffness Analysis of Parallel Manipulator Using Matrix Structural Analysis
In: Ceccarelli, M. G. (ed.), Proceedings of the 2nd European Conference on Mechanism Science, Berlin: Springer Netherland, 2009, ISBN 1402089155.

[Ger12] Gerke, W.
Elektrische Maschinen und Aktoren, Eine anwendungsorientierte Einführung
München: Oldenbourg, 2012, ISBN 348671984X.

[GF11] Grote, K.-H.; Feldhusen, J.
Dubbel, Taschenbuch für den Maschinenbau
Berlin: Springer, 23. ed., 2011, ISBN 9781283365703.

[GG97] Gao, F.; Gruver, W. A.
Performance evaluation criteria for analysis and design of robotic specimens
In: IEEE (ed.), Proceedings of the 8th International Conference on Advanced Robotics (ICAR'97), Monterey, CA, USA, 1997, pp. 879–884.

[GGG97] Gao, F.; Guy, F.; Gruver, W. A.
Criteria based analysis and design of three degree of freedom planar robotic manipulators
In: IEEE (ed.), International Conference on Robotics and Automation, Albuquerque, NM, USA, 1997, pp. 468–473.

[GGZ10] Gao, X.; Guo, X.; Zhou, K.
Analysis of dynamic performance indices of 3-RPC parallel mechanism
In: IEEE (ed.), 2nd Conference on Environmental Science and Information Application Technology (ESIAT), Wuhan, China, 2010, pp. 78–82.

[GGZ96] Gao, F.; Gruver, W. A.; Zhang, Y.
Performance charts for the design of robotic mechanisms with three moving links
In: IEEE (ed.), International Conference on Systems, Man and Cybernetics, Beijing, China, 1996, pp. 1471–1476.

[GHS11] Gross, D.; Hauger, W.; Schnell, W.
Technische Mechanik
Berlin [u.a.]: Springer, 11. revised ed., 2011, ISBN 3642199844.

[GKK04] Gerdes, I.; Klawonn, F.; Kruse, R.
Evolutionäre Algorithmen, Genetische Algorithmen - Strategien und Optimierungsverfahren - Beispielanwendungen
Wiesbaden: Vieweg, 1. ed., 2004, ISBN 9783528055707.

[GLG95] Gao, F.; Liu, X.; Gruver, W. A.
The global conditioning index in the solution space of two degree of freedom planar parallel manipulators
In: IEEE (ed.), International Conference on Systems, Man and Cybernetics. Intelligent Systems for the 21st Century, Vancouver, BC, Canada, 1995, pp. 4055–4058.

[GLG98] Gao, F.; Liu, X.; Gruver, W. A.
Performance evaluation of two-degree-of-freedom planar parallel robots
In: Mechanism and Machine Theory, 33 (1998) 6, DOI 10.1016/S0094-114X(97)00102-X, pp. 661–668.

[GMD07] Gosselin, C. M.; Masouleh, M. T.; Duchaine, V.; Richard, P.-L.; Foucault, S.; Kong, X.
Parallel Mechanisms of the Multipteron Family: Kinematic Architectures and Benchmarking
In: IEEE (ed.), International Conference on Robotics and Automation, Rome, Italy, 2007, pp. 555–560.

[Gog05] Gogu, G.
Mobility of mechanisms: a critical review
In: Mechanism and Machine Theory, 40 (2005) 9, DOI 10.1016/j.mechmachtheory.2004.12.014, pp. 1068–1097.

[Gog08] Gogu, G.
Structural Synthesis of Parallel Robots - Methodology
Berlin: Springer Netherland, 1. ed., 2008, ISBN 1402057105.

[Gog09] Gogu, G.
Translational topologies with two and three degrees of freedom
Dordrecht: Springer, 2009, ISBN 1402097948.

[Gol02] Goldsmith, P. B.
Kinematics and stiffness of a symmetrical 3-UPU translational parallel manipulator
In: IEEE (ed.), International Conference on Robotics and Automation, Washington, DC, USA, 2002, pp. 4102–4107.

[Gos90a] Gosselin, C.
Stiffness mapping for parallel manipulators
In: IEEE (ed.), Transactions on Robotics and Automation, 1990, pp. 377–382.

[Gos90b] Gosselin, C.
Dexterity indices for planar and spatial robotic manipulators
In: Volz, R. (ed.), International conference on robotics and automation, Cincinnati, Ohio, 1990, ISBN 9780818690617, pp. 650–655.

[GP02] Gregorio, R.; Parenti-Castelli, V.
Dynamic Performance Indices for 3-DOF Parallel Manipulators
In: Lenarčič, J.; Thomas, F. (eds.), Advances in Robot Kinematics, Theory and applications, Dordrecht: Springer Netherlands, 2002, ISBN 978-90-481-6054-9, pp. 11–20.

[GRN95] Gosselin, C. M.; Ricard, R.; Nahon, M. A.
A comparison of architectures of parallel mechanisms for workspace and kinematic properties
In: Design Engineering Technical Conferences, 82 (1995) 1, pp. 951–958.

[HA86] Homsup, W.; Anderson, J. N.
Performance evaluation of robotic mechanisms
In: IEEE (ed.), American Control Conference, Seattle, WA, USA, 1986, pp. 130–140.

[Han10] Handling
Marktübersicht Roboter
In: Handling, - (2010) 5, pp. 64–69.

[HEA14] HEAD acoustics
HEAD acoustics - Kopfbezogene Aufnahme- und Wiedergabetechnik
http://www.head-acoustics.de (visited on 08/11/2014).

[Her77] Hervé, J. M.
Analyse structurelle des mécanismes par groupe des déplacements
In: Mechanism and Machine Theory, 13 (1977) 4, DOI 10.1016/0094-114X(78)90017-4, pp. 437–450.

[Her99] Hervé, J. M.
The Lie group of rigid body displacements, a fundamental tool for mechanism design
In: Mechanism and Machine Theory, 34 (1999) 5, DOI 10.1016/S0094-114X(98)00051-2, pp. 719–730.

[Hiw13] Hiwin
Ball Screws and Equipment
http://www.hiwin.de/de/Produkte.html&download=share/public/Downloads/Kataloge/Kugelgewindetriebe/BS_06_1_DE_1304_K.pdf (visited on 11/27/2013).

[HKK02] Han, C.; Kim, J.; Kim, J.; Park, F. C.
Kinematic sensitivity analysis of the 3-UPU parallel mechanism
In: Mechanism and Machine Theory, 37 (2002) 8, DOI 10.1016/S0094-114X(02)00021-6, pp. 787–798.

[HKS97] Husty M. L.; Karger, A.; Sachs, H.; Steinhilper, W.
Kinematik und Robotik
Berlin, Heidelberg: Springer Berlin Heidelberg, 1997, ISBN 3642590292.

[HL01] Huang, Z.; Li, Q.
Type synthesis principle of minor-mobility parallel manipulators
In: Science in China Series E, 45 (2001) 3, DOI 10.1360/02ye9028, p. 241.

[HL02] Huang, Z.; Li, Q. C.
General Methodology for Type Synthesis of Symmetrical Lower-Mobility Parallel Manipulators and Several Novel Manipulators
In: The International Journal of Robotics Research, 21 (2002) 2, DOI 10.1177/027836402760475342, pp. 131–145.

[HL03] Huang, Z.; Li, Q. C.
Type Synthesis of Symmetrical Lower-Mobility Parallel Mechanisms Using the Constraint-Synthesis Method
In: The International Journal of Robotics Research, 22 (2003) 1, DOI 10.1177/0278364903022001005, pp. 59–79.

[HS91] Herve, J. M.; Sparacino, F.
Structural synthesis of 'parallel' robots generating spatial translation
In: IEEE (ed.), Fifth International Conference on Robots in Unstructured Environments, Pisa, Italy, 1991, ISBN 9780780300781, pp. 808–813.

[IAI14] IAI
IAI America, Inc.
http://www.intelligentactuator.com (visited on 08/01/2014).

[IFR14] IFR Statistical Department
World Robotics, Industrial Robots 2014
2014.

[Jac12] Jacobs, G.
Vorlesungsumdruck für das Wintersemester, (engl.: Lecture notes for the winter term)
Ausg. 09/2012, 2012, ISBN 978-3-8613074-8-8.

[JT03] Joshi, S.; Tsai, L.-W.
A comparison study of two 3-DOF parallel manipulators: one with three and the other with four supporting legs
In: IEEE Transactions on Robotics and Automation, 19 (2003) 2, DOI 10.1109/TRA.2003.808857, pp. 200–209.

[JY04] Jin, Q.; Yang, T.-L.
Theory for Topology Synthesis of Parallel Manipulators and Its Application to Three-Dimension-Translation Parallel Manipulators

In: Journal of Mechanical Design, 126 (2004) 4, DOI 10.1115/1.1758253, p. 625.

[KB06] Kucuk, S.; Bingul, Z.
Comparative study of performance indices for fundamental robot manipulators
In: Robotics and Autonomous Systems, 54 (2006) 7, DOI 10.1016/j.robot.2006.04.002, pp. 567–573.

[KG02] Kong, X.; Gosselin, C. M.
Kinematics and Singularity Analysis of a Novel Type of 3-CRR 3-DOF Translational Parallel Manipulator
In: The International Journal of Robotics Research, 21 (2002) 9, DOI 10.1177/027836490202100989O, pp. 791–798.

[KG04a] Kong, X.; Gosselin, C. M.
Type Synthesis of 3T1R 4-DOF Parallel Manipulators Based on Screw Theory
In: IEEE Transactions on Robotics and Automation, 20 (2004) 2, DOI 10.1109/TRA.2003.820853, pp. 181–190.

[KG04b] Kong, X.; Gosselin, C. M.
Type Synthesis of 3-DOF Spherical Parallel Manipulators Based on Screw Theory
In: Journal of Mechanical Design, 126 (2004) 1, DOI 10.1115/1.1637655, p. 101.

[KG04c] Kong, X.; Gosselin, C. M.
Type Synthesis of 3-DOF Translational Parallel Manipulators Based on Screw Theory
In: Journal of Mechanical Design, 126 (2004) 1, DOI 10.1115/1.1637662, p. 83.

[KG04d] Kong, X.; Gosselin, C. M.
Type synthesis of 3-DOF translational parallel manipulators based on screw theory and a virtual joint
In: CISM/IFToMM (ed.), 15th CISM-IFToMM Symposium on Robot Design, Dynamics and Control (RoManSy2004), Montreal, Canada, 2004.

[KG04e] Kong, X.; Gosselin, C. M.
Type Synthesis of Three-Degree-of-Freedom Spherical Parallel Manipulators
In: The International Journal of Robotics Research, 23 (2004) 3, DOI 10.1177/0278364904041562, pp. 237–245.

[KG05] Kong, X.; Gosselin, C. M.
Discussion: "Kinematics of the Translational 3-URC Mechanism" [Di Gregorio, R., 2004, ASME J. Mech. Des., 126, pp. 1113–1117]
In: Journal of Mechanical Design, 128 (2005) 4.

[KG06] Kong, X.; Gosselin, C. M.
Type synthesis of 4-DOF SP-equivalent parallel manipulators: A virtual chain approach
In: Mechanism and Machine Theory, 41 (2006) 11, DOI 10.1016/j.mechmachtheory.2006.01.004, pp. 1306–1319.

[KG07] Kong, X.; Gosselin, C. M.
Type synthesis of parallel mechanisms
Berlin and New York: Springer, 2007, ISBN 9783540719892.

[Kie14] Kiesewetter, C.
Entwicklung einer Kennzahlsystematik zum Vergleich von translatorischen 3-DOF Parallelmanipulatoren auf Basis verschiedener Optimierungsstrategien, (engl.: Development of a system of indices for comparison of translational 3-DOF parallel manipulators based on different optimization strategies)
Master Thesis, Aachen: RWTH Aachen University, Department of Mechanism Theory and Dynamics of Machines, 2014.

[KK14] Kähler, F.; Keller, D.
Erstellung einer graphischen Benutzeroberfläche zur Analyse parallelkinematischer Roboter mit drei translatorischen Freiheitsgraden, Darstellung von deren Eigenschaften in Form von Steckbriefen sowie Aufbau eines Komponentenkatalogs, (engl.: Implementation of a graphical user interface for the analysis of parallelkinematic machines with three translational degrees of freedom, presentation of their characteristics using profiles and compilation of a catalog of components)
Student Project Work, Aachen: RWTH Aachen University, Department of Mechanism Theory and Dynamics of Machines, 2014.

[KPK00] Kim, J.; Park, C.; Kim, J.; Park, F. C.
Performance Analysis of Parallel Mechanism Architectures for CNC Machining Applications
In: Journal of Manufacturing Science and Engineering, 122 (2000) 4, DOI 10.1115/1.1289290, p. 753.

[KT03] Kim, H. S.; Tsai, L.-W.
Design Optimization of a Cartesian Parallel Manipulator
In: Journal of Mechanical Design, 125 (2003) 1, DOI 10.1115/1.1543977, p. 43.

[KUK14] KUKA
KUKA Roboter GmbH
http://www.kuka-robotics.com/germany/de (visited on 08/01/2014).

[LDJ09] Lenssen, S.; Degtiarev, A.; Jacobs, G.
Simulation von Windenergieanlagen, Prozesse, Modellverbesserungen und Schnittstellen
In: Jacobs, G. (ed.), Antriebstechnisches Kolloqium.

[LH04] Li, Q. C.; Huang, Z.
Mobility Analysis of a Novel 3-5R Parallel Mechanism Family
In: Journal of Mechanical Design, 126 (2004) 1, DOI 10.1115/1.1637651, p. 79.

[LHH04] Li, Q.; Huang, Z.; Herve, J. M.
Type Synthesis of 3R2T 5-DOF Parallel Mechanisms Using the Lie Group of Displacements
In: IEEE Transactions on Robotics and Automation, 20 (2004) 2, DOI 10.1109/TRA.2004.824650, pp. 173–180.

[LJL04] Li-Wen Guan; Jin-Song Wang; Li-Ping Wang
Mobility analysis of the 3-UPU parallel mechanism based on screw theory
In: IEEE (ed.), International Conference on Intelligent Mechatronics and Automation, Chengdu, China, 2004, pp. 309–314.

[LMZ07] Li, S.; Ma, N.; Zhang, Y.
Kinematics analysis of a novel 3-RPUR parallel mechanism
In: IEEE (ed.), International Conference on Robotics and biomimetics (ROBIO), Sanya, China, 2007, pp. 2200–2205.

[LW07] Liu, X.-J.; Wang, J.
A new methodology for optimal kinematic design of parallel mechanisms
In: Mechanism and Machine Theory, 42 (2007) 9, DOI 10.1016/j.mechmachtheory.2006.08.002, pp. 1210–1224.

[LWK06] Liu, X.-J.; Wang, J.; Kim, J.
Determination of the Link Lengths for a Spatial 3-DOF Parallel Manipulator

In: Journal of Mechanical Design, 128 (2006) 2, DOI 10.1115/1.2159028, p. 365.

[LWL10] Li, Y.; Wang, J.; Liu, X.-J.; Wang, L.-P.
Dynamic performance comparison and counterweight optimization of two 3-DOF parallel manipulators for a new hybrid machine tool
In: Mechanism and Machine Theory, 45 (2010) 11, DOI 10.1016/j.mechmachtheory.2010.06.009, pp. 1668–1680.

[LWP06] Liu, X.-J.; Wang, J.; Pritschow, G.
On the optimal kinematic design of the PRRRP 2-DoF parallel mechanism
In: Mechanism and Machine Theory, 41 (2006) 9, DOI 10.1016/j.mechmachtheory.2005.10.008, pp. 1111–1130.

[LX06a] Li, Y.; Xu, Q.
A New Approach to the Architecture Optimization of a General 3-PUU Translational Parallel Manipulator
In: Journal of Intelligent and Robotic Systems, 46 (2006) 1, DOI 10.1007/s10846-006-9044-6, pp. 59–72.

[LX06b] Li, Y.; Xu, Q.
Kinematic Analysis and Design of a New 3-DOF Translational Parallel Manipulator
In: Journal of Mechanical Design, 128 (2006) 4, DOI 10.1115/1.2198254, pp. 729–737.

[LX08] Li, Y.; Xu, Q.
Stiffness analysis for a 3-PUU parallel kinematic machine
In: Mechanism and Machine Theory, 43 (2008) 2, DOI 10.1016/j.mechmachtheory.2007.02.002, pp. 186–200.

[LXS11] Li, Y.; Xu, Q.; Staicu, S.
Kinematics of the 3-PUU Translational parallel manipulator
In: U.P.B. Scientific Bulletin, Series D, 73 (2011) 4, pp. 3–14.

[LZL10] Liu, S.; Zhu, Z.; Li, Z.; Liu, C.; Yu, Y.
Kinematics and Dynamics of 3-RRC Flexible Parallel Manipulator
In: IEEE (ed.), International Conference on E-Product E-Service and E-Entertainment (ICEEE 2010), Henan, China, 2010, pp. 1–4.

[MA91] Ma, O.; Angeles, J.
Optimum architecture design of platform manipulators
In: IEEE (ed.), Fifth International Conference on Robots in Unstructured Environments, Pisa, Italy, 1991, ISBN 9780780300781, pp. 1130–1135.

[McC90] McCloy, D.
Some comparisons of serial-driven and parallel-driven manipulators
In: Robotica, 8 (1990) 4, DOI 10.1017/S0263574700000485, p. 355.

[Mer06] Merlet, J.-P.
Parallel robots
Dordrecht and Boston, MA: Kluwer Academic Publishers, 2nd ed., 2006, ISBN 1402041330.

[Mer97] Merlet, J.-P.
DEMOCRAT: A DEsign MethOdology for the Conception of Robots with parallel ArchiTecture
In: Robotica, 15 (1997) 4, DOI 10.1017/S0263574797000453, pp. 367–373.

[Mie13] Mielke, T.
Konzeptionierung, Entwicklung und Gestaltung einer aktiven 7. Achse für ein Mehrarm-Robotersystem
Bachelor Thesis, Aachen: RWTH Aachen University, Department of Mechanism Theory and Dynamics of Machines, 2013.

[Mik14] Mikrolar
Mikrolar - Custom Hexapods
http://mikrolar.com/ (visited on 08/01/2014).

[Mit14] Mitsubishi
Mitsubishi Electric Automation Inc.
http://www.meau.com/eprise/main/sites/public/About_Us/-Home (visited on 08/22/2014).

[MLL07] Meng, J.; Liu, G.; Li, Z.
A Geometric Theory for Analysis and Synthesis of Sub-6 DoF Parallel Manipulators
In: IEEE Transactions on Robotics, 23 (2007) 4, DOI 10.1109/TRO.2007.898995, pp. 625–649.

[Moo14] Moog
Moog
http://www.moog.de (visited on 08/01/2014).

[Nef10] Nefzi, M.
Analysis and optimisation of 4UPS - 1UPU parallel robots, Doctoral Thesis
Aachen: Apprimus-Verl, 1. ed., 2010, ISBN 394056575X.

[Neu06] Neugebauer, R.
Parallelkinematische Maschinen, Entwurf, Konstruktion, Anwendung
Berlin and Heidelberg, New York: Springer, 2006, ISBN 3540209913.

[Neu14] Neuronics
Neuronics AG
http://www.neuronics.ch (visited on 08/01/2014).

[NRC07] Nefzi, M.; Riedel, M.; Corves, B.
Optimal Design of a Parallel Manipulator for Use in a High-Speed Sewing Machine
In: IEEE (ed.), 13th IFAC International Conference on Methods and Models in Automation and Robotics, Szczecin, Poland, 2007.

[PBG07] Pahl, G.; Beitz, W.; Grote, K.-H.
Engineering Design, A Systematic Approach
London: Springer, 7th ed., 2007, ISBN 978-1-84628-319-2.

[PC15] Prause, I.; Corves, B.
Dynamic modelling of the Translational RPC-Manipulator with Prismatic or Revolute Joint Actuation for Different Frame Configurations
In: IEEE (ed.), International Conference on Intelligent Robots and Systems (IROS), Hamburg, Germany, 2015.

[PCC14] Prause, I.; Charaf Eddine, S.; Corves, B.
Comparison of Parallel Kinematic Structures with Three Translational Degrees of Freedom and Linear Actuation
In: IFToMM (ed.), Asian Conference on Mechanism and Machine Science, Tianjin, China, 2014.

[PCW08] Pashkevich, A.; Chablat, D.; Wenger, P.
Stiffness analysis of 3-d.o.f. overconstrained translational parallel manipulators
In: IEEE (ed.), International Conference on Robotics and Automation (ICRA), Pasadena, CA, USA, 2008, pp. 1562–1567.

[PCW09] Pashkevich, A.; Chablat, D.; Wenger, P.
Stiffness analysis of overconstrained parallel manipulators
In: Mechanism and Machine Theory, 44 (2009) 5, DOI 10.1016/j.mechmachtheory.2008.05.017, pp. 966–982.

[PI14] PI
Physics Instruments
http://www.physikinstrumente.de/de/index.php (visited on 08/01/2014).

[PKC11] Pashkevich, A.; Klimchik, A.; Caro, S.; Chablat, D.
Cartesian stiffness matrix of manipulators with passive joints: Analytical approach
In: IEEE/RSJ (ed.), International Conference on Intelligent Robots and Systems (IROS 2011), San Francisco, CA, 2011, pp. 4034–4041.

[PLC15] Prause, I.; Lorenz, M.; Corves, B.
Kinetostatic Analysis of the Translational RPC-Manipulator with Different Actuator and Frame Configurations
In: IEEE (ed.), International Conference on Robotics and Automation (ICRA), Seattle, USA, 2015.

[PMC14] Prause, I.; Mbarek, T.; Corves, B.
Increasing the stiffness of a 3-PUU parallel kinematic positioning device for high payloads by modifying the leg configuration
In: IFToMM (ed.), Workshop on Fundamental Issues and Future Research Directions for Parallel Mechanisms and Manipulators, Tianjin, China, 2014.

[POI11] Pavlović, N.; Otremba, R.; Inkermann, D.; Franke, H.-J.; Vietor, T.
Passive and Adaptive Joints for Parallel Robots
In: Siciliano, B.; Khatib, O.; Groen, F.; Schütz, D.; Wahl, F. M. (eds.), Robotic Systems for Handling and Assembly, Berlin, Heidelberg: Springer Berlin Heidelberg, 2011, ISBN 978-3-642-16784-3, pp. 429–444.

[Pok04] Pokar, G.
Untersuchung zum Einsatz von ebenen Parallelrobotern in der Mikromontage
Essen: Vulkan-Verlag, 2004, ISBN 9783802786808.

[PS14] Patel, S.; Sobh, T.
Manipulator Performance Measures - A Comprehensive Literature Survey
In: Journal of Intelligent & Robotic Systems, 77 (2014) 3-4, DOI 10.1007/s10846-014-0024-y, pp. 547–570.

[QFG12] Qu, H.; Fang, Y.; Guo, S.
Parasitic rotation evaluation and avoidance of 3-UPU parallel mechanism
In: Frontiers of Mechanical Engineering, 7 (2012) 2, DOI 10.1007/s11465-012-0317-4, pp. 210–218.

[QG11] Quennouelle, C.; Gosselin, C.
Kinematostatic modeling of compliant parallel mechanisms
In: Meccanica, 46 (2011) 1, DOI 10.1007/s11012-010-9408-7, pp. 155–169.

[QSp16] QSpider
QSpider
http://www.qspider.org/en/qspider/qspider.html (visited on 03/21/2016).

[Qua14] Quanser
Quanser
http://www.quanser.com (visited on 08/01/2014).

[QY06] Qingsong, X.; Yangmin, L.
GA-Based Architecture Optimization of a 3-PUU Parallel Manipulator for Stiffness Performance
In: IFToMM (ed.), 6th World Congress on Intelligent Control and Automation, Dalian, China, 2006, pp. 9099–9103.

[QY07] Qingsong, X.; Yangmin, L.
Design modification of a 3-PRC compliant parallel micromanipulator for micro/nano scale manipulation
In: IEEE (ed.), 7th Conference on Nanotechnology (IEEE-NANO), Hong Kong, China, 2007, pp. 426–431.

[QZ03] Qinchuan Li; Zhen Huang
Mobility analysis of a 3-5R parallel mechanism family
In: IEEE (ed.), International Conference on Robotics and Automation, Taipei, Taiwan, 2003, pp. 1887–1892.

[RAF02] Romdhane, L.; Affi, Z.; Fayet, M.
Design and Singularity Analysis of a 3-Translational-DOF In-Parallel Manipulator
In: Journal of Mechanical Design, 124 (2002) 3, DOI 10.1115/1.1480815, p. 419.

[RDP13] Rodriguez-Leal, E.; Dai, J. S.; Pennock, G. R.
Screw-System-Based Mobility Analysis of a Family of Fully Translational Parallel Manipulators
In: Mathematical Problems in Engineering, 2013 (2013) 3, DOI 10.1155/2013/262801, pp. 1–9.

[Rei14] Reis
Reis Robotics
http://www.reisrobotics.de/de/home (visited on 08/01/2014).

[RGK06] Richard, P.-L.; Gosselin, C. M.; Kong, X.
Kinematic Analysis and Prototyping of a Partially Decoupled 4-DOF 3T1R Parallel Manipulator

In: ASME (ed.), International Design Engineering Technical Conferences and Computers and Information in Engineering Conference, Philadelphia, Pennsylvania, USA, 2006, pp. 1029–1036.

[Rie13] Riedel, M.
Flexible Bauteilhandhabung auf Basis einer rekonfigurierbaren parallelkinematischen Struktur
Herzogenrath: Shaker, 1. ed., 2013, ISBN 3844025340.

[Riv88] Rivin, E. I.
Mechanical design of robots
New York: McGraw-Hill, 1988, ISBN 0-07-052992-2.

[ROL01] ROLLON
Monorail (Rollon), Linear Evoltion
http://www.bibusmenos.pl/fileadmin/editors/countries/bimen/MECHATRONIKA / Dokumenty / BIBUS_MENOS_-_Mechatronika_MONORAIL-Catalogue-EN.pdf (visited on 06/22/2015).

[ROL15] ROLLON
ROLLON LinearEvolution
http://www.rollon.com/DE/de/ (visited on 06/23/2015).

[RR01] Rauf, A.; Ryu, J.
Fully autonomous calibration of parallel manipulators by imposing position constraint
In: IEEE (ed.), International Conference on Robotics and Automation, Seoul, South Korea, 2001, pp. 2389–2394.

[RR11] Rodrıguez-Velazco, E. A.; Rodriguez-Leal, E.
Kinematic Analysis of the 3-RPC-T Fully Translational Mechanism
In: IFToMM (ed.), 13th World Congress in Mechanism and Machine Science, Guanajuato, Mexico, 2011.

[Ruc13] Rucker, M.
Konzeptionierung und Entwicklung eines variablen Greifsystems zur automatischen Anpassung der Ablegeanordnung von Lebensmitteln, (engl.: Engineering design and development of a variable gripper system for automated adjustment of the placement order of food)
Diploma Thesis, Aachen: RWTH Aachen University, Department of Mechanism Theory and Dynamics of Machines, 2013.

[Rug08] Ruggiu, M.
Kinematics analysis of the CUR translational manipulator
In: Mechanism and Machine Theory, 43 (2008) 9, DOI 10.1016/j.mechmachtheory.2007.10.001, pp. 1087–1098.

[Saa08] Saaty, T.
Decision making with the analytic hierarchy process
In: International Journal of Services Sciences, 1 (2008) 1, pp. 83–98.

[Sal80] Salisbury, J.
Active stiffness control of a manipulator in cartesian coordinates
In: IEEE (ed.), 19th Conference on Decision and Control including the Symposium on Adaptive Processes, Albuquerque, NM, USA, 1980, pp. 95–100.

[SBS02] Staffetti, E.; Bruyninckx, H.; Schutter, J. d.
On the Invariance of Manipulability Indices
In: Lenarčič, J.; Thomas, F. (eds.), Advances in Robot Kinematics, Theory and applications, Dordrecht: Springer Netherlands, 2002, ISBN 978-90-481-6054-9, pp. 57–66.

[Sch13] Schäfer, B.
Vergleichende Maßsynthese zweier Parallelmanipulatoren mit drei Freiheitsgraden und anschließende Bewertung ihrer Leistungsfähigkeit gegenüber einer seriellen Struktur, (engl.: Comparitive Dimensional Synthesis of two Parallel Manipulators with three Degrees of Freedom and Evaluation of their Performance Compared with a Serial Structure)
Diploma Thesis, Aachen: RWTH Aachen University, Department of Mechanism Theory and Dynamics of Machines, 2013.

[Sch14] Schlecht, B.
Untersuchung und Optimierung des dynamischen Verhaltens von Schaufelradantrieben
Schlussbericht zu dem IGF-Vorhaben, Dresden: Technical University Dresden, IMM - Department for machine elements, 2014.

[Sch15] Schaeffler
medias professional - Produktkatalog
http://medias.schaeffler.de/medias/de (visited on 07/14/2015).

[Sch87] Schopen, M.
Die Auswahl von Handhabungsgeräten aufgrund der charakteristischen Merkmale ihrer kinematischen Strukturen
Düsseldorf: VDI-Verlag, 1987, ISBN 9783181427026.

[Sch97] Schönherr, J.
Auslegung von Getrieben und Manipulatoren nach der Übertragungsgüte
In: Kolloquium Getriebetechnik, Rostock: Institut für Allgemeinen Maschinenbau, Fachbereich Maschinenbau und Schiffstechnik, 1997, pp. 189–200.

[SCZ06] Shihua, L.; Chongjie, D.; Zhen, H.
Position Analysis of a Novel 3-5R Parallel Platform Mechanism Using Continuation Method
In: IEEE (ed.), International Conference on Mechatronics and Automation, Luoyang, China, 2006, pp. 2036–2041.

[Seb14] Sebteini, A.
Herleitung und Implementierung von Steifigkeitsmodellen für 3-DOF Parallelmanipulatoren und Validierung der Modelle mittels MATLAB SimMechanics, (engl.: Derivation and Implementation of Stiffness Models for 3-DOF Parallel Manipulators and Validation of the Models using MATLAB SimMechanics)
Master Thesis, Aachen: RWTH Aachen University, Department of Mechanism Theory and Dynamics of Machines, 2014.

[SK08] Siciliano, B.; Khatib, O.
Springer handbook of robotics
Berlin and Heidelberg: Springer, 2008.

[SKC14] Shayya, S.; Krut, S.; Company, O.; Baradat, C.; Pierrot, F.
On the performance evaluation and analysis of general robots with mixed dofs
In: IEEE (ed.), International Conference on Intelligent Robots and Systems (IROS 2014), Chicago, IL, USA, 2014, pp. 490–497.

[SKF04] SKF
SKF Handbuch Linearführungen, Linear Motion
http://www.hausmann-haensgen.de/documents/SKF_Linearfuehrungen.pdf.

[SLT09] Shen, H.; Li, J.; Tao, S.; Ma, L.-z.
A Novel 3-Dof Three-Translation Parallel Mechanism and Displacement Analysis
In: ASME/IFToMM (ed.), International Conference on Reconfigurable Mechanisms and Robotics, London, UK, 2009, ISBN 9781876346584.

[SNC08] Shihua Li; Ning Ma; Changcheng Yu
Position and singularity analysis of a novel 3-RPUR parallel platform mechanism
In: IEEE/ASME (ed.), International Conference on Advanced Intelligent Mechatronics (AIM), Xian, China, 2008, pp. 510–515.

[Spo05] Spong, M. W.
Modern robot dynamics and control
Hoboken, N.J. and Chichester: Wiley, 2005, ISBN 9780471649908.

[Stä14] Stäubli
Stäubli Deutschland
http://www.staeubli.de (visited on 08/01/2014).

[STY00] Shen, H.; Ting, K.-L.; Yang, T.
Configuration analysis of complex multiloop linkages and manipulators
In: Mechanism and Machine Theory, 35 (2000) 3, DOI 10.1016/S0094-114X(99)00018-X, pp. 353–362.

[SY98] Sen, P.; Yang, J.
Multiple Criteria Decision Support in Engineering Design
London: Springer London, 1998, ISBN 1447130200.

[SYM05] Shen, H.; Yang, T.; Ma, L.-z.
Synthesis and structure analysis of kinematic structures of 6-dof parallel robotic mechanisms
In: Mechanism and Machine Theory, 40 (2005) 10, DOI 10.1016/j.mechmachtheory.2004.12.020, pp. 1164–1180.

[SZ05] Shihua Li; Zhen Huang
Kinematics analysis of a novel 3-RRUR parallel mechanism
In: IEEE (ed.), International Conference on Mechatronics and Automation, Niagara Falls, Ont., Canada, 2005, pp. 1422–1428.

[Tab01] Tabandeh, S.
Development of Novel Task-Based Configuration Optimization Methodologies for Modular and Reconfigurable Robots Using Multi-Solution Inverse Kinematic Algorithms
Dissertation, Ontario, Canada: University of Waterloo, 2009-01-01.

[TAL12] Taghvaeipour, A.; Angeles, J.; Lessard, L.
On the elastostatic analysis of mechanical systems
In: Mechanism and Machine Theory, 58 (2012), DOI 10.1016/j.mechmachtheory.2012.07.011, pp. 202–216.

[TH11] Tian, D. X.; Han, S. K.
Actual Motion of 3-DOF Parallel Robot
In: Advanced Materials Research, 383-390 (2011), DOI 10.4028/www.scientific.net/AMR.383-390.5059, pp. 5059–5065.

[The14] The Mathworks Inc.
Matlab R2014b

[The15] The Mathworks Inc.
MATLAB - The Language of Technical Computing, R2015a Documentation

[TJ00] Tsai, L.-W.; Joshi, S.
Kinematics and Optimization of a Spatial 3-UPU Parallel Manipulator
In: Journal of Mechanical Design, 122 (2000) 4, DOI 10.1115/1.1311612, p. 439.

[TJ01] Tsai, L.-W.; Joshi, S.
Comparison study of architectures of four 3 degree-of-freedom translational parallel manipulators
In: IEEE (ed.), International Conference on Robotics and Automation, Seoul, South Korea, 2001, pp. 1283–1288.

[TJ02] Tsai, L.-W.; Joshi, S.
Kinematic Analysis of 3-DOF Position Mechanisms for Use in Hybrid Kinematic Machines
In: Journal of Mechanical Design, 124 (2002) 2, DOI 10.1115/1.1468860, p. 245.

[Tri14] Tricept
tricept PKM
http://www.pkmtricept.com (visited on 08/01/2014).

[Tsa01] Tsai, L.-W.
Mechanism design, Enumeration of kinematic structures according to function
Boca Raton: CRC press, 2001, ISBN 9780849309014.

[Tsa10] Tsai, L.-W.
Mechanism design, Enumeration of kinematic structures according to function
CRC press, 2010, ISBN 0849309018.

[Tsa96] Tsai, L.-W.
Kinematics of A Three-Dof Platform with Three Extensible Limbs
In: Lenarčič, J.; Parenti-Castelli, V. (eds.), Recent Advances in Robot Kinematics, Dordrecht: Springer Netherlands, 1996, ISBN 978-94-010-7269-4, pp. 401–410.

[Tsa97] Tsai, L. W.
Multi-degree-of-freedom mechanisms for machine tools and the like
Patent, 1997.

[Tsa99] Tsai, L.-W.
Robot analysis, The mechanics of serial and parallel manipulators
New York: Wiley, 1999, ISBN 9780471325932.

[TT10] Tanabe, M.; Takeda, Y.
Kinematic Design of a Translational Parallel Manipulator with Fine Adjustment of Platform Orientation
In: Advances in Mechanical Engineering, 2010 (2010) 6, DOI 10.1155/2010/485358, pp. 1–9.

[TTE93] Tachiya, H.; Tsujimura, Y.; Ebata, Y.; Chatani, A.
Characteristic Evaluation and Comparisons of Robotic Mechanisms. 1st Report, Evaluation and Comparisons Based on Static Characteristics
In: Transactions of the Japan Society of Mechanical Engineers Series C, 59 (1993) 559, DOI 10.1299/kikaic.59.932, pp. 932–938.

[TTE95] Tachiya, H.; Tsujimura, Y.; Ebata, Y.; Chatani, A.
Characteristic Evaluation and Comparison of Robotic Mechanisms, Evaluation and Comparison Based on Static Characteristics
In: JSME international journal. Ser. C, Dynamics, control, robotics, design and manufacturing, 38 (1995) 2, pp. 276–284.

[TTH08] Tanabe, M.; Takeda, Y.; Huda, S.
Utility workspace of 3-5r translational parallel mechanism
In: IEEE (ed.), Conference on Robotics, Automation and Mechatronics (RAM), Chengdu, China, 2008, pp. 761–767.

[van06] van Beek, A.
Advanced engineering design, Lifetime performance and reliability
[S.l.]: TU Delft, 2006, ISBN 978-90-810406-1-7.

[VDI2222] VDI 2222
VDI 2222 - Konstruktionsmethodik - Methodisches Entwickeln von Lösungsprinzipien

Norm, VDI - Society Product and Process Design, Beuth Verlag GmbH, 1997-06-01.

[VDI2225] VDI 2225
VDI 2225 - Technisch-wirtschaftliches Konstruieren
Norm, VDI - Society Product and Process Design, Beuth Verlag GmbH, 1997-11-01.

[VDI2861] VDI 2861
VDI 2861 - Montage- und Handhabungstechnik
Norm, VDI - Society Product and Process Design, 1988-06-01.

[WC11] Wahle, M.; Corves, B.
Stiffness Analysis of Clavel's DELTA Robot
In: Hutchison, D.; Kanade, T.; Kittler, J.; Kleinberg, J. M.; Mattern, F.; Mitchell, J. C.; Naor, M.; Nierstrasz, O.; Pandu Rangan, C.; Steffen, B.; Sudan, M.; Terzopoulos, D.; Tygar, D.; Vardi, M. Y.; Weikum, G.; Jeschke, S.; Liu, H.; Schilberg, D. (eds.), Intelligent Robotics and Applications, Berlin, Heidelberg: Springer Berlin Heidelberg, 2011, ISBN 978-3-642-25485-7, pp. 240–249.

[Wei02] Weicker, K.
Evolutionäre Algorithmen
Stuttgart: Teubner, 1. ed., 2002, ISBN 9783519003625.

[WH11] Walter, D. R.; Husty M. L.
Kinematic Analysis of the TSAI-3UPU Parallel Manipulator using Algebraic Methods
In: IFToMM (ed.), 13th World Congress in Mechanism and Machine Science, Guanajuato, Mexico, 2011.

[Wit14a] Wittenstein AG
Products and Services Catalogue 2013/2014
http://www-alt.alphagetriebe.%20de/pdf/%20alpha_gesamtkatalogd0813.pdf (visited on 03/27/2014).

[Wit14b] Wittenstein AG
Wittenstein Cymex® CAD Software & Servo Sizing Design Tool
http://www.wittenstein-us.com/tech-support/design-tools/cymex-software.cfm (visited on 08/01/2014).

[WLF05] Wu, G.; Li, J.; Fei, R.; Wang, X.; Liu, D.
Analysis and Design of A Novel Micro-Dissection Manipulator Based on Ultrasonic Vibration

In: IEEE (ed.), International Conference on Robotics and Automation, Barcelona, Spain, 2005, pp. 466–471.

[WSP02] Wolf, A.; Shoham, M.; Park, F. C.
Investigation of the singularies and self-motions of the 3-UPU Robot
In: Lenarčič, J.; Thomas, F. (eds.), Advances in Robot Kinematics, Theory and applications, Dordrecht: Springer Netherlands, 2002, ISBN 978-90-481-6054-9, pp. 165–174.

[WW11] Wang, X.; Wei, C.
Kinematics and workspace of 3-RUU parallel manipulator
In: IEEE (ed.), International Conference on Consumer Electronics, Communications and Networks (CECNet), Xianning, China, 2011, pp. 438–441.

[WWW10] Wu, J.; Wang, J.; Wang, L.
A comparison study of two planar 2-DOF parallel mechanisms: one with 2-RRR and the other with 3-RRR structures
In: Robotica, 28 (2010) 06, DOI 10.1017/S0263574709990828, pp. 937–942.

[www15] www01
www.wirautomatisierer.de
http://www.wirautomatisierer.de/home/-/article/33568397/38718972 (visited on 03/18/2015).

[XL06a] Xu, Q.; Li, Y.
Accuracy-Based Architecture Optimization of a 3-DOF Parallel Kinematic Machine
In: IEEE (ed.), International Conference on Automation Science and Engineering, Shanghai, China, 2006, pp. 63–68.

[XL06b] Xu, Q.; Li, Y.
Stiffness Modeling for an Orthogonal 3-PUU Compliant Parallel Micromanipulator
In: IEEE (ed.), International Conference on Mechatronics and Automation, Luoyang, China, 2006, pp. 124–129.

[XL06c] Xu, Q.; Li, Y.
Stiffness Optimization of a 3-DOF Parallel Kinematic Machine Using Particle Swarm Optimization
In: IEEE (ed.), International Conference on Robotics and Biomimetics, Kunming, China, 2006, pp. 1169–1174.

[XL07] Xu, Q.; Li, Y.
Design and analysis of a new singularity-free three-prismatic-revolute-cylindrical translational parallel manipulator
In: Proceedings of the Institution of Mechanical Engineers, Part C: Journal of Mechanical Engineering Science, 221 (2007) 5, DOI 10.1243/0954406JMES267, pp. 565–576.

[XYH07] Xiangzhou, Z.; Yougao, L.; Hongzan, B.
Inverse Dynamics of 3-UPU Parallel Mechanism with Pure Rotation Based on D'Alembert Principle
In: IEEE (ed.), International Conference on Mechatronics and Automation, Harbin, China, 2007, pp. 2842–2847.

[Yam] Yam
Yamaha Robotics
http://www.yamaharobotics.com/ (visited on 08/22/2014).

[YHT13] Yahyapour, I.; Hasanvand, M.; Tale Masouleh, M.; Yazdani, M.; Tavakoli, S.
On the inverse dynamic problem of a 3-PRRR parallel manipulator, the Tripteron
In: RSI/ISM (ed.), First RSI/ISM International Conference 2013, Tehran, Iran, 2013, pp. 390–395.

[YLL09a] Yang, T.-L.; Liu, A.-x.; Luo, Y.-F.; Zhang, L.-P.; Jun Yun
Comparative Study of Two Methods for Type Synthesis of Robot Mechanisms
In: ASME/IFToMM (ed.), London, United Kingdom, 2009, ISBN 1424437962, pp. 205–214.

[YLL09b] Yang, T.-L.; Liu, A.-x.; Luo, Y.-F.; Zhang, L.-P.; Shen, H.-P.; Hang, L.-B.
Comparison Study on Three Approaches for Type Synthesis of Robot Mechanisms
In: ASME (ed.), International Design Engineering Technical Conferences and Computers and Information in Engineering Conference, San Diego, California, USA, 2009, pp. 453–462.

[YLP11] Yu, J.; Li, S.; Pei, X.; Bi, S.; Zong, G.
A unified approach to type synthesis of both rigid and flexure parallel mechanisms
In: Science China Technological Sciences, 54 (2011) 5, DOI 10.1007/s11431-011-4324-1, pp. 1206–1219.

[YO09] Yang, Y.; O'Brien, J. F.
A geometric approach for the design of singularity-free parallel robots
In: IEEE (ed.), International Conference on Robotics and Automation (ICRA), Kobe, Japan, 2009, pp. 1801–1806.

[YO10] Yang, Y.; O'Brien, J. F.
Singularity-free workspace design for the translational 3-UPU parallel robot
In: IEEE (ed.), International Conference on Automation Science and Engineering (CASE 2010), Toronto, ON, 2010.

[Yos85] Yoshikawa, T.
Manipulability of Robotic Mechanisms
In: The International Journal of Robotics Research, 4 (1985) 2, DOI 10.1177/027836498500400201, pp. 3–9.

[YQ05a] Yangmin, L.; Qingsong, X.
Kinematic analysis and dynamic control of a 3-PUU parallel manipulator for cardiopulmonary resuscitation
In: IEEE (ed.), International Conference on Advanced Robotics (ICAR '05), Seatle, WA, USA, 2005, pp. 344–351.

[YQ05b] Yangmin, L.; Qingsong, X.
Kinematics and Dexterity Analysis for a Novel 3-DOF Translational Parallel Manipulator
In: IEEE (ed.), International Conference on Robotics and Automation, Barcelona, Spain, 2005, pp. 2944–2949.

[YQ05c] Yangmin, L.; Qingsong, X.
Novel design of a 3-PUU spatial compliant parallel micromanipulator for nanomanipulation
In: IEEE (ed.), International Conference on Mechatronics and Automation, Niagara Falls, Ont., Canada, 2005, pp. 1575–1580.

[YQ07] Yangmin, L.; Qingsong, X.
Dynamics analysis of a modified 3-PRC compliant parallel micromanipulator
In: IEEE (ed.), 7th Conference on Nanotechnology (IEEE-NANO), Hong Kong, China, 2007, pp. 432–437.

[YWS12] Yu, L.; Wang, T.; Song, H.; Wang, Z.; Yu, P.
Static analysis for a 3-RUU parallel mechanism
In: IEEE (ed.), International Conference on Mechatronics and Automation (ICMA), Chengdu, China, 2012, pp. 749–754.

[ZBM04] Zoppi, M.; Bruzzone, L. E.; Molfino, R. M.
Position Analysis of a Class of Translational Parallel Mechanisms
In: International Journal of Robotics and Automation, 19 (2004) 3, DOI 10.2316/Journal.206.2004.3.206-2728.

[ZDC00] Zhang, Y.; Duffy, J.; Crane, C.
The Optimum Quality Index for a Spatial Redundant 4–8 in-Parallel Manipulator
In: Lenarčič, J.; Stanišić, M. M. (eds.), Advances in Robot Kinematics, Dordrecht: Springer Netherlands, 2000, ISBN 978-94-010-5803-2, pp. 239–248.

[ZFD06] Zhao, J.-S.; Feng, Z.-J.; Dong, J.-X.
Computation of the configuration degree of freedom of a spatial parallel mechanism by using reciprocal screw theory
In: Mechanism and Machine Theory, 41 (2006) 12, DOI 10.1016/j.mechmachtheory.2006.01.006, pp. 1486–1504.

[Zha00] Zhang, D.
Kinetostatic analysis and optimization of parallel and hybrid architectures for machine tools
Dissertation, Qeubec, Canada: University of LAVAL Quebec, 2000.

[Zha01] Zhao, T.S., Huang, Z.
Kinematics of a Three-dimension Translational Parallel Platform Mechanism
In: China Mechanical Engineering, 12 (2001) 6, pp. 613–616.

[ZHL06] Zeng, D.; Huang, Z.; Lu, W.
Kinematic Analysis of A Novel 3-DOF Translational Parallel Mechanism
In: IEEE (ed.), International Conference on Mechatronics and Automation, Luoyang, China, 2006, pp. 2030–2035.

[ZSZ10] Zhu, X. R.; Shen, H. P.; Zhu, W.
Optimal Kinematic Design of a 2-DOF Planar Parallel Manipulator
In: Applied Mechanics and Materials, 44-47 (2010), DOI 10.4028/www.scientific.net/AMM.44-47.1843, pp. 1843–1847.

List of Tables

Tab. 2.1 Properties of serial robots (extrema) . . . 8
Tab. 2.2 Properties of serial robots (median values) . . . 9
Tab. 2.3 Properties of parallel robots (extrema) . . . 11
Tab. 2.4 Properties of parallel robots (median values) . . . 11

Tab. 3.1 Evaluation methods and applicability . . . 20

Tab. 4.1 Limb-connectivities with respect to the desired DoF . . . 30
Tab. 4.2 Number of possible configurations . . . 35
Tab. 4.3 Synthesized structures by Tsai [Tsa01] . . . 36
Tab. 4.4 Joint distributions by Neugebauer [Neu06] . . . 37
Tab. 4.5 Reduced number of structures . . . 38
Tab. 4.6 Possible frame configurations for the selected PKS . . . 40
Tab. 4.7 Final selection . . . 43

Tab. 5.1 Further considered and not relevant main features according to [PBG07] 47
Tab. 5.2 Manipulation tasks ([Han10] and information on websites of robot suppliers) . . . 52
Tab. 5.3 Properties of chosen robots and selected tasks . . . 59

Tab. 6.1 Available research on considered structures and related work . . . 67

Tab. 8.1 Bounds of optimization parameters . . . 85
Tab. 8.2 Further limits . . . 87
Tab. 8.3 Actuator properties [Wit14a; Hiw13] . . . 89
Tab. 8.4 Dimensions resulting from first analysis . . . 90

Tab. 9.1 Different groups based on number of geometrical parameters . . . 98
Tab. 9.2 Bounds of parameters and step size . . . 98
Tab. 9.3 Parameter ranges . . . 108
Tab. 9.4 Benchmark metrics (I) . . . 109
Tab. 9.5 Benchmark metrics (II) . . . 110
Tab. 9.6 Sensitivity of weighting factors . . . 111

Tab. 10.1 Task-dependent demands 114
Tab. 10.2 Selected PKS for final optimization and analysis 114
Tab. 10.3 Preference matrix and respective weighting factors 115
Tab. 10.4 Properties of selected actuators 121
Tab. 10.5 Bounds of optimization parameters 124
Tab. 10.6 Optimized parameters for pick & place task 125
Tab. 10.7 Optimized parameters for positioning task 128
Tab. 10.8 Optimized parameters for guidance task 131

Tab. 11.1 Derived and implemented mathematical models within the framework of this thesis 148
Tab. 11.2 Analyses done within the framework of this thesis 149

Tab. 3 Geometrical conditions (GC) for joint arrangements according to [KG04c; KG07] 220
Tab. 4 Considered structures - rotational actuation 221
Tab. 5 Considered structures - linear actuation (cylindrical joint) 222
Tab. 6 Considered structures - linear actuation (prismatic joint) 223
Tab. 7 Workspaces of the considered structures for case 1 optimization (I) . . . 224
Tab. 8 Workspaces of the considered structures for case 1 optimization (II) . . . 225
Tab. 9 Workspaces of the considered structures for case 2 optimization (I) . . . 226
Tab. 10 Workspaces of the considered structures for case 2 optimization (II) . . . 227
Tab. 11 Description of the selected components (provided by the respective manufacturer) 228

List of Figures

Fig. 1.1 Worldwide annual supply of industrial robots [IFR14] 1
Fig. 1.2 Main structure of this thesis 6

Fig. 2.1 Serial robots in industry - vertical jointed-arm [KUK14] (left), horizontal jointed-arm [Mit14] (middle), portal system [Yam] (right) 8
Fig. 2.2 DELTA robots - PocketDELTA [Asy14] (left), Adept Quattro [Ade14] (middle), ABB Flex Picker [ABB14] (right) 9
Fig. 2.3 Parallel robots in industry - Hexapod [PI14] (left), Festo Tripod [Fes14] (middle), Tricept [Tri14] (right) 10
Fig. 2.4 Overview of self-weight/payload ratio of industrial robots 12

Fig. 3.1 Evaluation methods with regard to time and effort 15

Fig. 4.1 Methods for type synthesis 23
Fig. 4.2 *Twist (ξ)/wrench (ζ)*-system of PKS with three translational DoF [KG04c] 32
Fig. 4.3 Selection scheme (1) 33
Fig. 4.4 Selection scheme (2) 34
Fig. 4.5 Frame configurations (Δ, $\perp$, $\parallel$, $\star$, $\cup/\mathsf{T}$) 39

Fig. 5.1 Classifying of requirements [BK97] 46
Fig. 5.2 Manipulation tasks in different areas (from left to right: handling of heavy cast parts [KUK14], packaging of sausages [Ben08], milling task [car14]) 50
Fig. 5.3 Spray robot in automotive industry [Aud14] and palletizing of beverages [KUK14] 51
Fig. 5.4 left: stringer positioning [www15], right: positioning system [Moo14] . . 51
Fig. 5.5 Stress testing of car seats [KUK14], head positioner [HEA14] 53
Fig. 5.6 pick & place trajectory, velocity (left) and acceleration (right) distribution 54
Fig. 5.7 Positioning system, PM = parallel manipulator, B = Bipod, S = shell, Pos = positioning unit 55
Fig. 5.8 Basic structure of the 3D fiber injection plant (left) [Ben14] and system with mobile and global air extraction (right) [Wer11] 56

Fig. 5.9 Adept Cobra s600, Festo Tripod EXPT 120, Autonox24 Delta IP65 RL4 1200, PI M-850 Hexapod (from left to right) 57

Fig. 6.1 Reference frames and parameter definition (Δ and $\star$-shaped) 61
Fig. 6.2 Reference frames and parameter definition ($\|$-shaped) 62
Fig. 6.3 Graphical interface of a MATLAB SimMechanics© model 66

Fig. 7.1 Criteria based on the robotic structure 70
Fig. 7.2 Criteria based on the kinematic model 71
Fig. 7.3 Criteria based on the Jacobian matrix 76
Fig. 7.4 Criteria based on the stiffness model 77
Fig. 7.5 Criteria based on the dynamic model 79

Fig. 8.1 Prescribed workspaces and considered points 84
Fig. 8.2 Relations of geometrical parameters for all PKS 91
Fig. 8.3 Optimized parameters 91
Fig. 8.4 Min. local dexterity index distribution - prismatic actuation 93
Fig. 8.5 Min. local dexterity index distribution - rotational actuation 93

Fig. 9.1 Applied analysis steps 97
Fig. 9.2 Object time for different methods calculating the workspace of R$\underline{\text{P}}$C [Com15] 99
Fig. 9.3 Fundamentals of the bisection method 100
Fig. 9.4 Implementation of the bisection method using normals of the sphere [Com15] 101
Fig. 9.5 Object time for different methods [Com15] 102
Fig. 9.6 Workspace and largest enclosed sphere of RPC-PKS 102
Fig. 9.7 $\underline{\text{R}}$PC median values 105
Fig. 9.8 $\underline{\text{P}}$RC* median values 106

Fig. 10.1 Geometrical parameters for pick & place task 126
Fig. 10.2 Performance index for pick & place task 127
Fig. 10.3 r_B over r_A for positioning task; straight lines for $r_B = r_A$ and $r_B = r_A - 0.2m$ 129
Fig. 10.4 Relations of geometrical parameters for positioning task 129
Fig. 10.5 Performance index for positioning task 130
Fig. 10.6 Reachable and prescribed workspace for guidance task 131
Fig. 10.7 Results pick & place task (I) 133
Fig. 10.8 Strength chart pick & place task 134
Fig. 10.9 Results positioning task (I) 135

Fig. 10.10 Distribution of reachable workspace with respect to z-axis 137
Fig. 10.11 Strength chart positioning task (black = pos 1, red = pos 2) 138
Fig. 10.12 Analysis results for guidance task 139
Fig. 10.13 Elasticity contributors for sideways mounting of positioning task 140
Fig. 10.14 Elasticity contributors for pick & place task 141

Fig. 1 Group 3R-1P 189
Fig. 2 Group 2R-2P 189
Fig. 3 Group 5R 189
Fig. 4 Group 4R-1P 190
Fig. 5 Max. force distribution - prismatic actuation 191
Fig. 6 Max. torque distribution - rotational actuation 191
Fig. 7 Max. velocity distribution - prismatic actuation 191
Fig. 8 Max. velocity distribution - rotational actuation 192
Fig. 9 Max. power distribution - prismatic actuation 192
Fig. 10 Max. power distribution - rotational actuation 192
Fig. 11 Distribution of max. end-effector displacements - prismatic actuation . . 193
Fig. 12 Distribution of max. end-effector displacements - rotational actuation . . 193
Fig. 13 Distribution of max. positioning error - prismatic actuation 194
Fig. 14 Distribution of max. positioning error - rotational actuation 194
Fig. 15 Activity plan of the bisection method (according to [Com15]) 195
Fig. 16 R$\underline{\text{P}}$C median values 196
Fig. 17 $\underline{\text{C}}$PR* median values 197
Fig. 18 U$\underline{\text{P}}$U$^{\Delta}$ median values 198
Fig. 19 $\underline{\text{C}}$PR$^{\Delta}$ median values 199
Fig. 20 $\underline{\text{P}}$RC$^{\parallel}$ median values 200
Fig. 21 $\underline{\text{U}}$UP$^{\Delta}$ median values 201
Fig. 22 $\underline{\text{P}}$UU$^{\parallel}$ median values 202
Fig. 23 $\underline{\text{P}}$UU* median values 203
Fig. 24 $\underline{\text{R}}$RC$^{\Delta}$ median values, $r_B = 0.3$ m 204
Fig. 25 $\underline{\text{C}}$RR* median values, $\psi = 15°$ 205
Fig. 26 $\underline{\text{U}}$RC$^{\Delta}$ median values, $r_B = 0.3$ m 206
Fig. 27 $\underline{\text{C}}$UR* median values, $\psi = 15°$ 207
Fig. 28 $\underline{\text{U}}$RU$^{\Delta}$ median values, $r_B = 0.3$ m 208
Fig. 29 $\underline{\text{U}}$UR$^{\Delta}$ median values, $r_B = 0.3$ m 209
Fig. 30 $\underline{\text{R}}$UU$^{\Delta}$ median values, $r_B = 0.3$ m 210
Fig. 31 $\underline{\text{C}}$RR$^{\Delta}$ median values, $r_B = 0.3$ m, $\delta = 30°$ 211
Fig. 32 $\underline{\text{C}}$RR$^{\parallel}$ median values, $r_B = 0.3$ m, $\delta = 50°$ 212
Fig. 33 $\underline{\text{C}}$UR$^{\Delta}$ median values, $r_B = 0.3$ m, $\delta = 50°$ 213

Fig. 34 $\underline{\mathrm{C}}\mathrm{UR}^{\parallel}$ median values, $r_B = 0.3$ m, $\delta = 50°$ 214
Fig. 35 Results pick & place task (II) 215
Fig. 36 Results positioning task (II) 216
Fig. 37 Results positioning task (III) 217

Fig. 38 Vector loop and inertia properties of RRC-PKS 230
Fig. 39 Static equilibrium of forces at the end-effector of RRC-PKS 231
Fig. 40 Vector loop and inertia properties of CRR^{Δ}-PKS 233
Fig. 41 Vector loop and inertia properties of $\mathrm{CRR}^{\parallel}$-PKS 236
Fig. 42 Vector loop and inertia properties of $\mathrm{CRR}^{\star}$-PKS 238
Fig. 43 Static equilibrium of forces at the end-effector of CRR-PKS 239
Fig. 44 Vector loop and inertia properties of RPC 241
Fig. 45 Vector loop and inertia properties of CPR^{Δ} 242
Fig. 46 Vector loop and inertia properties of $\mathrm{CPR}^{\star}$ 244
Fig. 47 Vector loop and inertia properties of $\mathrm{PRC}^{\star}$-PKS 248
Fig. 48 Vector loop and inertia properties of $\mathrm{PRC}^{\parallel}$-PKS 249
Fig. 49 Vector loop of UUP-PKS 251
Fig. 50 Vector loop of UCR-PKS 255
Fig. 51 Vector loop and inertia properties of UPU-PKS 257
Fig. 52 Static equilibrium of forces/moments at the end-effector of UPU-PKS . . 258
Fig. 53 Vector loop of CRU^{Δ}-PKS 261
Fig. 54 Vector loop and inertia properties of $\mathrm{PUU}^{\star}$-PKS 264
Fig. 55 Vector loop and inertia properties of $\mathrm{PUU}^{\parallel}$-PKS 265
Fig. 56 Vector loop of RUC-PKS 267
Fig. 57 Vector loop and inertia properties of CUR^{Δ}-PKS 270
Fig. 58 Vector loop and inertia properties of $\mathrm{CUR}^{\parallel}$-PKS 271
Fig. 59 Vector loop and inertia properties of $\mathrm{CUR}^{\star}$-PKS 273
Fig. 60 Vector loop and inertia properties of URU-PKS 278
Fig. 61 Vector loop and inertia properties of UUR-PKS 278
Fig. 62 Vector loop and inertia properties of RUU-PKS 281

Figures

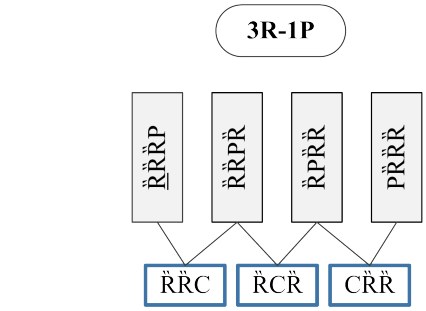

Fig. 1: Group 3R-1P

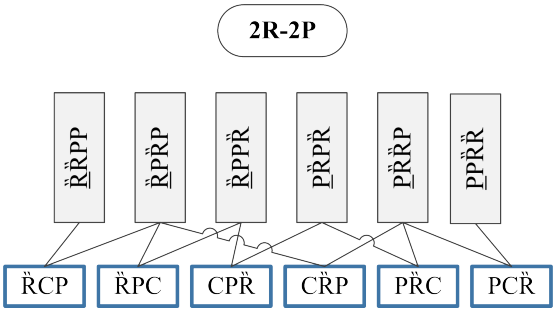

Fig. 2: Group 2R-2P

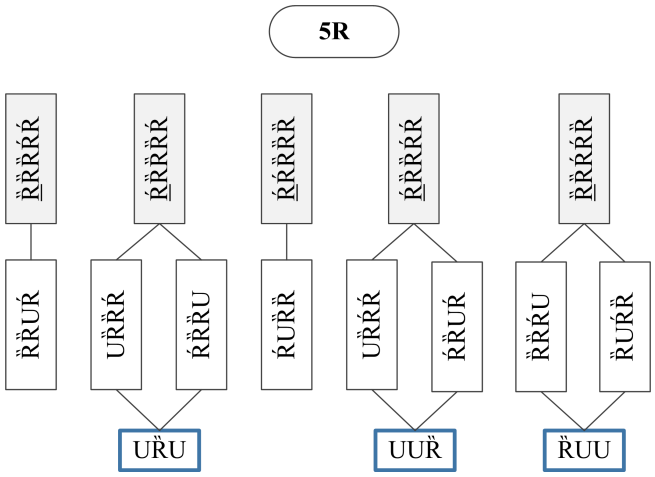

Fig. 3: Group 5R

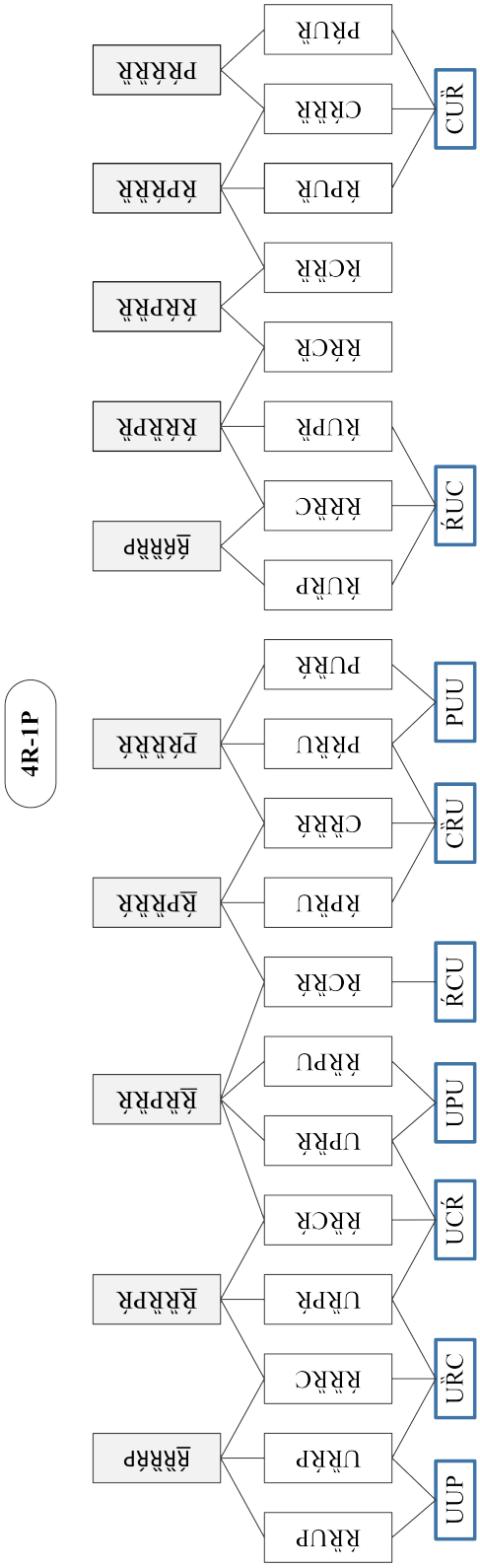

Fig. 4: Group 4R-1P

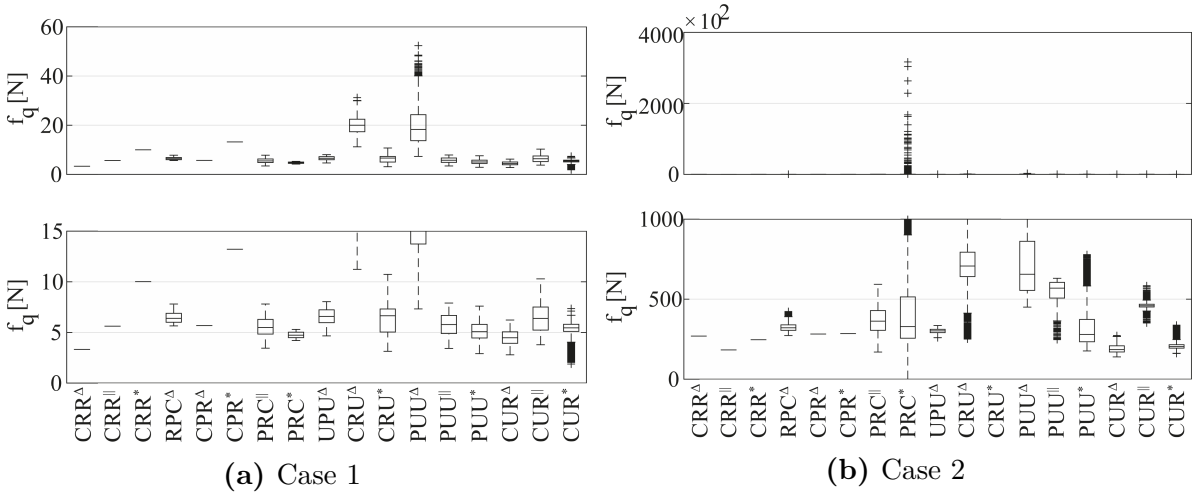

(a) Case 1 **(b)** Case 2

Fig. 5: Max. force distribution - prismatic actuation

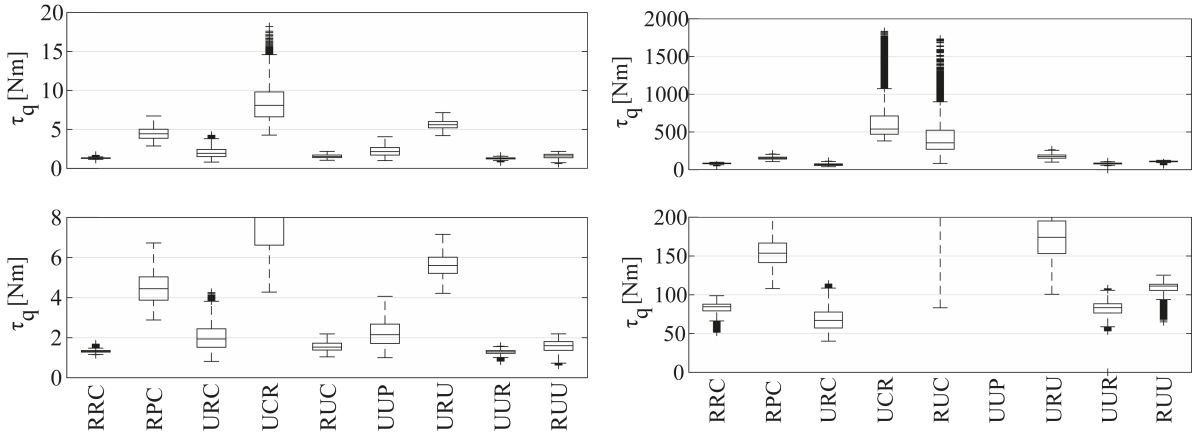

(a) Case 1 **(b)** Case 2

Fig. 6: Max. torque distribution - rotational actuation

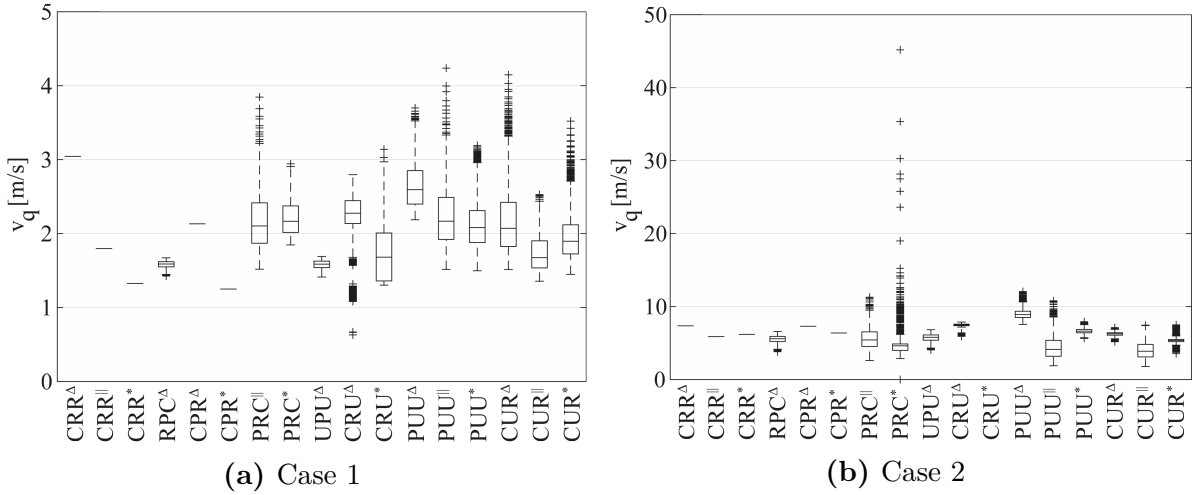

(a) Case 1 **(b)** Case 2

Fig. 7: Max. velocity distribution - prismatic actuation

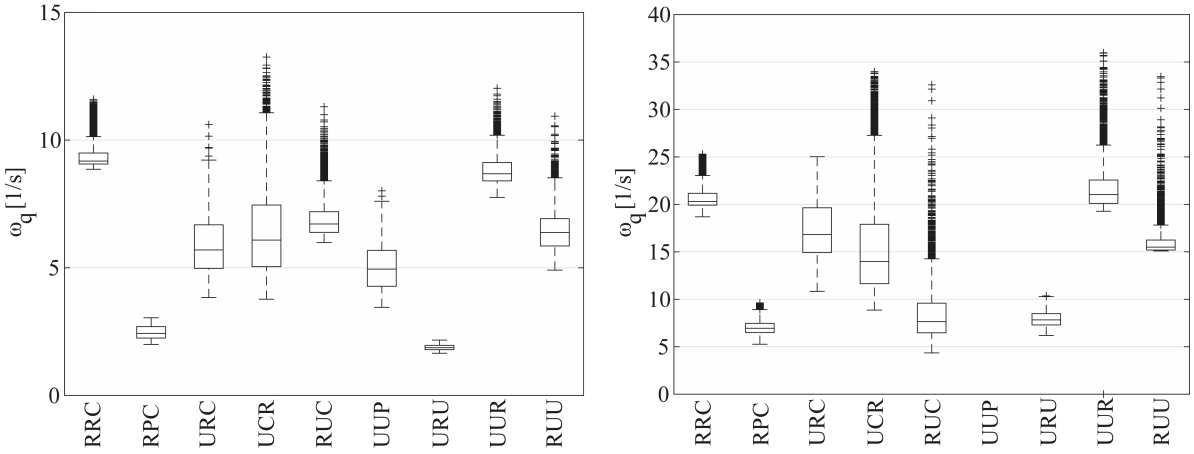

(a) Case 1 **(b)** Case 2

Fig. 8: Max. velocity distribution - rotational actuation

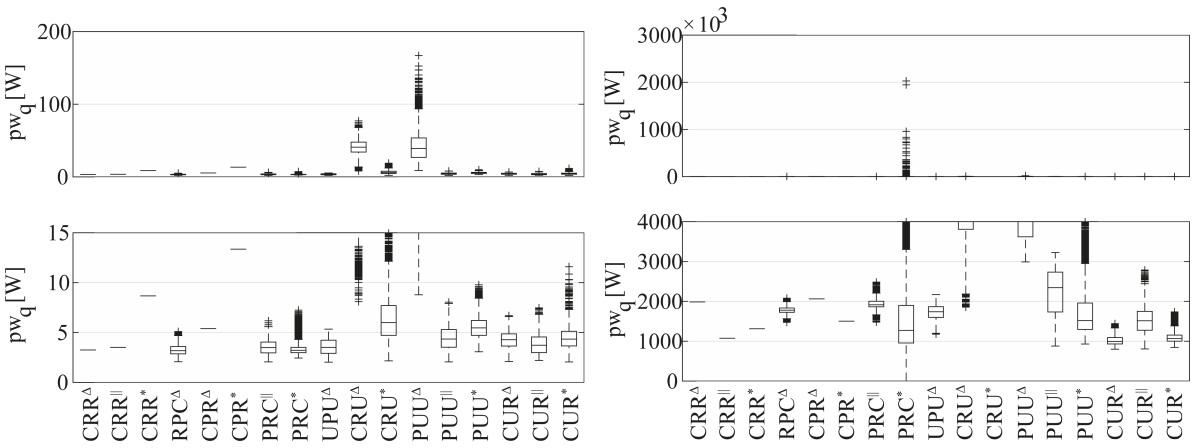

(a) Case 1 **(b)** Case 2

Fig. 9: Max. power distribution - prismatic actuation

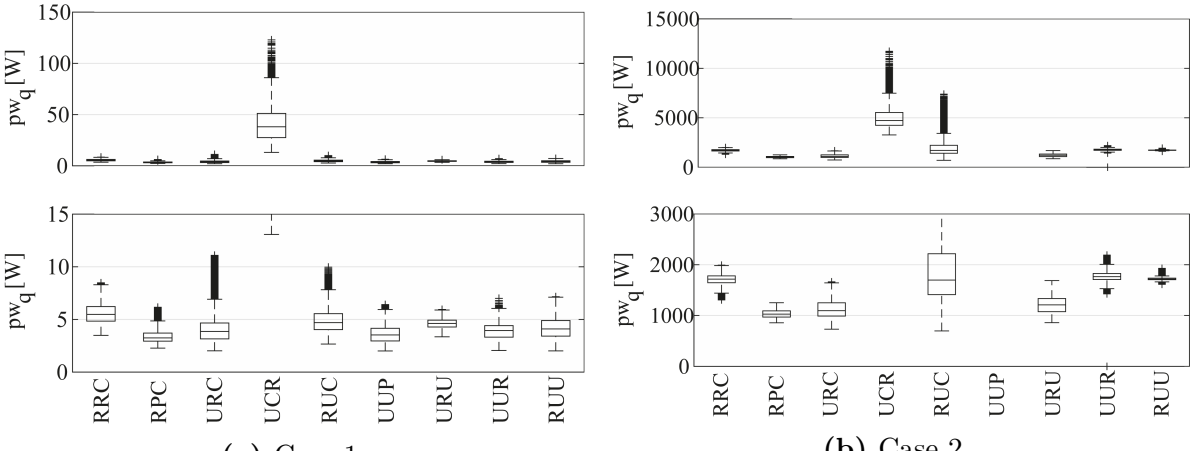

(a) Case 1 **(b)** Case 2

Fig. 10: Max. power distribution - rotational actuation

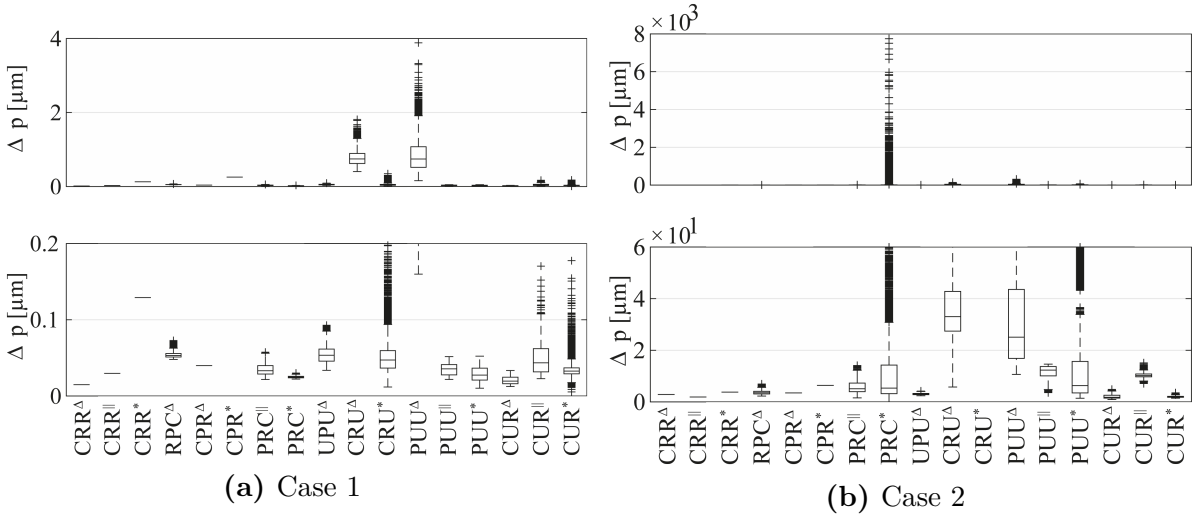

(a) Case 1 **(b)** Case 2

Fig. 11: Distribution of max. end-effector displacements - prismatic actuation

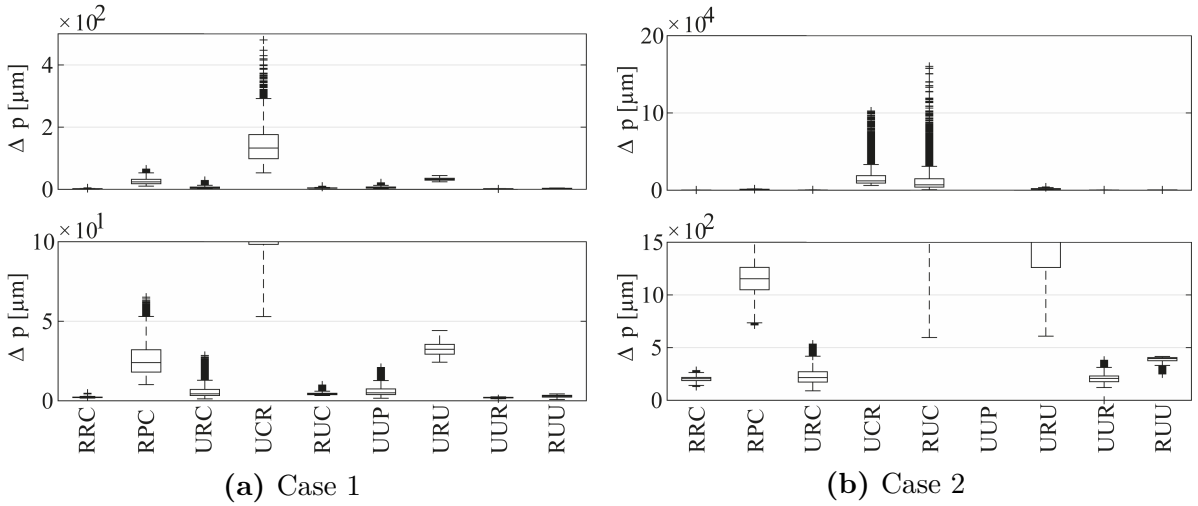

(a) Case 1 **(b)** Case 2

Fig. 12: Distribution of max. end-effector displacements - rotational actuation

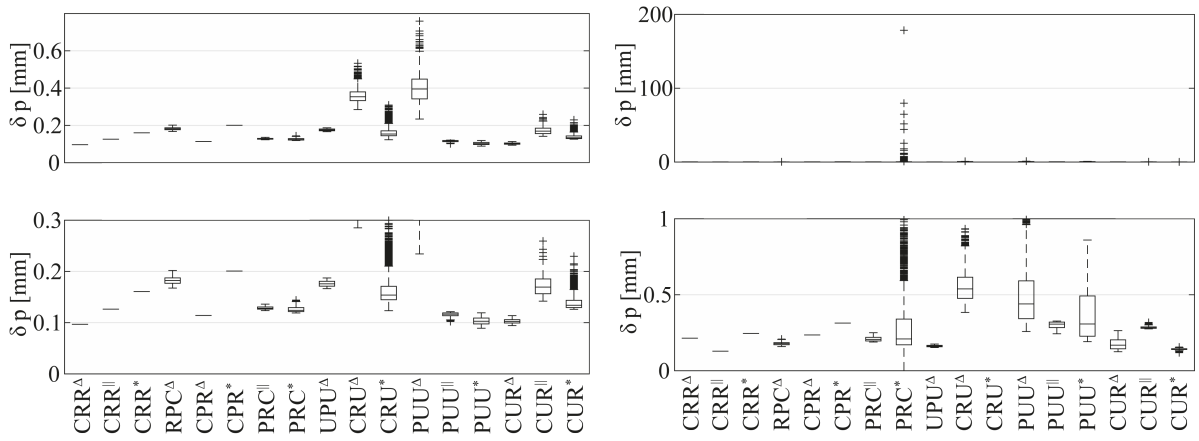

(a) Case 1 **(b)** Case 2

Fig. 13: Distribution of max. positioning error - prismatic actuation

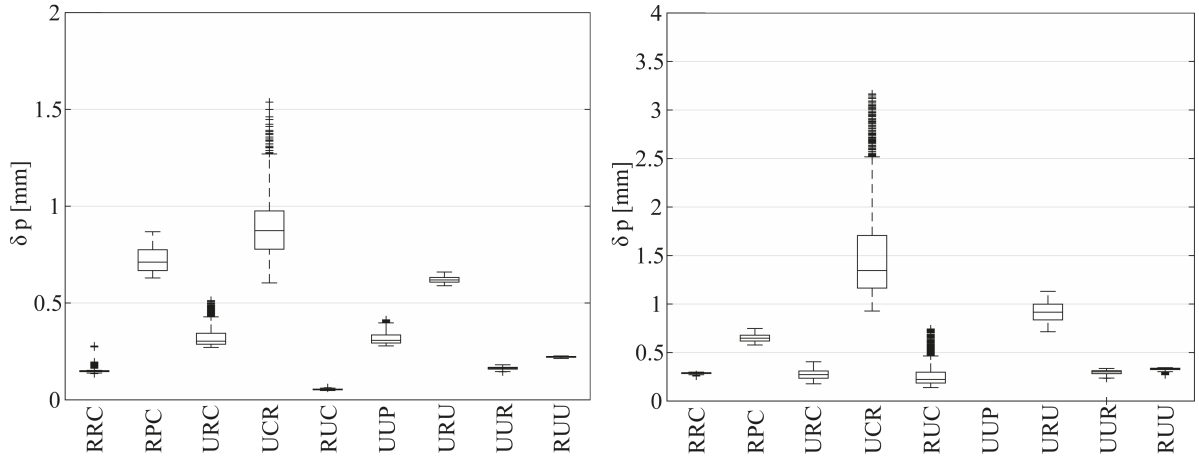

(a) Case 1 **(b)** Case 2

Fig. 14: Distribution of max. positioning error - rotational actuation

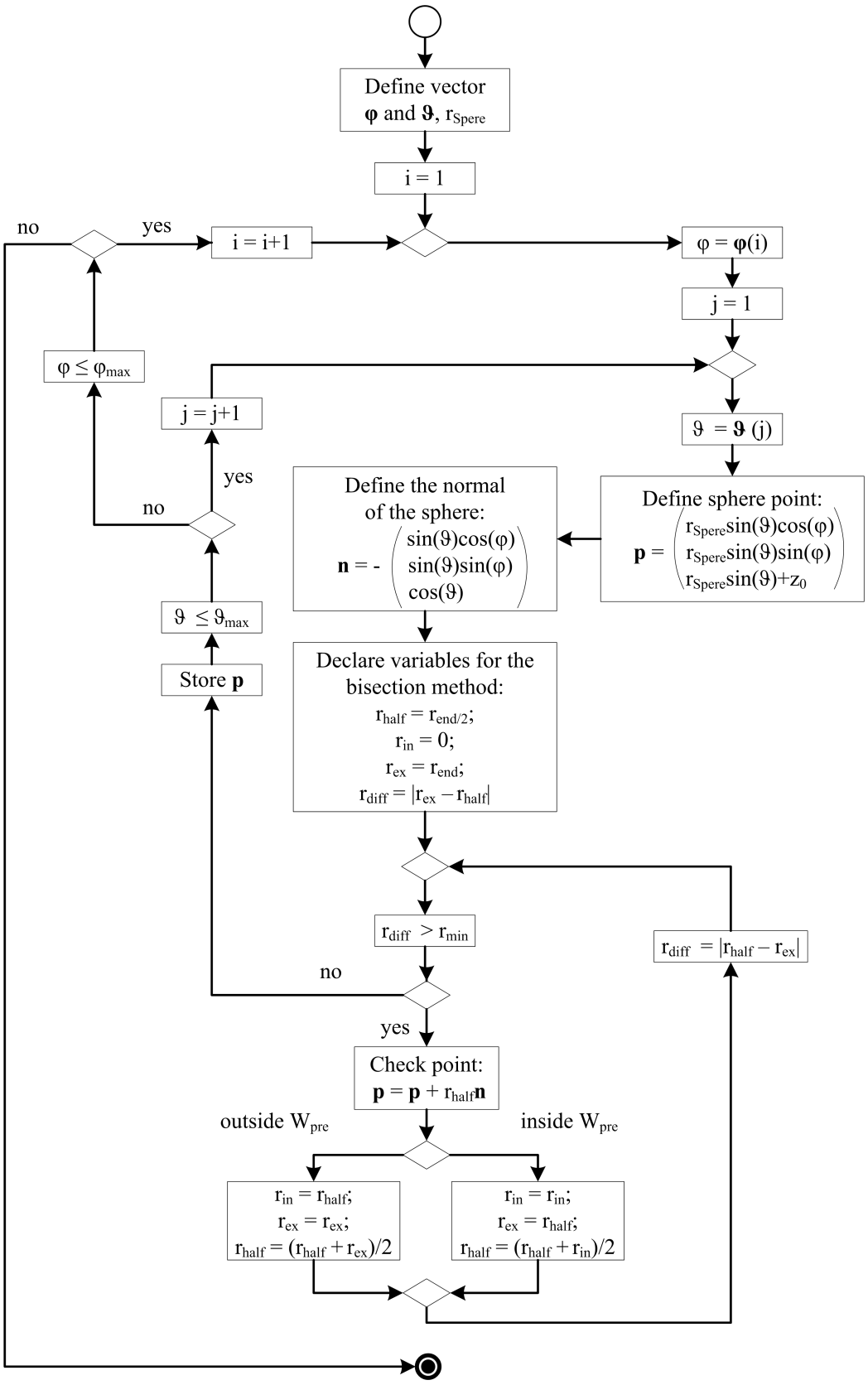

Fig. 15: Activity plan of the bisection method (according to [Com15])

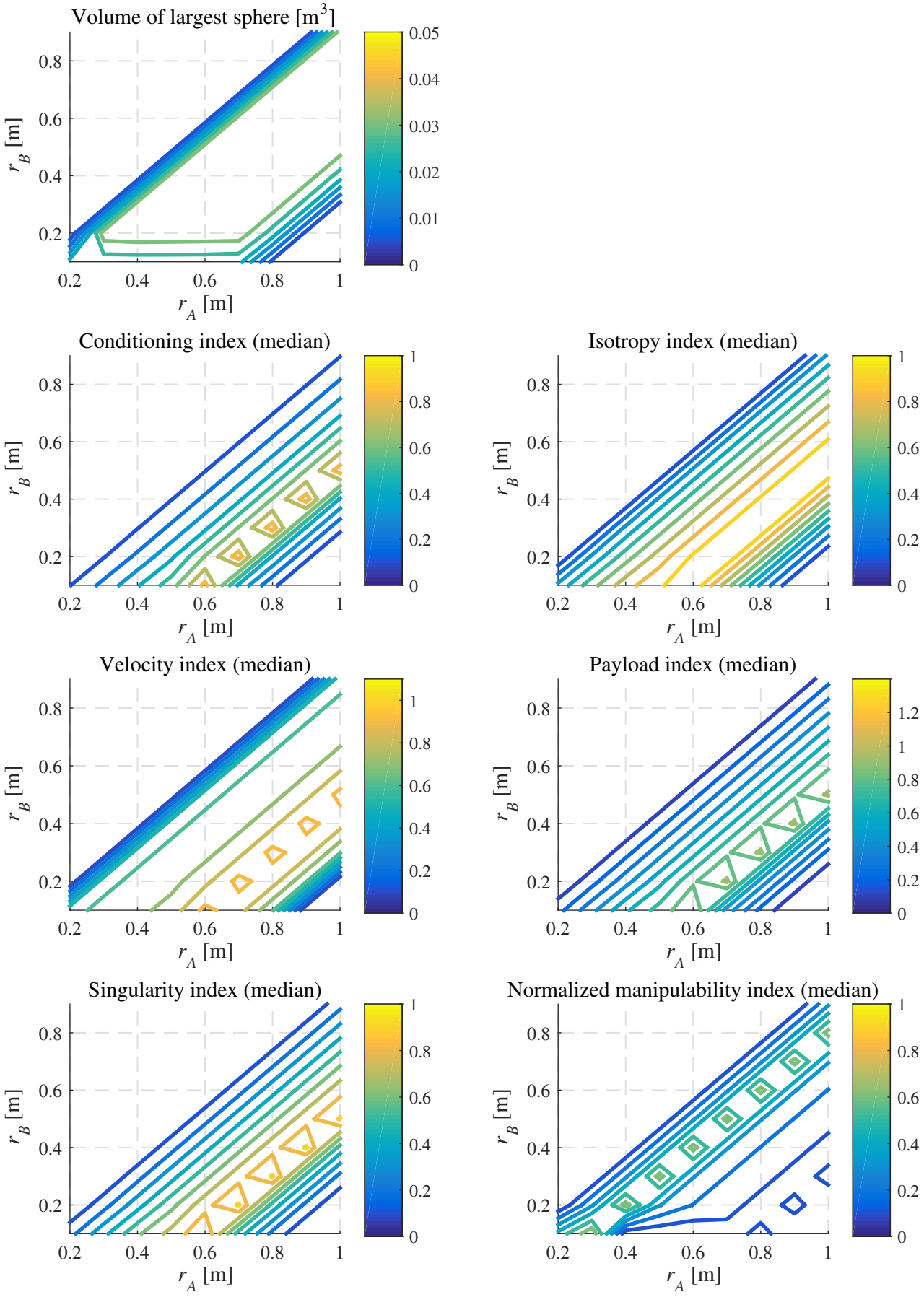

Fig. 16: RPC median values

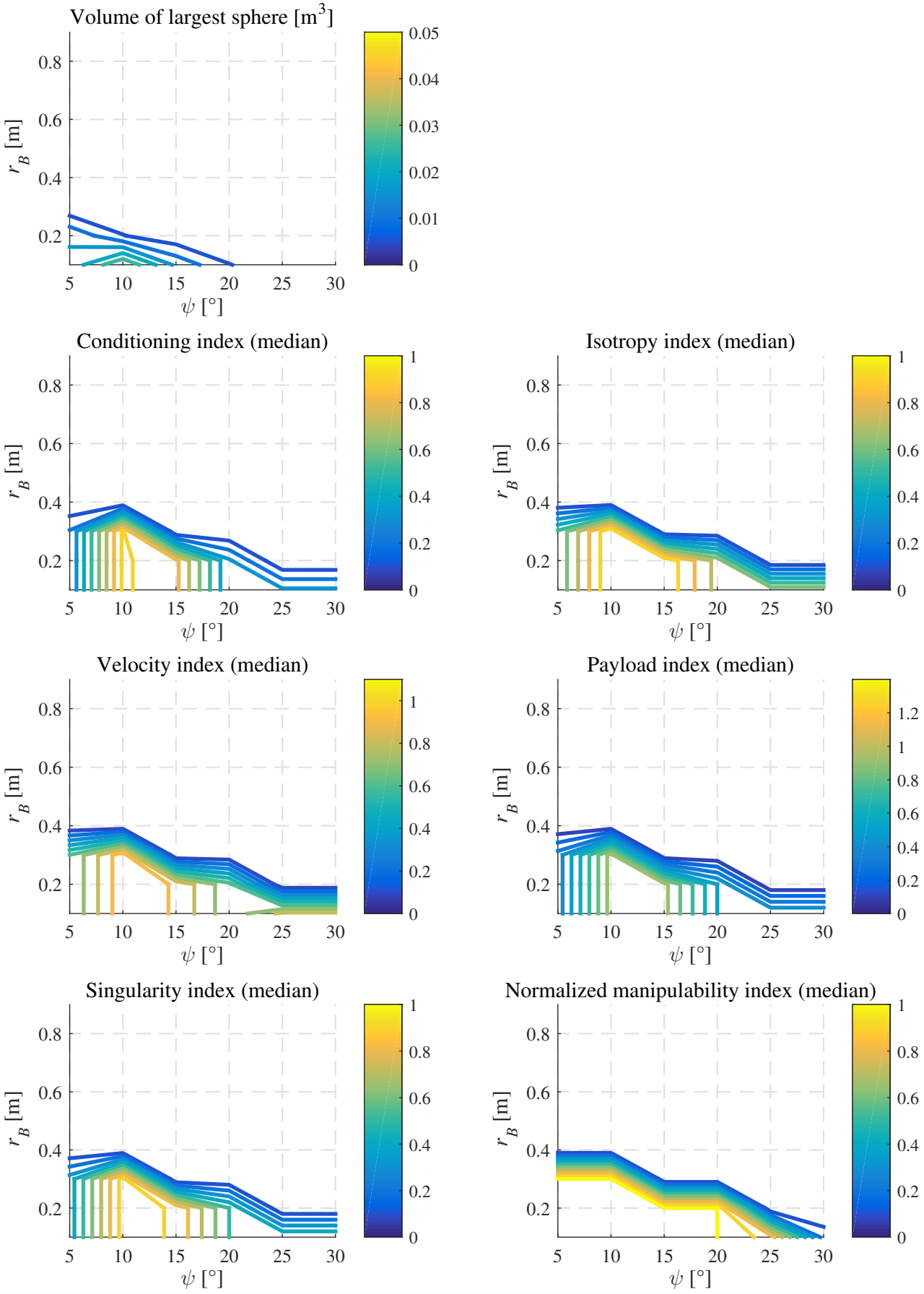

Fig. 17: CPR* median values

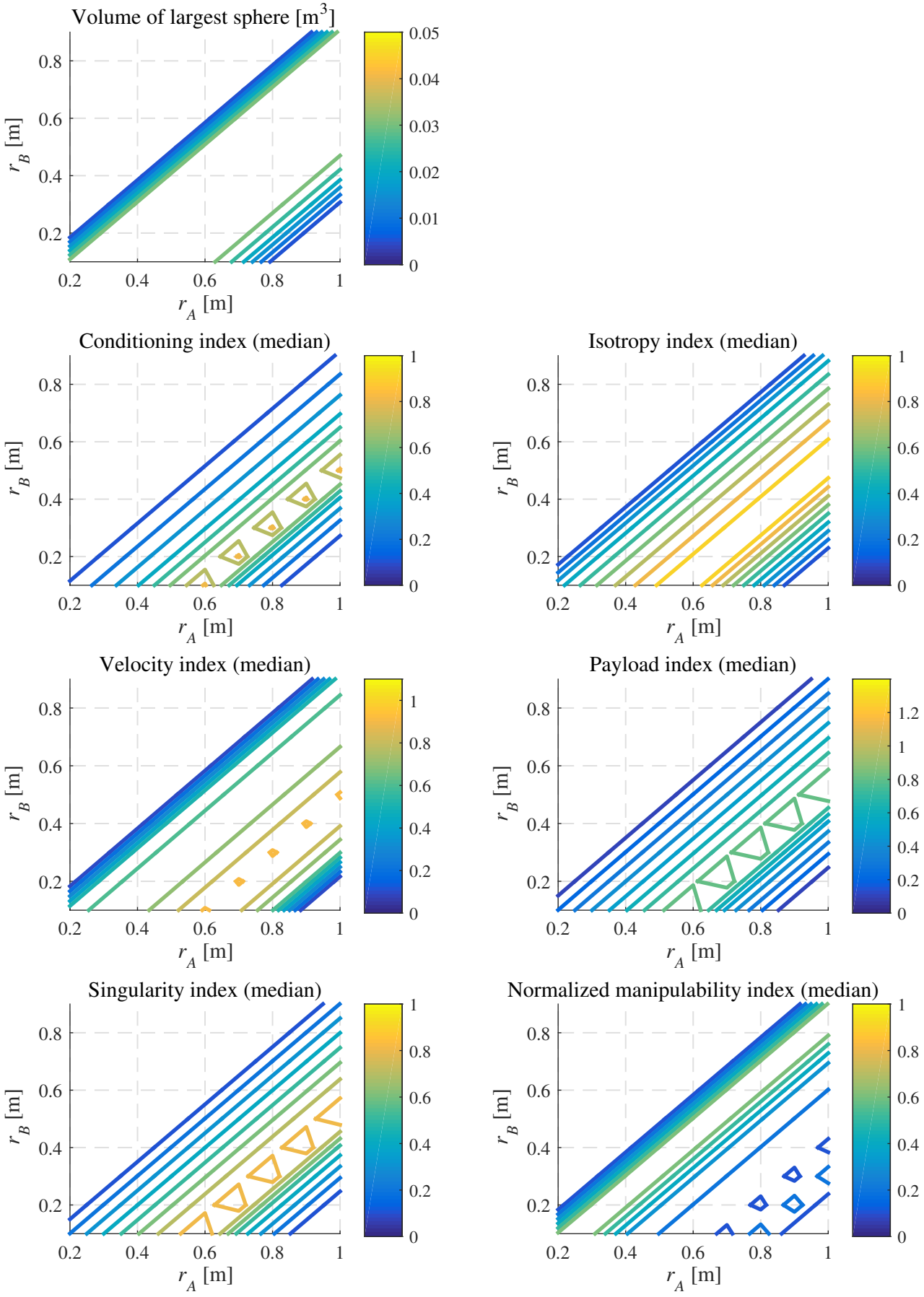

Fig. 18: $\underline{\mathrm{UPU}}^{\Delta}$ median values

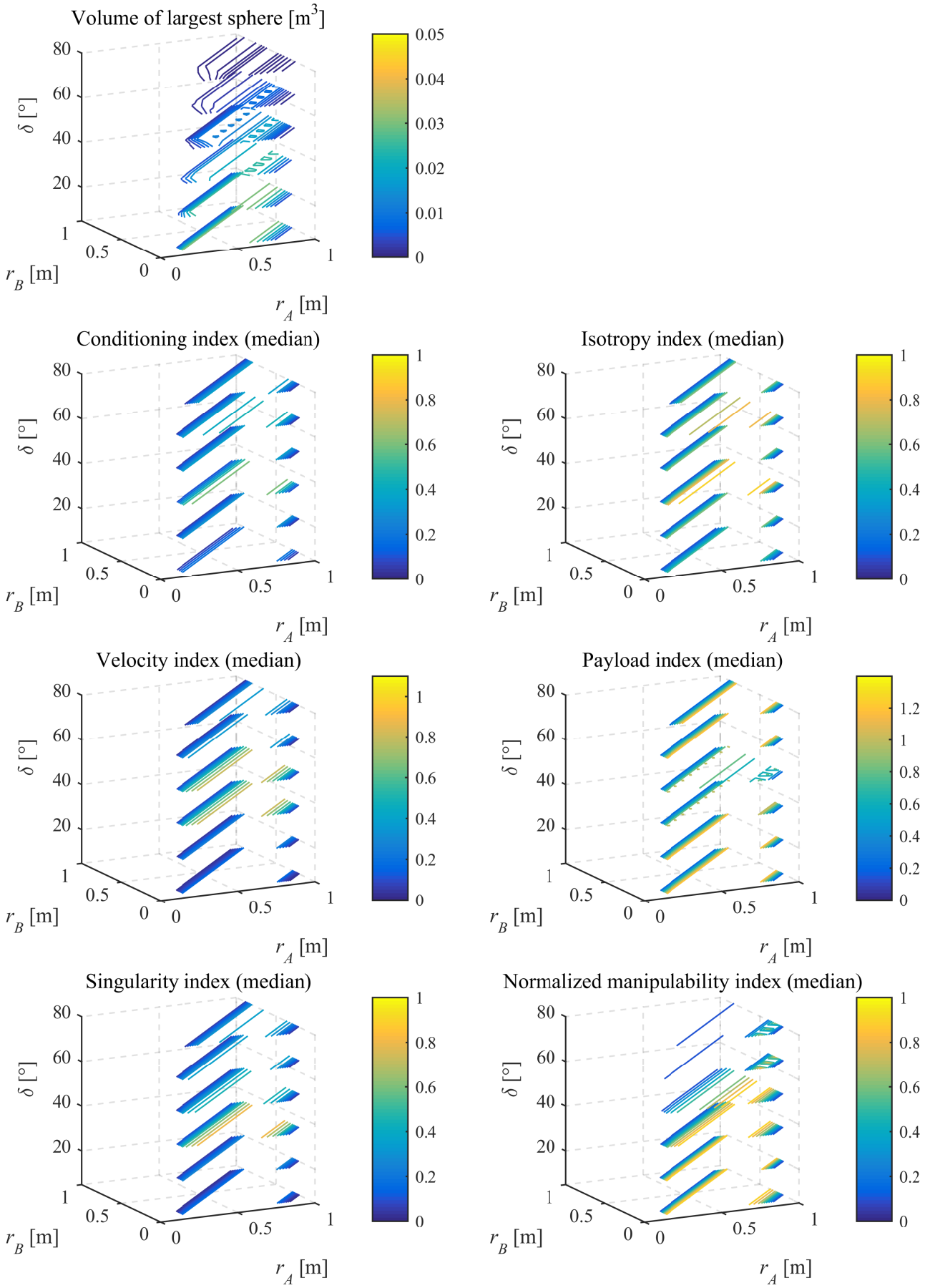

Fig. 19: $\underline{\text{C}}\text{PR}^{\Delta}$ median values

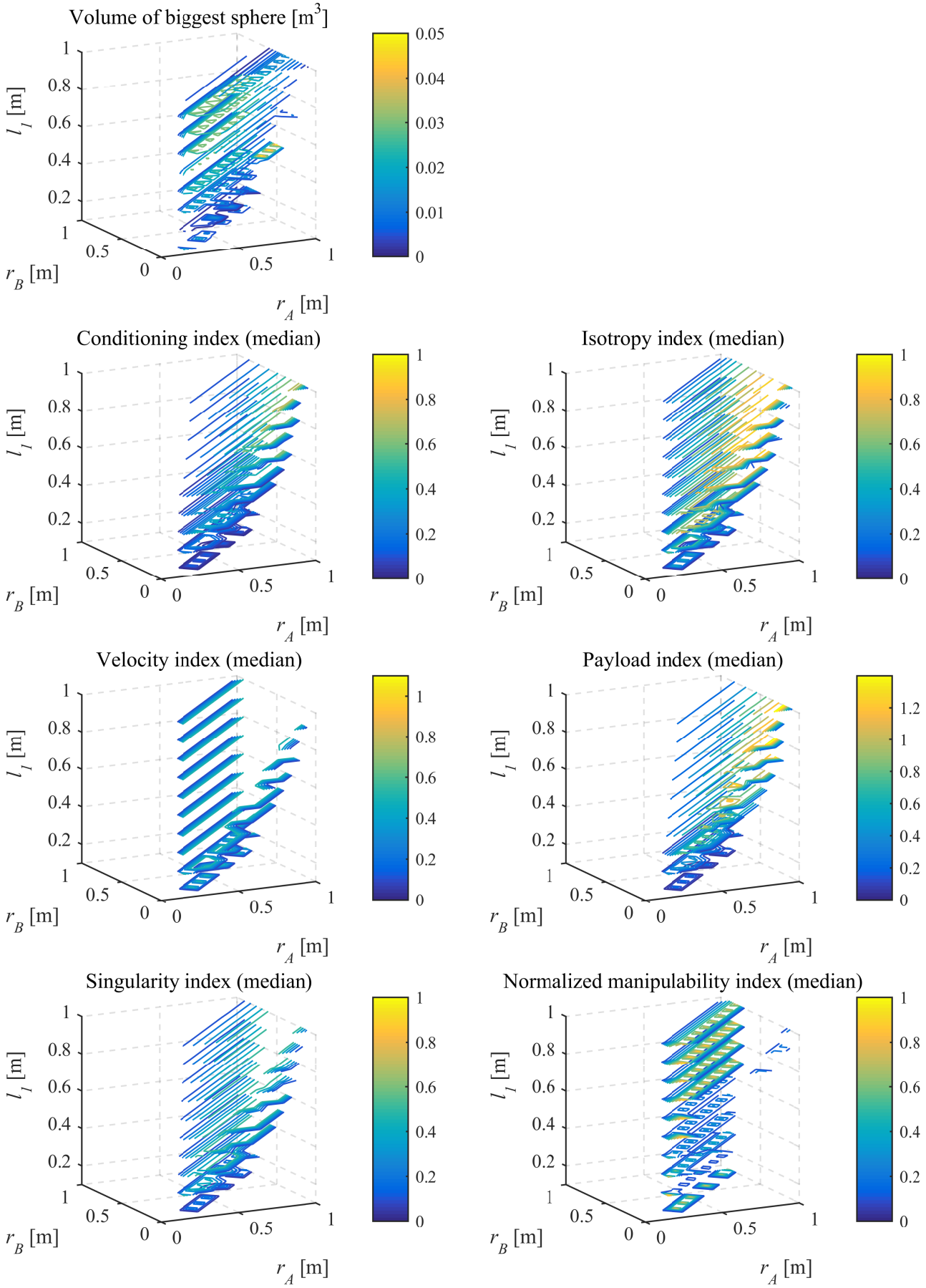

Fig. 20: $\underline{\mathrm{P}}\mathrm{RC}^{\|}$ median values

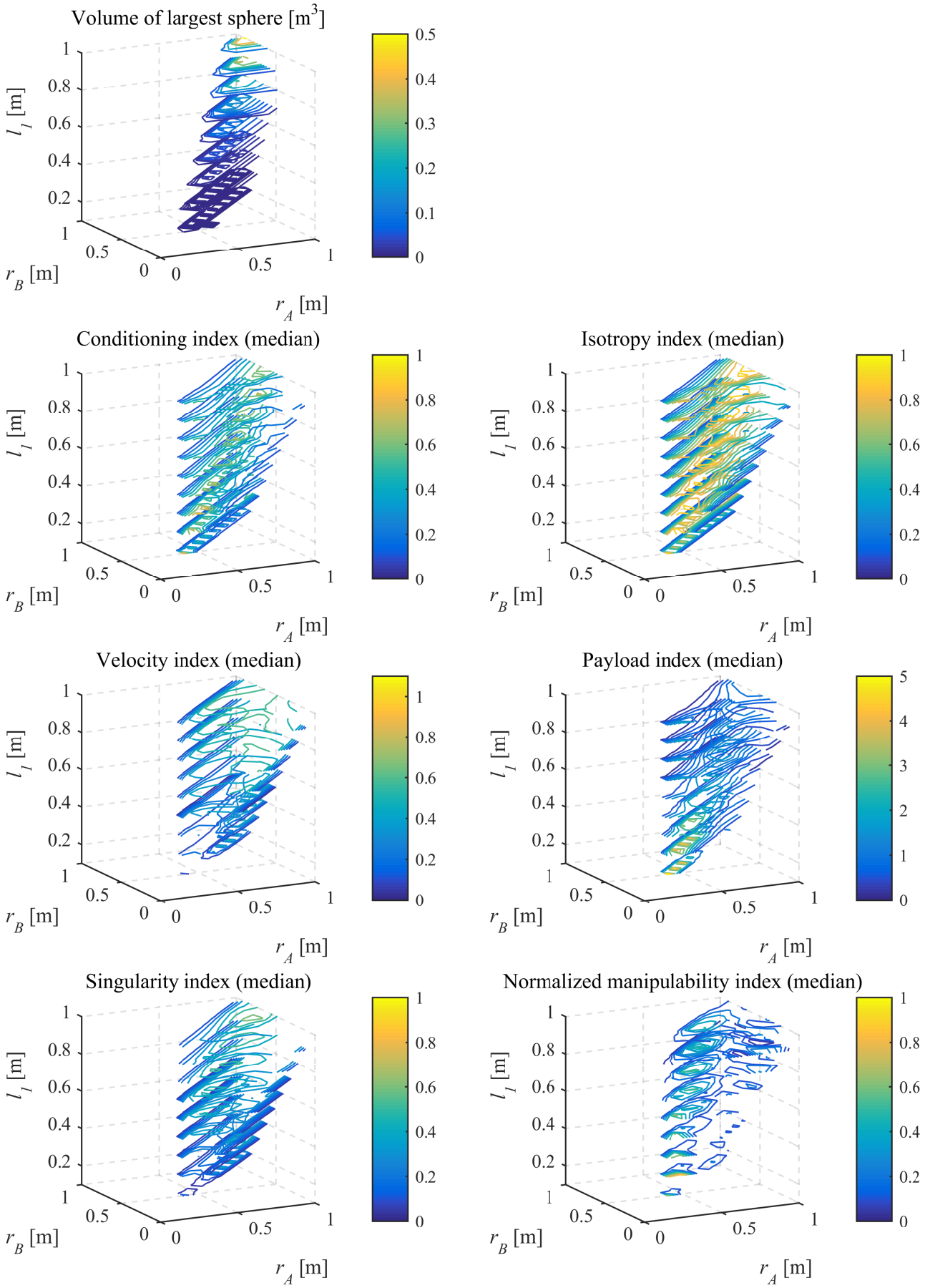

Fig. 21: $\underline{\text{UUP}}^{\Delta}$ median values

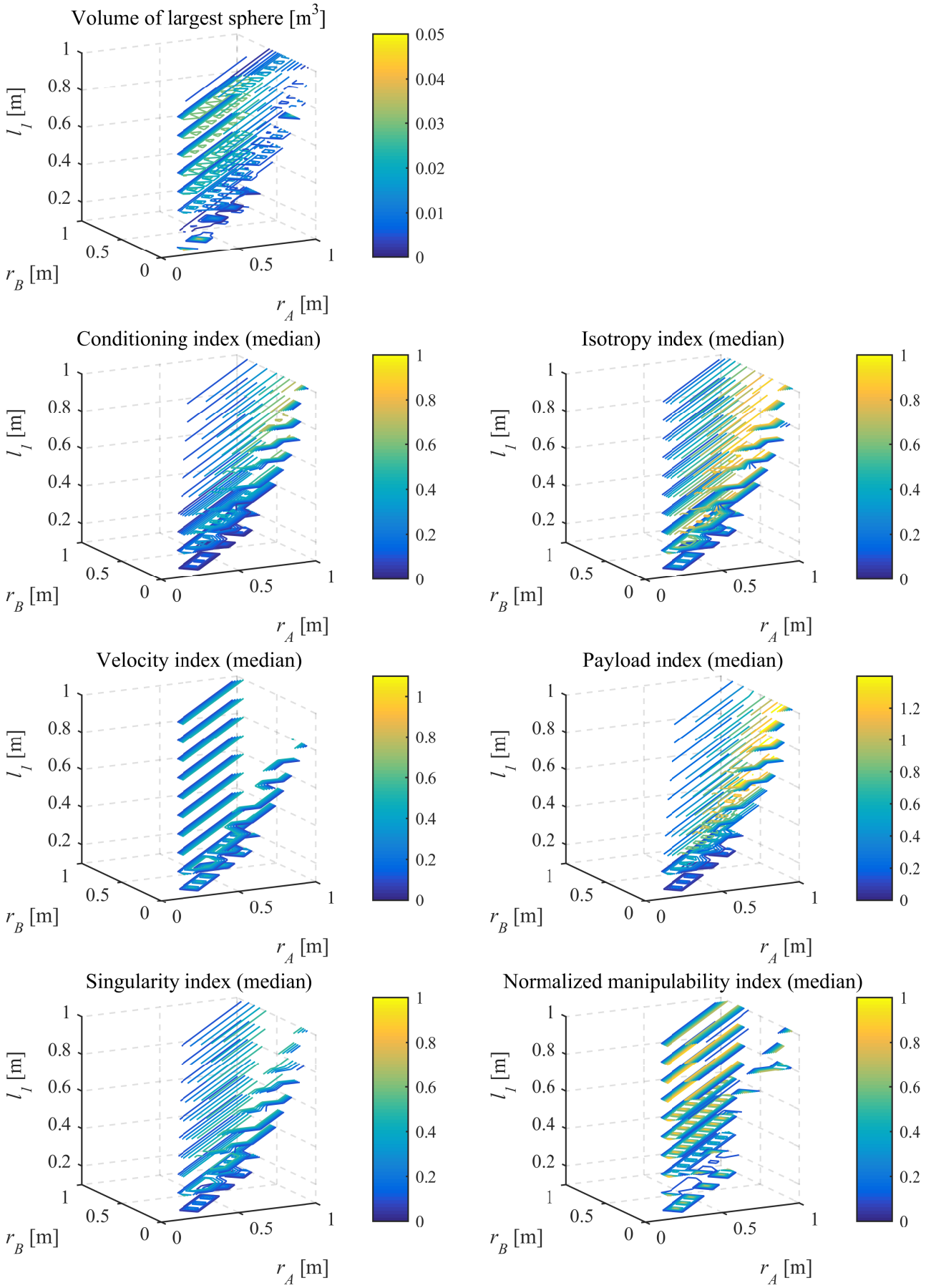

Fig. 22: $\underline{\text{P}}\text{UU}^{\|}$ median values

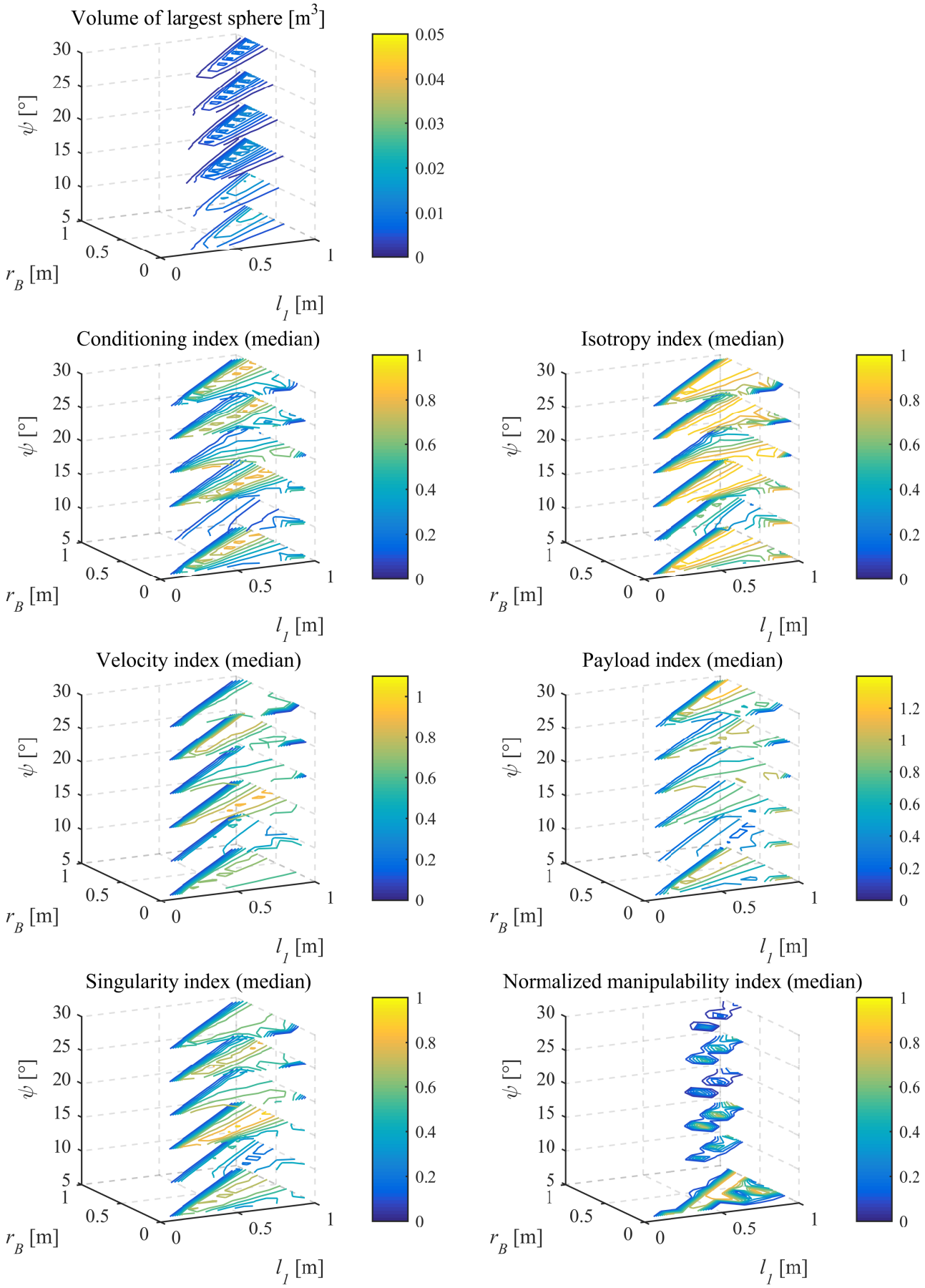

Fig. 23: PUU* median values

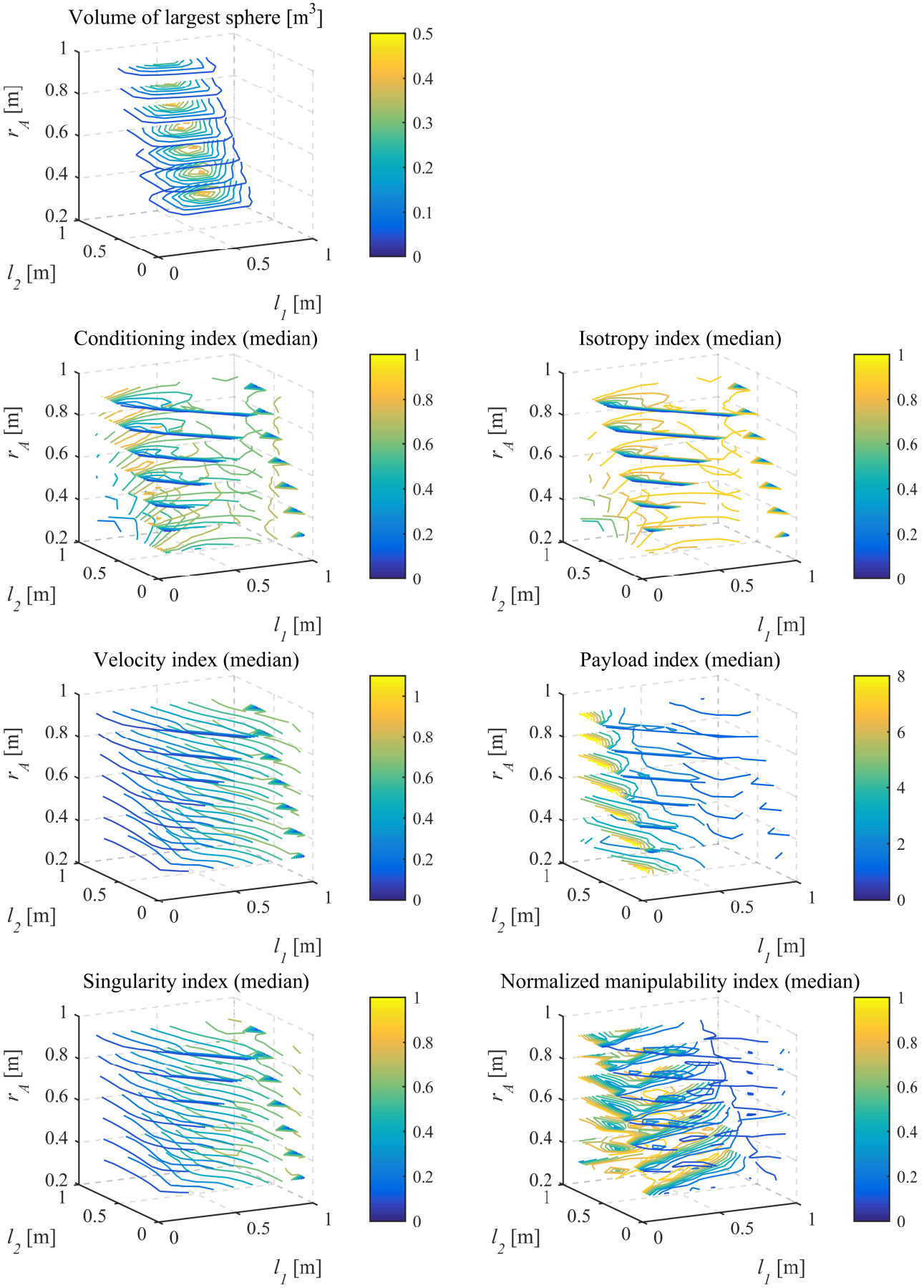

Fig. 24: $\underline{\text{RRC}}^{\Delta}$ median values, $r_B = 0.3$ m

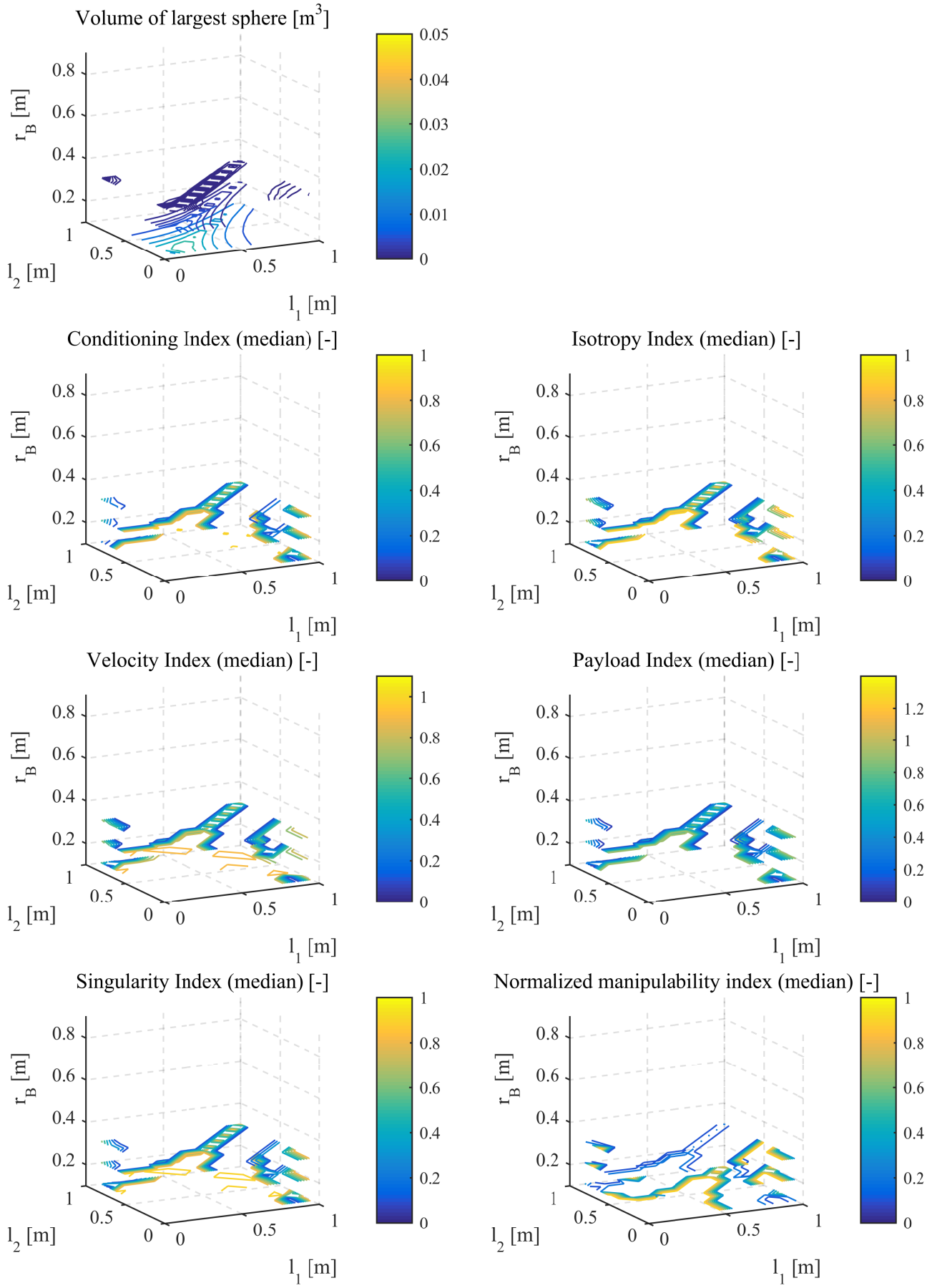

Fig. 25: $\underline{\text{C}}$RR* median values, $\psi = 15°$

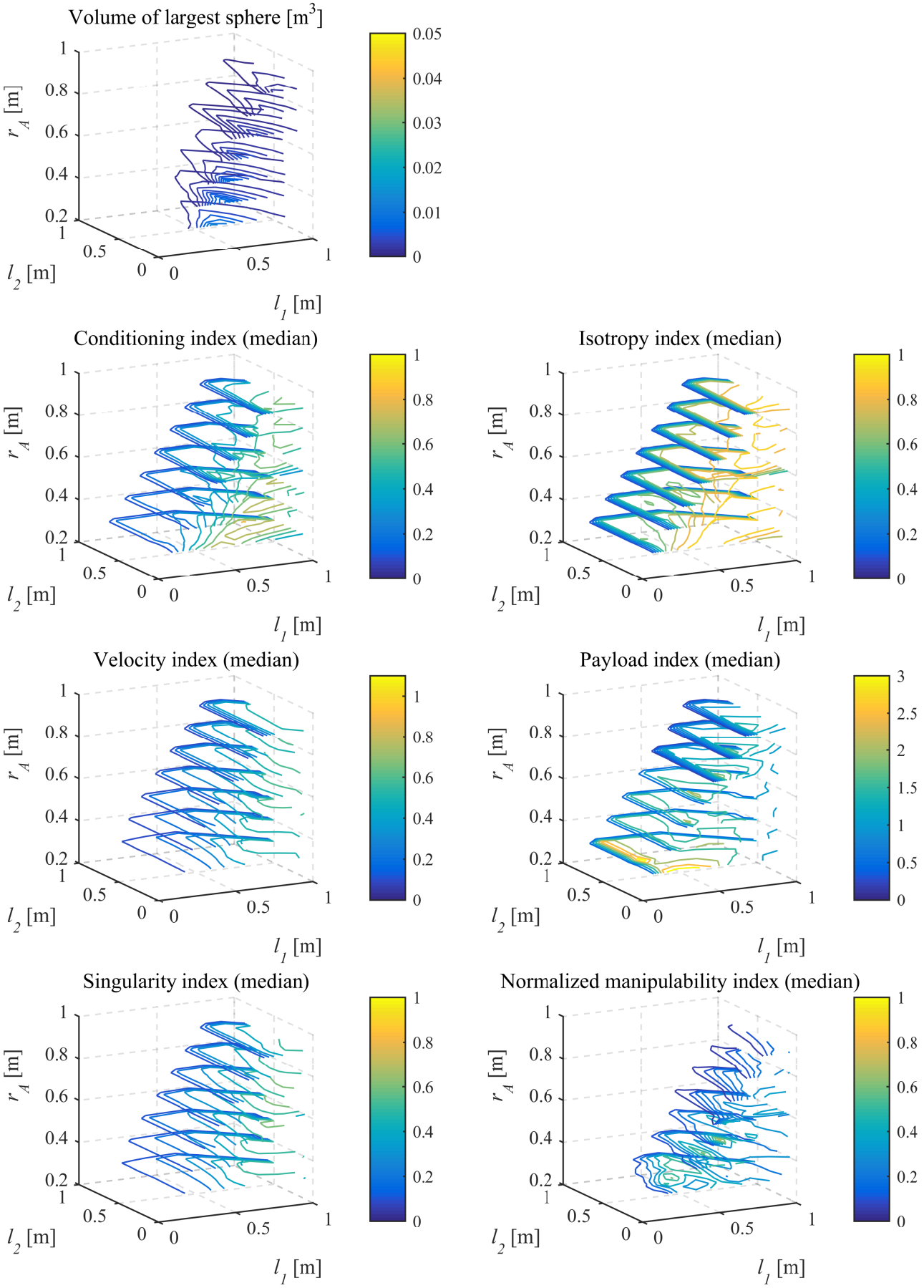

Fig. 26: $\underline{\text{URC}}^{\Delta}$ median values, $r_B = 0.3$ m

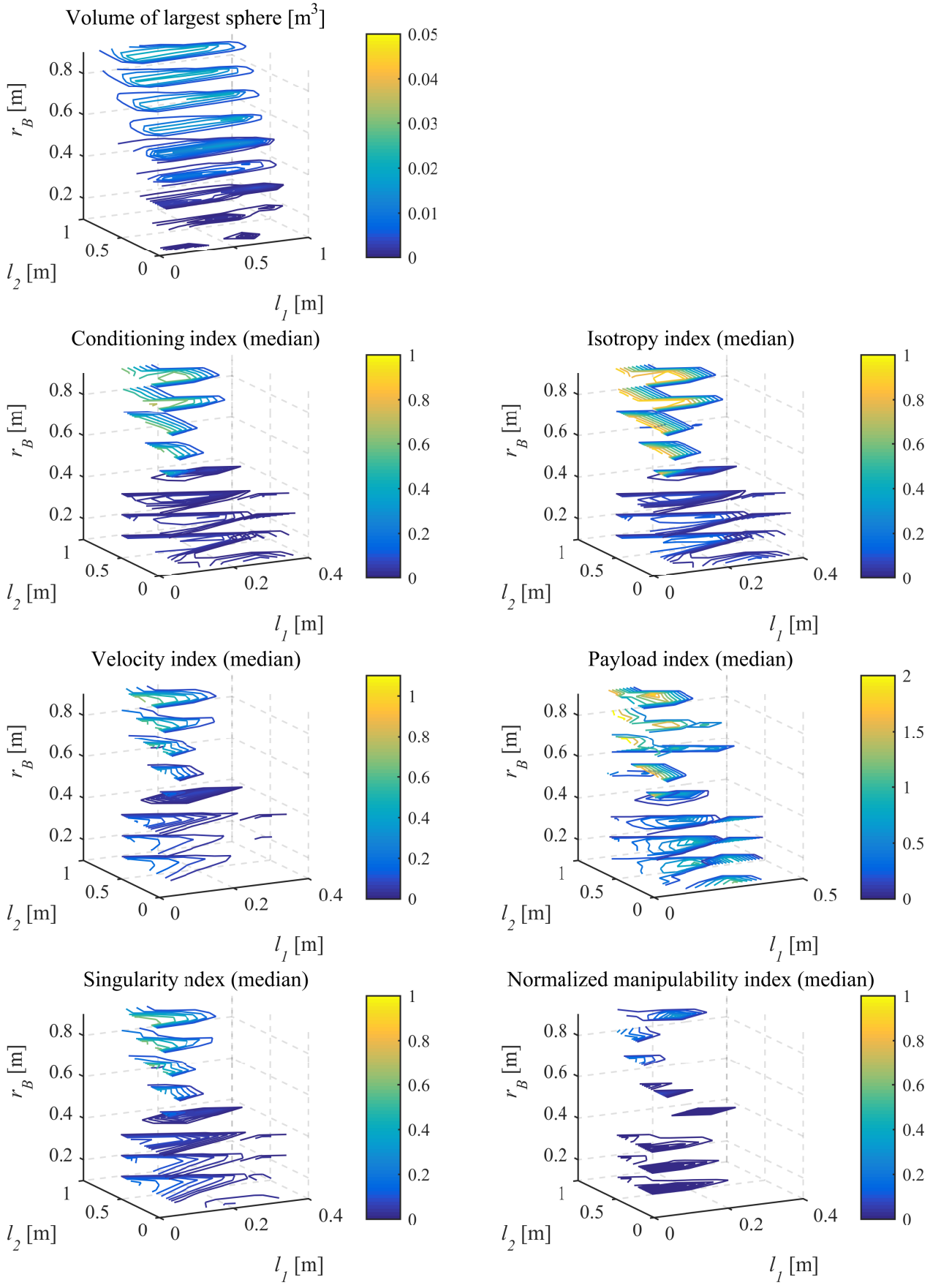

Fig. 27: $\underline{\mathrm{C}}\mathrm{UR}^{\star}$ median values, $\psi = 15°$

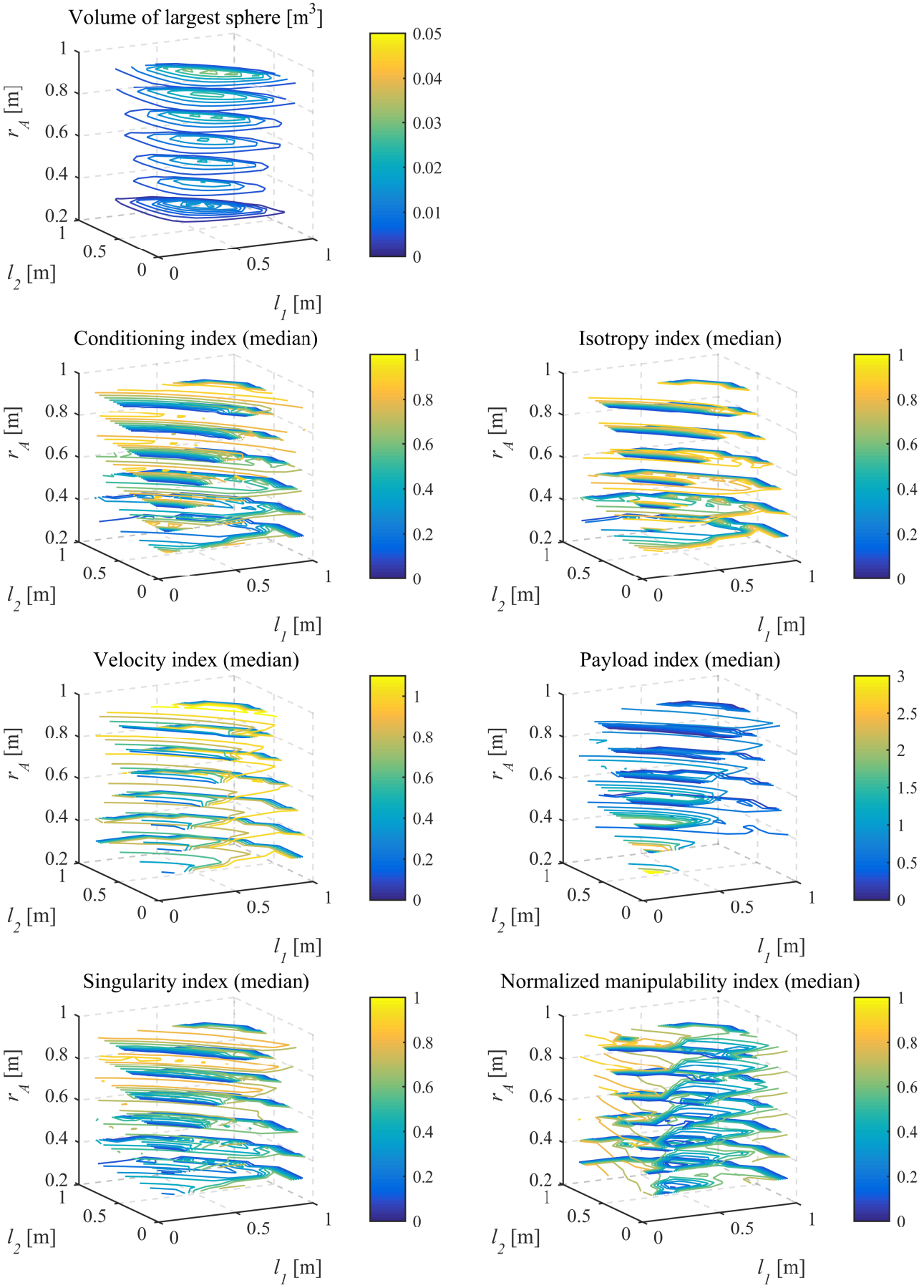

Fig. 28: $\underline{\text{URU}}^{\Delta}$ median values, $r_B = 0.3$ m

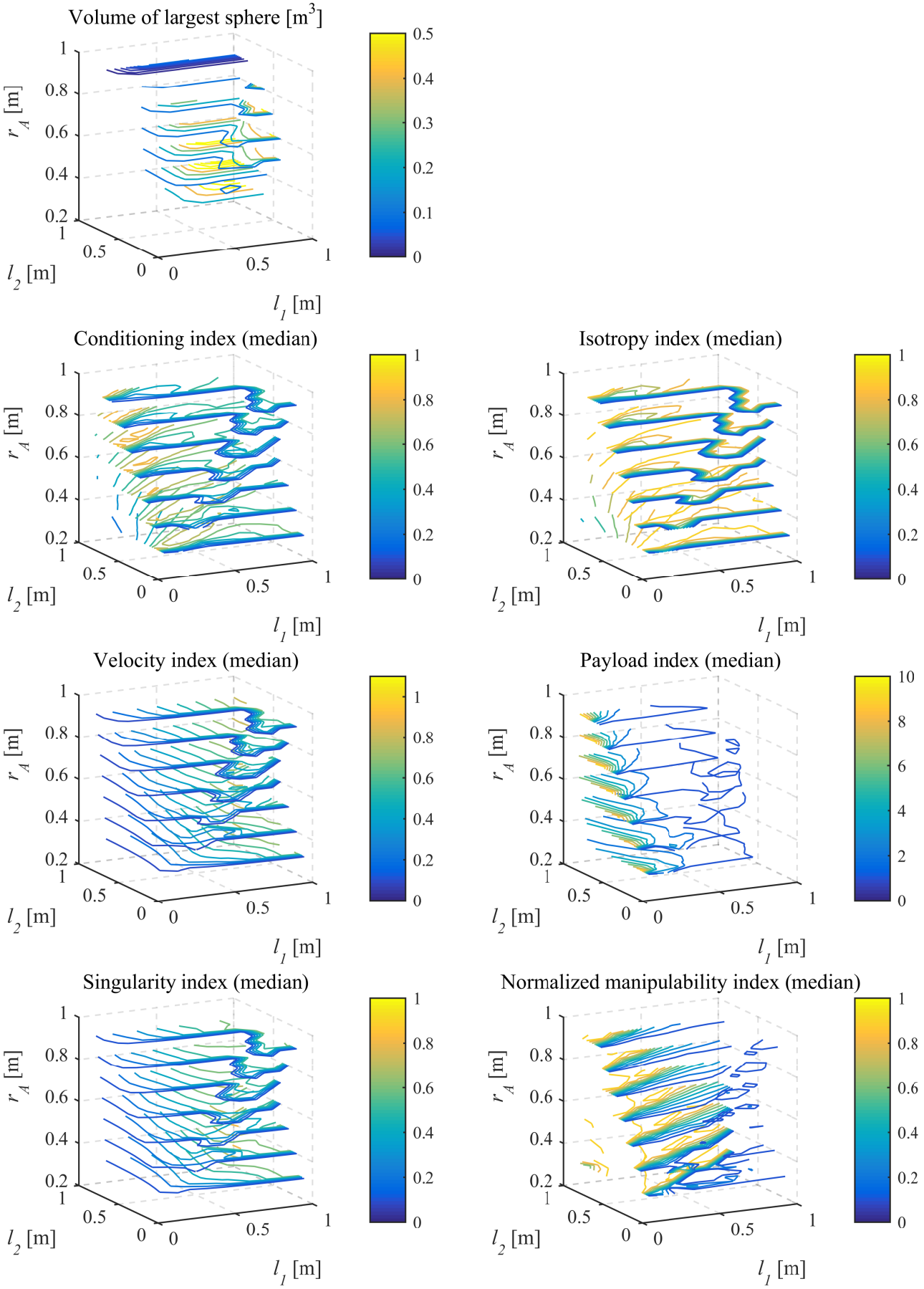

Fig. 29: $\underline{\mathrm{UUR}}^{\Delta}$ median values, $r_B = 0.3$ m

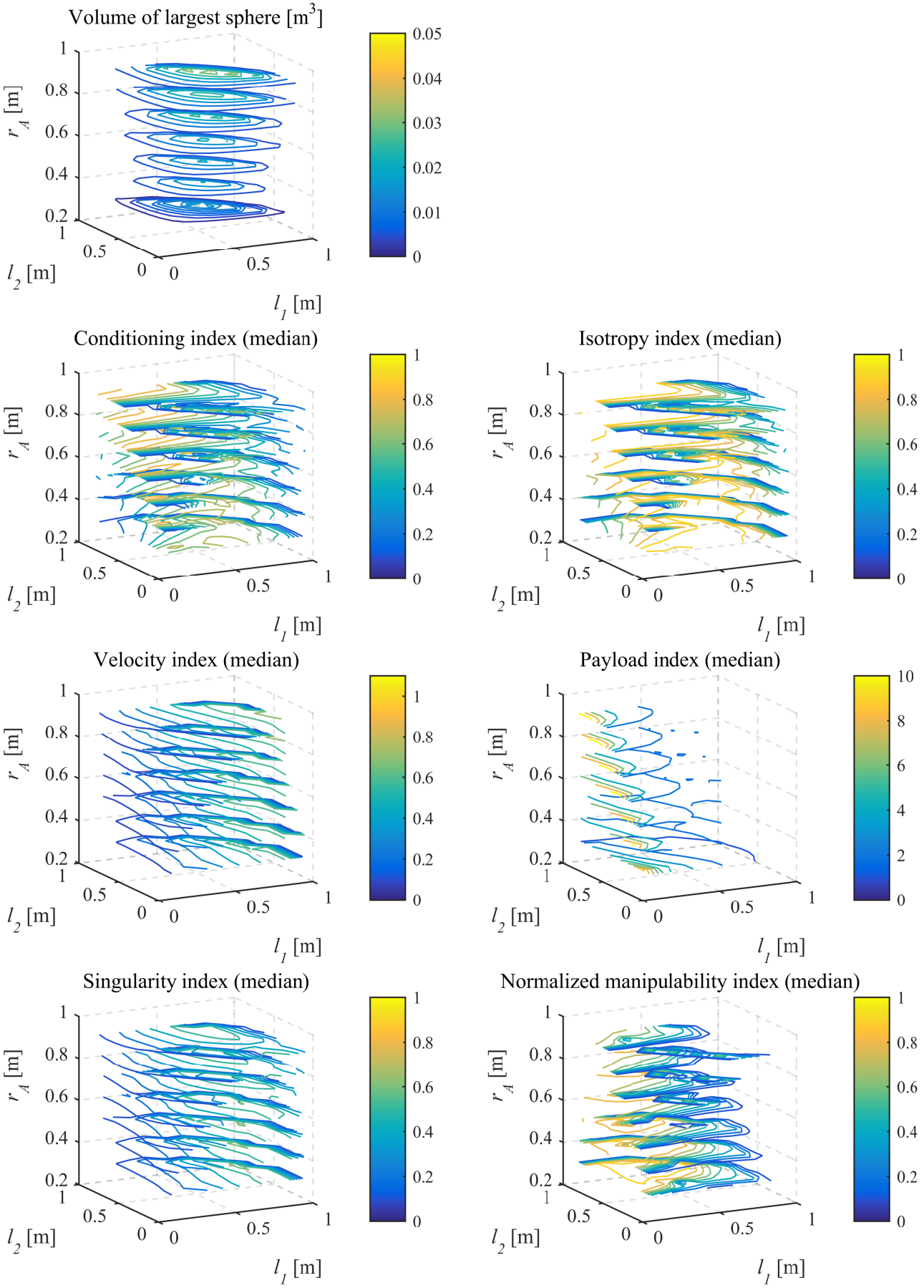

Fig. 30: $\underline{\mathrm{R}}\mathrm{UU}^{\Delta}$ median values, $r_B = 0.3$ m

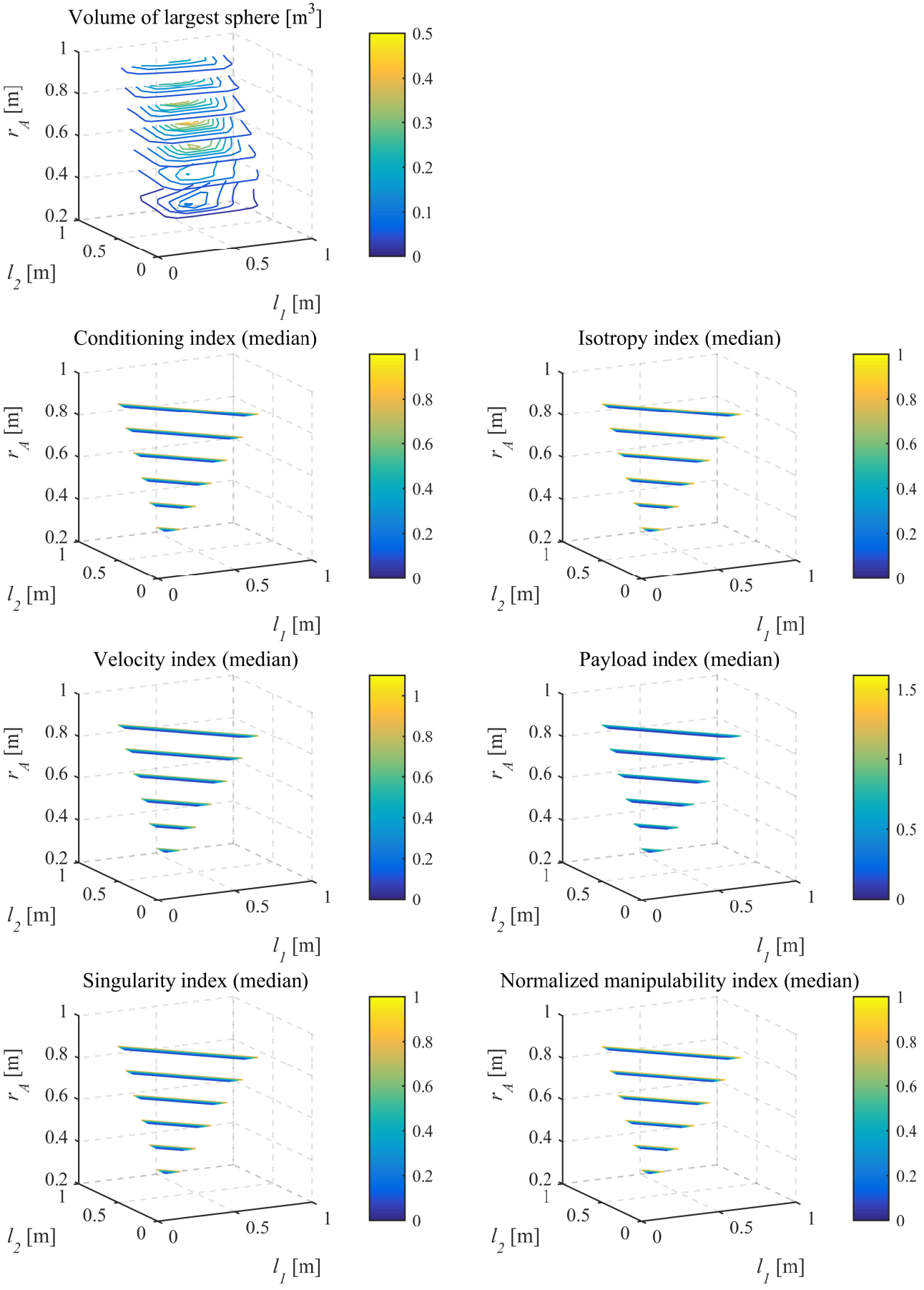

Fig. 31: $\underline{\mathrm{C}}\mathrm{RR}^{\Delta}$ median values, $r_B = 0.3$ m, $\delta = 30°$

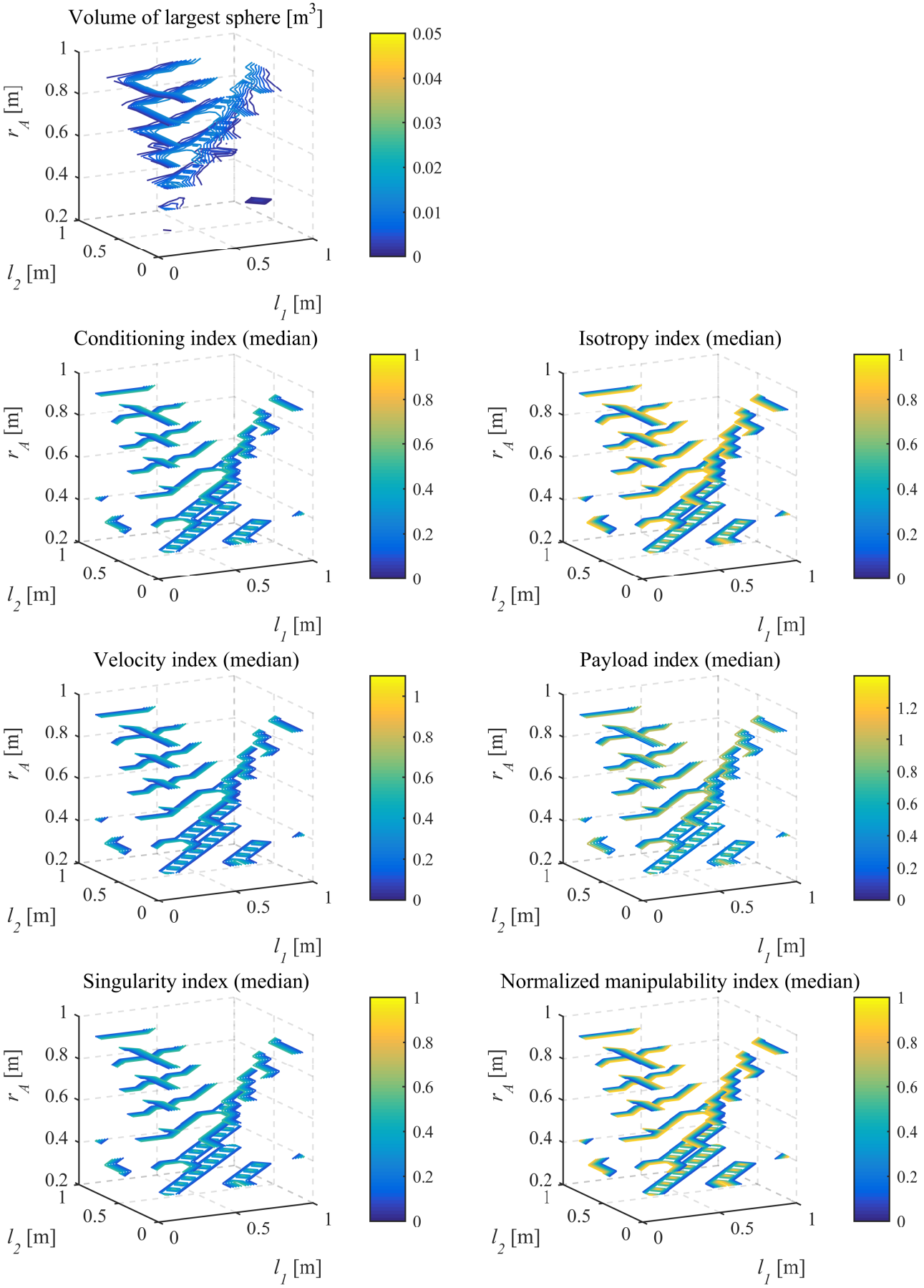

Fig. 32: $\underline{\mathrm{C}}\mathrm{RR}^{\|}$ median values, $r_B = 0.3$ m, $\delta = 50°$

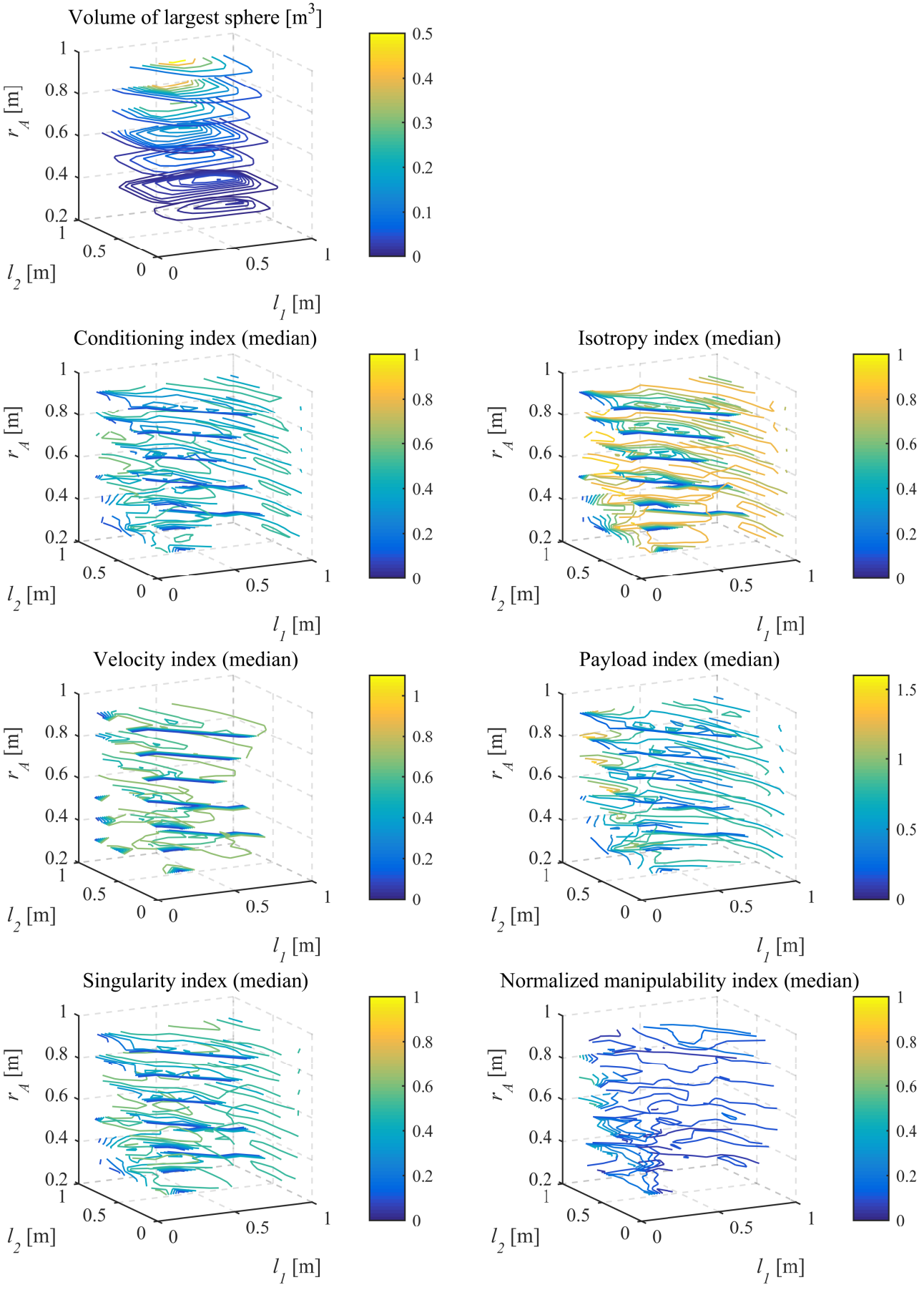

Fig. 33: $\underline{\mathrm{C}}\mathrm{UR}^{\Delta}$ median values, $r_B = 0.3$ m, $\delta = 50°$

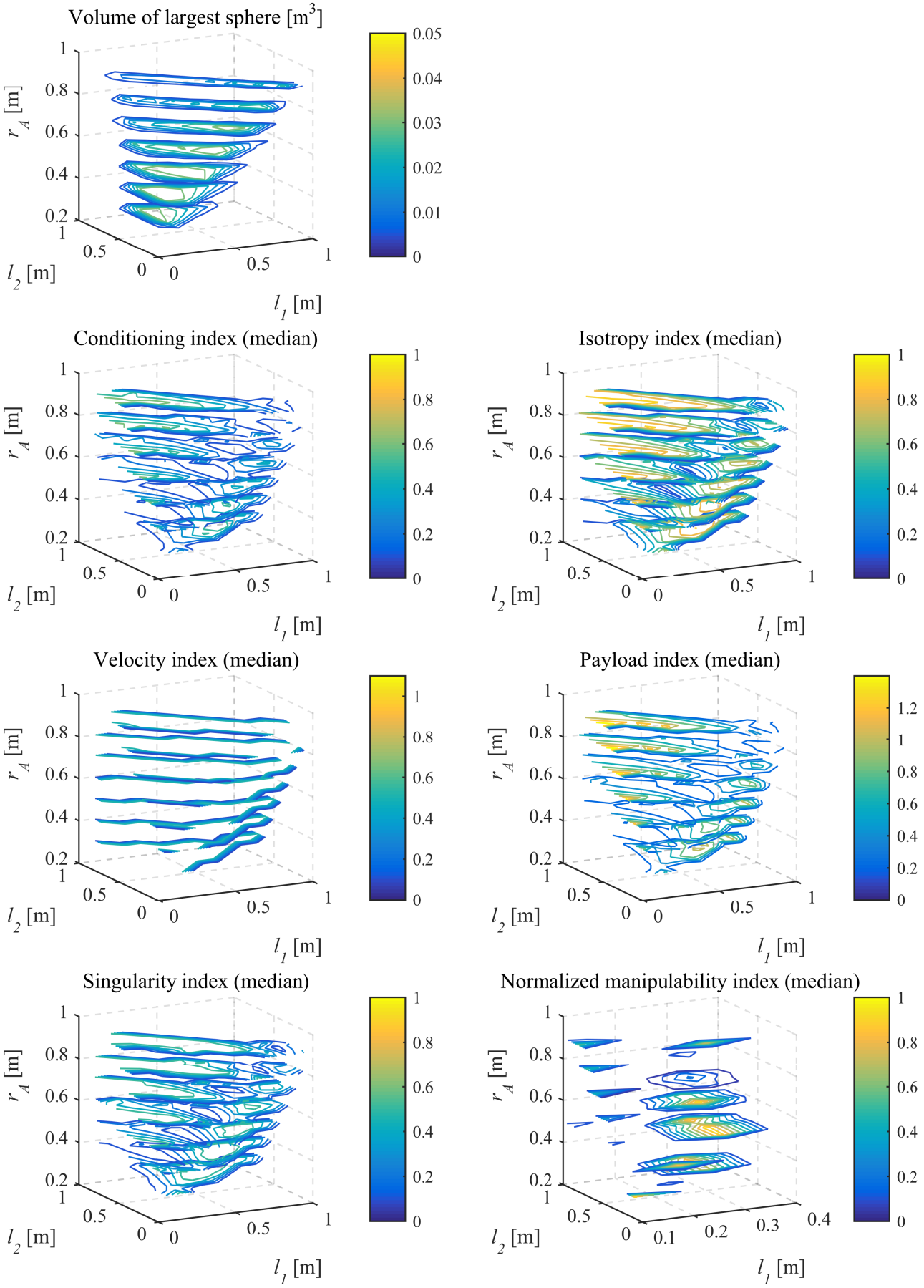

Fig. 34: $\underline{\mathrm{C}}\mathrm{UR}^{\|}$ median values, $r_B = 0.3$ m, $\delta = 50°$

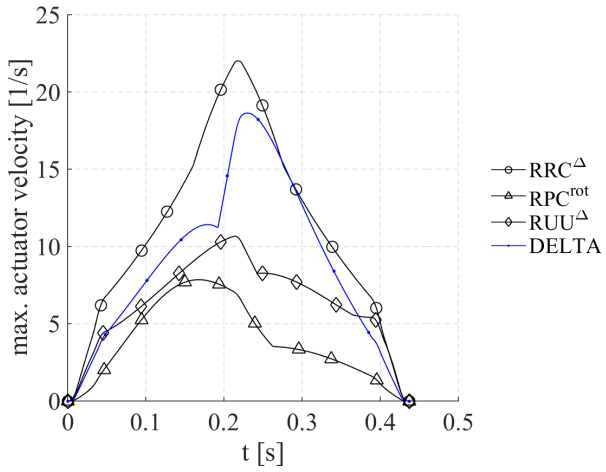

(a) Actuation angular velocities

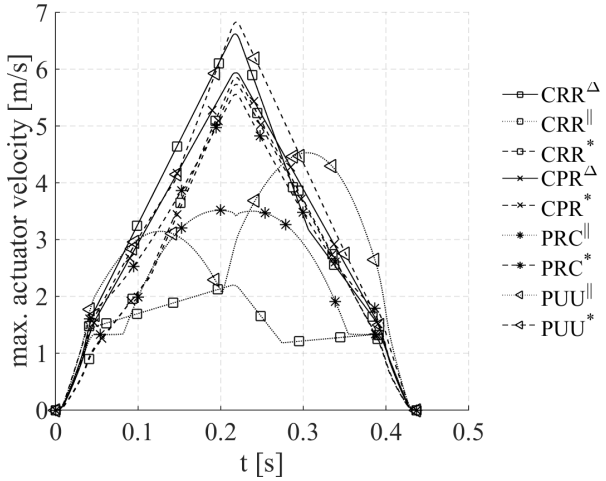

(b) Actuation linear velocities

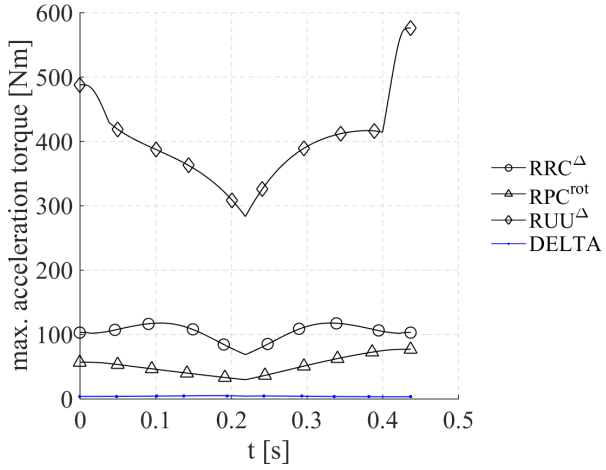

(c) Acceleration torques

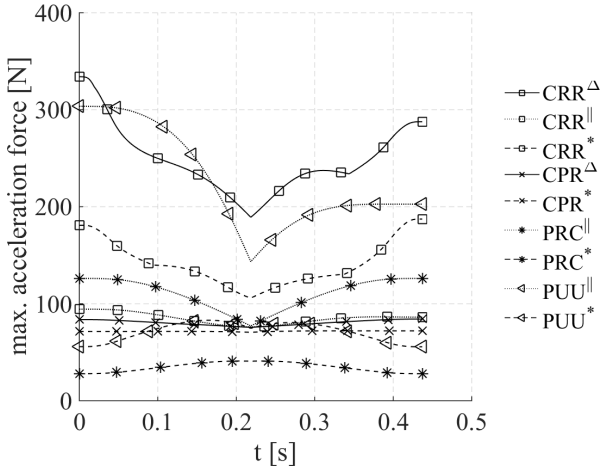

(d) Acceleration forces

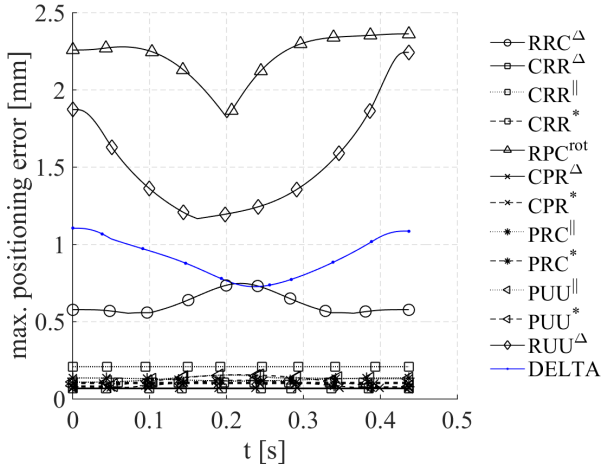

(e) Positioning error

Fig. 35: Results pick & place task (II)

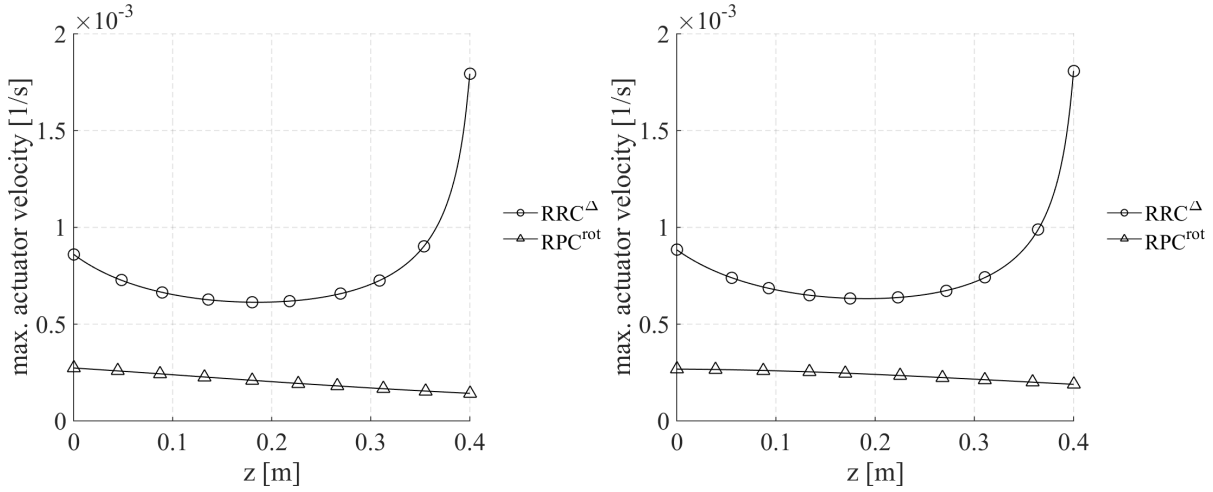

(a) Actuation angular velocities (pos 1)

(b) Actuation angular velocities (pos 2)

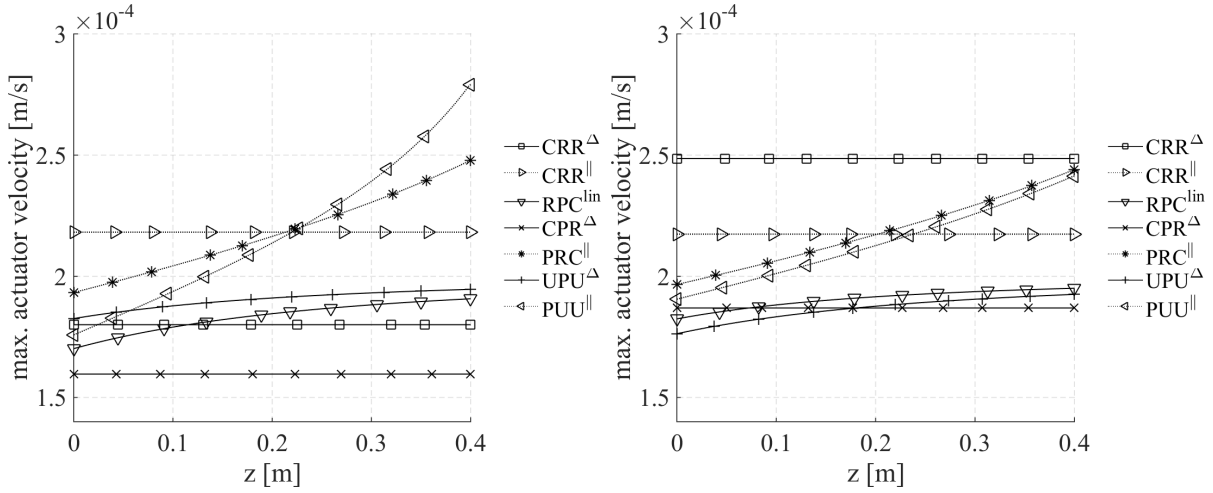

(c) Actuation linear velocities (pos 1)

(d) Actuation linear velocities (pos 2)

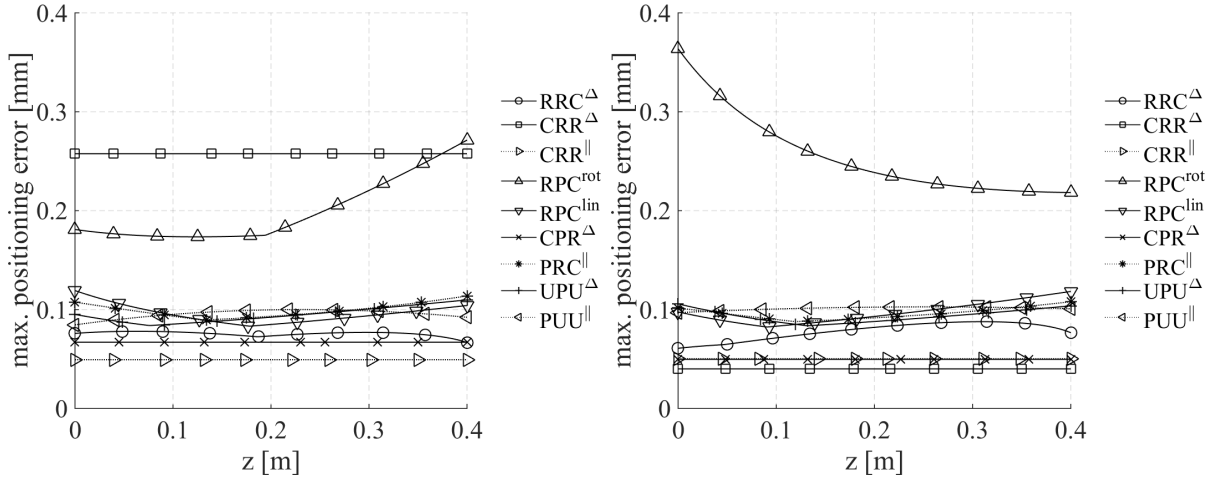

(e) Positioning error (pos 1)

(f) Positioning error (pos 2)

Fig. 36: Results positioning task (II)

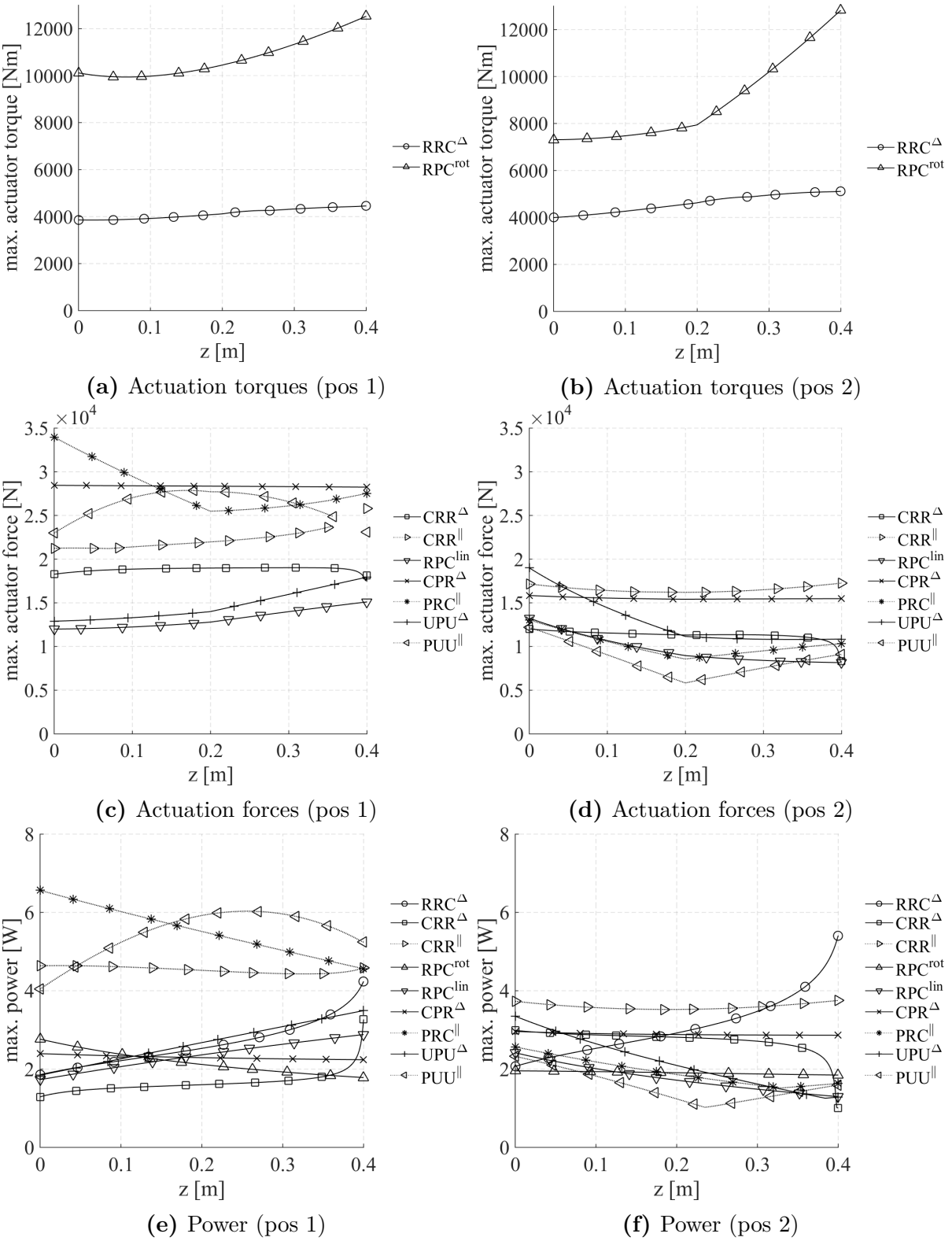

(a) Actuation torques (pos 1)

(b) Actuation torques (pos 2)

(c) Actuation forces (pos 1)

(d) Actuation forces (pos 2)

(e) Power (pos 1)

(f) Power (pos 2)

Fig. 37: Results positioning task (III)

Tables

Tab. 3: Geometrical conditions (GC) for joint arrangements according to [KG04c; KG07]

	Structure groups				
	3P	**3R-1P**	**2R-2P**	**5R**	**4R-1P**
GC within a limb	-	The axes of the revolute joints are parallel.		The axes of two or three revolute joints in a row are parallel, whereas the axes of the other revolute joints are parallel as well.	The axes of two successive revolute joints or two revolute joints with prismatic joint in between are parallel. The other revolute joint axes are parallel as well.
GC for PKS with three identical limbs	-	The axes of the revolute joints are not all parallel.		*Only for* $R_1R_1R_2R_2R_2$ and $R_1R_1R_1R_2R_2$: Three axes perpendicular to the revolute joint axes within a limb are not parallel to a plane.*	Three axes perpendicular to the revolute joint axes within a limb are not parallel to a plane.*
GC for PKS with three identical limbs and 1st joint actuated	Three axes perpendicular to the prismatic axes of the actuated joints within a limb are not parallel to a plane.	*Only for* $PR_1R_1R_1$: All axes of the revolute joints are not parallel to a plane.	*Only for* R_1R_1PP: Three axes perpendicular to the non actuated prismatic joints axes within a limb are not parallel to a plane.	*Only for* $R_1R_1R_2R_2R_2$: All revolute joint axes are not parallel to a plane.	-

* The normal vectors (vectors normal to the plane of the revolute joint axes) are linearly independent.

Tab. 4: Considered structures - rotational actuation

	Δ frame configuration	
R	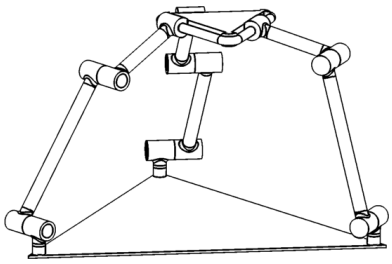 RRC	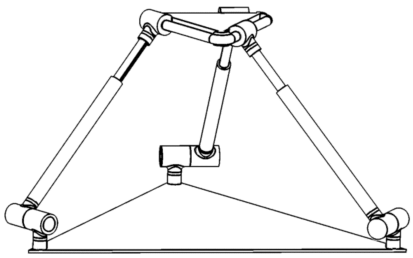 RPC
	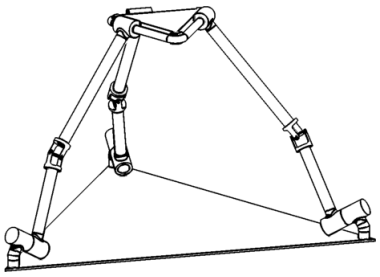 RUC	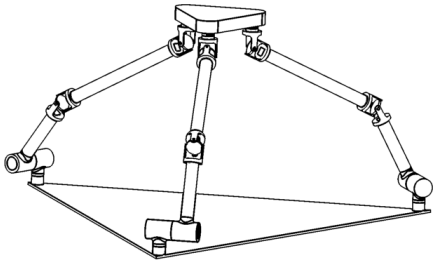 RUU
U	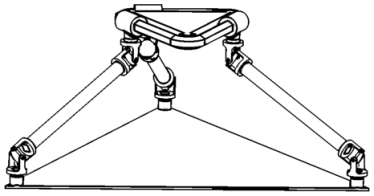 UUP	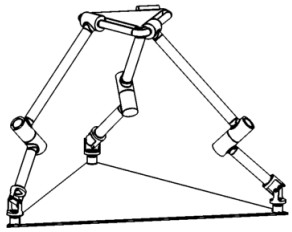 URC
	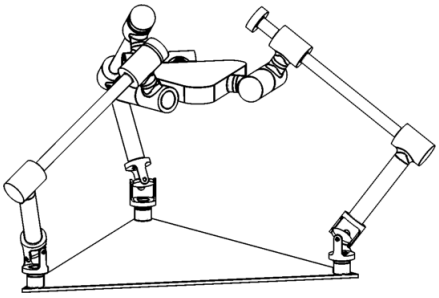 UCR	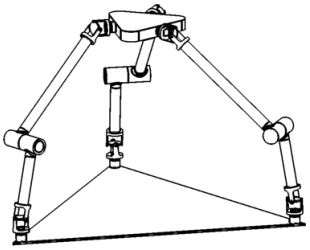 URU
	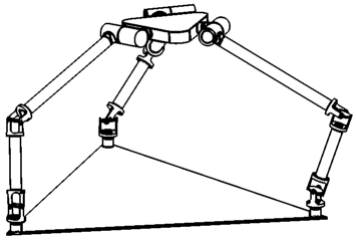 UUR	

Tab. 5: Considered structures - linear actuation (cylindrical joint)

		Frame configuration		
		Δ	$\parallel$	$\star$
C	CRR	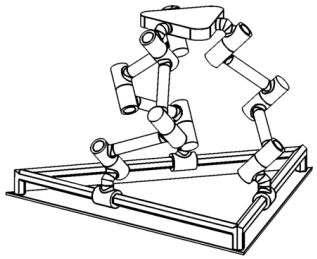	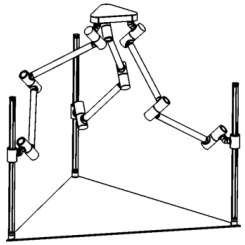	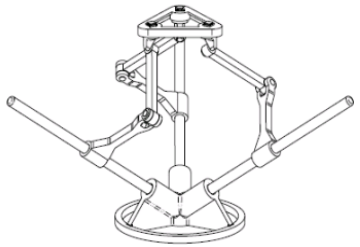
	CRU	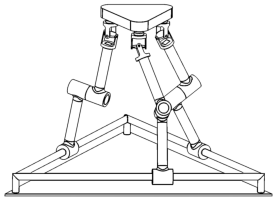	-	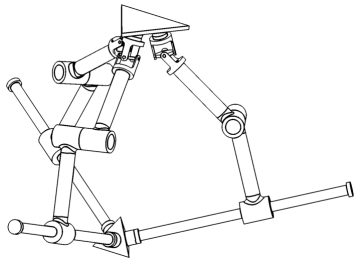
	CUR	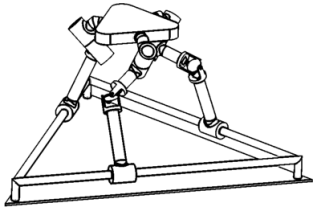	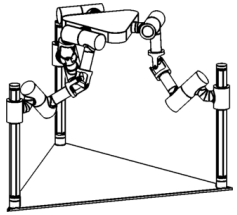	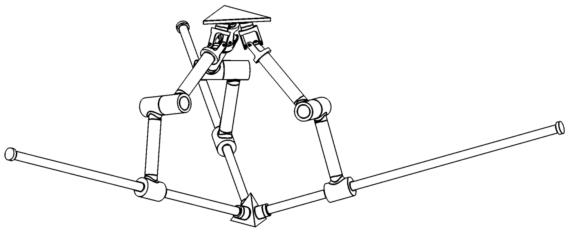
	CPR	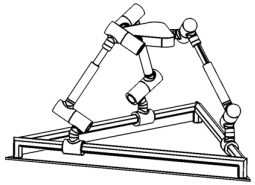	-	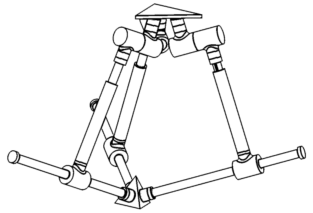

Tab. 6: Considered structures - linear actuation (prismatic joint)

		Frame configuration		
		Δ	$\parallel$	$\star$
P	RPC	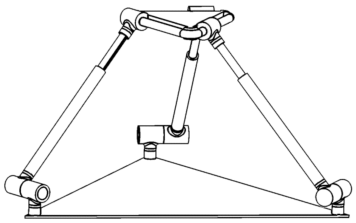	-	-
	UPU	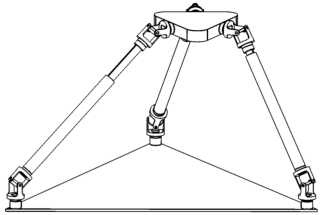	-	-
	PUU	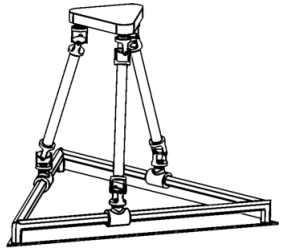	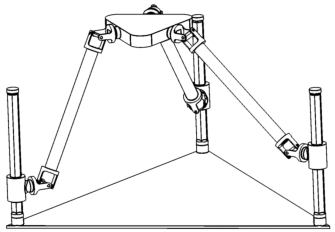	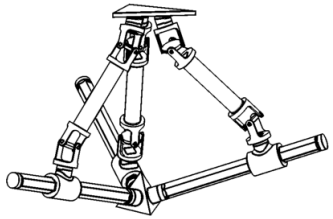
	PRC	-	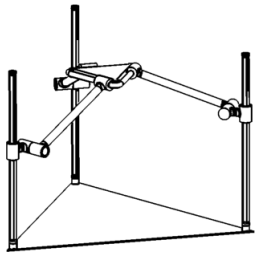	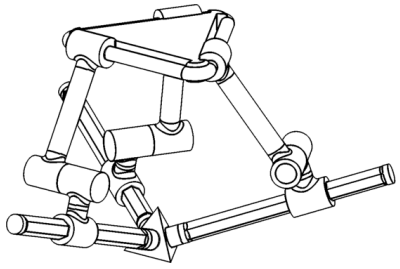

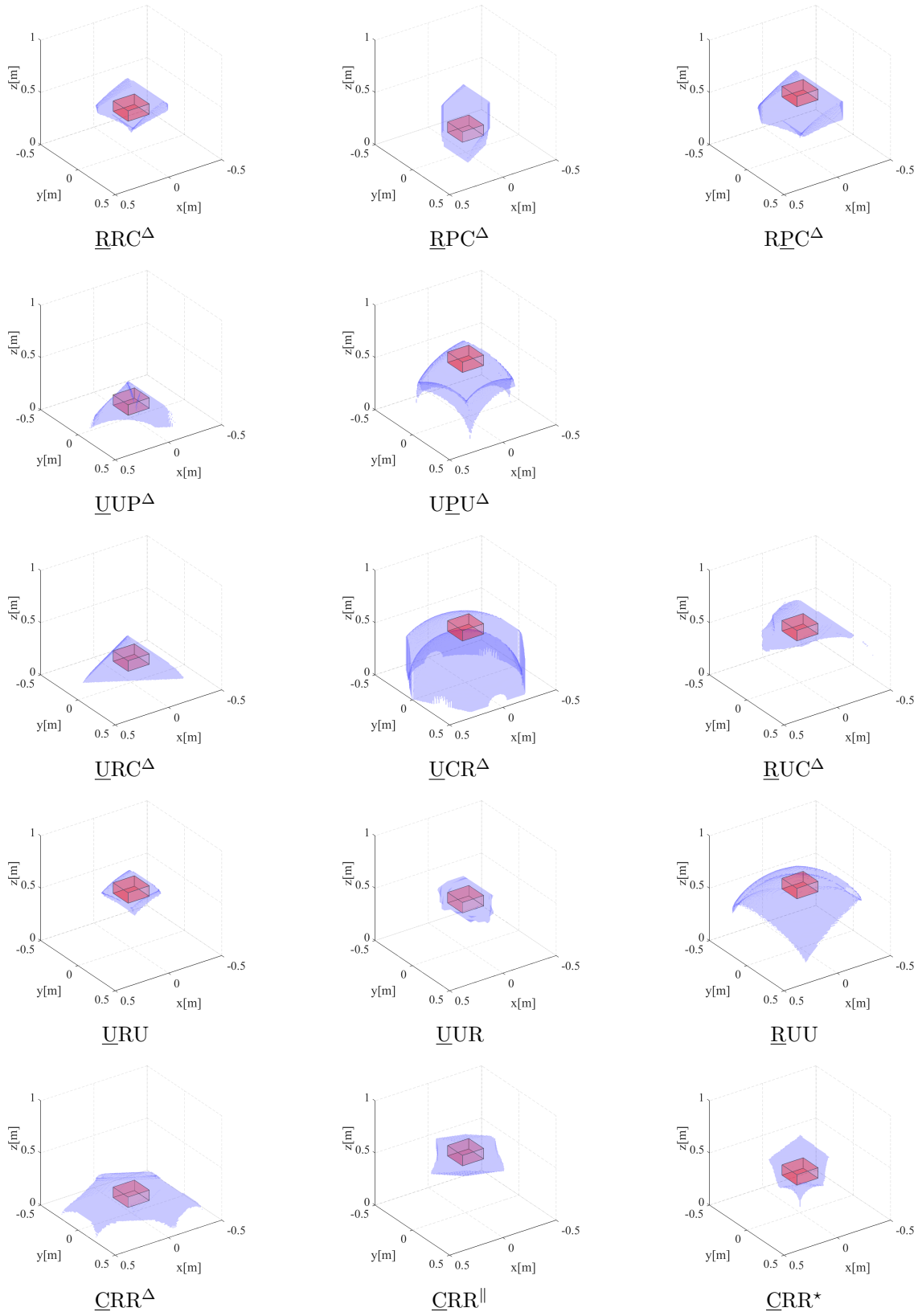

Tab. 7: Workspaces of the considered structures for case 1 optimization (I)

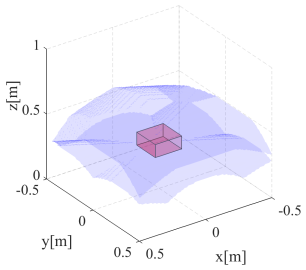

$\underline{\mathrm{C}}\mathrm{PR}^{\Delta}$

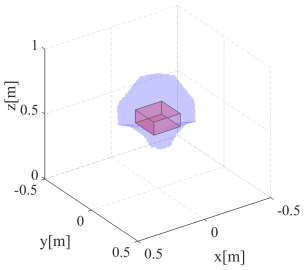

$\underline{\mathrm{C}}\mathrm{PR}^{\star}$

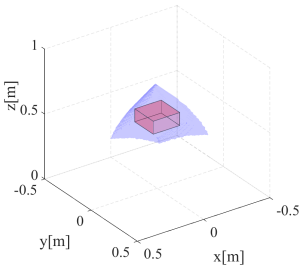

$\underline{\mathrm{P}}\mathrm{RC}^{\parallel}$

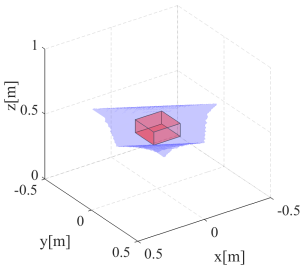

$\underline{\mathrm{P}}\mathrm{RC}^{\star}$

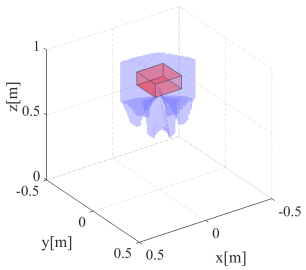

$\underline{\mathrm{C}}\mathrm{RU}^{\Delta}$

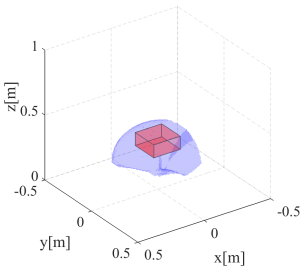

$\underline{\mathrm{C}}\mathrm{RU}^{\star}$

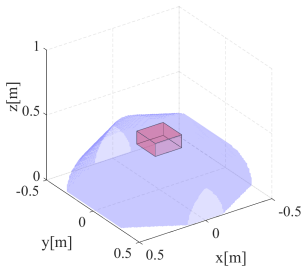

$\underline{\mathrm{P}}\mathrm{UU}^{\Delta}$

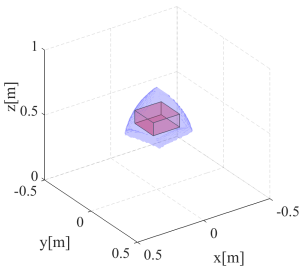

$\underline{\mathrm{P}}\mathrm{UU}^{\parallel}$

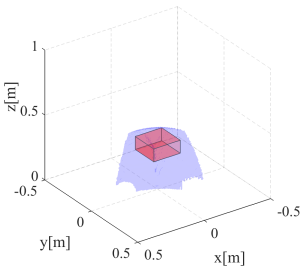

$\underline{\mathrm{P}}\mathrm{UU}^{\star}$

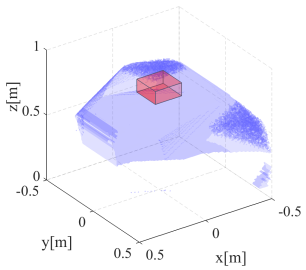

$\underline{\mathrm{C}}\mathrm{UR}^{\Delta}$

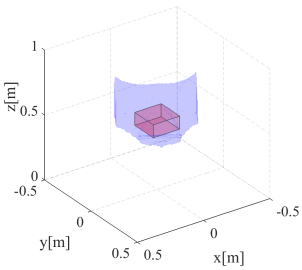

$\underline{\mathrm{C}}\mathrm{UR}^{\parallel}$

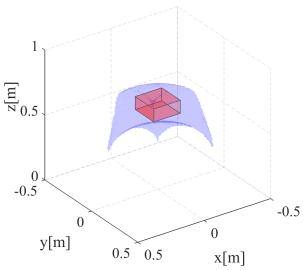

$\underline{\mathrm{C}}\mathrm{UR}^{\star}$

Tab. 8: Workspaces of the considered structures for case 1 optimization (II)

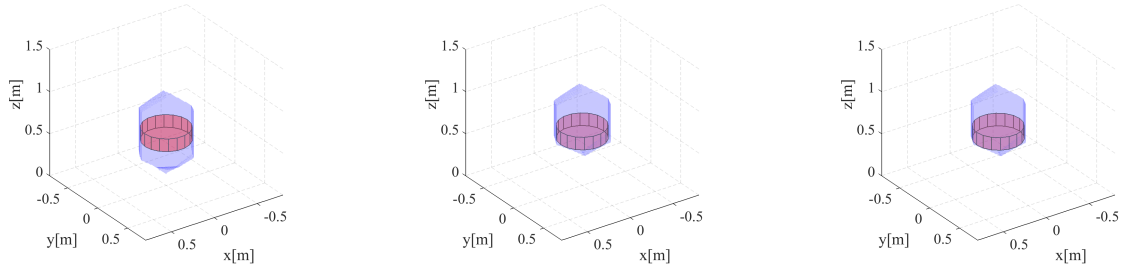

$\underline{\mathrm{R}}\mathrm{RC}^{\Delta}$ $\underline{\mathrm{R}}\mathrm{PC}^{\Delta}$ $\mathrm{R}\underline{\mathrm{P}}\mathrm{C}^{\Delta}$

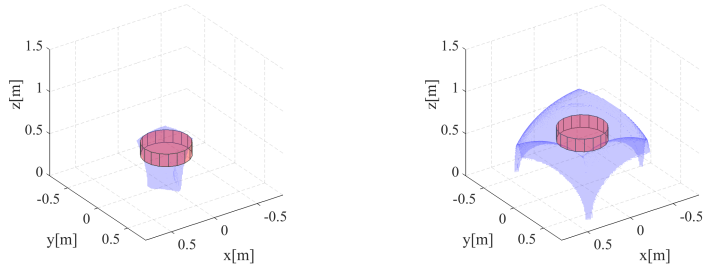

$\underline{\mathrm{U}}\mathrm{UP}^{\Delta}$ $\mathrm{U}\underline{\mathrm{P}}\mathrm{U}^{\Delta}$

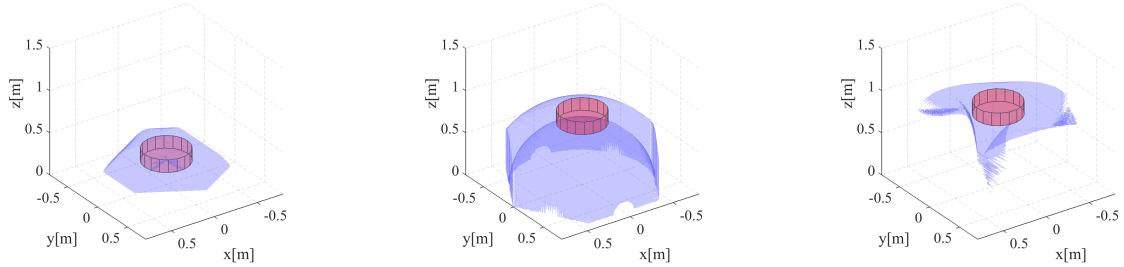

$\underline{\mathrm{U}}\mathrm{RC}^{\Delta}$ $\underline{\mathrm{U}}\mathrm{CR}^{\Delta}$ $\underline{\mathrm{R}}\mathrm{UC}^{\Delta}$

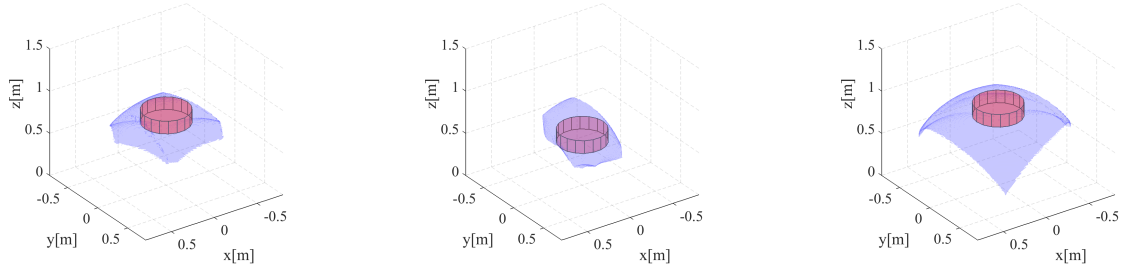

$\underline{\mathrm{U}}\mathrm{RU}$ $\underline{\mathrm{U}}\mathrm{UR}$ $\underline{\mathrm{R}}\mathrm{UU}$

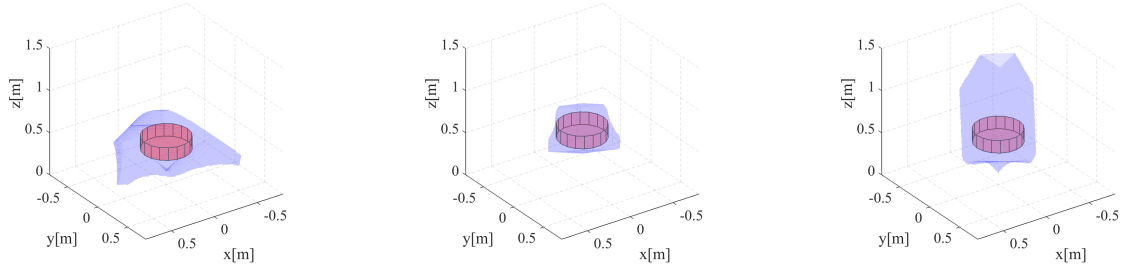

$\underline{\mathrm{C}}\mathrm{RR}^{\Delta}$ $\underline{\mathrm{C}}\mathrm{RR}^{\|}$ $\underline{\mathrm{C}}\mathrm{RR}^{\star}$

Tab. 9: Workspaces of the considered structures for case 2 optimization (I)

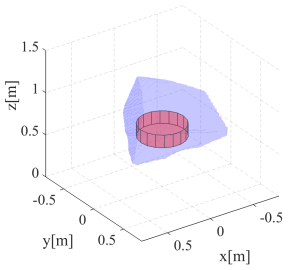

$\underline{\text{C}}\text{PR}^{\Delta}$

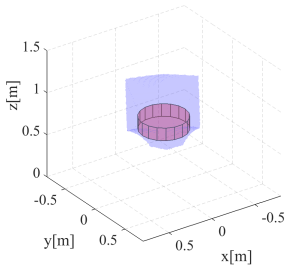

$\underline{\text{C}}\text{PR}^{\star}$

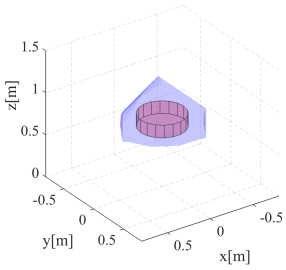

$\underline{\text{P}}\text{RC}^{\parallel}$

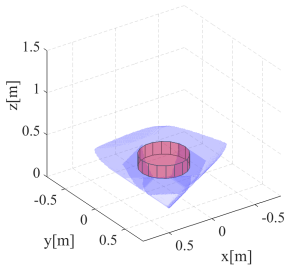

$\underline{\text{P}}\text{RC}^{\star}$

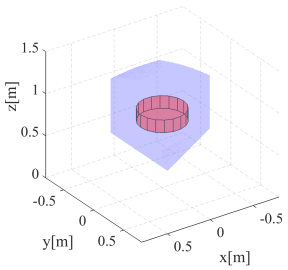

$\underline{\text{C}}\text{RU}^{\Delta}$

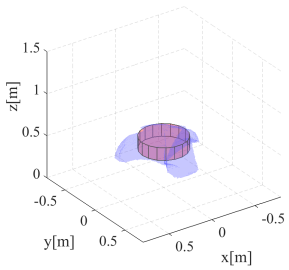

$\underline{\text{C}}\text{RU}^{\star}$

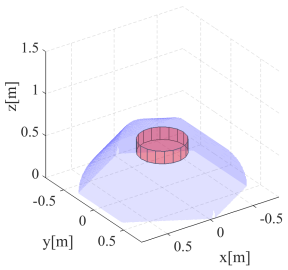

$\underline{\text{P}}\text{UU}^{\Delta}$

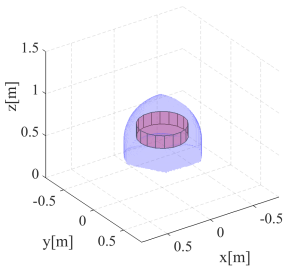

$\underline{\text{P}}\text{UU}^{\parallel}$

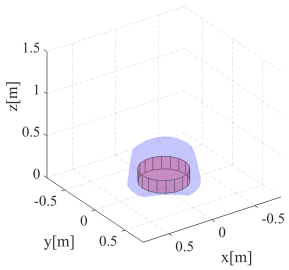

$\underline{\text{P}}\text{UU}^{\star}$

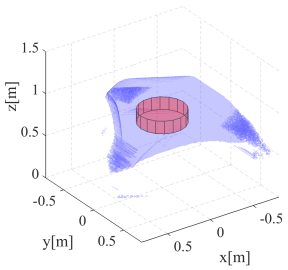

$\underline{\text{C}}\text{UR}^{\Delta}$

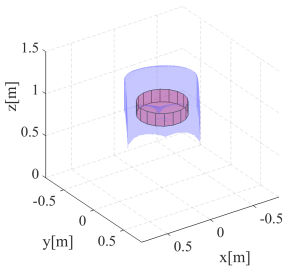

$\underline{\text{C}}\text{UR}^{\parallel}$

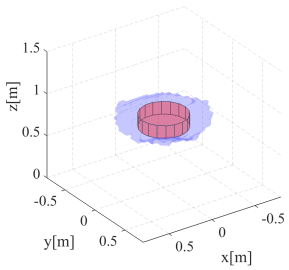

$\underline{\text{C}}\text{UR}^{\star}$

Tab. 10: Workspaces of the considered structures for case 2 optimization (II)

B&R, 8LSA55.EB030D000-1 mit 8GP60-070hh032klmm „Die Drehstrom-Synchronmotoren der Baureihe 8LS sind permanenterregte, elektronisch kommutierte Synchronmotoren für Applikationen mit hohen Anforderungen an Dynamik und Positioniergenauigkeit bei gleichzeitig geringem Bauvolumen und Gewicht. Diese Getriebe zeichnen sich durch ein sehr geringes Verdrehspiel gepaart mit einer hohen Verdrehsteifigkeit aus. Sie eignen sich insbesonders für den Einsatz in Handlingssystemen mit hohen Geschwindigkeiten und Beschleunigungen und Anwendungen in denen das optional erhältliche Verdrehspiel von <1 Winkelminute von Bedeutung ist.“
B&R, 8LTJC4.ee005ffgg-0 „Die Drehstrom-Synchronmotoren der Baureihe 8LT sind permanenterregte, elektronisch kommutierte Synchronmotoren für Applikationen mit hohen Anforderungen an Dynamik und Positioniergenauigkeit bei gleichzeitig geringem Bauvolumen und Gewicht.“
Nadella, Double-Line AXDL 240-Z „Starke Linearachse mit Zahnriemenantrieb und paralleler Kugelumlauf-Schienenführung oder Rollenführung mit Abdeckband (Standard).“
Nadella, Double-Line AXDL 160-S „Linearachse mit Kugelgewinde- oder Trapezgewindetrieb, mit paralleler Kugelumlauf-Schienenführung mit Abdeckband (Standard).“
Bosch Rexroth, EMC-40-16x16 „Für Elektromechanische Zylinder EMC bestehen vielfältige Einsatzmöglichkeiten. Auf Grund ihrer spezifischen Eigenschaften bieten sie Vorteile hinsichtlich der Genauigkeit, Dynamik und Regelbarkeit und können damit sowohl zur Verkürzung von Taktzeiten, als auch zur Erhöhung von Flexibilität und Qualität im Fertigungsprozess beitragen. Durch ihre kompakte Bauweise sind sie bestens für den Einsatz bei beschränkten Platzverhältnissen geeignet.“
RK Rose + Krieger, LZ 70 PL „Die Elektrozylinder LZ 70 überzeugen mit 100% Einschaltdauer und exzellenter Dynamik. Wahlweise mit Kugel- oder Trapezgewindespindel ausgestattet eignen sie sich damit für einfache Verstellarbeiten ebenso wie für hochpräzise Positionieraufgaben. In der PowerLine-Version LZ 70 PL schultert er hohe Druck-/Zuglasten bis 5.000 N mit einer Höchstgeschwindigkeit von 13 $\frac{mm}{s}$. Die FastLine-Variante LZ 70 FL bewegt leichtere Lasten bis zu 1000 $\frac{mm}{s}$.“

Tab. 11: Description of the selected components (provided by the respective manufacturer)

Mathematical descriptions of PKS

1 RRC

The RRC-PKS was first proposed by Tsai [Tsa97] in 1997. Two years later, Zhao et al. [Zha01] studied in detail this kind of parallel mechanism. Furthermore, the PKS is analyzed by [SLT09], but only with RRPa^{4R}R structure and in ∪-shaped frame configuration. Here, the sliding part of the C-joint is replaced by a parallelogram substructure. This substructure consists of four revolute joints whose axes are perpendicular to the other joint axes. Liu et al. [LZL10] analyzes the kinematics and dynamics of the RRC structure in ∪-shaped frame configuration.

But for this study, the RRC-PKS should be described without parallelogram substitution and in triangular frame configuration. Therefore, all joint axes ($\mathbf{w}_{ji}$, $\mathbf{s}_{0i}$) within one limb are parallel to each other (cf. Fig. 38a),

$$\mathbf{w}_{1i} = \mathbf{w}_{2i} = \mathbf{w}_{3i} = \mathbf{s}_{0i} = \mathbf{R}_{zi} \cdot \begin{pmatrix} 0 \\ 1 \\ 0 \end{pmatrix} = \mathbf{e}_{iy}.$$

The structure is proposed in [DHZ12] as an upper limb rehabilitation robot. In the mentioned paper the authors derive the forward and inverse kinematic solutions and perform a workspace analysis. Simulation results show that the PKS has a relatively large workspace.

[Dan13; Deo14] summarize the calculation steps for the inverse kinematic problem and the Jacobian matrix.

Inverse dynamics

First, the motion state of all components should be known. The actuator velocities can be calculated by using the Jacobian matrix. The linear velocity of the cylindrical joint is:

$$\dot{s}_i = \mathbf{w}_{1i}^T \dot{\mathbf{p}}, \tag{1}$$

and the angular velocity of link 2 is:

$$\omega_{2i} = \frac{\frac{1}{l_2}\mathbf{l}_{10i}^T\dot{\mathbf{p}}}{\mathbf{l}_{10i}^T(\mathbf{w}_{1i} \times \mathbf{l}_{20i})}. \tag{2}$$

To calculate the accelerations, the vector loop equation (cf. [Dan13; Deo14]) is derivated twice:

$$\ddot{\mathbf{p}} = l_1\left((\boldsymbol{\omega}_{1i} \times (\boldsymbol{\omega}_{1i} \times \mathbf{l}_{10i})) + \dot{\boldsymbol{\omega}}_{1i} \times \mathbf{l}_{10i}\right) + l_2\left((\boldsymbol{\omega}_{2i} \times (\boldsymbol{\omega}_{2i} \times \mathbf{l}_{20i})) + \dot{\boldsymbol{\omega}}_{2i} \times \mathbf{l}_{20i}\right) + \ddot{s}_i\mathbf{s}_{i0}. \tag{3}$$

Dot-multiplying Eq. (3) with $\mathbf{l}_{20i}^T$ yields:

$$\dot{\omega}_{1i} = \frac{\frac{1}{l_1}\left(\mathbf{l}_{20i}^T\ddot{\mathbf{p}} + l_2\boldsymbol{\omega}_{20i}^T\boldsymbol{\omega}_{20i}\right) + \left(\boldsymbol{\omega}_{10i}^T\boldsymbol{\omega}_{10i}\right) \cdot \mathbf{l}_{20i}^T\mathbf{l}_{10i}}{\mathbf{l}_{20i}^T\left(\mathbf{w}_{1i} \times \mathbf{l}_{10i}\right)}, \tag{4}$$

and dot-multiplying Eq. (3) with $\mathbf{l}_{10i}^T$ results in the angular acceleration of link 2:

$$\dot{\omega}_{2i} = \frac{\frac{1}{l_2}\left(\mathbf{l}_{10i}^T\ddot{\mathbf{p}} + l_1\boldsymbol{\omega}_{10i}^T\boldsymbol{\omega}_{10i}\right) + \left(\boldsymbol{\omega}_{20i}^T\boldsymbol{\omega}_{20i}\right) \cdot \mathbf{l}_{10i}^T\mathbf{l}_{20i}}{\mathbf{l}_{10i}^T\left(\mathbf{w}_{2i} \times \mathbf{l}_{20i}\right)}. \tag{5}$$

Similar to Eq. (1), the linear acceleration of the cylindrical joint is:

$$\ddot{s}_i = \mathbf{w}_{1i}^T\ddot{\mathbf{p}}. \tag{6}$$

Finally, the accelerations of the centers of gravity of both links can be calculated:

$$\mathbf{a}_{1i} = \dot{\boldsymbol{\omega}}_{1i} \times \frac{l_1}{2}\mathbf{l}_{10i} + \boldsymbol{\omega}_{1i} \times \left(\boldsymbol{\omega}_{1i} \times \frac{l_1}{2}\mathbf{l}_{10i}\right), \tag{7}$$

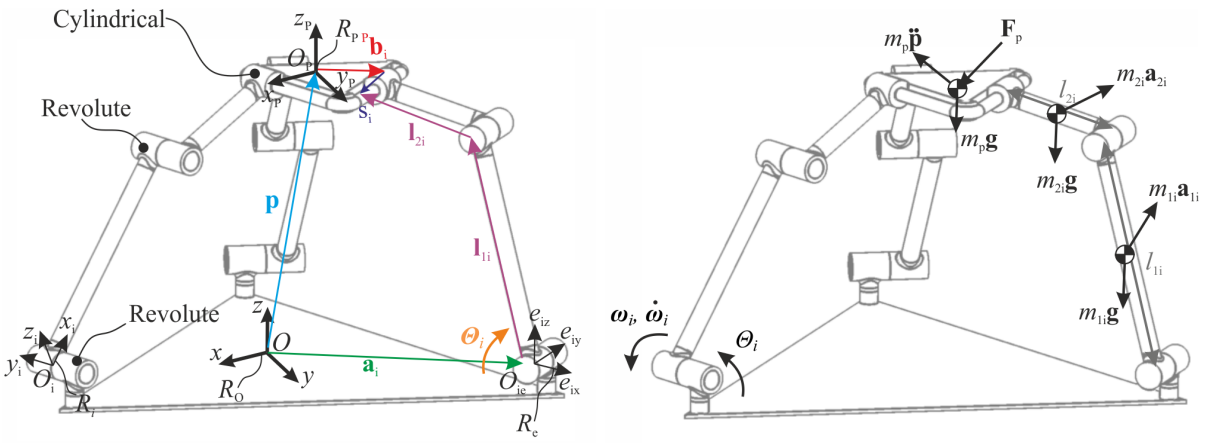

(a) Vector loop **(b)** Dynamic forces

Fig. 38: Vector loop and inertia properties of RRC-PKS

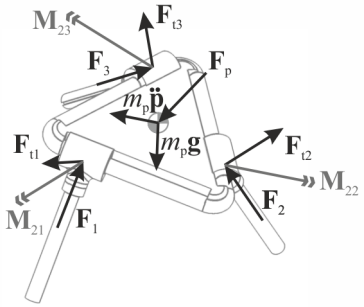

Fig. 39: Static equilibrium of forces at the end-effector of RRC-PKS

$$\mathbf{a}_{2i} = 2\mathbf{a}_{1i} + \dot{\boldsymbol{\omega}}_{2i} \times \frac{l_2}{2}\mathbf{l}_{20i} + \boldsymbol{\omega}_{2i} \times \left(\boldsymbol{\omega}_{2i} \times \frac{l_2}{2}\mathbf{l}_{20i}\right). \tag{8}$$

Because of the cylindrical joint at the end-effector (no moment transmission through joint axis), the axes of moment transmission at the end-effector joints are as follows:

$$\mathbf{n}_{2i} = \frac{\mathbf{l}_{20i} + \mathbf{l}_{20i} \times \mathbf{w}_{1i}}{|\mathbf{l}_{20i} + \mathbf{l}_{20i} \times \mathbf{w}_{1i}|}. \tag{9}$$

To calculated the necessary actuator torques based on inertia and acceleration properties, first, the force F_{ti} (cf. Fig. 39) perpendicular to link 2 and the cylindrical joint axis is calculated. It is derived from the static equilibrium of moments about the revolute joint axis of revolute joint 2 connecting link 1 and link 2 of each limb:

$$F_{ti} = \frac{\mathbf{w}_{1i}^T \left(\frac{l_2}{2}\mathbf{l}_{20i} \times m_{2i}\left(\mathbf{a}_{2i} - \mathbf{g}\right) + \mathbf{I}_{2,tot}\dot{\boldsymbol{\omega}}_{2i} + \boldsymbol{\omega}_{2i} \times \left(\mathbf{I}_{2,tot}\boldsymbol{\omega}_{2i}\right)\right)}{\mathbf{w}_{1i}^T\left(\left(\mathbf{w}_{1i} \times \mathbf{l}_{20i}\right) \times l_2\mathbf{l}_{20i}\right)}. \tag{10}$$

Consequently, the force vector is:

$$\mathbf{F}_{ti} = F_{ti}\left(\mathbf{w}_{1i} \times \mathbf{l}_{20i}\right), \tag{11}$$

and the resulting moment about the origin O_p of R_p is:

$$\mathbf{M}_{ti} = \mathbf{F}_{ti} \times \left(\mathbf{b}_i + s_i\mathbf{s}_{i0}\right). \tag{12}$$

Finally, all known forces and moments acting on the end-effector can be summarized in one vector:

$$\mathbf{F}_{ext} = \begin{pmatrix} m_p\mathbf{g} - m_p\ddot{\mathbf{p}} + \mathbf{F}_p + \sum\limits_{i=1}^{3}\mathbf{F}_{ti} \\ \sum\limits_{i=1}^{3}\mathbf{M}_{ti} \end{pmatrix}. \tag{13}$$

According to Eq. (6.7), the vector of internal forces is:

$$\mathbf{F}_{int} = \begin{pmatrix} F_1 & F_2 & F_3 & M_{21} & M_{22} & M_{23} \end{pmatrix}^T, \tag{14}$$

and the Jacobian of force transmission based on the static equilibrium of forces and moments at the end-effector is:

$$\mathbf{J}_p = \begin{pmatrix} \mathbf{l}_{201} & \mathbf{l}_{202} & \mathbf{l}_{203} & \mathbf{0} & \mathbf{0} & \mathbf{0} \\ (\mathbf{b}_1 + s_1\mathbf{s}_{01}) \times \mathbf{l}_{201} & (\mathbf{b}_2 + s_2\mathbf{s}_{02}) \times \mathbf{l}_{202} & (\mathbf{b}_3 + s_3\mathbf{s}_{03}) \times \mathbf{l}_{203} & \mathbf{n}_{21} & \mathbf{n}_{22} & \mathbf{n}_{23} \end{pmatrix}. \tag{15}$$

With the calculated internal forces the internal force vector acting on the second revolute joint of each limb can be calculated:

$$\mathbf{F}_{oi} = m_{2i}\left(\mathbf{a}_{2i} - \mathbf{g}\right) + \mathbf{F}_{ti} - F_i\mathbf{l}_{20i}. \tag{16}$$

Finally, the static equilibrium of moments about the first revolute joints of each limb gives the necessary actuator torques:

$$\tau_{q,i} = \mathbf{w}_{1i}\left(\mathbf{F}_{oi} \times l_1\mathbf{l}_{10i} - \frac{l_1}{2}\mathbf{l}_{10i} \times m_{1i}\left(\mathbf{a}_{1i} - \mathbf{g}\right) - \mathbf{I}_{1tot,i}\dot{\boldsymbol{\omega}}_{1i} - \boldsymbol{\omega}_{1i} \times \left(\mathbf{I}_{1tot,i}\boldsymbol{\omega}_{1i}\right)\right). \tag{17}$$

2 CRR

2.1 Δ configuration

To comply with the geometrical conditions summarized in Tab. 3, p. 220 in case of CRR$^{\Delta}$ and CRR$^{\parallel}$, the cylindrical joint is reduced to a prismatic and revolute joint whose axes are not coincident (Fig. 40):

$$\mathbf{w}_{1i} = \mathbf{w}_{2i} = \mathbf{w}_{3i} = \mathbf{R}_{zi} \cdot \mathbf{R}_{xi} \cdot \begin{pmatrix} 0 \\ 1 \\ 0 \end{pmatrix}; \qquad \mathbf{s}_{0i} = \mathbf{R}_{zi} \cdot \begin{pmatrix} 0 \\ 1 \\ 0 \end{pmatrix}.$$

Here, instead of ψ, the inclination angle δ is used within $\mathbf{R}_{xi}$.

Inverse kinematics

Based on the vector loop equation,

$$\mathbf{p} = \mathbf{a}_i + s_i\mathbf{s}_{0i} + l_1\mathbf{l}_{10i} + l_2\mathbf{l}_{20i} - \mathbf{b}_i, \tag{18}$$

the known components are replaced by

$$\mathbf{g}_i = \mathbf{p} + \mathbf{b}_i - \mathbf{a}_i. \tag{19}$$

Dot-multiplying Eq. (18) with $\mathbf{w}_{1i}^T$ leads to the stroke length of the first joint:

$$s_i = \frac{\mathbf{w}_{1i}^T \mathbf{g}_i}{\mathbf{w}_{1i}^T \mathbf{s}_{0i}}. \tag{20}$$

To calculate the link vectors a new help vector is defined:

$$\mathbf{h}_i = \mathbf{p} + \mathbf{b}_i - \mathbf{a}_i - s_i \mathbf{s}_{0i}. \tag{21}$$

Vector $\mathbf{h}_i$ is transferred to the limb-side reference frame R_e (cf. Fig. 40a):

$${}^e\mathbf{h}_i = \mathbf{R}_{zi}^{-1} \cdot \mathbf{R}_{xi}^{-1} \cdot \mathbf{h}_i. \tag{22}$$

The angle between link 1 (vector ${}^e\mathbf{l}_{10}$) and vector ${}^e\mathbf{h}$ is calculated using the cosine-theorem:

$$\phi_{1i} = arccos\left(\frac{l_2^2 - l_1^2 - \|{}^e\mathbf{h}_i\|}{-2l_1\|{}^e\mathbf{h}_i\|}\right). \tag{23}$$

The angle between the z-axis of the limb-side reference frame and the vector ${}^e\mathbf{h}$ reads as

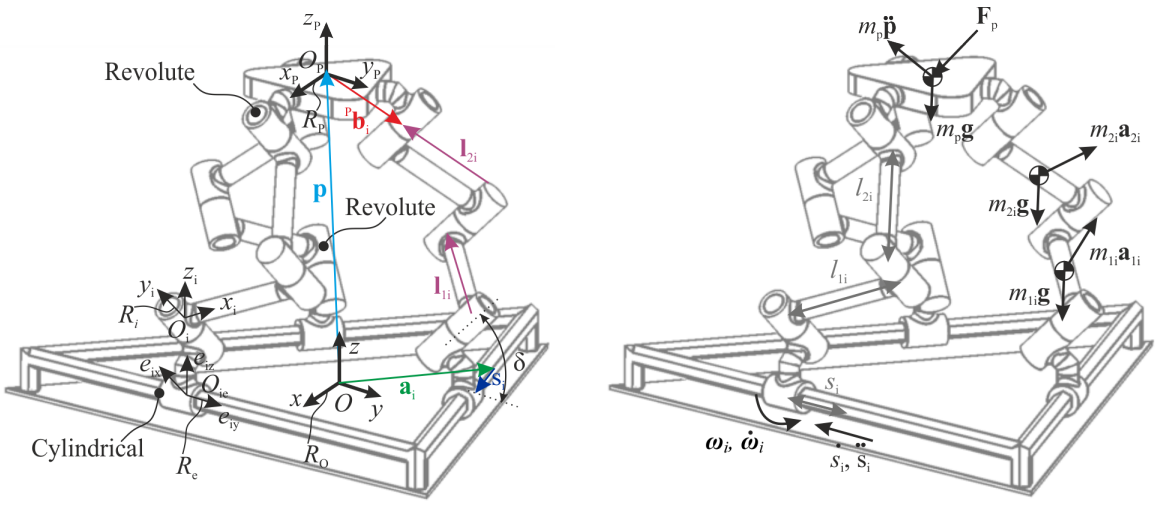

(a) Vector loop **(b)** Dynamic forces

Fig. 40: Vector loop and inertia properties of CRR$^{\Delta}$-PKS

follows:

$$\phi_{2i} = arccos\left(\frac{{}^{e}\mathbf{h}_i \cdot \begin{pmatrix}0 & 0 & 1\end{pmatrix}^T}{\|{}^{e}\mathbf{h}_i\|}\right). \tag{24}$$

A x-component of the help vector ${}^{e}\mathbf{h}$ smaller than 0 results in the link vector ${}^{e}\mathbf{l}_{10}$:

$${}^{e}\mathbf{l}_{10} = \begin{pmatrix}-\sin(\phi_{1i} + \phi_{2i}) \\ 0 \\ \cos(\phi_{1i} + \phi_{2i})\end{pmatrix}, \tag{25}$$

in all other cases it is

$${}^{e}\mathbf{l}_{10} = \begin{pmatrix}-\sin(\phi_{1i} - \phi_{2i}) \\ 0 \\ \cos(\phi_{1i} - \phi_{2i})\end{pmatrix}. \tag{26}$$

Finally, the link vector can be transferred to the global reference frame R_0:

$$\mathbf{l}_{10} = \mathbf{R}_{zi} \cdot \mathbf{R}_{xi} \cdot^{c} \mathbf{l}_{10}. \tag{27}$$

$\mathbf{l}_{20}$ follows using Eq. (18).

Jacobian matrix

Time derivating Eq. (18) and dot-multiplying with $\mathbf{w}_{1i}^T$ leads to the linear velocity of the first joint:

$$\dot{s}_i = \frac{\mathbf{w}_{1i}^T}{\mathbf{w}_{1i}^T \mathbf{s}_{0i}} \cdot \dot{\mathbf{p}} = \mathbf{J}_{(i,:)} \cdot \dot{\mathbf{p}}. \tag{28}$$

Finally, the Jacobian can be written as follows:

$$\dot{\mathbf{q}} = \dot{\boldsymbol{s}} = \begin{pmatrix}\mathbf{J}_{(1,:)} \\ \mathbf{J}_{(2,:)} \\ \mathbf{J}_{(3,:)}\end{pmatrix} \cdot \dot{\mathbf{p}}. \tag{29}$$

Inverse dynamics

Since the cylindrical joint is divided into a revolute and prismatic joint whose motion axes are not parallel to each other, the derivation of the inverse dynamics is slightly different

compared to CRR*.

The angular velocity of link 1 is:

$$\omega_{1i} = \frac{\frac{1}{l_1}\left(\mathbf{l}_{20i}^T\dot{\mathbf{p}} - \dot{s}_i\mathbf{l}_{20i}^T\mathbf{s}_{0i}\right)}{\mathbf{l}_{20i}^T(\mathbf{w}_{1i}\times\mathbf{l}_{10i})}, \tag{30}$$

and the angular velocity of link 2 is:

$$\omega_{2i} = \frac{\frac{1}{l_2}\left(\mathbf{l}_{10i}^T\dot{\mathbf{p}} - \dot{s}_i\mathbf{l}_{10i}^T\mathbf{s}_{0i}\right)}{\mathbf{l}_{10i}^T(\mathbf{w}_{1i}\times\mathbf{l}_{20i})}. \tag{31}$$

The linear acceleration of the reduced cylindrical joint is calculated as follows:

$$\ddot{s}_i = \frac{\mathbf{w}_{1i}^T\ddot{\mathbf{p}}}{\mathbf{w}_{1i}^T\mathbf{s}_{0i}}. \tag{32}$$

By dot-multiplying Eq. (18) with $\mathbf{l}_{20i}^T$ the angular acceleration of link 1 is calculated:

$$\dot{\omega}_{1i} = \frac{\frac{1}{l_1}\left(\mathbf{l}_{20i}^T\ddot{\mathbf{p}} + l_2\boldsymbol{\omega}_{20i}^T\boldsymbol{\omega}_{20i} - \ddot{s}_i\mathbf{l}_{20i}^T\mathbf{s}_{0i}\right) + \left(\boldsymbol{\omega}_{10i}^T\boldsymbol{\omega}_{10i}\right)\cdot\mathbf{l}_{20i}^T\mathbf{l}_{10i}}{\mathbf{l}_{20i}^T\left(\mathbf{w}_{1i}\times\mathbf{l}_{10i}\right)}, \tag{33}$$

and subsequently by dot-multiplying Eq. (18) with $\mathbf{l}_{10i}^T$ the angular acceleration of link 2:

$$\dot{\omega}_{2i} = \frac{\frac{1}{l_2}\left(\mathbf{l}_{10i}^T\ddot{\mathbf{p}} + l_1\boldsymbol{\omega}_{10i}^T\boldsymbol{\omega}_{10i} - \ddot{s}_i\mathbf{l}_{10i}^T\mathbf{s}_{0i}\right) + \left(\boldsymbol{\omega}_{20i}^T\boldsymbol{\omega}_{20i}\right)\cdot\mathbf{l}_{10i}^T\mathbf{l}_{20i}}{\mathbf{l}_{10i}^T\left(\mathbf{w}_{1i}\times\mathbf{l}_{20i}\right)}. \tag{34}$$

Finally, the accelerations of the centers of gravity of both links can be calculated:

$$\mathbf{a}_{1i} = \ddot{s}_i\mathbf{s}_{0i} + \dot{\boldsymbol{\omega}}_{1i}\times\frac{l_1}{2}\mathbf{l}_{10i} + \boldsymbol{\omega}_{1i}\times\left(\boldsymbol{\omega}_{1i}\times\frac{l_1}{2}\mathbf{l}_{10i}\right), \tag{35}$$

$$\mathbf{a}_{2i} = 2\mathbf{a}_{1i} - \ddot{s}_i\mathbf{s}_{0i} + \dot{\boldsymbol{\omega}}_{2i}\times\frac{l_2}{2}\mathbf{l}_{20i} + \boldsymbol{\omega}_{2i}\times\left(\boldsymbol{\omega}_{2i}\times\frac{l_2}{2}\mathbf{l}_{20i}\right). \tag{36}$$

Internal forces/moments, i.e. the Jacobian of force transmission and the static equilibrium of forces/moments, are calculated by Eq. (43)–Eq. (48). The necessary actuator forces are derived by the following equation:

$$f_{q,i} = -m_{1i}\left(\mathbf{a}_{1i} - \mathbf{g}\right)^T\mathbf{s}_{0i} + \mathbf{F}_{1i}^T\mathbf{s}_{0i}, \tag{37}$$

with $\mathbf{F}_{1i}$ = internal force vector acting on the second revolute joint of limb i.

2.2 ∥ configuration

For the parallel frame configuration the first rotational joint axis is not parallel to the prismatic joint axis (Fig. 41). This means that the cylindrical joint is divided in two parts. Otherwise, the PKS has not three translational DoF [KG02].

$$\mathbf{s}_{0i} = \begin{pmatrix} 0 \\ 0 \\ 1 \end{pmatrix}; \qquad \mathbf{w}_{1i} = \mathbf{w}_{2i} = \mathbf{w}_{3i} = \mathbf{R}_{zi} \cdot \mathbf{R}_{xi} \cdot \begin{pmatrix} 0 \\ 1 \\ 0 \end{pmatrix}.$$

The derivation of the inverse kinematics, the Jacobian and the inverse dynamics follow the approach described for CRR$^{\Delta}$.

Inverse kinematics

Based on the vector loop equation,

$$\mathbf{p} = \mathbf{a}_i + s_i \mathbf{s}_{0i} + l_1 \mathbf{l}_{10i} + l_2 \mathbf{l}_{20i} - \mathbf{b}_i, \tag{38}$$

the known components are replaced by

$$\mathbf{g}_i = \mathbf{p} + \mathbf{b}_i - \mathbf{a}_i. \tag{39}$$

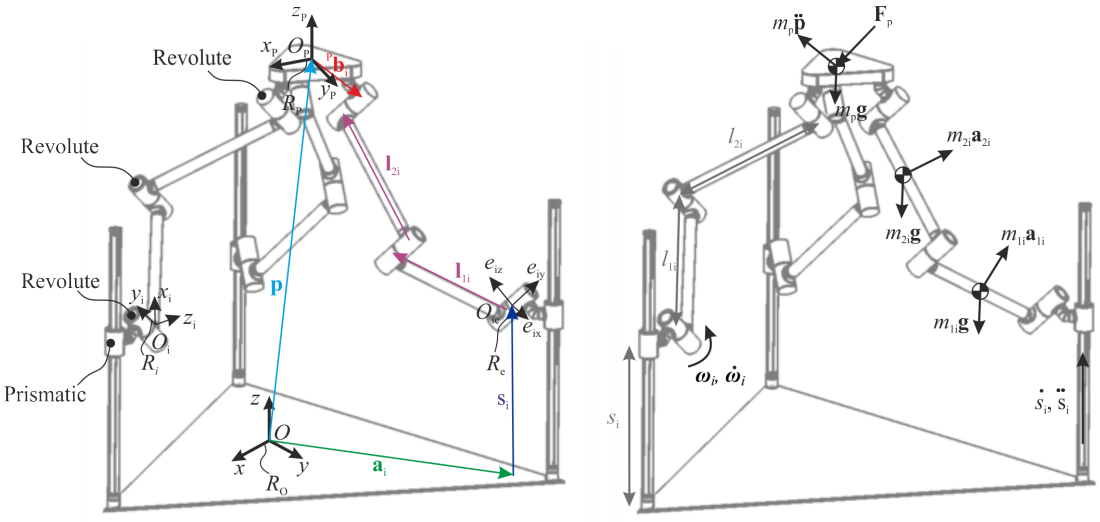

(a) Vector loop **(b)** Dynamic forces

Fig. 41: Vector loop and inertia properties of CRR$^{\parallel}$-PKS

Dot-multiplying Eq. (38) with $\mathbf{w}_{1i}^T$ leads to the stroke length of the first joint:

$$s_i = \frac{\mathbf{w}_{1i}^T \mathbf{g}_i}{\mathbf{w}_{1i}^T \mathbf{s}_{0i}}. \tag{40}$$

Jacobian matrix

The calculation of the Jacobian matrix is the same as for the Δ-shaped frame configuration.

Inverse dynamics

The inverse dynamics of CRR$^{\parallel}$ follow the approach described for CRR$^{\Delta}$.

2.3 $\star$ configuration

The kinematics of the CRR*-PKS were already derived in 2002 by [KG02] and has been used to perform a singularity analysis and to determine the workspace. The CRR* is controlled by three linear actuators, whose axes intersect in the origin of R_0 (cf. Fig. 42). The C-joint, which rotates around this prismatic axis is parallel to the axes of the two other joints within each limb:

$$\mathbf{w}_{1i} = \mathbf{w}_{2i} = \mathbf{w}_{3i} = \mathbf{s}_{0i} = \mathbf{R}_{zi} \cdot \mathbf{R}_{xi} \cdot \begin{pmatrix} 0 \\ 1 \\ 0 \end{pmatrix} = \mathbf{e}_{iy}.$$

This configuration allows purely translational motion of the mobile platform. If the cylindrical joint axes are orthogonal, the condition number is 1 within the entire workspace, i.e. the Jacobian matrix is not position dependent. This structures is called Tripteron. Furthermore, it is a decoupled structure, i.e. each actuator controls one DoF. Due to this characteristics, the manipulator has simple kinematics, a singularity-free workspace and it is insensitive to errors in link lengths [GMD07].

[TH11] takes the position error of the mobile platform in his research into account due to axes errors within an orthogonal frame configuration. A dynamic modeling is performed by [YHT13] using the Lagrangian and Newtonian approaches.

The inverse kinematic problem and the Jacobian matrix are derived and summarized in [Dan13] as well. Even as a compliant parallel mechanism, the CRR structure in an orthogonal frame configuration is used (cf. [QG11]).

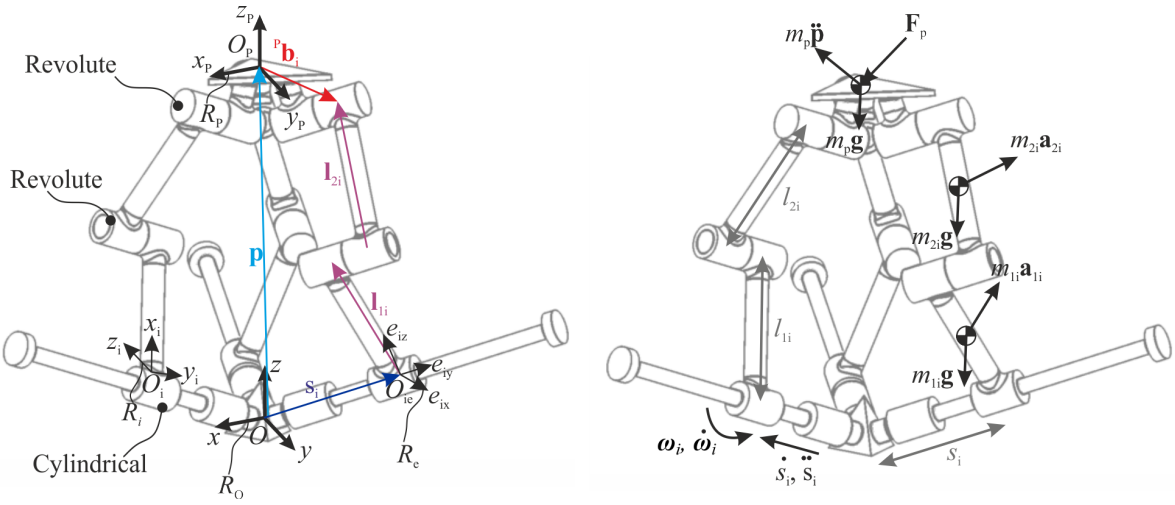

(a) Vector loop **(b)** Dynamic forces

Fig. 42: Vector loop and inertia properties of CRR*-PKS

Inverse dynamics

By derivating the vector loop equation twice (Eq. (18)) and dot-multiplying with either $\mathbf{w}_{1i}^T$, $\mathbf{l}_{20i}$, $\mathbf{l}_{10i}$, the linear acceleration of the cylindrical joint $\ddot{s}_i$, the angular acceleration $\dot{\omega}_{1i}$ of link 1 and the angular velocity $\dot{\omega}_{2i}$ of link 2 of limb i are calculated (cf. Eq. (4)–Eq. (6)). The necessary angular velocities of link 1 and 2 are determined based on Eq. (2) and

$$\omega_{1i} = \frac{\frac{1}{l_1}\mathbf{l}_{20i}^T\dot{\mathbf{p}}}{\mathbf{l}_{20i}^T(\mathbf{w}_{1i} \times \mathbf{l}_{10i})}. \tag{41}$$

The accelerations of the centers of gravity are calculated in the same way as for CRR$^{\Delta}$, i.e. cf. Eq. (35) and Eq. (36). The axis of moment transmission at the end-effector is equal to Eq. (9).

The necessary actuator forces are calculated with the following equation:

$$f_{q,i} = -m_{1i}\left(\mathbf{a}_{1i} - \mathbf{g}\right)^T \mathbf{w}_{1i} - m_{2i}\left(\mathbf{a}_{2i} - \mathbf{g}\right)^T \mathbf{w}_{1i} + F_{yi}. \tag{42}$$

Here, the internal force vector is as follows (cf. Fig. 43):

$$\mathbf{F}_{int} = \begin{pmatrix}\mathbf{F}^T & \mathbf{F}_t^T & \mathbf{F}_y^T & \mathbf{F}_{1x}^T & \mathbf{F}_{1y}^T & \mathbf{F}_{1z}^T\end{pmatrix}^T, \tag{43}$$

with $\mathbf{F} = (F_1F_2F_3)^T$, $\mathbf{F}_t = (F_{t1}F_{t2}F_{t3})^T$, $\mathbf{F}_y = (F_{y1}F_{y2}F_{y3})^T$, $\mathbf{F}_{1x} = (F_{11x}F_{12x}F_{13x})^T$, $\mathbf{F}_{1y} = (F_{11y}F_{12y}F_{13y})^T$ and $\mathbf{F}_{1z} = (F_{11z}F_{12z}F_{13z})^T$. $\mathbf{F}_1$ is the internal joint force vector acting on the second revolute joint. With regard to Eq. (6.7), the vector of external forces

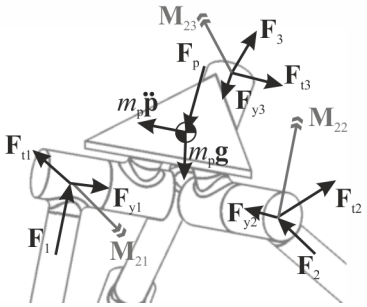

Fig. 43: Static equilibrium of forces at the end-effector of CRR-PKS

is composed of the following components:

$$\mathbf{F}_{ext} = \begin{pmatrix} m_p\mathbf{g} - m_p\ddot{\mathbf{p}} + \mathbf{F}_p \\ \mathbf{0}_{3x3} \\ \mathbf{M}_2 \\ \mathbf{F}_2 \\ \mathbf{M}_1 \end{pmatrix}, \tag{44}$$

with $\mathbf{M}_2 = (M_{21}M_{22}M_{23})^T$, $\mathbf{F}_2 = \left(\mathbf{F}_{21}^T\mathbf{F}_{22}^T\mathbf{F}_{23}^T\right)^T$ and $\mathbf{M}_1 = (M_{11}M_{12}M_{13})^T$. The first six rows are based on the static equilibrium of forces/torques at the end-effector. M_{2i} is calculated from the static equilibrium of moments about the revolute joint axis $\mathbf{w}_{2i}$ of the second revolute joint. F_{2i} is the external force acting on link 2 of limb i.

$$M_{2i} = m_{2i}\left(\mathbf{a}_{2i} - \mathbf{g}\right)^T \left(\frac{l_2}{2}\mathbf{l}_{20i} \times \mathbf{w}_{2i}\right) - \mathbf{w}_{2i}^T\left(\mathbf{I}_{2tot,i}\dot{\boldsymbol{\omega}}_{2i}\right) - \mathbf{w}_{2i}^T\left(\boldsymbol{\omega}_{2i} \times \left(\mathbf{I}_{2tot,i}\boldsymbol{\omega}_{2i}\right)\right), \tag{45}$$

$$\mathbf{F}_{2i} = m_{2i}\left(\mathbf{a}_{2i} - \mathbf{g}\right). \tag{46}$$

Finally, the result of the static equilibrium of moments about the first revolute joint is summarized in M_{1i}.

$$M_{1i} = m_{1i}\left(\mathbf{a}_{1i} - \mathbf{g}\right)^T \left(\frac{l_1}{2}\mathbf{l}_{10i} \times \mathbf{w}_{1i}\right) - \mathbf{w}_{1i}^T\left(\mathbf{I}_{1tot,i}\dot{\boldsymbol{\omega}}_{1i}\right) - \mathbf{w}_{1i}^T\left(\boldsymbol{\omega}_{1i} \times \left(\mathbf{I}_{1tot,i}\boldsymbol{\omega}_{1i}\right)\right). \tag{47}$$

Hence, the Jacobian of force transmission $\mathbf{J}_p$ is a 21x21 matrix:

$$\mathbf{J}_p = \begin{pmatrix} \mathbf{J}_{p1,(3x21)} \\ \mathbf{J}_{p2,(3x21)} \\ \mathbf{J}_{p3,(3x21)} \\ \mathbf{J}_{p4,(9x21)} \\ \mathbf{J}_{p5,(3x21)} \end{pmatrix}, \tag{48}$$

with the following components:

$$\begin{aligned}
\mathbf{J}_{p1,(:,i)} &= \mathbf{l}_{20i}, \\
\mathbf{J}_{p1,(:,i+3)} &= \mathbf{l}_{20i} \times \mathbf{w}_{1i}, \\
\mathbf{J}_{p1,(:,i+6)} &= \mathbf{w}_{1i},
\end{aligned} \tag{49}$$

$$\begin{aligned}
\mathbf{J}_{p2,(:,i)} &= \mathbf{l}_{20i} \times \mathbf{b}_i, \\
\mathbf{J}_{p2,(:,i+3)} &= (\mathbf{l}_{20i} \times \mathbf{w}_{1i}) \times \mathbf{b}_i, \\
\mathbf{J}_{p2,(:,i+6)} &= \mathbf{w}_{1i} \times \mathbf{b}_i, \\
\mathbf{J}_{p2,(:,i+9)} &= \mathbf{n}_{2i},
\end{aligned} \tag{50}$$

$$\mathbf{J}_{p3,(1:3,4:6)} = \begin{pmatrix} l_2 & 0 & 0 \\ 0 & l_2 & 0 \\ 0 & 0 & l_2 \end{pmatrix}, \tag{51}$$

$$\begin{aligned}
\mathbf{J}_{p4,(1:3,1)} &= \mathbf{l}_{201}, \\
\mathbf{J}_{p4,(1:3,4)} &= \mathbf{l}_{201} \times \mathbf{w}_{11}, \\
\mathbf{J}_{p4,(1:3,7)} &= \mathbf{w}_{11}, \\
\mathbf{J}_{p4,(1:3,13)} &= -1, \\
\mathbf{J}_{p4,(1:3,16)} &= -1, \\
\mathbf{J}_{p4,(1:3,19)} &= -1.
\end{aligned} \tag{52}$$

Rows 4 to 6 and 7 to 9 are derived in the same way for the other two limbs.

$$\begin{aligned}
\mathbf{J}_{p5,(i,i+12)} &= (l_1 \mathbf{l}_{10i} \times \mathbf{w}_{1i})_x, \\
\mathbf{J}_{p5,(i,i+15)} &= (l_1 \mathbf{l}_{10i} \times \mathbf{w}_{1i})_y, \\
\mathbf{J}_{p5,(i,i+18)} &= (l_1 \mathbf{l}_{10i} \times \mathbf{w}_{1i})_z.
\end{aligned} \tag{53}$$

3 RPC

The limbs of the RPC-PKS are connected to the base by revolute joints and to the end-effector by cylindrical joints. The prismatic joints define the length of the limbs. The PKS can be actuated by rotational or linear drives; mixed actuation is possible as well. The

prismatic joint axes are perpendicular to the revolute joint axes. Futhermore, the revolute and cylindrical joint axes are parallel within each limb. The RPC structure is described in detail in [PLC15] including the derivation of the inverse kinematics and the Jacobian matrix for different actuator and frame configurations. In this work, only the triangular frame configuration with either rotational or linear actuation is considered. The inverse dynamics are completely derived in [PC15]. For the sake of completeness, the vector loop equation and the inertia properties are shown in Fig. 44.

4 CPR

There are no references concerning the analysis of this structure. Hence, the necessary mathematical descriptions are derived in this section.

4.1 Δ configuration

For the triangular frame configuration, the orientation of the joint axes is as follows:

$$\mathbf{s}_{0i} = \mathbf{R}_{zi} \cdot \mathbf{R}_{xi} \cdot \begin{pmatrix} 0 \\ 1 \\ 0 \end{pmatrix} \qquad \mathbf{w}_{1i} = \mathbf{w}_{2i} = \mathbf{R}_{zi} \cdot \begin{pmatrix} 0 \\ 1 \\ 0 \end{pmatrix} .$$

Here, instead of ψ, the inclination angle δ is used within $\mathbf{R}_{xi}$. All relevant parameters for the following mathematical descriptions are shown in Fig. 45.

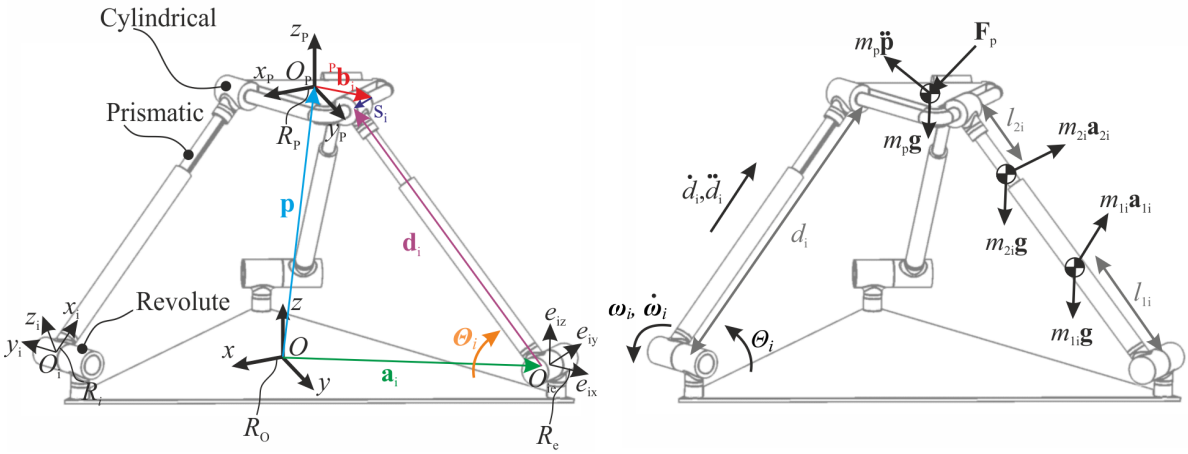

(a) Vector loop **(b)** Dynamic forces

Fig. 44: Vector loop and inertia properties of RPC

Inverse kinematics

Based on the vector loop equation,

$$\mathbf{p} = \mathbf{a}_i + s_i \mathbf{s}_{0i} + d_i \mathbf{d}_{i0} - \mathbf{b}_i, \tag{54}$$

the known components are replaced by

$$\mathbf{g}_i = \mathbf{p} + \mathbf{b}_i - \mathbf{a}_i. \tag{55}$$

Eq. (54) is dot-multiplied with $\mathbf{w}_{1i}$ and hence, the stroke length of the first prismatic joint is known:

$$s_i = \frac{\mathbf{w}_{1i}^T \mathbf{g}_i}{\mathbf{w}_{1i}^T \mathbf{s}_{0i}}. \tag{56}$$

Inserting s_i into Eq. (54) leads to the vector $\mathbf{d}_i$ of the second prismatic joint. Its norm is the length between frame joint and end-effector.

Jacobian matrix

The Jacobian matrix calculation is related to the ⋆-shaped configuration. But here, the actuator velocities and hence, the entries of the Jacobian are:

$$\dot{s}_i = \frac{\mathbf{w}_{1i}^T}{\mathbf{w}_{1i}^T \mathbf{s}_{0i}} \cdot \dot{\mathbf{p}} = \mathbf{J}_{(i,:)} \cdot \dot{\mathbf{p}}. \tag{57}$$

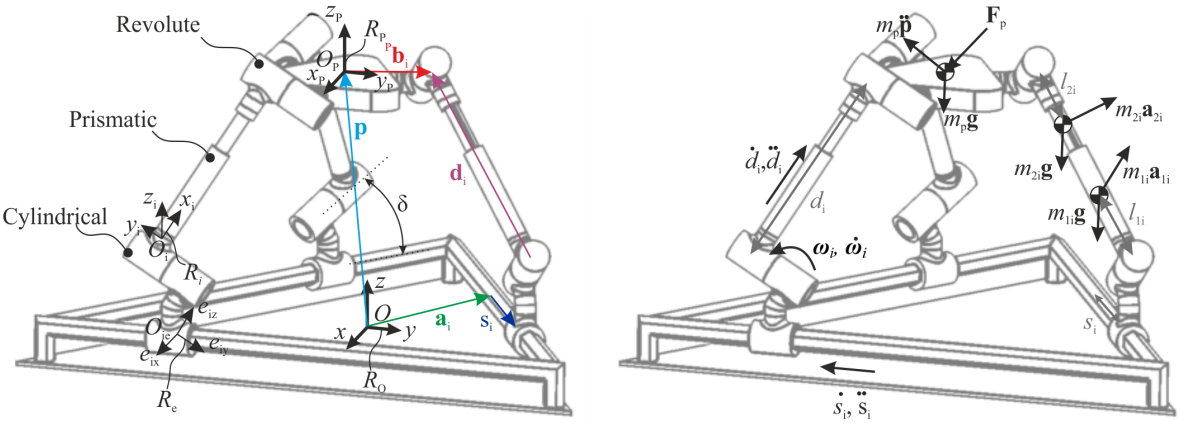

(a) Vector loop **(b)** Dynamic forces

Fig. 45: Vector loop and inertia properties of CPR$^{\Delta}$

Inverse dynamics

The actuator velocities are determined by Eq. (57). Dot-multiplying Eq. (68) with $\mathbf{d}_{0i}^T$ leads to the velocity of the prismatic joint:

$$\dot{d}_i = \mathbf{d}_{0i}^T \dot{\mathbf{p}} - \dot{s}_i \mathbf{d}_{0i}^T \mathbf{s}_{0i}. \tag{58}$$

The angular velocity of each limb is:

$$\omega_{1i} = (\mathbf{s}_{0i} \times \mathbf{d}_{0i})^T \cdot \frac{1}{d_i} \cdot \left(\dot{\mathbf{p}} - \dot{s}_i \mathbf{s}_{0i} - \dot{d}_i \mathbf{d}_{0i} \right). \tag{59}$$

The vector loop equation is derivated twice and dot-multiplied by $\mathbf{w}_{1i}^T$ to calculate the acceleration of the first prismatic joint (the cylindrical joint part):

$$\ddot{s}_i = \frac{\mathbf{w}_{1i}^T \ddot{\mathbf{p}}}{\mathbf{w}_{1i}^T \mathbf{s}_{0i}}. \tag{60}$$

Then, the second time-derivative of Eq. (54) is dot-multiplied with $\mathbf{s}_{0i}^T$ in order to determine the acceleration of the prismatic joint:

$$\ddot{d}_i = \mathbf{d}_{0i}^T \ddot{\mathbf{p}} + d_i \left(\boldsymbol{\omega}_{1i}^T \boldsymbol{\omega}_{1i} \right) - \ddot{s}_i \mathbf{d}_{0i}^T \mathbf{s}_{0i}. \tag{61}$$

Finally, the angular acceleration of limb i is:

$$\dot{\omega}_{1i} = (\mathbf{w}_{1i} \times \mathbf{d}_{0i})^T \cdot \frac{1}{d_i} \cdot \left(\ddot{\mathbf{p}} - \ddot{s}_i \mathbf{s}_{0i} - \ddot{d}_i \mathbf{d}_{0i} + d_i \left(\boldsymbol{\omega}_{1i}^T \boldsymbol{\omega}_{1i} \right) \mathbf{d}_{0i} - 2\dot{d}_i \left(\boldsymbol{\omega}_{1i} \times \mathbf{d}_{0i} \right) \right). \tag{62}$$

The Jacobian of force transmission is calculated with Eq. (86), the vectors of moment transmission with Eq. (79) and Eq. (80) and the accelerations of the centers of gravity with Eq. (77) and Eq. (78). The vector of external forces $\mathbf{F}_{ext}$ is determined as for CRR*, Eq. (83) with F_{2i}, Eq. (85). $\mathbf{M}_{1i}$ is calculated from the static equilibrium of moments about the revolute joint axis $\mathbf{w}_{1i}$:

$$M_i = -\mathbf{w}_{1i}^T \left(m_{2i} \left(\mathbf{a}_{2i} - \mathbf{g} \right) \times \left(d_i - l_2 \right) \mathbf{d}_{0i} \right) - \mathbf{w}_{1i}^T \left(m_{1i} \left(\mathbf{a}_{1i} - \mathbf{g} \right) \times l_1 \mathbf{d}_{0i} \right). \tag{63}$$

Solving Eq. (6.7) leads to the vector of internal forces (cf. Eq. (82)). Finally, the required actuator forces can be determined:

$$f_{q,i} = \mathbf{s}_{0i}^T \left(F_{yi} \mathbf{w}_{1i} + F_{ti} \left(\mathbf{w}_{1i} \times \mathbf{d}_{0i} \right) + F_i \mathbf{d}_{0i} \right) - \ldots \tag{64}$$

$$\mathbf{s}_{0i}^T \left(m_{2i} \left(\mathbf{a}_{2i} - \mathbf{g} \right) \right) - \mathbf{s}_{0i}^T \left(m_{1i} \left(\mathbf{a}_{1i} - \mathbf{g} \right) \right). \tag{65}$$

4.2 ⋆ configuration

Within the CPR⋆-PKS the cylindrical joint axis $\mathbf{s}_{i0} = \mathbf{w}_{1i}$ is parallel to the revolute joint axis $\mathbf{w}_{2i}$:

$$\mathbf{s}_{i0} = \mathbf{w}_{1i} = \mathbf{w}_{2i};$$

The prismatic joint connects the cylindrical and revolute joint.

Inverse kinematics

Based on the vector loop equation (cf. Fig. 46a),

$$\mathbf{p} = s_i\mathbf{s}_{0i} + d_i\mathbf{d}_{0i} - \mathbf{b}_i, \tag{66}$$

the known components are replaced by

$$\mathbf{g}_i = \mathbf{p} + \mathbf{b}_i. \tag{67}$$

It follows:

$$\mathbf{g}_i = s_i\mathbf{s}_{0i} + d_i\mathbf{d}_{0i}. \tag{68}$$

Dot-multiplying Eq. (68) with $\mathbf{s}_{0i}^T$ leads to the stroke length of the cylindrical joint:

$$s_i = \mathbf{s}_{0i}^T\mathbf{g}_i. \tag{69}$$

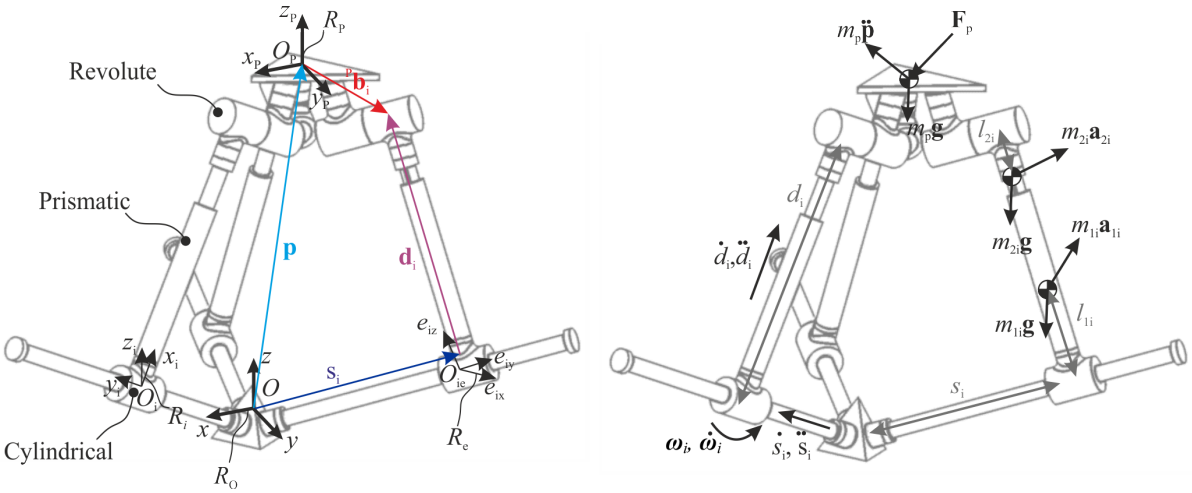

(a) Vector loop **(b)** Dynamic forces

Fig. 46: Vector loop and inertia properties of CPR⋆

Subsequently, Eq. (68) is solved for $\mathbf{d}_i$. The norm of $\mathbf{d}_i$ is the stroke length of the prismatic joint.

Jacobian matrix

Time derivating Eq. (66) leads to

$$\dot{\mathbf{p}} = \dot{s}_i \mathbf{s}_{0i} + d_i(\boldsymbol{\omega}_{1i} \times \mathbf{d}_{0i}) + \dot{d}_i \mathbf{d}_{0i}, \tag{70}$$

with $\boldsymbol{\omega}_{1i}$ = angular velocity vector of the prismatic joint of limb i.

Dot-multiplying Eq. (70) with $\mathbf{s}_{0i}^T$ and solving for $\dot{s}_i$ results in:

$$\dot{s}_i = \mathbf{s}_{0i}^T \cdot \dot{\mathbf{p}} = \mathbf{J}_{(i,:)} \cdot \dot{\mathbf{p}}. \tag{71}$$

Finally, the Jacobian can be written as follows:

$$\dot{\mathbf{q}} = \dot{\boldsymbol{s}} = \begin{pmatrix} \mathbf{J}_{(1,:)} \\ \mathbf{J}_{(2,:)} \\ \mathbf{J}_{(3,:)} \end{pmatrix} \cdot \dot{\mathbf{p}}. \tag{72}$$

Inverse dynamics

First, the velocities of all joints are calculated. The actuator velocities are determined by the use of the Jacobian (cf. Eq. (72)). Dot-multiplying Eq. (66) with $\mathbf{d}_{0i}^T$ leads to the velocity of the prismatic joint:

$$\dot{d}_i = \mathbf{d}_{0i}^T \dot{\mathbf{p}}. \tag{73}$$

The angular velocity of each limb is:

$$\omega_{1i} = (\mathbf{s}_{0i} \times \mathbf{d}_{0i})^T \cdot \frac{1}{d_i} \cdot \left(\dot{\mathbf{p}} - \dot{s}_i \mathbf{s}_{0i} - \dot{d}_i \mathbf{d}_{0i} \right). \tag{74}$$

The vector loop equation is derivated a second time, dot-multiplied by $\mathbf{d}_{0i}^T$ to calculate the acceleration of the prismatic joint and by $\mathbf{s}_{0i}^T$ to calculate the linear acceleration of the cylindrical joint:

$$\ddot{d}_i = \mathbf{d}_{0i}^T \ddot{\mathbf{p}} + d_i \left(\boldsymbol{\omega}_{1i}^T \boldsymbol{\omega}_{1i} \right), \tag{75}$$

$$\ddot{s}_i = \mathbf{s}_{0i}^T \ddot{\mathbf{p}}. \tag{76}$$

It follows the angular acceleration of the cylindrical joint through insertion. Subsequently, the accelerations of the centers of gravity of stator and slider of the prismatic joint can be calculated (cf. Fig. 46b):

$$\mathbf{a}_{1i} = \ddot{s}_i \mathbf{s}_{0i} + \dot{\boldsymbol{\omega}}_{1i} \times l_1 \mathbf{d}_{0i} + \boldsymbol{\omega}_{1i} \times (\boldsymbol{\omega}_{1i} \times l_1 \mathbf{d}_{0i}) \,, \tag{77}$$

$$\begin{aligned} \mathbf{a}_{2i} =& \ddot{s}_i \mathbf{s}_{0i} + \dot{\boldsymbol{\omega}}_{1i} \times (d_i - l_2)\, \mathbf{d}_{0i} + \boldsymbol{\omega}_{1i} \times (\boldsymbol{\omega}_{1i} \times (d_i - l_2)\, \mathbf{d}_{0i}) + \ldots \\ & 2\boldsymbol{\omega}_{1i} \times \dot{d}_i \mathbf{d}_{0i} + \ddot{d}_i \mathbf{d}_{0i}. \end{aligned} \tag{78}$$

Since revolute joints do not transfer torques about their rotational axis, the axes of moment transmission at the frame ($\mathbf{n}_{1i}$) and the end-effector ($\mathbf{n}_{2i}$) are:

$$\mathbf{n}_{1i} = \frac{\mathbf{d}_{0i} + \mathbf{d}_{0i} \times \mathbf{s}_{0i}}{|\mathbf{s}_{0i} + \mathbf{d}_{0i} \times \mathbf{s}_{0i}|}, \tag{79}$$

$$\mathbf{n}_{2i} = -\mathbf{n}_{1i}. \tag{80}$$

The necessary actuator forces are calculated with the following equation:

$$f_{q,i} = F_{yi} - m_{2i} \left(\mathbf{a}_{2i} - \mathbf{g}\right)^T \mathbf{s}_{0i} - m_{1i} \left(\mathbf{a}_{1i} - \mathbf{g}\right)^T \mathbf{s}_{0i}. \tag{81}$$

Here, the internal force vector reads as follows (cf. Fig. 43):

$$\mathbf{F}_{int} = \begin{pmatrix} \mathbf{F} & \mathbf{F}_t & \mathbf{F}_y & \mathbf{M}_2 \end{pmatrix}^T, \tag{82}$$

with $\mathbf{F} = (F_1 F_2 F_3)^T$, $\mathbf{F}_t = (F_{t1} F_{t2} F_{t3})^T$, $\mathbf{F}_y = (F_{y1} F_{y2} F_{y3})^T$, $\mathbf{M}_2 = (M_{21} M_{22} M_{23})^T$. The vector of external forces is composed of the following components:

$$\mathbf{F}_{ext} = \begin{pmatrix} m_p \mathbf{g} - m_p \ddot{\mathbf{p}} + \mathbf{F}_p \\ \mathbf{0}_{3x3} \\ \mathbf{F}_2 \\ \mathbf{M}_1 \end{pmatrix}, \tag{83}$$

with $\mathbf{F}_2 = (F_{21} F_{22} F_{23})$ and $\mathbf{M}_1 = (M_{11} M_{12} M_{13})$. The first six rows are based on the static equilibrium of forces/torques at the end-effector. $\mathbf{M}_{1i}$ is calculated from the static equilibrium of moments about the revolute joint axis $\mathbf{s}_{0i} = \mathbf{w}_{1i}$:

$$M_i = -\mathbf{s}_{0i}^T \left(m_{2i} \left(\mathbf{a}_{2i} - \mathbf{g}\right) \times (d_i - l_2)\, \mathbf{d}_{0i}\right) - \mathbf{s}_{0i}^T \left(m_{1i} \left(\mathbf{a}_{1i} - \mathbf{g}\right) \times l_1 \mathbf{d}_{0i}\right). \tag{84}$$

F_{2i} is the internal force acting along the prismatic joint axis of limb i:

$$F_{2i} = m_{2i} \left(\mathbf{a}_{2i} - \mathbf{g} \right)^T \mathbf{d}_{0i}. \tag{85}$$

Hence, the Jacobian of force transmission $\mathbf{J}_p$ is a 12x12 matrix:

$$\mathbf{J}_p = \begin{pmatrix} \mathbf{J}_{p1,(3x9)} & \mathbf{0}_{3x3} \\ \mathbf{J}_{p2,(3x9)} & \mathbf{J}_{p3,(3x3)} \\ \mathbf{J}_{p4,(3x9)} & \mathbf{0}_{3x3} \\ \mathbf{J}_{p5,(3x9)} & \mathbf{0}_{3x3} \end{pmatrix}, \tag{86}$$

with

$$\begin{aligned} \mathbf{J}_{p1,(:,i)} &= \mathbf{d}_{0i}, \\ \mathbf{J}_{p1,(:,i+3)} &= \mathbf{s}_{0i} \times \mathbf{d}_{0i}, \\ \mathbf{J}_{p1,(:,i+6)} &= \mathbf{s}_{0i}, \end{aligned} \tag{87}$$

$$\begin{aligned} \mathbf{J}_{p2,(:,i)} &= \mathbf{b}_i \times \mathbf{d}_{0i}, \\ \mathbf{J}_{p2,(:,i+3)} &= \mathbf{b}_i \times \left(\mathbf{s}_{0i} \times \mathbf{d}_{0i} \right), \\ \mathbf{J}_{p2,(:,i+6)} &= \mathbf{b}_i \times \mathbf{s}_{0i}, \end{aligned} \tag{88}$$

$$\mathbf{J}_{p3,(:,i)} = \mathbf{n}_{2i}, \tag{89}$$

$$\mathbf{J}_{p4,(:,1:3)} = \begin{pmatrix} 1 & 0 & 0 \\ 0 & 1 & 0 \\ 0 & 0 & 1 \end{pmatrix}, \tag{90}$$

$$\mathbf{J}_{p5,(i,i+3)} = d_i. \tag{91}$$

5 PRC

The kinematic description of the PRC-PKS is completely described in [YQ05b; LX06b]. Furthermore, a dexterity analysis is performed. In [XL07] the kinematic analysis (forward and inverse) and a velocity analysis is carried out for this PKS in orthogonal frame configuration.

Within a limb the revolute and cylindrical joint axes are parallel and perpendicular to the prismatic joint axis. For the ⋆-shaped frame configuration the axes are:

$$\mathbf{s}_{0i} = \mathbf{w}_{1i} = \mathbf{w}_{2i} = \mathbf{R}_{zi} \cdot \mathbf{R}_{xi} \cdot \begin{pmatrix} 0 \\ 1 \\ 0 \end{pmatrix}, \qquad \mathbf{d}_{0i} = \mathbf{R}_{zi} \cdot \mathbf{R}_{xi} \cdot \begin{pmatrix} 1 \\ 0 \\ 0 \end{pmatrix},$$

and for the ∥-shaped frame configuration:

$$\mathbf{s}_{0i} = \mathbf{w}_{1i} = \mathbf{w}_{2i} = \mathbf{R}_{zi} \cdot \begin{pmatrix} 0 \\ 1 \\ 0 \end{pmatrix}, \qquad \mathbf{d}_{0i} = \begin{pmatrix} 0 \\ 0 \\ 1 \end{pmatrix}.$$

For the ⋆-shaped frame configuration the solution of the inverse kinematic problem and the derivation of the Jacobian matrix can be found in [Dan13] as well.

No reference is available for this PKS in ∥-shaped frame configuration, but here, only the definition of the prismatic joint axes changes so that the calculation of the inverse kinematics and the Jacobian matrix is the same as for the ⋆-shaped configuration.

In [YQ07] and [QY07] the structure is used to built a compliant parallel micro-manipulator.

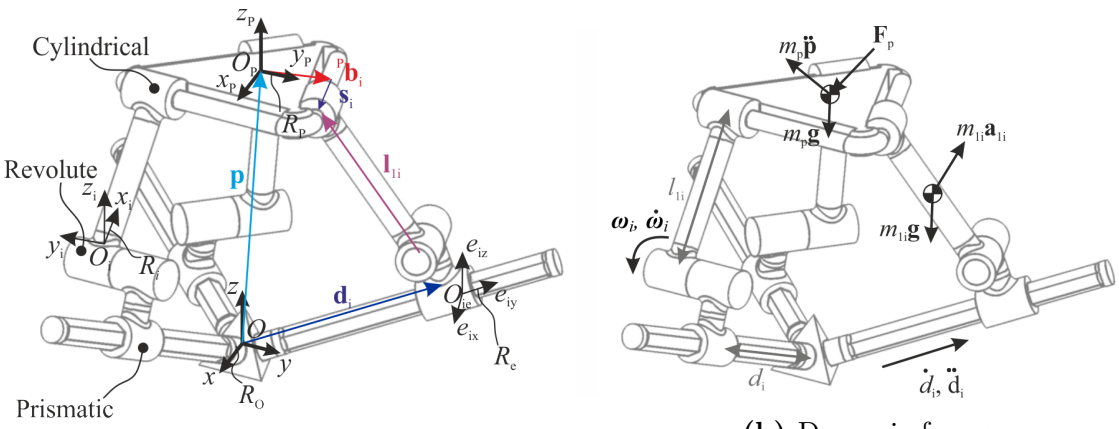

(a) Vector loop **(b)** Dynamic forces

Fig. 47: Vector loop and inertia properties of PRC⋆-PKS

Inverse dynamics

The inverse dynamics are derived in the same way for both, $\star$ and $\|$-shaped configuration. The velocities of the actuators are calculated with the Jacobian matrix. The velocity of the cylindrical joint is:

$$\dot{s}_i = \mathbf{s}_{0i}^T \dot{\mathbf{p}}. \tag{92}$$

Solving the derivated vector loop equation (cf. Fig. 48a) leads to the angular velocity of limb i:

$$\omega_{1i} = (\mathbf{s}_{0i} \times \mathbf{l}_{10i})^T \left(\frac{1}{l_1} \left(\dot{\mathbf{p}} - \dot{d}_i \mathbf{d}_{0i} + \dot{s}_i \mathbf{s}_{0i} \right) \right). \tag{93}$$

Dot-multiplying the second time-derivative of the vector loop equation with $\mathbf{l}_{10i}^T$ leads to the acceleration of the prismatic joint:

$$\ddot{d}_i = \frac{\mathbf{l}_{10i}^T \ddot{\mathbf{p}} + l_1 \boldsymbol{\omega}_{1i}^T \boldsymbol{\omega}_{1i}}{\mathbf{l}_{10i}^T \mathbf{d}_{0i}}. \tag{94}$$

Similar to Eq. (92), the acceleration of the cylindrical joint is:

$$\ddot{s}_i = \mathbf{s}_{0i}^T \ddot{\mathbf{p}}. \tag{95}$$

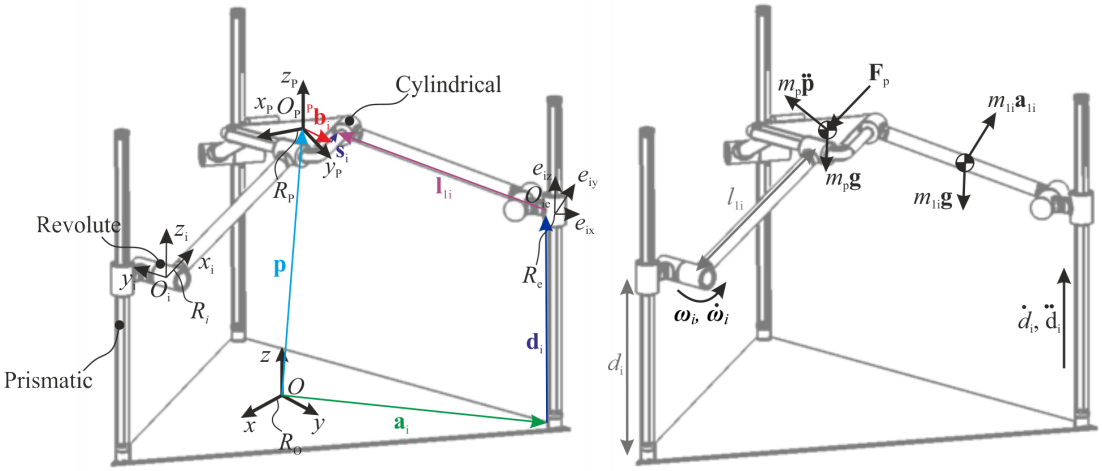

(a) Vector loop **(b)** Dynamic forces

Fig. 48: Vector loop and inertia properties of PRC$^{\|}$-PKS

Finally, the angular acceleration of limb i can be calculated with the following equation:

$$\dot{\omega}_{1i} = (\mathbf{s}_{0i} \times \mathbf{l}_{10i})^T \left(\frac{1}{l_1} \left(\ddot{\mathbf{p}} - \ddot{d}_i \mathbf{d}_{0i} + \ddot{s}_i \mathbf{s}_{0i} + \left(\boldsymbol{\omega}_{1i}^T \boldsymbol{\omega}_{1i} \right) \mathbf{l}_{10i} \right) \right). \tag{96}$$

Consequently, the acceleration of the center of gravity of each link is:

$$\mathbf{a}_{1i} = \ddot{d}_i \mathbf{d}_{0i} + \dot{\boldsymbol{\omega}}_{1i} \times \frac{l_1}{2} \mathbf{l}_{10i} + \boldsymbol{\omega}_{1i} \times \left(\boldsymbol{\omega}_{1i} \times \frac{l_1}{2} \mathbf{l}_{10i} \right). \tag{97}$$

The axis of moment transmission at the end-effector is:

$$\mathbf{n}_{2i} = -\frac{\mathbf{l}_{10i} + \mathbf{s}_{0i} \times \mathbf{l}_{10i}}{|\mathbf{l}_{10i} + \mathbf{s}_{0i} \times \mathbf{l}_{10i}|}. \tag{98}$$

The force acting perpendicular to the link and cylindrical joint axes can be calculated as follows (cf. Fig. 39):

$$F_{ti} = \frac{\mathbf{s}_{0i}^T \left(\frac{l_1}{2} \mathbf{l}_{10i} \times m_{1i} \left(\mathbf{a}_{1i} - \mathbf{g} \right) \right) + \mathbf{s}_{0i}^T \left(\mathbf{I}_{1tot,i} \dot{\boldsymbol{\omega}}_{1i} \right) + \mathbf{s}_{0i}^T \left(\boldsymbol{\omega}_{1i} \times \mathbf{I}_{1tot,i} \boldsymbol{\omega}_{1i} \right)}{\mathbf{s}_{0i}^T \left((\mathbf{s}_{0i}^T \times l_{10i}) \times l_1 \mathbf{l}_{10i} \right)}, \tag{99}$$

with the respective force vector is:

$$\mathbf{F}_{ti} = -F_{ti} \left(\mathbf{l}_{10i} \times \mathbf{s}_{0i} \right). \tag{100}$$

This force results in a torque about the origin of the origin of R_p:

$$\mathbf{M}_{ti} = \mathbf{F}_{ti} \times \left(\mathbf{b}_i + s_i \mathbf{s}_{0i} \right). \tag{101}$$

Thus, the vector of external forces is:

$$\mathbf{F}_{ext} = \begin{pmatrix} m_p \mathbf{g} - m_p \ddot{\mathbf{p}} + \mathbf{F}_p + \sum_{i=1}^{3} \mathbf{F}_{ti} \\ \sum_{i=1}^{3} \mathbf{M}_{ti} \end{pmatrix}. \tag{102}$$

With Eq. (6.7) the vector of internal forces is calculated:

$$\mathbf{F}_{int} = \begin{pmatrix} F_1 & F_2 & F_3 & M_{21} & M_{22} & M_{23} \end{pmatrix}^T. \tag{103}$$

Here, the Jacobian of force transmission $\mathbf{J}_p$ is a 6x6 matrix:

$$\mathbf{J}_p = \begin{pmatrix} \mathbf{l}_{101} & \mathbf{l}_{102} & \mathbf{l}_{103} & \mathbf{0}_{3x1} & \mathbf{0}_{3x1} & \mathbf{0}_{3x1} \\ (\mathbf{b}_1 + s_1\mathbf{s}_{01}) \times \mathbf{l}_{101} & (\mathbf{b}_2 + s_2\mathbf{s}_{02}) \times \mathbf{l}_{102} & (\mathbf{b}_3 + s_3\mathbf{s}_{03}) \times \mathbf{l}_{103} & \mathbf{n}_{21} & \mathbf{n}_{22} & \mathbf{n}_{23} \end{pmatrix}. \tag{104}$$

Finally, the required actuator force is:

$$f_{q,i} = -\mathbf{d}_{0i}^T \left(F_i \mathbf{l}_{10i} - \mathbf{F}_{ti} - m_{1i} \left(\mathbf{a}_{1i} - \mathbf{g} \right) \right). \tag{105}$$

6 UUP

From the current state of the art, no research on the UUP-PKS is known. The structure consists of two universal joint whose axes are pairwise parallel to each other: the first rotational axis of the first universal joint and the second rotational axis of the second universal joint. The remaining axes are parallel as well. The prismatic joint axes form a triangular shape at the end-effector and are parallel to the first rotational joint axes of the respective limb (cf. Fig. 49).

Inverse kinematics

Due to the geometrical design, the unit vectors of the first universal joint axis of joint 1 ($\mathbf{w}_{1i}$), of the second universal joint axis of joint 2 ($\mathbf{w}_{4i}$) and the prismatic joint ($\mathbf{s}_{0i}$) at

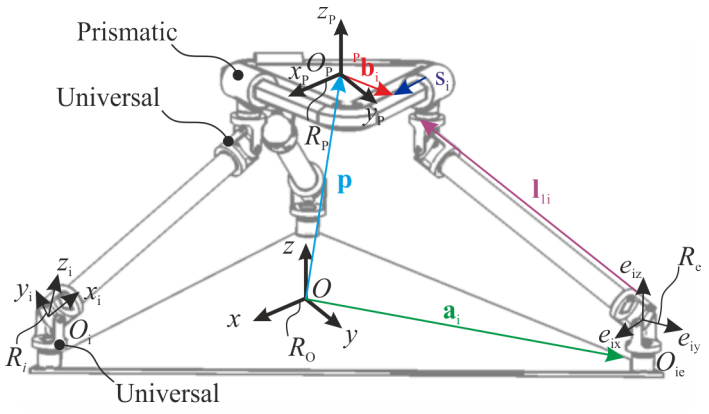

Fig. 49: Vector loop of UUP-PKS

the end-effector are known:

$$\mathbf{w}_{1i} = \mathbf{w}_{4i} = \mathbf{s}_{0i} = \mathbf{R}_{zi} \cdot \begin{pmatrix} 0 \\ 1 \\ 0 \end{pmatrix}.$$

Based on the vector loop equation,

$$\mathbf{p} = \mathbf{a}_i + l_1 \mathbf{l}_{10i} + s_i \mathbf{s}_{0i} - \mathbf{b}_i, \tag{106}$$

the known components are replaced by

$$\mathbf{g}_i = \mathbf{p} - \mathbf{a}_i + \mathbf{b}_i. \tag{107}$$

It follows Eq. (108):

$$\mathbf{g}_i - s_i \mathbf{s}_{0i} = l_1 \mathbf{l}_{10i}, \tag{108}$$

which is squared and solved for s_i:

$$s_i = \mathbf{s}_{0i}^T \mathbf{g}_i \pm \sqrt{(\mathbf{s}_{0i}^T \mathbf{g}_i)^2 - \mathbf{g}_i^T \mathbf{g}_i + l_1^2}. \tag{109}$$

The unknown unit vector of link 1 can be calculated:

$$\mathbf{l}_{10i} = \begin{pmatrix} l_{10xi} \\ l_{10yi} \\ l_{10zi} \end{pmatrix} = \frac{\mathbf{g}_i - s_i \mathbf{s}_{0i}}{l_1}. \tag{110}$$

Three transformations are necessary to determine the driving angle θ_{1i}. The unit vector of link 1 can be written as follows:

$$\mathbf{l}_{10i} = \mathbf{R}_{zi} \begin{pmatrix} \cos\theta_{1i} & 0 & sin\theta_{1i} \\ 0 & 1 & 0 \\ -sin\theta_{1i} & 0 & \cos\theta_{1i} \end{pmatrix} \begin{pmatrix} 1 & 0 & 0 \\ 0 & \cos\theta_{2i} & -sin\theta_{2i} \\ 0 & sin\theta_{2i} & \cos\theta_{2i} \end{pmatrix} \begin{pmatrix} 0 \\ 0 \\ 1 \end{pmatrix}. \tag{111}$$

This leads to three equations with two unknowns (θ_{1i} and θ_{2i}):

$$\begin{aligned} \mathbf{i} \quad & l_{10xi} = sin\varphi_i sin\theta_{2i} + \cos\varphi_i sin\theta_{1i} \cos\theta_{2i} \\ \mathbf{ii} \quad & l_{10yi} = -\cos\varphi_i sin\theta_{2i} + sin\varphi_i sin\theta_{1i} \cos\theta_{2i} \\ \mathbf{iii} \quad & l_{10zi} = \cos\theta_{1i} \cos\theta_{2i} \end{aligned} \tag{112}$$

Solving now Eq. (112) for θ_{1i}:

$$\theta_{1i} = arctan\left(\frac{l_{10xi} + \tan\varphi_i \cdot l_{10yi}}{(sin\varphi_i \tan\varphi_i + \cos\varphi_i) \cdot l_{10zi}}\right). \tag{113}$$

Finally, the unit vector of the second universal joint axis $\mathbf{w}_{2i}$ is calculated:

$$\mathbf{w}_{2i} = \mathbf{l}_{10i} \times \mathbf{s}_{0i}. \tag{114}$$

Jacobian matrix

Derivating Eq. (106) with respect to time leads to:

$$\dot{\mathbf{p}} = l_1(\boldsymbol{\omega}_{1i} \times \mathbf{l}_{10i} + \boldsymbol{\omega}_{2i} \times \mathbf{l}_{10i}) + \dot{s}_i\mathbf{s}_{0i}, \tag{115}$$

with $\boldsymbol{\omega}_{1i}$, $\boldsymbol{\omega}_{2i}$ = angular velocity vectors of link 1 of limb i. Dot-multiplying Eq. (115) with $\mathbf{w}_{2i}^T$ ($\boldsymbol{\omega}_{1i} = \dot{\theta}_{1i}\mathbf{w}_{1i}$) and solving for $\dot{\theta}_{1i}$:

$$\dot{\theta}_{1i} = \frac{\mathbf{w}_{2i}^T}{l_1\mathbf{w}_{2i}^T(\mathbf{w}_{1i} \times \mathbf{l}_{10})} \cdot \dot{\mathbf{p}} = \mathbf{J}_{(i,:)} \cdot \dot{\mathbf{p}}. \tag{116}$$

Finally, the Jacobian can be written as follows:

$$\dot{\mathbf{q}} = \dot{\boldsymbol{\theta}}_\mathbf{1} = \begin{pmatrix} \mathbf{J}_{(1,:)} \\ \mathbf{J}_{(2,:)} \\ \mathbf{J}_{(3,:)} \end{pmatrix} \cdot \dot{\mathbf{p}}. \tag{117}$$

7 URC

A universal joint, a revolute joint and one cylindrical joint form the kinematic chain of the URC-PKS. The first universal joint axis $\mathbf{w}_{1i}$ and the cylindrical joint axis $\mathbf{s}_{0i}$ are parallel to each other, whereas the other rotational axes are parallel as well.

$$\mathbf{w}_{1i} = \mathbf{s}_{0i}; \qquad \mathbf{w}_{2i} = \mathbf{w}_{3i}.$$

The structure is analyzed in [Di 04]. However, [KG05] could find a mistake which was finally revised in [Di 06]. Furthermore, the calculation procedure for inverse kinematics and Jacobian matrix is documented in [Cha13].

8 UCR

No analysis of the UCR-PKS can be found in literature so far. Each limb consists of a universal joint (U), a cylindrical joint (C) and a revolute joint (R). The first universal joint axis and the revolute joint axis are parallel to each other, whereas the cylindrical joint axis and the second universal joint axis are parallel as well:

$$\mathbf{w}_{1i} = \mathbf{w}_{4i}; \qquad \mathbf{w}_{2i} = \mathbf{w}_{3i} = \mathbf{s}_{0i}.$$

Inverse kinematics

Based on the vector loop equation,

$$\mathbf{p} = \mathbf{a}_i + l_1\mathbf{l}_{10i} + s_i\mathbf{s}_{0i} - \mathbf{b}_i, \tag{118}$$

the known components are replaced by

$$\mathbf{g}_i = \mathbf{p} - \mathbf{a}_i + \mathbf{b}_i. \tag{119}$$

This leads to

$$\mathbf{g}_i = l_1\mathbf{l}_{10i} + s_i\mathbf{s}_{0i}. \tag{120}$$

Eq. (120) is dot-multiplied by $\mathbf{s}_{0i}^T$:

$$s_i = \mathbf{s}_{0i}^T\mathbf{g}_i. \tag{121}$$

Furthermore, Eq. (120) is squared and solved for s_i:

$$\mathbf{g}_i^T\mathbf{g}_i - 2s_i\mathbf{s}_{0i}^T\mathbf{g}_i + s_i^2 - l_1^2 = 0, \tag{122}$$

$$s_i = \mathbf{s}_{0i}^T\mathbf{g}_i + \sqrt{(\mathbf{s}_{0i}^T\mathbf{g}_i)^2 - \mathbf{g}_i^T\mathbf{g}_i + l_1^2}. \tag{123}$$

By inserting Eq. (121), Eq. (123) is simplified:

$$s_i = \sqrt{\mathbf{g}_i^T\mathbf{g}_i - l_1^2}. \tag{124}$$

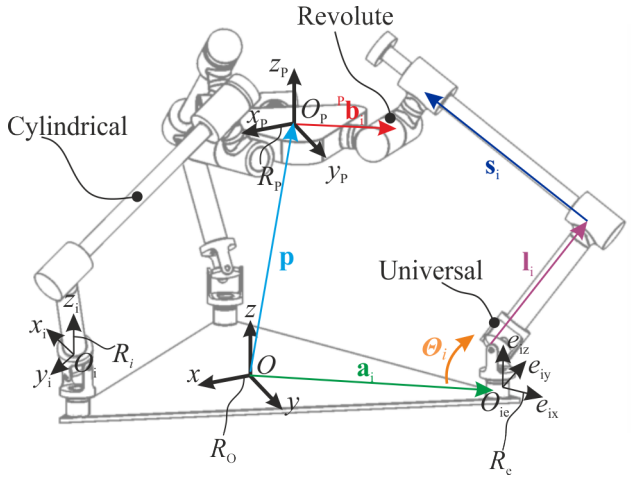

Fig. 50: Vector loop of UCR-PKS

The unit vector of link i and the unit vector of the cylindrical joint axis are calculated based on known vector transformations:

$$\begin{aligned}\mathbf{l}_{10i} &= \begin{pmatrix}\cos(\varphi_i) & -\sin(\varphi_i) & 0\\ \sin(\varphi_i) & \cos(\varphi_i) & 0\\ 0 & 0 & 1\end{pmatrix}\begin{pmatrix}\cos(\theta_{1i}) & 0 & \sin(\theta_{1i})\\ 0 & 1 & 0\\ -\sin(\theta_{1i}) & 0 & \cos(\theta_{1i})\end{pmatrix}\begin{pmatrix}1 & 0 & 0\\ 0 & \cos(\theta_{2i}) & -\sin(\theta_{2i})\\ 0 & \sin(\theta_{2i}) & \cos(\theta_{2i})\end{pmatrix}\begin{pmatrix}0\\0\\1\end{pmatrix}\\ &= \begin{pmatrix}\sin(\theta_{1i})\cos(\theta_{2i})\cos(\varphi_i)+\sin(\theta_{2i})\sin(\varphi_i)\\ \sin(\theta_{1i})\cos(\theta_{2i})\sin(\varphi_i)-\sin(\theta_{2i})\cos(\varphi_i)\\ \cos(\theta_{1i})\cos(\theta_{2i})\end{pmatrix},\end{aligned} \tag{125}$$

$$\begin{aligned}\mathbf{s}_{0i} &= -\begin{pmatrix}\cos(\varphi_i) & -\sin(\varphi_i) & 0\\ \sin(\varphi_i) & \cos(\varphi_i) & 0\\ 0 & 0 & 1\end{pmatrix}\begin{pmatrix}\cos(\theta_{1i}) & 0 & \sin(\theta_{1i})\\ 0 & 1 & 0\\ -\sin(\theta_{1i}) & 0 & \cos(\theta_{1i})\end{pmatrix}\begin{pmatrix}1\\0\\0\end{pmatrix}\\ &= \begin{pmatrix}-\cos(\theta_{1i})\cos(\varphi_i)\\ -\cos(\theta_{1i})\sin(\varphi_i)\\ \sin(\theta_{1i})\end{pmatrix}.\end{aligned} \tag{126}$$

It yields with Eq. (121):

$$s_i = -\cos(\theta_{1i})\left(\cos(\varphi_i)g_x+\sin(\varphi_i)g_y\right)+\sin(\theta_{1i})g_z, \tag{127}$$

$$\sin(\theta_{1i}) = \frac{1}{g_z}\left(s_i+\cos(\theta_{1i})\cdot A\right), \tag{128}$$

with $A = \cos(\varphi_i)g_x+\sin(\varphi_i)g_y$.

Finally, Eq. (128) is inserted in Eq. (120) and solved separately for $\cos(\theta_{1i})$:

$$\cos(\theta_{1i}) = \frac{-2s_i^2 AB - g_z^2\left(g_x - AB + g_y \tan(\varphi_i)\right)}{-2s_i B\left(g_z^2 - A^2\right)} \ldots \\ \pm \sqrt{\left(\frac{-2s_i^2 AB - g_z^2\left(g_x - AB + g_y \tan(\varphi_i)\right)}{-2s_i B\left(g_z^2 + A^2\right)}\right)^2 + \frac{g_z^2 - s_i^2}{g_z^2 + A^2}}, \tag{129}$$

with $B = \sin(\varphi_i)\tan(\varphi_i) + \cos(\varphi_i)$.

Jacobian matrix

The time-derivative of Eq. (118) reads as follows:

$$\dot{\mathbf{p}} = l_1(\boldsymbol{\omega}_{1i} \times \mathbf{l}_{10i}) + \dot{s}_i \mathbf{s}_{0i}, \tag{130}$$

with $\boldsymbol{\omega}_{1i}$ = angular velocity vector of link 1 of limb i. Dot-multiplying Eq. (130) with $\mathbf{s}_{0i}^T$ ($\boldsymbol{\omega}_{1i} = \dot{\theta}_{1i}\mathbf{w}_{1i}$) yields:

$$\mathbf{s}_{0i}^T \dot{\mathbf{p}} = l_1 \dot{\theta}_{1i} \mathbf{s}_{0i}^T (\boldsymbol{\omega}_{1i} \times \mathbf{l}_{10i}) + \dot{s}_i, \tag{131}$$

with $\mathbf{w}_{1i} = \mathbf{R}_{zi} \cdot \begin{pmatrix} 1 \\ 0 \\ 0 \end{pmatrix}$.

$\dot{s}_i$ is calculated by derivating Eq. (124) with respect to time:

$$\dot{s}_i = \frac{1}{\sqrt{\mathbf{g}_i^T \mathbf{g}_i - l_1^2}} \mathbf{g}_i^T \dot{\mathbf{p}}. \tag{132}$$

It is

$$\mathbf{s}_{0i}^T (\boldsymbol{\omega}_{1i} \times \mathbf{l}_{10i}) = -\cos(\theta_{2i}). \tag{133}$$

Solving Eq. (131) for $\dot{\theta}_{1i}$ by inserting Eq. (133):

$$\dot{\theta}_{1i} = \frac{1}{-l_{1i}\cos\theta_{2i}} \left(\mathbf{s}_{0i}^T - \frac{1}{\sqrt{\mathbf{g}_i^T \mathbf{g}_i - l_1^2}} \mathbf{g}_i^T \right) \dot{\mathbf{p}} = \mathbf{J}_{(i,:)} \cdot \dot{\mathbf{p}}. \tag{134}$$

Finally, the Jacobian can be written as follows:

$$\dot{\mathbf{q}} = \dot{\boldsymbol{\theta}}_\mathbf{1} = \begin{pmatrix} \mathbf{J}_{(1,:)} \\ \mathbf{J}_{(2,:)} \\ \mathbf{J}_{(3,:)} \end{pmatrix} \cdot \dot{\mathbf{p}}. \tag{135}$$

9 UPU

A variety of scientific articles deals with the UPU-PKS, including [Che11; HKK02; CP13; DP99; HKK02; QFG12; TJ00; TJ01; TJ02; Tsa96; WH11; WSP02]. The complete position and velocity analysis is referred to [TJ00; TJ01; TJ02]. Each of the three limbs has an actuated prismatic joint and two Cardan joints, which connect the kinematic chain with the end-effector and the frame. The outer and the inner rotational axes respectively of the universal joints are parallel to each other.

$$\mathbf{w}_{1i} = \mathbf{w}_{4i}, \qquad \mathbf{w}_{2i} = \mathbf{w}_{3i}.$$

Fig. 51 shows the vector loop and the inertia properties for the following described inverse dynamics analysis.

Inverse dynamics

The angular velocity vector of limb i is:

$$\boldsymbol{\omega}_{\mathbf{1}i} = \mathbf{s}_{0i} \times \frac{1}{s_i} \left(\dot{\mathbf{p}} - s_i \mathbf{s}_{0i} \right). \tag{136}$$

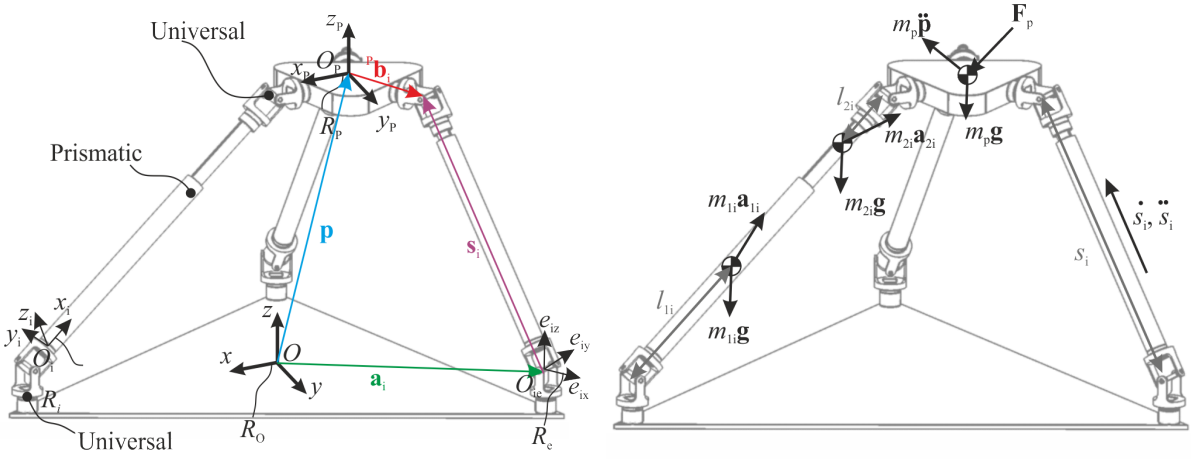

(a) Vector loop **(b)** Dynamic forces

Fig. 51: Vector loop and inertia properties of UPU-PKS

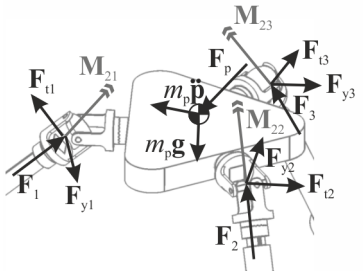

Fig. 52: Static equilibrium of forces/moments at the end-effector of UPU-PKS

The acceleration of the prismatic joint follows from the second time-derivative of the vector loop equation:

$$\ddot{s}_i = \mathbf{s}_{0i}^T \ddot{\mathbf{p}} + s_i \boldsymbol{\omega}_{1i}^T \boldsymbol{\omega}_{1i}, \tag{137}$$

and subsequently, the angular acceleration vector of limb i:

$$\dot{\boldsymbol{\omega}}_{1i} = \mathbf{s}_{0i} \times \left(\frac{1}{s_i} \left(\ddot{\mathbf{p}} - 2\dot{s}_i \left(\boldsymbol{\omega}_{1i} \times \mathbf{s}_{0i} \right) \right) \right). \tag{138}$$

The approach to calculate the required actuator forces is similar to the one of the RPC-PKS, cf. [PC15].

Since universal joints transfer torques only about the axis perpendicular to both joint axes, the axes of moment transmission for the UPU-PKS at the frame and end-effector are:

$$\mathbf{n}_{1i} = \frac{\mathbf{w}_{2i} \times \mathbf{w}_{1i}}{|\mathbf{w}_{2i} \times \mathbf{w}_{1i}|}, \tag{139}$$

$$\mathbf{n}_{2i} = -\frac{\mathbf{w}_{2i} \times \mathbf{w}_{1i}}{|\mathbf{w}_{2i} \times \mathbf{w}_{1i}|}. \tag{140}$$

Here, the vector $\mathbf{F}_{int}$ of internal forces and moments is (cf. Fig. 52):

$$\mathbf{F}_{int} = \begin{pmatrix} \mathbf{F}^T & \mathbf{F}_t^T & \mathbf{F}_y^T & \mathbf{M}_1^T & \mathbf{M}_2^T \end{pmatrix}_{1\times 15}^T, \tag{141}$$

with $\mathbf{F} = (F_1 F_2 F_3)^T$, $\mathbf{F}_t = (F_{t1} F_{t2} F_{t3})^T$, $\mathbf{F}_y = (F_{y1} F_{y2} F_{y3})^T$, $\mathbf{M}_1 = (M_{11} M_{12} M_{13})^T$ and $\mathbf{M}_2 = (M_{21} M_{22} M_{23})^T$. $\mathbf{F}$, $\mathbf{F}_t$, $\mathbf{F}_y$ and $\mathbf{M}_2$ are end-effector related quantities whereas the vector $\mathbf{M}_1$ summarizes the torque of each link transmitted at the frame-side Cardan joint.

Hence, the Jacobian of force transmission $\mathbf{J}_p$ is a 15x15 matrix:

$$\mathbf{J}_p = \begin{pmatrix} \mathbf{J}_{p1,(3x9)} & \mathbf{0}_{3x6} \\ \mathbf{J}_{p2,(3x9)} & \mathbf{J}_{p4,(3x6)} \\ \mathbf{J}_{p3,(3x9)} & \mathbf{J}_{p5,(3x6)} \end{pmatrix}, \tag{142}$$

with the following entries:

$$\begin{aligned} \mathbf{J}_{p1,(1,1:3)} &= \begin{pmatrix} 1 & 1 & 1 \end{pmatrix}, \\ \mathbf{J}_{p1,(2,4:6)} &= \begin{pmatrix} 1 & 1 & 1 \end{pmatrix}, \\ \mathbf{J}_{p1,(3,7:9)} &= \begin{pmatrix} 1 & 1 & 1 \end{pmatrix}, \end{aligned} \tag{143}$$

$$\begin{aligned} \mathbf{J}_{p2,(1,4:6)} &= \begin{pmatrix} -b_{1z} & -b_{2z} & -b_{3z} \end{pmatrix}, \\ \mathbf{J}_{p2,(1,7:9)} &= \begin{pmatrix} b_{1y} & b_{2y} & b_{3y} \end{pmatrix}, \\ \mathbf{J}_{p2,(2,1:3)} &= \begin{pmatrix} b_{1z} & b_{2z} & b_{3z} \end{pmatrix}, \\ \mathbf{J}_{p2,(2,7:9)} &= \begin{pmatrix} -b_{1x} & -b_{2x} & -b_{3x} \end{pmatrix}, \\ \mathbf{J}_{p2,(3,1:3)} &= \begin{pmatrix} -b_{1y} & -b_{2y} & -b_{3y} \end{pmatrix}, \\ \mathbf{J}_{p2,(3,4:6)} &= \begin{pmatrix} b_{1x} & b_{2x} & b_{3x} \end{pmatrix}, \end{aligned} \tag{144}$$

$$\begin{aligned} \mathbf{J}_{p3,(1,4)} &= s_1 \cdot s_{01z}, \\ \mathbf{J}_{p3,(1,7)} &= -s_1 \cdot s_{01y}, \\ \mathbf{J}_{p3,(2,1)} &= -s_1 \cdot s_{01z}, \\ \mathbf{J}_{p3,(2,7)} &= s_1 \cdot s_{01x}, \\ \mathbf{J}_{p3,(3,1)} &= s_1 \cdot s_{01y}, \\ \mathbf{J}_{p3,(3,4)} &= -s_1 \cdot s_{01x}. \end{aligned} \tag{145}$$

It is the same for row 4-6 for limb 2 and for row 7-9 for limb 3 with s_2, s_3 and $\mathbf{s}_{02}, \mathbf{s}_{03}$ respectively.

$$\begin{aligned} \mathbf{J}_{p4,(:,2)} &= \mathbf{n}_{21}, \\ \mathbf{J}_{p4,(:,4)} &= \mathbf{n}_{22}, \\ \mathbf{J}_{p4,(:,6)} &= \mathbf{n}_{23}, \end{aligned} \tag{146}$$

$$
\begin{aligned}
\mathbf{J}_{p5,(1:3,1)} &= \mathbf{n}_{11},\\
\mathbf{J}_{p5,(1:3,2)} &= -\mathbf{n}_{21},\\
\mathbf{J}_{p5,(4:6,3)} &= \mathbf{n}_{12},\\
\mathbf{J}_{p5,(4:6,4)} &= -\mathbf{n}_{22},\\
\mathbf{J}_{p5,(7:9,5)} &= \mathbf{n}_{13},\\
\mathbf{J}_{p5,(7:9,6)} &= -\mathbf{n}_{23}.
\end{aligned} \tag{147}
$$

Finally, the actuator forces can be calculated:

$$
f_{q,i} = \begin{pmatrix} F_i & F_{ti} & F_{yi} \end{pmatrix} \mathbf{s}_{0i} + m_{2i}\mathbf{g}^T\mathbf{s}_{0i} - m_{2i}\left(\ddot{s}_i\mathbf{s}_{0i}^T\mathbf{s}_{0i} - |\dot{\boldsymbol{\omega}}_{1i}|^2 \cdot (s_i - l_2)\right). \tag{148}
$$

10 CRU

The CRU-PKS has one cylindrical joint (C) ($\mathbf{s}_{0i}, \mathbf{w}_{1i}$), one revolute joint (R) ($\mathbf{w}_{2i}$) and one universal joint (U) ($\mathbf{w}_{3i}, \mathbf{w}_{4i}$) within each limb. The orientation of the joint axes is as follows:

$$
\mathbf{w}_{1i} = \mathbf{w}_{4i} = \mathbf{s}_{0i}; \qquad \mathbf{w}_{2i} = \mathbf{w}_{3i}.
$$

In [CCC13] a similar PKS is described and analyzed kinematically: the PRRU. But this PKS has due to the joint arrangements only one translational but two rotational DoF. The prismatic joint axes are assembled in parallel frame configuration.

10.1 Δ configuration

The vector loop of CRU$^{\Delta}$ is shown in Fig. 53.

Inverse kinematics

For the triangular frame configuration, the orientation of the joint axes is as follows:

$$
\mathbf{w}_{1i} = \mathbf{w}_{4i} = \mathbf{s}_{0i} = \mathbf{R}_{zi} \cdot \begin{pmatrix} 0 \\ 1 \\ 0 \end{pmatrix}; \qquad \mathbf{w}_{2i} = \mathbf{w}_{3i} = \mathbf{l}_{10i} \times \mathbf{w}_{1i}.
$$

The unit vector of link 1 (of limb i) depends on the revolute joint angle θ_{1i} of the cylindrical joint:

$$\mathbf{l}_{10i} = \mathbf{R}_{zi} \cdot \begin{pmatrix} \cos\theta_{1i} \\ 0 \\ \sin\theta_{1i} \end{pmatrix}$$

Based on the vector loop equation,

$$\mathbf{p} = \mathbf{a}_i + l_1\mathbf{l}_{10i} + l_2\mathbf{l}_{20i} + s_i\mathbf{s}_{0i} - \mathbf{b}_i, \tag{149}$$

the known components are replaced by

$$\mathbf{g}_i = \mathbf{p} - \mathbf{a}_i + \mathbf{b}_i. \tag{150}$$

Dot-multiplying Eq. (149) with $\mathbf{w}_{2i}^T$ ($\mathbf{w}_{2i}^T \perp \mathbf{l}_{10i}, \mathbf{l}_{20i}$) results in:

$$\mathbf{w}_{2i}^T\mathbf{g}_i = 0. \tag{151}$$

For further calculations the two vectors in Eq. (151) have to be expressed in the limb-side

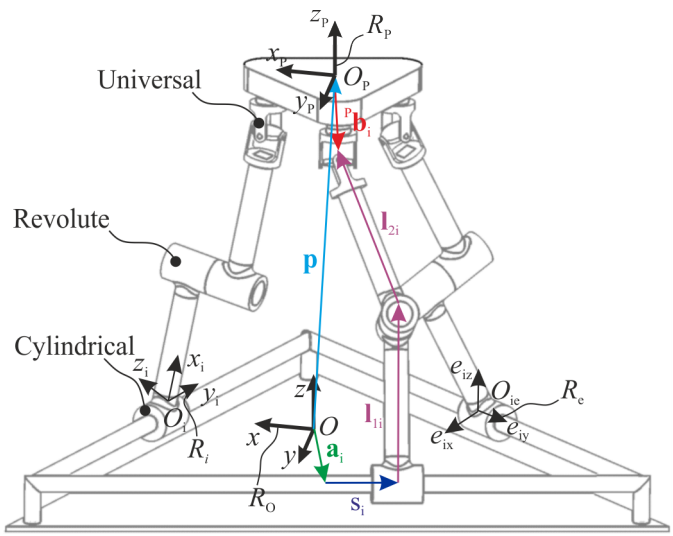

Fig. 53: Vector loop of CRU$^{\Delta}$-PKS

reference frame:

$$ {}^{e}\mathbf{w}_{2i} = \begin{pmatrix} -\cos\theta_{1i} \\ 0 \\ \sin\theta_{1i} \end{pmatrix}, \tag{152} $$

$$ {}^{e}\mathbf{g}_i = \begin{pmatrix} {}^{e}g_{ix} \\ {}^{e}g_{iy} \\ {}^{e}g_{iz} \end{pmatrix} = \mathbf{R}_{zi}^{-1}\mathbf{g}_i. \tag{153} $$

The following equation results by inserting Eq. (152) and Eq. (153) in Eq. (151):

$$ -\cos\theta_{1i} \cdot {}^{e}\, g_{ix} + \sin\theta_{1i} \cdot {}^{e}\, g_{iz} = 0. \tag{154} $$

Solving for $\tan\theta_{1i}$:

$$ \tan\theta_{1i} = \frac{{}^{e}g_{ix}}{{}^{e}g_{iz}}. \tag{155} $$

With θ_{1i} the vector $\mathbf{l}_{10}$ is known. Introducing a second auxiliary vector ($\mathbf{h}_i$) yields:

$$ \mathbf{h}_i = \mathbf{g}_i - l_1\mathbf{l}_{10i} = l_2\mathbf{l}_{20i} + s_i\mathbf{s}_{0i}. \tag{156} $$

Eq. (156) is squared and solved for s_i:

$$ s_i = \mathbf{s}_{0i}^T\mathbf{h} \pm \sqrt{(\mathbf{s}_{0i}^T\mathbf{h})^2 - \mathbf{h}^T\mathbf{h} + l_2^2}. \tag{157} $$

The unit vector of link 2 is calculated with the known values of θ_{1i} and s_i.

Jacobian matrix

Differentiating Eq. (149) with respect to time, dot-multiplying with $\mathbf{l}_{20i}$ and solving for $\dot{s}_i$:

$$ \dot{s}_i = \frac{\mathbf{l}_{20i}^T}{\mathbf{l}_{20i}^T\mathbf{s}_{i0}} \cdot \dot{\mathbf{p}} = \mathbf{J}_{(i,:)} \cdot \dot{\mathbf{p}}. \tag{158} $$

Finally, the Jacobian can be written as follows:

$$ \dot{\mathbf{q}} = \dot{\boldsymbol{s}} = \begin{pmatrix} \mathbf{J}_{(1,:)} \\ \mathbf{J}_{(2,:)} \\ \mathbf{J}_{(3,:)} \end{pmatrix} \cdot \dot{\mathbf{p}}. \tag{159} $$

10.2 ⋆ configuration

The calculation procedure for the inverse kinematics and the Jacobian matrix of the ⋆-shaped configuration is similar to the triangular configuration. Only the joint axes are defined in a different way and the vector $\mathbf{a}_i$ is equal to zero. It is:

$$\mathbf{w}_{1i} = \mathbf{w}_{4i} = \mathbf{s}_{0i} = \mathbf{R}_{zi} \cdot \mathbf{R}_{xi} \cdot \begin{pmatrix} 0 \\ 1 \\ 0 \end{pmatrix}; \qquad \mathbf{w}_{2i} = \mathbf{w}_{3i} = \mathbf{l}_{10i} \times \mathbf{w}_{1i},$$

and

$$\mathbf{l}_{10i} = \mathbf{R}_{zi} \cdot \mathbf{R}_{xi} \cdot \begin{pmatrix} \cos\theta_{1i} \\ 0 \\ \sin\theta_{1i} \end{pmatrix}.$$

The transfomation of the vector $\mathbf{g}$ in the limb-side reference frame is:

$${}^e\mathbf{g}_i = \begin{pmatrix} {}^e g_{ix} \\ {}^e g_{iy} \\ {}^e g_{iz} \end{pmatrix} = (\mathbf{R}_{zi} \cdot \mathbf{R}_{xi})^{-1} \mathbf{g}_i. \tag{160}$$

11 PUU

The PUU-PKS is described in [YQ05b; LX06a; LX06b; LXS11; TJ01; TJ02]. Both, the position and velocity analysis correspond to the approaches presented in [TJ01; TJ02]. For the star-shaped configuration, inverse kinematics and Jacobian matrix calculation are documented in [Cha13] as well. An approach for forward position analysis can be found in [ZBM04].

Pashkevich et al. [PCW08; PCW09] present for different translational parallel manipulators – among these the PUU-PKS in star-shaped configuration – stiffness modeling based on a lumped-parameter model. The stiffness properties of the considered parallel manipulators are compared. Further stiffness analysis of the PUU-PKS can be found in [LX08]. By using a genetic algorithm, Xu et al. [QY06] try to find an optimal design of the PUU-PKS with regard to its stiffness properties. A similar approach is done in [XL06c; XL06a], but here, a particle swarm optimization is used. The results are compared to those obtained by previous optimizations.

In [YQ05c] the PUU-PKS in orthogonal frame configuration is used for nanomanipulation as a compliant parallel micromanipulator with flexure hinges. Necessary calculation mod-

els are derived for optimization of the structure in order to obtain a large usable workspace. This study is followed in [XL06b] by a stiffness analysis. The developed analytical model is validated by finite element analysis.

Inverse dynamics

For the $\star$ and $\|$-shaped frame configuration the calculation procedure to determine the actuator forces is the same. In general, the approach described here is similar to the UPU-PKS inverse dynamics. Therefore, only the differences should be pointed out. The vector loop and the inertia properties are presented in Fig. 55 for the $\|$ frame configuration. The angular velocity vector of limb i is:

$$\boldsymbol{\omega}_{1i} = \mathbf{l}_{10i} \times \frac{1}{l_1} \left(\dot{\mathbf{p}} - s_i \mathbf{s}_{0i} \right). \tag{161}$$

The second time-derivative of the vector loop equation is dot-multiplied with $\mathbf{l}_{10i}^T$ in order to determine the acceleration of the prismatic joint:

$$\ddot{s}_i = \frac{\mathbf{l}_{10i}^T \ddot{\mathbf{p}} + l_1 \boldsymbol{\omega}_{1i}^T \boldsymbol{\omega}_{1i}}{l_{10i} \times \mathbf{s}_{0i}}. \tag{162}$$

It follows the angular acceleration vector of limb i:

$$\dot{\boldsymbol{\omega}}_{1i} = \mathbf{l}_{10i} \times \left(\frac{1}{l_1} \left(\ddot{\mathbf{p}} - \ddot{s}_i \mathbf{s}_{0i} \right) + \left(\boldsymbol{\omega}_{1i}^T \boldsymbol{\omega}_{1i} \right) \mathbf{l}_{10i} \right). \tag{163}$$

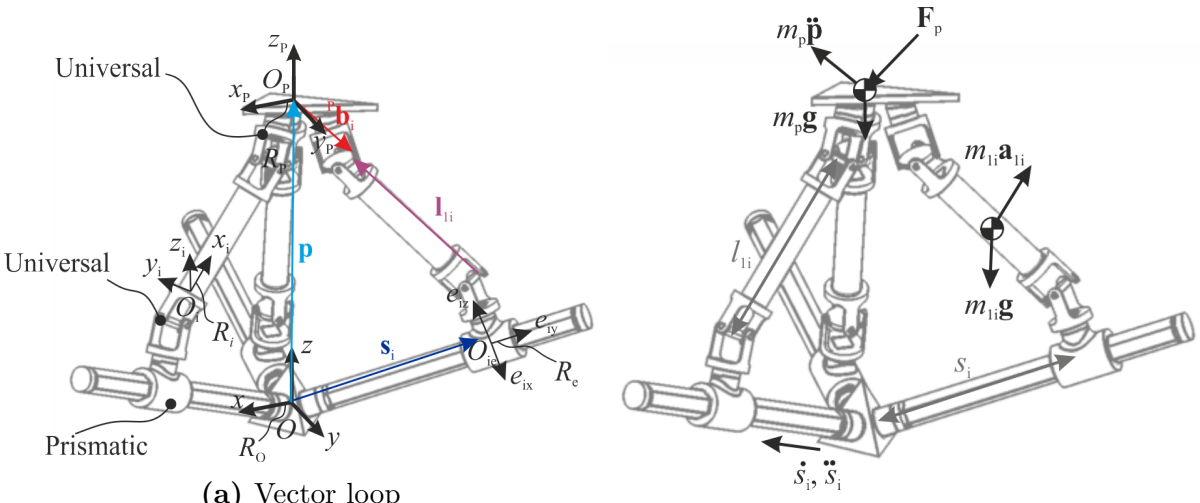

(a) Vector loop **(b)** Dynamic forces

Fig. 54: Vector loop and inertia properties of PUU*-PKS

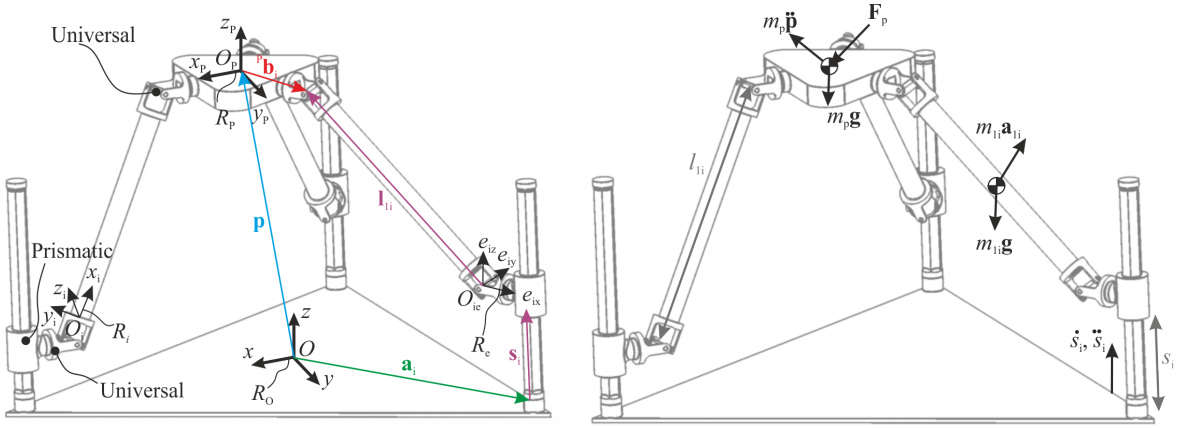

(a) Vector loop **(b)** Dynamic forces

Fig. 55: Vector loop and inertia properties of PUU$^{\|}$-PKS

Thereby, the acceleration of the center of gravity of each link can be calculated:

$$\mathbf{a}_{1i} = \ddot{s}_i \mathbf{s}_{0i} + \dot{\boldsymbol{\omega}}_{1i} \times \frac{l_1}{2}\mathbf{l}_{10i} + \boldsymbol{\omega}_{1i} \times \left(\boldsymbol{\omega}_{1i} \times \frac{l_1}{2}\mathbf{l}_{10i}\right). \tag{164}$$

Compared to $\mathbf{J}_p$ of UPU, only $\mathbf{J}_{p3}$ has to be adapted:

$$\begin{aligned}
\mathbf{J}_{p3,(1,4)} &= l_1 \cdot l_{101z}, \\
\mathbf{J}_{p3,(1,7)} &= -l_1 \cdot l_{101y}, \\
\mathbf{J}_{p3,(2,1)} &= -l_1 \cdot l_{101z}, \\
\mathbf{J}_{p3,(2,7)} &= l_1 \cdot l_{101x}, \\
\mathbf{J}_{p3,(3,1)} &= l_1 \cdot l_{101y}, \\
\mathbf{J}_{p3,(3,4)} &= -l_1 \cdot l_{101x}.
\end{aligned} \tag{165}$$

It is the same for row 4-6 for limb 2 and for row 7-9 for limb 3 with l_2, l_3 and l_{102}, l_{103} respectively.

The vector of external forces is:

$$\mathbf{F}_{ext} = \begin{pmatrix} m_p\mathbf{g} - m_p\ddot{\mathbf{p}} + \mathbf{F}_p \\ \mathbf{0}_{3x3} \\ \mathbf{temp}_1 \\ \mathbf{temp}_2 \\ \mathbf{temp}_3 \end{pmatrix}, \tag{166}$$

with

$$\mathbf{temp}_i = m_{1i}\left(\mathbf{a}_{1i} - \mathbf{g}\right) \times \frac{l_1}{2}\mathbf{l}_{10i} - \mathbf{I}_{tot,i}\dot{\boldsymbol{\omega}}_{1i} - \boldsymbol{\omega}_{1i} \times \left(\mathbf{I}_{tot,i}\boldsymbol{\omega}_{1i}\right), \tag{167}$$

based on the angular momentum about the first universal joint of each limb.

Here, the vector $\mathbf{F}_{int}$ of internal forces and moments is composed of the same entries as it is for UPU-PKS (cf. Fig. 52):

$$\mathbf{F}_{int} = \begin{pmatrix}\mathbf{F}^T & \mathbf{F}_t^T & \mathbf{F}_y^T & \mathbf{M}_1^T & \mathbf{M}_2^T\end{pmatrix}_{1\times 15}^T, \tag{168}$$

with $\mathbf{F} = \begin{pmatrix}F_1 & F_2 & F_3\end{pmatrix}^T$, $\mathbf{F}_t = \begin{pmatrix}F_{t1} & F_{t2} & F_{t3}\end{pmatrix}^T$, $\mathbf{F}_y = \begin{pmatrix}F_{y1} & F_{y2} & F_{y3}\end{pmatrix}^T$, $\mathbf{M}_1 = \begin{pmatrix}M_{11} & M_{12} & M_{13}\end{pmatrix}^T$ and $\mathbf{M}_2 = \begin{pmatrix}M_{21} & M_{22} & M_{23}\end{pmatrix}^T$. Finally, the actuator forces can be calculated:

$$f_{q,i} = \begin{pmatrix}F_i & F_{ti} & F_{yi}\end{pmatrix}\mathbf{s}_{0i} - m_{1i}\left(\mathbf{a}_{1i} - \mathbf{g}\right)^T\mathbf{s}_{0i}. \tag{169}$$

12 RUC

Each limb of the RUC-PKS consists of one revolute (R), one universal (U) and a cylindrical joint whereas the revolute joint axis $\mathbf{w}_{1i}$ and the first universal joint axis $\mathbf{w}_{2i}$ are parallel to each other. The second universal joint axis $\mathbf{w}_{3i}$ is parallel to the cylindrical joint axis $\mathbf{s}_{0i}$. The unit vectors of the axes can be calculated:

$$\mathbf{w}_{1i} = \mathbf{w}_{2i} = \mathbf{R}_{zi} \cdot \begin{pmatrix}-\cos\delta \\ 0 \\ \sin\delta\end{pmatrix}, \qquad \mathbf{w}_{3i} = \mathbf{s}_{0i} = \mathbf{R}_{zi} \cdot \begin{pmatrix}0 \\ 1 \\ 0\end{pmatrix}.$$

For the RUC-PKS no publication can be found. Therefore, the respective mathematical models have to be derived.

Inverse kinematics

Based on the vector loop equation (cf. Fig. 56),

$$\mathbf{p} = \mathbf{a}_i + l_1\mathbf{l}_{10i} + l_2\mathbf{l}_{20i} - s_i\mathbf{s}_{0i} - \mathbf{b}_i, \tag{170}$$

the known components are replaced by

$$\mathbf{g}_i = \mathbf{p} - \mathbf{a}_i + \mathbf{b}_i. \tag{171}$$

Dot-multiplying Eq. (170) with $\mathbf{w}_{1i}^T$ yields ($\mathbf{w}_{1i}^T \perp \mathbf{l}_{10i}, \mathbf{s}_{0i}$):

$$\frac{\mathbf{w}_{1i}^T \cdot \mathbf{g}_i}{l_2} = \mathbf{w}_{1i}^T \cdot \mathbf{l}_{20i}. \tag{172}$$

The unit vector of link 2 depends on the rotational angle θ_{4i} of the C-joint:

$$\mathbf{l}_{20i} = \mathbf{R}_{zi} \cdot \begin{pmatrix} \cos\theta_{4i} \\ 0 \\ \sin\theta_{4i} \end{pmatrix}. \tag{173}$$

Solving the right-hand side of Eq. (172) leads to:

$$\begin{aligned} \frac{\mathbf{w}_{1i}^T \cdot \mathbf{p}}{l_2} &= -\cos\delta\cos\theta_{4i} + \sin\delta\sin\theta_{4i} \\ &= A \cdot \cos\theta_{4i} + B \cdot \sin\theta_{4i} \\ &:= C_\alpha. \end{aligned} \tag{174}$$

The unknown value of θ_{4i} can be calculated by using Eq. (175) and (176) and thus the vector components of $\mathbf{l}_{20i}$ are known.

$$\sin\theta_{4i} = \frac{C_\alpha B \pm A\sqrt{A^2+B^2-C_\alpha}}{A^2+B^2}, \tag{175}$$

$$\cos\theta_{4i} = \frac{C_\alpha A \mp B\sqrt{A^2+B^2-C_\alpha}}{A^2+B^2}. \tag{176}$$

Dot-multiplying Eq. (170) with $\mathbf{s}_{0i}^T$ yields ($\mathbf{s}_{0i}^T \perp \mathbf{a}_i, \mathbf{b}_i, \mathbf{l}_{20i}$):

$$\mathbf{s}_{0i}^T\mathbf{p} = l_1\mathbf{s}_{0i}^T\mathbf{l}_{10i} - s_i. \tag{177}$$

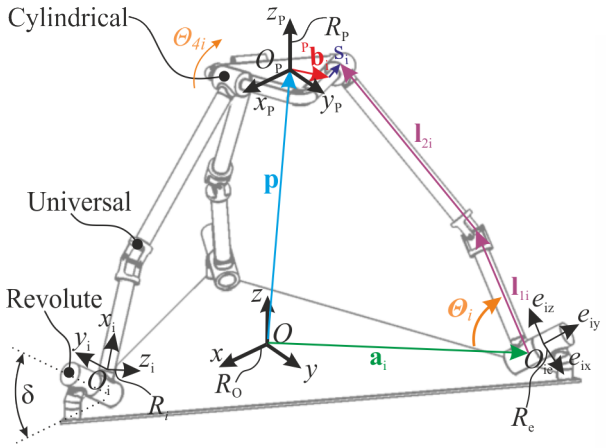

Fig. 56: Vector loop of RUC-PKS

The unit vector of link 1 of limb i is written as follows:

$$\mathbf{l}_{10i} = \mathbf{R}_{zi} \cdot \begin{pmatrix} \cos\delta & 0 & \sin\delta \\ 0 & 1 & 0 \\ -\sin\delta & 0 & \cos\delta \end{pmatrix} \begin{pmatrix} 0 \\ \cos\theta_{1i} \\ \sin\theta_{1i} \end{pmatrix}. \tag{178}$$

Solving Eq. (177) for $\cos\theta_{1i}$ yields:

$$\cos\theta_{1i} = \frac{\mathbf{s}_{0i}^T \cdot \mathbf{p} + s_i}{l_1}. \tag{179}$$

The displacement of the C-joint is still unknown, but can be calculated with the following two equations:

$$\mathbf{h}_i = \mathbf{g}_i - l_2\mathbf{l}_{20i} = l_1\mathbf{l}_{10i} - s_i\mathbf{s}_{0i}. \tag{180}$$

Eq. (180) is squared and solved for s_i:

$$s_i = -\mathbf{s}_{0i}^T\mathbf{h}_i \pm \sqrt{(\mathbf{s}_{0i}^T\mathbf{h}_i)^2 - \mathbf{h}_i^T\mathbf{h}_i + l_1^2}. \tag{181}$$

Jacobian matrix

The time-derivative of Eq. (170) reads as follows:

$$\dot{\mathbf{p}} = l_1(\boldsymbol{\omega}_{1i} \times \mathbf{l}_{10i}) + l_2(\boldsymbol{\omega}_{2i} \times \mathbf{l}_{20i}) - \dot{s}_i\mathbf{s}_{0i}, \tag{182}$$

with $\boldsymbol{\omega}_{1i}$, $\boldsymbol{\omega_{2i}}$ = angular velocity vectors of link 1 and 2 of limb i. Dot-multiplying Eq. (182) with $\mathbf{l}_{20i}^T$ ($\boldsymbol{\omega}_{1i} = \dot{\theta}_{1i}\mathbf{w}_{1i}$) and solving for $\dot{\theta}_{1i}$:

$$\dot{\theta}_{1i} = \frac{\mathbf{l}_{20i}^T}{l_1\mathbf{l}_{20i}^T(\mathbf{w}_{1i} \times \mathbf{l}_{10})} \cdot \dot{\mathbf{p}} = \mathbf{J}_{(i,:)} \cdot \dot{\mathbf{p}}. \tag{183}$$

Finally, the Jacobian can be written as follows:

$$\dot{\mathbf{q}} = \dot{\boldsymbol{\theta}} = \begin{pmatrix} \mathbf{J}_{(1,:)} \\ \mathbf{J}_{(2,:)} \\ \mathbf{J}_{(3,:)} \end{pmatrix} \cdot \dot{\mathbf{p}}. \tag{184}$$

13 CUR

The CUR-PKS consists of a cylindrical joint (C) fixed to the frame, a universal joint (U) in between two links and a revolute joint (R) connecting the limb with the end-effector. Ruggiu [Rug08] derived the forward and inverse kinematic equations for the orthogonal frame configuration of the CUR-PKS. Furthermore, he derived the Jacobian matrix and performed a singularity analysis based on joint axes orientations and the conditioning index. The rotational part of the cylindrical joints is actuated due to the fact that the motion equations for calculating the joint angles are fully-decoupled. However, Ruggiu mentioned that the actuation of the prismatic part of the cylindrical joint is more convenient from a technical point of view. Therefore, in this work the linear part of the cylindrical joint is actuated and all necessary calculation methods are derived according to this assumption.

Based on the geometrical conditions (cf. Tab. 3, p. 220), the cylindrical joint axis $\mathbf{w}_{1i}$ and the first universal joint axis $\mathbf{w}_{2i}$ have to be parallel; as well as the second universal joint axis $\mathbf{w}_{3i}$ and the revolute joint axis $\mathbf{w}_{4i}$:

$$\mathbf{w}_{1i} = \mathbf{w}_{2i} = \mathbf{s}_{0i}, \qquad \mathbf{w}_{3i} = \mathbf{w}_{4i}.$$

13.1 Δ configuration

In this case the revolute joint axes at the end-effector are inclined by the angle δ. Therefore, the unit vectors of the joint axes are written as follows:

$$\mathbf{w}_{1i} = \mathbf{w}_{2i} = \mathbf{s}_{0i} = \mathbf{R}_{zi} \cdot \begin{pmatrix} 0 \\ 1 \\ 0 \end{pmatrix}; \qquad \mathbf{w}_{3i} = \mathbf{w}_{4i} = \mathbf{R}_{zi} \cdot \begin{pmatrix} -\sin\delta \\ 0 \\ \cos\delta \end{pmatrix}.$$

The calculation of the inverse kinematics for the triangular frame configuration is similar to those of the $\star$-shaped frame configuration. Therefore, compare Section 13.3 for the vector loop equation and the unit vector of link 1. But in this case, Eq. (194) is written as follows:

$$\begin{aligned} \mathbf{w}_{4i}^T \mathbf{l}_{10i} &= -\sin\delta\cos\theta_{1i} + \cos\delta\sin\theta_{1i} \\ &= A \cdot \cos\theta_{1i} + B \cdot \sin\theta_{1i} \\ &:= C_\alpha. \end{aligned} \tag{185}$$

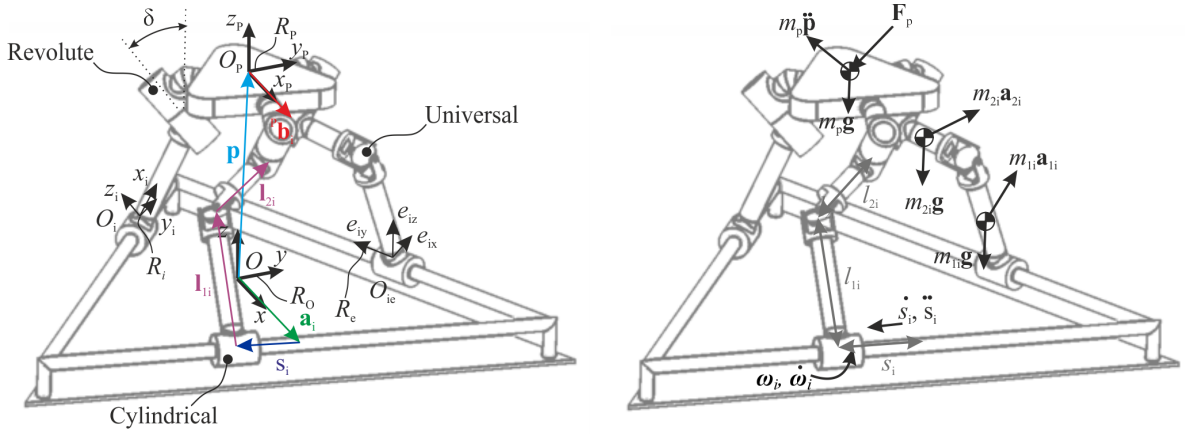

(a) Vector loop **(b)** Dynamic forces

Fig. 57: Vector loop and inertia properties of CUR$^{\Delta}$-PKS

Solving Eq. (185) with Eq. (175) and (176) results in θ_{1i}. In turn Eq. (195) and (198) can be used to calculate the displacement of the C-joint. The calculation of the Jacobian matrix is the same as for CUR*, as well as the procedure for the inverse dynamics.

13.2 $\parallel$ configuration

For the parallel frame configuration the motion axes of the prismatic and the revolute part of the cylindrical joint are separated, because the rotational axis is inclined by the angle δ:

$$\mathbf{w}_{1i} = \mathbf{w}_{2i} = \mathbf{R}_{zi} \cdot \begin{pmatrix} 1 & 0 & 0 \\ 0 & \cos\delta & -\sin\delta \\ 0 & \sin\delta & \cos\delta \end{pmatrix}, \qquad \mathbf{w}_{3i} = \mathbf{w}_{4i} = \mathbf{R}_{zi} \cdot \begin{pmatrix} 0 \\ 1 \\ 0 \end{pmatrix}, \qquad \mathbf{s}_{0i} = \begin{pmatrix} 0 \\ 0 \\ 1 \end{pmatrix}.$$

The calculation of the inverse kinematics solution and the Jacobian matrix is the same as for CUR*. The inverse dynamics follows the procedure for the $\star$-shaped configuration as well. Only the velocities and accelerations are calculated slightly different due to the

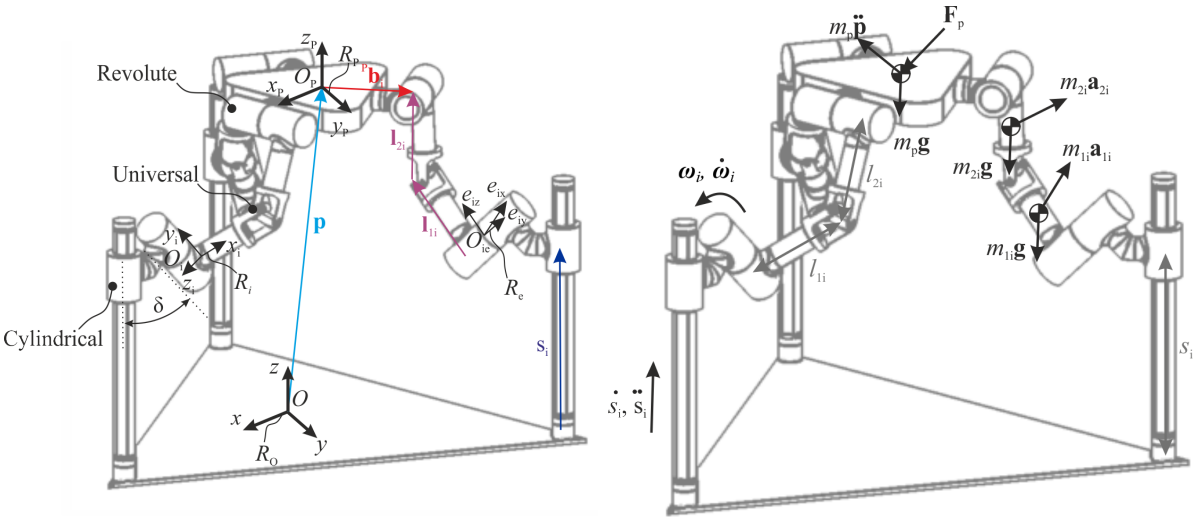

(a) Vector loop

(b) Dynamic forces

Fig. 58: Vector loop and inertia properties of CUR$^{\|}$-PKS

inclined revolute axis of the cylindrical joint:

$$\omega_{1i} = \frac{\frac{1}{l_1}\mathbf{l}_{20i}^T\dot{\mathbf{p}} - \dot{s}_i\mathbf{l}_{20i}^T\mathbf{s}_{0i}}{\mathbf{l}_{20i}^T(\mathbf{w}_{1i}\times\mathbf{l}_{10i})}, \tag{186}$$

$$\omega_{2i} = \frac{\frac{1}{l_2}\mathbf{l}_{10i}^T\dot{\mathbf{p}} - \dot{s}_i\mathbf{l}_{10i}^T\mathbf{s}_{0i}}{\mathbf{l}_{10i}^T(\mathbf{w}_{4i}\times\mathbf{l}_{20i})}, \tag{187}$$

$$\dot{\omega}_{1i} = \frac{\frac{1}{l_1}\left(\mathbf{w}_{4i}^T\ddot{\mathbf{p}} + l_1\left(\boldsymbol{\omega}_{1i}^T\boldsymbol{\omega}_{1i}\right)\mathbf{w}_{4i}^T\mathbf{l}_{10i}\right)}{\mathbf{w}_{4i}^T(\mathbf{w}_{1i}\times\mathbf{l}_{10i})}, \tag{188}$$

$$\ddot{s}_i = \frac{\mathbf{l}_{20i}^T\ddot{\mathbf{p}} - l_1\mathbf{l}_{20i}^T(\boldsymbol{\omega}_{1i}\times(\boldsymbol{\omega}_{1i}\times\mathbf{l}_{10i})) + \dot{\boldsymbol{\omega}}_{1i}\times\mathbf{l}_{10i} + l_2\left(\boldsymbol{\omega}_{2i}^T\boldsymbol{\omega}_{2i}\right)}{\mathbf{l}_{20i}^T\mathbf{s}_{0i}}, \tag{189}$$

$$\dot{\omega}_{2i} = \frac{\frac{1}{l_2}\left(\mathbf{l}_{10i}^T\ddot{\mathbf{p}} - \ddot{s}_i\mathbf{l}_{10i}^T\mathbf{s}_{0i} + l_1\left(\boldsymbol{\omega}_{1i}^T\boldsymbol{\omega}_{1i}\right) - l_2\mathbf{l}_{10i}^T(\boldsymbol{\omega}_{2i}\times(\boldsymbol{\omega}_{2i}\times\mathbf{l}_{20i}))\right)}{\mathbf{l}_{10i}^T(\mathbf{w}_{4i}\times\mathbf{l}_{20i})}. \tag{190}$$

Here, the axis of moment transmission is:

$$\mathbf{n}_{1i} = \mathbf{w}_{1i}\times\mathbf{w}_{4i}. \tag{191}$$

13.3 $\star$ configuration

Inverse kinematics

For the $\star$-shaped frame configuration of the CUR-PKS the unit vectors of the joint axes are as follows:

$$\mathbf{w}_{1i} = \mathbf{w}_{2i} = \mathbf{s}_{0i} = \mathbf{R}_{zi} \cdot \mathbf{R}_{xi} \cdot \begin{pmatrix} 0 \\ 1 \\ 0 \end{pmatrix}, \qquad \mathbf{w}_{3i} = \mathbf{w}_{4i} = \mathbf{R}_{zi} \cdot \begin{pmatrix} 1 \\ 0 \\ 0 \end{pmatrix}.$$

The unknown unit vector of link 1 depends on the rotational angle θ_{1i}, that is

$$\mathbf{l}_{10i} = \mathbf{R}_{zi} \cdot \begin{pmatrix} \cos\theta_{1i} \\ 0 \\ \sin\theta_{1i} \end{pmatrix}.$$

Based on the vector loop equation,

$$\mathbf{p} = s_i \mathbf{s}_{0i} + l_1 \mathbf{l}_{10i} + l_2 \mathbf{l}_{20i} - \mathbf{b}_i, \tag{192}$$

the known components are replaced by

$$\mathbf{g}_i = \mathbf{p} + \mathbf{b}_i. \tag{193}$$

Dot-multiplying Eq. (192) with $\mathbf{w}_{4i}^T$ yields ($\mathbf{w}_{4i}^T \perp \mathbf{b}_i \mathbf{l}_{20i}, \mathbf{s}_{0i}$):

$$\begin{aligned} \frac{\mathbf{w}_{4i}^T \cdot \mathbf{p}}{l_1} &= \mathbf{w}_{4i}^T \cdot \mathbf{l}_{10i} \\ &= \cos\theta_{1i}. \end{aligned} \tag{194}$$

The displacement of the C-joint is still unknown, so that the following auxiliary vector is introduced:

$$\mathbf{h}_i = \mathbf{g}_i - l_1 \mathbf{l}_{10i} = l_2 \mathbf{l}_{20i} + s_i \mathbf{s}_{0i}. \tag{195}$$

Eq. (195) is squared and solved for s_i:

$$s_i = \mathbf{s}_{0i}^T \mathbf{h} \pm \sqrt{(\mathbf{s}_{0i}^T \mathbf{h})^2 - \mathbf{h}^T \mathbf{h} + l_2^2}. \tag{196}$$

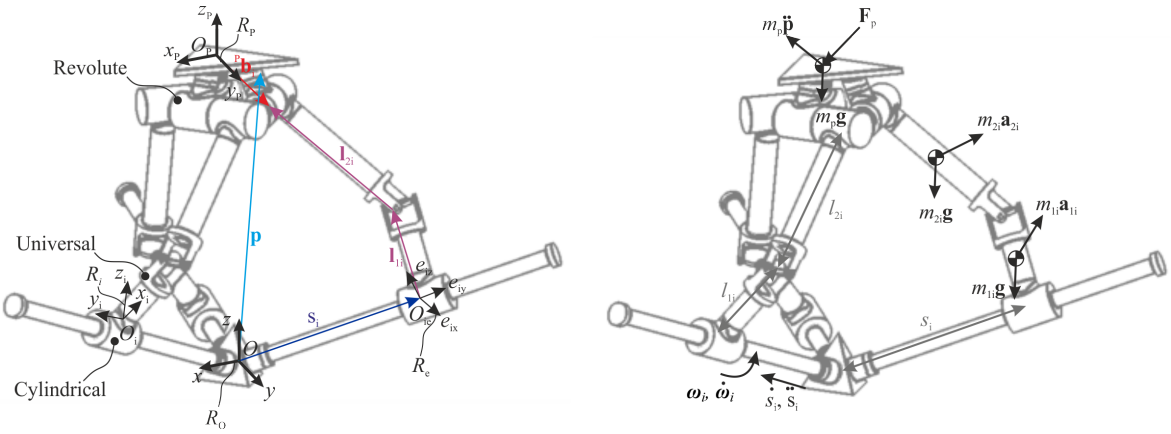

(a) Vector loop **(b)** Dynamic forces

Fig. 59: Vector loop and inertia properties of CUR*-PKS

At last, the still missing unit vector of link 2 is

$$l_{20i} = \frac{\mathbf{h}_i - s_i \mathbf{s}_{0i}}{l_2}. \tag{197}$$

Jacobian matrix

Differentiating Eq. (192) with respect to time yields:

$$\dot{\mathbf{p}} = \dot{s}_i \mathbf{s}_{0i} + l_1(\boldsymbol{\omega}_{1i} \times \mathbf{l}_{10i}) + l_2(\boldsymbol{\omega}_{2i} \times \mathbf{l}_{20i}), \tag{198}$$

with $\boldsymbol{\omega}_{1i}, \boldsymbol{\omega_{2i}}$ = angular velocity vectors of link 1 and 2 of limb i. Dot-multiplying Eq. (198) with $\mathbf{w}_{4i}^T$ ($\boldsymbol{\omega}_{1i} = \dot{\theta}_{1i}\mathbf{w}_{1i}$) and solving to $\dot{\theta}_{1i}$:

$$\dot{\theta}_{1i} = \frac{\mathbf{w}_{4i}^T}{l_1 \mathbf{w}_{4i}^T(\mathbf{w}_{1i} \times \mathbf{l}_{10i})} \cdot \dot{\mathbf{p}} = \mathbf{C}_{(i,:)} \cdot \dot{\mathbf{p}}. \tag{199}$$

Hence, the Jacobian matrix for rotational actuation is derived:

$$\dot{\mathbf{q}} = \dot{\boldsymbol{\theta}} = \begin{pmatrix} \mathbf{C}_{(1,:)} \\ \mathbf{C}_{(2,:)} \\ \mathbf{C}_{(3,:)} \end{pmatrix} \cdot \dot{\mathbf{p}}. \tag{200}$$

Dot-multiplying Eq. (198) with $\mathbf{l}_{20i}^T$ and solving for $\dot{s}_{0i}$:

$$\dot{s}_i = \frac{\mathbf{l}_{20i}^T - l_1 \mathbf{l}_{20i}^T \mathbf{s}_{0i} \times \mathbf{l}_{10i} \cdot \mathbf{C}_{(i,:)}}{\mathbf{l}_{20i}^T \mathbf{s}_{0i}} \cdot \dot{\mathbf{p}} = \mathbf{J}_{(i,:)} \cdot \dot{\mathbf{p}}. \tag{201}$$

Finally, the Jacobian can be written as follows:

$$\dot{\mathbf{q}} = \dot{\boldsymbol{s}} = \begin{pmatrix} \mathbf{J}_{(1,:)} \\ \mathbf{J}_{(2,:)} \\ \mathbf{J}_{(3,:)} \end{pmatrix} \cdot \dot{\mathbf{p}}. \tag{202}$$

Inverse dynamics

First, the velocities and accelerations of all joints and links must be calculated. Since ω_{1i} and $\dot{s}_i$ are already known from Eq. (199) and Eq. (201) respectively, the missing angular velocity ω_{2i} is determined as follows:

$$\omega_{2i} = \frac{\frac{1}{l_2}\mathbf{l}_{10i}^T\dot{\mathbf{p}}}{\mathbf{l}_{10i}^T\left(\mathbf{w}_{4i} \times \mathbf{l}_{20i}\right)}. \tag{203}$$

The accelerations of link 1, link 2 and the cylindrical joint are derived from the second time-derivative of Eq. (198):

$$\dot{\omega}_{1i} = \frac{\frac{1}{l_1}\left(\mathbf{w}_{4i}^T\ddot{\mathbf{p}} + l_1\left(\boldsymbol{\omega}_{1i}^T\boldsymbol{\omega}_{1i}\right)\mathbf{w}_{4i}^T\mathbf{l}_{10i}\right)}{\mathbf{w}_{4i}^T\left(\mathbf{s}_{0i} \times \mathbf{l}_{10i}\right)}, \tag{204}$$

$$\ddot{s}_i = \frac{\mathbf{l}_{20i}^T\ddot{\mathbf{p}} - l_1\mathbf{l}_{20i}^T\left(\boldsymbol{\omega}_{1i} \times \left(\boldsymbol{\omega}_{1i} \times \mathbf{l}_{10i}\right)\right) + \dot{\boldsymbol{\omega}}_{1i} \times \mathbf{l}_{10i} + l_2\left(\boldsymbol{\omega}_{2i}^T\boldsymbol{\omega}_{2i}\right)}{\mathbf{l}_{20i}^T\mathbf{s}_{0i}}, \tag{205}$$

$$\dot{\omega}_{2i} = \frac{\frac{1}{l_2}\left(\mathbf{l}_{10i}^T\ddot{\mathbf{p}} + l_1\left(\boldsymbol{\omega}_{1i}^T\boldsymbol{\omega}_{1i}\right) - l_2\mathbf{l}_{10i}^T\left(\boldsymbol{\omega}_{2i} \times \left(\boldsymbol{\omega}_{2i} \times \mathbf{l}_{20i}\right)\right)\right)}{\mathbf{l}_{10i}^T\left(\mathbf{w}_{4i} \times \mathbf{l}_{20i}\right)}. \tag{206}$$

The accelerations $\mathbf{a}_{1i}$ and $\mathbf{a}_{2i}$ of the centers of gravity of link 1 and link 2 are related to Eq. (35) and Eq. (36) of CRR-PKS.

To calculate the required actuator forces, Eq. (6.7) is taken into account. The vector of external forces is composed of the same entries as it is for CRR (cf. Eq. (44)). But here, $\mathbf{M}_2 = \left(\mathbf{M}_{21}^T\mathbf{M}_{22}^T\mathbf{M}_{23}^T\right)^T$ and $\mathbf{M}_1 = \left(\mathbf{M}_{11}\mathbf{M}_{12}\mathbf{M}_{13}\right)^T$ are:

$$\mathbf{M}_{2i} = m_{2i}\left(\mathbf{a}_{2i} - \mathbf{g}\right) \times \frac{l_2}{2}\mathbf{l}_{20i} - \mathbf{I}_{2tot,i}\dot{\boldsymbol{\omega}}_{2i} - \boldsymbol{\omega}_{2i} \times \left(\mathbf{I}_{2tot,i}\boldsymbol{\omega}_{2i}\right), \tag{207}$$

$$\mathbf{M}_{1i} = m_{1i}\left(\mathbf{a}_{1i} - \mathbf{g}\right) \times \frac{l_1}{2}\mathbf{l}_{10i} - \mathbf{I}_{1tot,i}\dot{\boldsymbol{\omega}}_{1i} - \left(\boldsymbol{\omega}_{1i} \times \left(\mathbf{I}_{1tot,i}\boldsymbol{\omega}_{1i}\right)\right). \tag{208}$$

The internal forces are the forces acting on the revolute joint, $\mathbf{F}_{ix}$, $\mathbf{F}_{iy}$ and $\mathbf{F}_{iz}$, the reaction forces at the universal joint, $\mathbf{F}_{uix}$, $\mathbf{F}_{uiy}$, $\mathbf{F}_{uiz}$, the torque about the axis perpendicular to link 2 and the revolute joint, $\mathbf{M}_{2it}$, the torque about axis of link 2, $\mathbf{M}_{2ix}$, the torque about the universal joint axis, $\mathbf{M}_{ui}$ and finally the two torques acting on the cylindrical joint,

$\mathbf{M}_{1i}$, $\mathbf{M}_{3i}$:

$$\mathbf{F}_{int} = \begin{pmatrix} \mathbf{F}_{ix}^T & \mathbf{F}_{iy}^T & \mathbf{F}_{iz}^T & \mathbf{M}_{2ix}^T & \mathbf{M}_{2it}^T & \mathbf{M}_{ui}^T & \mathbf{F}_{uix}^T & \mathbf{F}_{uiy}^T & \mathbf{F}_{uiz}^T & \mathbf{M}_{1i}^T & \mathbf{M}_{3i}^T \end{pmatrix}_{1\times 33}^T. \quad (209)$$

Hence, the Jacobian of force transmission $\mathbf{J}_p$ is a 33x33 matrix:

$$\mathbf{J}_p = \begin{pmatrix} \mathbf{J}_{p1,(3x9)} & \mathbf{0}_{3x6} & \mathbf{0}_{3x3} & \mathbf{0}_{3x15} \\ \mathbf{J}_{p2,(3x9)} & \mathbf{J}_{p4,(3x6)} & \mathbf{0}_{3x3} & \mathbf{0}_{3x15} \\ \mathbf{J}_{p3,(9x9)} & \mathbf{J}_{p5,(9x9)} & & \mathbf{0}_{3x15} \\ & \mathbf{J}_{p6,(9x33)} & & \\ \mathbf{0}_{9x15} & \mathbf{J}_{p7,(9x3)} & \mathbf{J}_{p8,(9x9)} & \mathbf{J}_{p9,(9x6)} \end{pmatrix}, \quad (210)$$

with the following entries:

$$\begin{aligned} \mathbf{J}_{p1,(1,1:3)} &= \begin{pmatrix} 1 & 1 & 1 \end{pmatrix}, \\ \mathbf{J}_{p1,(2,4:6)} &= \begin{pmatrix} 1 & 1 & 1 \end{pmatrix}, \\ \mathbf{J}_{p1,(3,7:9)} &= \begin{pmatrix} 1 & 1 & 1 \end{pmatrix}, \end{aligned} \quad (211)$$

$$\begin{aligned} \mathbf{J}_{p2,(1,4:6)} &= \begin{pmatrix} -b_{1z} & -b_{2z} & -b_{3z} \end{pmatrix}, \\ \mathbf{J}_{p2,(1,7:9)} &= \begin{pmatrix} b_{1y} & b_{2y} & b_{3y} \end{pmatrix}, \\ \mathbf{J}_{p2,(2,1:3)} &= \begin{pmatrix} b_{1z} & b_{2z} & b_{3z} \end{pmatrix}, \\ \mathbf{J}_{p2,(2,7:9)} &= \begin{pmatrix} -b_{1x} & -b_{2x} & -b_{3x} \end{pmatrix}, \\ \mathbf{J}_{p2,(3,1:3)} &= \begin{pmatrix} -b_{1y} & -b_{2y} & -b_{3y} \end{pmatrix}, \\ \mathbf{J}_{p2,(3,4:6)} &= \begin{pmatrix} b_{1x} & b_{2x} & b_{3x} \end{pmatrix}, \end{aligned} \quad (212)$$

$$\begin{aligned} \mathbf{J}_{p3,(1,4)} &= l_2 \cdot l_{201z}, \\ \mathbf{J}_{p3,(1,7)} &= -l_2 \cdot l_{201y}, \\ \mathbf{J}_{p3,(2,1)} &= -l_2 \cdot l_{201z}, \\ \mathbf{J}_{p3,(2,7)} &= l_2 \cdot l_{201x}, \\ \mathbf{J}_{p3,(3,1)} &= l_2 \cdot l_{201y}, \\ \mathbf{J}_{p3,(3,4)} &= -l_2 \cdot l_{201x}, \end{aligned} \quad (213)$$

It is the same for row 4-6 for limb 2 and for row 7-9 for limb 3 with $\mathbf{l}_{202}, \mathbf{l}_{203}$.

$$\begin{aligned}
&\mathbf{J}_{p4,(:,1)} = \mathbf{l}_{201},\\
&\mathbf{J}_{p4,(:,2)} = \mathbf{l}_{202},\\
&\mathbf{J}_{p4,(:,3)} = \mathbf{l}_{203},\\
&\mathbf{J}_{p4,(:,4)} = \mathbf{l}_{201} \times \mathbf{w}_{41},\\
&\mathbf{J}_{p4,(:,5)} = \mathbf{l}_{202} \times \mathbf{w}_{42},\\
&\mathbf{J}_{p4,(:,6)} = \mathbf{l}_{203} \times \mathbf{w}_{43},
\end{aligned} \tag{214}$$

$$\begin{aligned}
&\mathbf{J}_{p5,(1:3,1)} = \mathbf{l}_{201},\\
&\mathbf{J}_{p5,(1:3,4)} = \mathbf{l}_{201} \times \mathbf{w}_{41},\\
&\mathbf{J}_{p5,(1:3,7)} = -\mathbf{n}_{11},\\
&\mathbf{J}_{p5,(4:6,2)} = \mathbf{l}_{202},\\
&\mathbf{J}_{p5,(4:6,5)} = \mathbf{l}_{202} \times \mathbf{w}_{42},\\
&\mathbf{J}_{p5,(4:6,8)} = -\mathbf{n}_{12},\\
&\mathbf{J}_{p5,(7:9,3)} = \mathbf{l}_{203},\\
&\mathbf{J}_{p5,(7:9,6)} = \mathbf{l}_{203} \times \mathbf{w}_{43},\\
&\mathbf{J}_{p5,(7:9,9)} = -\mathbf{n}_{13},
\end{aligned} \tag{215}$$

$$\begin{aligned}
&\mathbf{J}_{p6,(1,1)} = 1,\\
&\mathbf{J}_{p6,(2,4)} = 1,\\
&\mathbf{J}_{p6,(3,7)} = 1,\\
&\mathbf{J}_{p6,(1,19)} = -1,\\
&\mathbf{J}_{p6,(2,22)} = -1,\\
&\mathbf{J}_{p6,(3,25)} = -1,
\end{aligned} \tag{216}$$

It is the same for row 4-6 for limb 2 and for row 7-9 for limb 3 at columns 2,5,8,20,23,26 and 3,6,9,21,24,26.

$$\begin{aligned}
&\mathbf{J}_{p7,(1:3,1)} = \mathbf{n}_{11},\\
&\mathbf{J}_{p7,(4:6,2)} = \mathbf{n}_{12},\\
&\mathbf{J}_{p7,(7:9,3)} = \mathbf{n}_{13},
\end{aligned} \tag{217}$$

$$
\begin{aligned}
\mathbf{J}_{p8,(1,4)} &= l_1 \cdot \mathbf{l}_{101z}, \\
\mathbf{J}_{p8,(1,7)} &= -l_1 \cdot \mathbf{l}_{101y}, \\
\mathbf{J}_{p8,(2,1)} &= -l_1 \cdot \mathbf{l}_{101z}, \\
\mathbf{J}_{p8,(2,7)} &= l_1 \cdot \mathbf{l}_{101x}, \\
\mathbf{J}_{p8,(3,1)} &= l_1 \cdot \mathbf{l}_{101y}, \\
\mathbf{J}_{p8,(3,4)} &= -l_1 \cdot \mathbf{l}_{101x}.
\end{aligned} \tag{218}
$$

It is the same for row 4-6 for limb 2 and for row 7-9 for limb 3 with $\mathbf{l}_{102}, \mathbf{l}_{103}$.

$$
\begin{aligned}
\mathbf{J}_{p9,(1:3,1)} &= -\mathbf{l}_{101}, \\
\mathbf{J}_{p9,(1:3,4)} &= \mathbf{l}_{101} \times \mathbf{n}_{11}, \\
\mathbf{J}_{p9,(4:6,2)} &= -\mathbf{l}_{102}, \\
\mathbf{J}_{p9,(4:6,5)} &= \mathbf{l}_{102} \times \mathbf{n}_{12}, \\
\mathbf{J}_{p9,(7:9,3)} &= -\mathbf{l}_{102}, \\
\mathbf{J}_{p9,(7:9,6)} &= \mathbf{l}_{102} \times \mathbf{n}_{13}.
\end{aligned} \tag{219}
$$

The actuator forces can be calculated in the following way:

$$
f_{q,i} = \mathbf{s}_{0i}^T \begin{pmatrix} F_{uix} \\ F_{uiy} \\ F_{uiz} \end{pmatrix} - \mathbf{s}_{0i}^T \left(m_{1i} \left(\mathbf{a}_{1i} - \mathbf{g} \right) \right). \tag{220}
$$

14 URU

A revolute joint (R) in each limb of the URU-PKS connects two links. The links are connected to the frame and the end-effector by two universal joints (U) (Fig. 60). All middle rotational axes are parallel to each other ($\mathbf{w}_{2i}, \mathbf{w}_{3i}, \mathbf{w}_{4i}$). It is the same for the remaining axes ($\mathbf{w}_{1i}, \mathbf{w}_{5i}$):

$$
\mathbf{w}_{1i} = \mathbf{w}_{5i} = \mathbf{R}_{zi} \cdot \begin{pmatrix} 0 \\ 1 \\ 0 \end{pmatrix}, \qquad \mathbf{w}_{2i} = \mathbf{w}_{3i} = \mathbf{w}_{4i}.
$$

More details for the calculation of the inverse kinematics and the Jacobian matrix can be found in [Fon14].

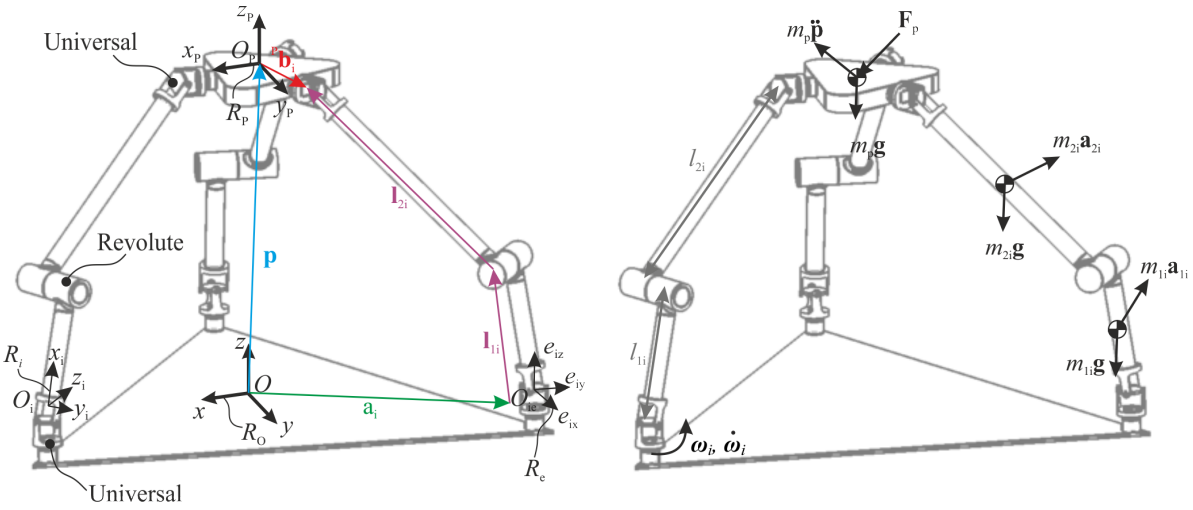

(a) Vector loop **(b)** Dynamic forces

Fig. 60: Vector loop and inertia properties of URU-PKS

15 UUR

The UUR-PKS consists of three limbs each with two universal joints (U) and one revolute joint (R) (Fig. 61). The joint axes are orientated as follows:

$$\mathbf{w}_{1i} = \mathbf{w}_{4i} = \mathbf{w}_{5i} = \mathbf{R}_{zi} \cdot \begin{pmatrix} 0 \\ 1 \\ 0 \end{pmatrix}; \qquad \mathbf{w}_{2i} = \mathbf{w}_{3i}.$$

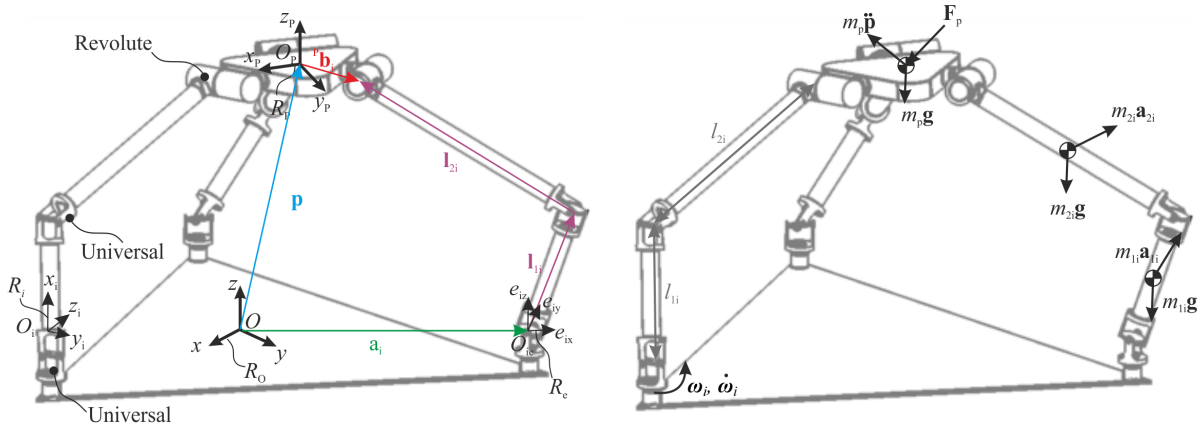

(a) Vector loop **(b)** Dynamic forces

Fig. 61: Vector loop and inertia properties of UUR-PKS

Inverse kinematics

The procedure to solve the inverse kinematics problem is similar to those of the RUU-PKS. Based on the closed-loop vector equation:

$$\mathbf{p} = \mathbf{a}_i + l_1\mathbf{l}_{10i} + l_2\mathbf{l}_{20i} - \mathbf{b}_i, \tag{221}$$

the known components are replaced by

$$\mathbf{g}_i = \mathbf{p} - \mathbf{a}_i + \mathbf{b}_i. \tag{222}$$

The coordinates of point B_i at the end-effector can be calculated with Eq. (223):

$$\mathbf{b}_i = \begin{pmatrix} b_{ix} \\ b_{iy} \\ b_{iz} \end{pmatrix} = \mathbf{R}_{zi}^{-1} \cdot \mathbf{p} + \begin{pmatrix} r_B - r_A \\ 0 \\ 0 \end{pmatrix}. \tag{223}$$

Eq. (224) expresses the coordinates of point B_i in another way:

$$\begin{pmatrix} b_{ix} \\ b_{iy} \\ b_{iz} \end{pmatrix} = \begin{pmatrix} -l_2\cos\theta_{5i} - l_1\sin\theta_{3i}\cos(\theta_{4i}+\theta_{5i}) \\ l_1\cos\theta_{3i} \\ l_2\sin\theta_{5i} + l_1\sin\theta_{3i}\sin(\theta_{4i}+\theta_{5i}) \end{pmatrix}. \tag{224}$$

Now, θ_{3i} is known:

$$\theta_{3i} = arccos\left(\frac{b_{iy}}{l_1}\right). \tag{225}$$

Using the cosine rule to solve for θ_{4i}:

$$\theta_{4i} = arccos\left(\frac{\|\mathbf{b}_i\|^2 - l_1^2 - l_2^2}{2l_1l_2\sin\theta_{3i}}\right), \tag{226}$$

and then for θ_{5i}:

$$\theta_{5i} = arctan\left(\frac{l_2b_{zi} + l_1b_{zi}\sin\theta_{3i}\cos\theta_{4i} + l_1b_{xi}\sin\theta_{3i}\sin\theta_{4i}}{-l_2b_{xi} - l_1b_{xi}\sin\theta_{3i}\cos\theta_{4i} + l_1b_{zi}\sin\theta_{3i}\sin\theta_{4i}}\right). \tag{227}$$

Hence, the unit vector of link 2 can be calculated:

$$\mathbf{l}_{20i} = \mathbf{R}_{zi} \cdot \begin{pmatrix} -\cos\theta_{5i} \\ 0 \\ \sin\theta_{5i} \end{pmatrix}, \tag{228}$$

and thus with Eq. (221) the unit vector of link 1. This vector is transferred to the limb-side reference frame to calculate the still missing angle θ_{1i}:

$$ {}^{e}\mathbf{l}_{10i} = \mathbf{R}_{zi}^{-1} \cdot \mathbf{l}_{10i} = \begin{pmatrix} \sin\theta_{1i}\cos\theta_{2i} \\ -\sin\theta_{2i} \\ \cos\theta_{1i}\cos\theta_{2i} \end{pmatrix}, \tag{229} $$

and it follows:

$$ \theta_{1i} = arctan\left(\frac{{}^{e}l_{10ix}}{{}^{e}l_{10iz}}\right). \tag{230} $$

Jacobian matrix

Differentiating Eq. (221) with respect to time yields:

$$ \dot{\mathbf{p}} = l_1(\boldsymbol{\omega}_{1i} \times \mathbf{l}_{10i}) + l_2(\boldsymbol{\omega}_{2i} \times \mathbf{l}_{20i}), \tag{231} $$

with $\boldsymbol{\omega}_{1i}$, $\boldsymbol{\omega_{2i}}$ = angular velocity vectors of link 1 and 2 of limb i. Dot-multiplying Eq. (231) with $\mathbf{l}_{10i}^T$ ($\boldsymbol{\omega}_{2i} = \dot{\theta}_{5i}\mathbf{w}_{5i}$) and solving for $\dot{\theta}_{5i}$

$$ \dot{\theta}_{5i} = \frac{\mathbf{l}_{10i}^T}{l_2\mathbf{l}_{10i}^T(\mathbf{w}_{5i} \times \mathbf{l}_{20i})} \cdot \dot{\mathbf{p}} = \mathbf{C}_{(i,:)} \cdot \dot{\mathbf{p}}. \tag{232} $$

Dot-multiplying Eq. (231) with $\mathbf{w}_{2i}^T$ ($\boldsymbol{\omega}_{1i} = \dot{\theta}_{1i}\mathbf{w}_{1i} + \dot{\theta}_{2i}\mathbf{w}_{2i}$), inserting $\mathbf{C}_{(i,:)}$ and solving for $\dot{\theta}_{1i}$:

$$ \dot{\theta}_{1i} = \frac{\mathbf{w}_{2i}^T - l_2((\mathbf{l}_{20i} \times \mathbf{w}_{2i})^T\mathbf{w}_{1i})^T \cdot \mathbf{C}_{(i,:)}^T}{l_1\mathbf{w}_{2i}^T(\mathbf{w}_{1i} \times \mathbf{l}_{10i})} \cdot \dot{\mathbf{p}} = \mathbf{J}_{(i,:)} \cdot \dot{\mathbf{p}}. \tag{233} $$

Finally, the Jacobian can be written as follows:

$$ \dot{\mathbf{q}} = \dot{\boldsymbol{\theta}}_1 = \begin{pmatrix} \mathbf{J}_{(1,:)} \\ \mathbf{J}_{(2,:)} \\ \mathbf{J}_{(3,:)} \end{pmatrix} \cdot \dot{\mathbf{p}}. \tag{234} $$

16 RUU

The RUU-PKS has one rotational joint (R) and to universal joints (U) within each limb (Fig. 62). The joint arrangement is as follows:

$$\mathbf{w}_{1i} = \mathbf{w}_{2i} = \mathbf{w}_{5i} = \mathbf{R}_{zi} \cdot \begin{pmatrix} 0 \\ 1 \\ 0 \end{pmatrix}; \qquad \mathbf{w}_{3i} = \mathbf{w}_{4i}.$$

The calculation of both, the inverse kinematics and the Jacobian matrix is revealed by [TJ02] and is documented as well by [Fon14]. [Di 01] presents a kinematic analysis to find all singular configurations including a geometrical interpretation. Furthermore, this PKS is part of a comparison study performed by [TJ01]. Considered evaluation criteria are the well-conditioned workspace, stiffness and inertia properties. For four 3-DoF translational parallel manipulators a performance index is determined. The results show that non of the architectures outperforms all others in all performance criteria. In contrast, a further comparison by [TJ02] shows that the RUU appears to be the best design among the four architectures. Moreover, [TJ02] derives the inverse kinematics and the Jacobian matrix. More in general, a forward position analysis for 3-DoF translational parallel manipulators is presented in [ZBM04]. The PKS is used in [WLF05] as a micro-dissection manipulator based on ultrasonic vibration. Further analysis is done by [TTH08] and [WW11] amongst others with regard to singularities and parameter variations for the workspace volume. The last known publication is from 2012, where [YWS12] gives equilibrium equations for forces and torques.

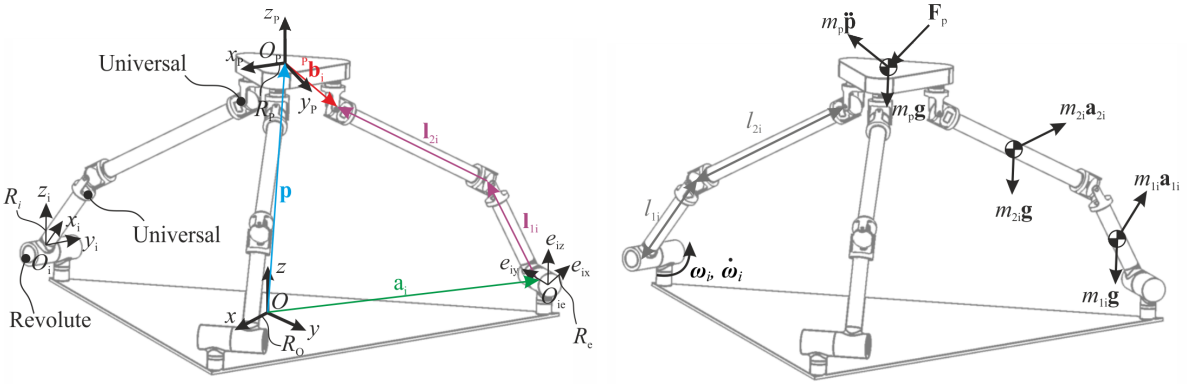

(a) Vector loop **(b)** Dynamic forces

Fig. 62: Vector loop and inertia properties of RUU-PKS

Inverse dynamics

If the vector loop equation is derivated, the angular velocity vectors of the links can be calculated:

$$\dot{\mathbf{p}} = l_1 \left(\boldsymbol{\omega}_{1i} \times \mathbf{l}_{10i}\right) + l_1 \left(\boldsymbol{\omega}_{2i} \times \mathbf{l}_{20i}\right), \tag{235}$$

$$\boldsymbol{\omega}_{2i} = \mathbf{l}_{20i} \times \left(\frac{1}{l_2}\left(\ddot{\mathbf{p}} - l_1 \left(\boldsymbol{\omega}_{1i} \times \mathbf{l}_{10i}\right)\right)\right). \tag{236}$$

Derivating Eq. (235) with respect to time and dot-multiplying with $\mathbf{l}_{20i}$ yields:

$$\dot{\boldsymbol{\omega}}_{1i} = \frac{\frac{1}{l_1}\left(\mathbf{l}_{20i}^T \ddot{\mathbf{p}} + l_2 \boldsymbol{\omega}_{2i}^T \boldsymbol{\omega}_{2i} + \mathbf{l}_{20i}^T \left(\boldsymbol{\omega}_{1i}^T \boldsymbol{\omega}_{1i}\right) \mathbf{l}_{10i}\right)}{\mathbf{l}_{20i}^T \left(\mathbf{w}_{1i} \times \mathbf{l}_{10i}\right)}. \tag{237}$$

Finally, the angular acceleration vector of link 2 can be calculated:

$$\dot{\boldsymbol{\omega}}_{2i} = \mathbf{l}_{20i} \times \left(\frac{1}{l_2}\left(\ddot{\mathbf{p}} + l_1 \left(\boldsymbol{\omega}_{1i}^T \boldsymbol{\omega}_{1i}\right)^T \mathbf{l}_{10i} - l_1 \left(\dot{\boldsymbol{\omega}}_{1i} \times \mathbf{l}_{10i}\right) - l_2 \left(\boldsymbol{\omega}_{2i}^T \mathbf{l}_{20i}\right) \boldsymbol{\omega}_{2i} + l_2 \left(\boldsymbol{\omega}_{2i}^T \boldsymbol{\omega}_{2i}\right) \mathbf{l}_{20i}\right)\right). \tag{238}$$

The axis of moment transmission at the end-effector and the accelerations vectors are:

$$\begin{aligned}
\mathbf{n}_{1i} &= \mathbf{w}_{1i} \times \mathbf{w}_{2i}, \\
\mathbf{a}_{1i} &= \dot{\boldsymbol{\omega}}_{1i} \times \frac{l_1}{2}\mathbf{l}_{10i} + \boldsymbol{\omega}_{1i} \times \left(\boldsymbol{\omega}_{1i} \times \frac{l_1}{2}\mathbf{l}_{10i}\right), \\
\mathbf{a}_{2i} &= 2\mathbf{a}_{1i} + \dot{\boldsymbol{\omega}}_{2i} \times \frac{l_2}{2}\mathbf{l}_{20i} + \boldsymbol{\omega}_{2i} \times \left(\boldsymbol{\omega}_{2i} \times \frac{l_2}{2}\mathbf{l}_{20i}\right).
\end{aligned} \tag{239}$$

The Jacobian of force transmission $\mathbf{J}_p$ is a 15x15 matrix:

$$\mathbf{J}_p = \begin{pmatrix} \mathbf{J}_{p1,(3x9)} & \mathbf{0}_{3x6} \\ \mathbf{J}_{p2,(3x9)} & \mathbf{J}_{p4,(3x6)} \\ \mathbf{J}_{p3,(9x9)} & \mathbf{J}_{p5,(9x6)} \end{pmatrix}, \tag{240}$$

with $\mathbf{J}_{p1,(3x9)}$ equal to Eq. (211), $\mathbf{J}_{p2,(3x9)}$ equal to Eq. (212) and $\mathbf{J}_{p3,(9x9)}$ equal to Eq. (213). $\mathbf{J}_{p4,(3x6)}$ and $\mathbf{J}_{p5,(9x6)}$ consist of the following entries:

$$\begin{aligned}
\mathbf{J}_{p4,(:,2)} &= \mathbf{n}_{11}, \\
\mathbf{J}_{p4,(:,4)} &= \mathbf{n}_{12}, \\
\mathbf{J}_{p4,(:,6)} &= \mathbf{n}_{13},
\end{aligned} \tag{241}$$

$$
\begin{aligned}
\mathbf{J}_{p5,(1:3,1)} &= \mathbf{n}_{11}, \\
\mathbf{J}_{p5,(1:3,2)} &= -\mathbf{n}_{11}, \\
\mathbf{J}_{p5,(4:6,3)} &= \mathbf{n}_{12}, \\
\mathbf{J}_{p5,(4:6,4)} &= -\mathbf{n}_{12}, \\
\mathbf{J}_{p5,(7:9,5)} &= \mathbf{n}_{13}, \\
\mathbf{J}_{p5,(7:9,6)} &= -\mathbf{n}_{13}.
\end{aligned} \tag{242}
$$

Here, the vector of internal forces and moments is:

$$
\mathbf{F}_{int} = \begin{pmatrix} \mathbf{F}_x^T & \mathbf{F}_y^T & \mathbf{F}_z^T & \mathbf{M}_2^T & \mathbf{M}_1^T \end{pmatrix}_{1\times 15}^T, \tag{243}
$$

with $\mathbf{F}_x = \begin{pmatrix} F_{x1} & F_{x2} & F_{x3} \end{pmatrix}^T$, $\mathbf{F}_y = \begin{pmatrix} F_{y1} & F_{y2} & F_{y3} \end{pmatrix}^T$, $\mathbf{F}_z = \begin{pmatrix} F_{z1} & F_{z2} & F_{z3} \end{pmatrix}^T$, $\mathbf{M}_2 = \begin{pmatrix} M_{21} & M_{22} & M_{23} \end{pmatrix}^T$ and $\mathbf{M}_1 = \begin{pmatrix} M_{11} & M_{12} & M_{13} \end{pmatrix}^T$. F_{xi}, F_{yi} and F_{zi} are the components of the force vector $\mathbf{F}_i$ transmitted from the limb i to the end-effector and vise versa. M_{2i} and M_{1i} are the torques transmitted by the second and first universal joint of limb i.

The vector of external forces is:

$$
\mathbf{F}_{ext} = \begin{pmatrix} m_p\mathbf{g} - m_p\ddot{\mathbf{p}} + \mathbf{F}_p \\ \mathbf{0}_{3x3} \\ \mathbf{temp}_1 \\ \mathbf{temp}_2 \\ \mathbf{temp}_3 \end{pmatrix}, \tag{244}
$$

with

$$
\mathbf{temp}_i = m_{2i}\left(\mathbf{a}_{2i} - \mathbf{g}\right) \times \frac{l_2}{2}\mathbf{l}_{20i} - \mathbf{I}_{2tot,i}\dot{\boldsymbol{\omega}}_{2i} - \boldsymbol{\omega}_{2i} \times \left(\mathbf{I}_{2tot,i}\boldsymbol{\omega}_{2i}\right), \tag{245}
$$

based on the angular momentum about the universal joint attached to the end-effector of each limb. Finally, the required actuation torque can be calculated:

$$
\tau_{q,i} = -\mathbf{w}_{1i}^T \left(\mathbf{n}_{1i}M_{1i} - m_{1i}\left(\mathbf{a}_{1i} - \mathbf{g}\right) \times \frac{l_1}{2}\mathbf{l}_{10i} + \mathbf{I}_{1tot,i}\dot{\boldsymbol{\omega}}_{1i} + \boldsymbol{\omega}_{1i} \times \left(\mathbf{I}_{1tot,i}\boldsymbol{\omega}_{1i}\right) + \mathbf{F}_{1i} \times l_1\mathbf{l}_{10i} \right), \tag{246}
$$

with

$$
\mathbf{F}_{1i} = -m_{2i}\left(\mathbf{a}_{2i} - \mathbf{g}\right) + \mathbf{F}_i. \tag{247}
$$

Index

Acceleration, 48
Acceleration capability, 78
Accuracy, 49
Actuators, 118–120
    Linear actuators, 119
    Rotary actuators, 118

Benchmark, 104
Bisection method, 99

Compliance ellipsoid, 77
Condition number, 72
Costs, 49
Coupling degree, 29, 70
Criteria, 36, 69–81

Dynamic manipulability ellipsoid, 78
Dynamic manipulability measure, 78
Dynamics, 64
    forward, 64
    inverse, 64

Energy supply, 49

Flexibility, 49
Forces, 48
Frame configurations, 38

Indices
    Conditioning index, 72, 103
    Deformation index, 77
    Dexterity index, 72, 89
    Error index, 75
    Isotropy index, 75, 103
    Manipulability index, 75, 103
    Payload index, 74, 103
    Sensitivity index, 76
    Singularity index, 74, 86, 103
    Stiffness index, 77
    Structural length index, 80
    Velocity index, 74, 103
Installation space, 48, 71
Inverse dynamics, 78

Jacobian, 63
Joint arrangements, 34
Joints, 115–118
    Cylindrical joints, 118
    Prsimatic joints, 117
    Revolute joints, 116
    Universal joints, 118

Kinematic condition, 72
Kinematics, 48, 63
    forward, 63
    inverse, 63

Manipulability ellipsoid, 74
Manipulability measure, 75
Manipulation tasks, 50
    handling, 50
    machine processing, 51
    pick & place, 53
    positioning, 51, 53
    surface treatment, 50
Monte Carlo Method, 99
Motion space, 48

Movability, 48

Operating space, 48, 71

Parallel robots, 9–12
  advantages, 10
  DELTA, 9, 13, 57
  Hexapod, 10
  PARAGRIP, 56
  Tricept, 11
  Tripod, 11
Performance charts, 104

Repeatability, 49
Requirements
  economical, 46
  functional, 45
  individual, 46
  main features, 46
  operational, 45
  psychological, 46
  technical, 46
Robot, 7
Robotic software, 13

Serial robots, 7–9, 12
  advantages, 7
  Hexapod, 57
  Horizontal jointed-arm, 8
  Portal robot, 8
  SCARA, 8, 13, 57
  Vertical jointed-arm robot, 7
Singularities, 103
Stiffness, 49, 64
Structural selection, 31
Structural synthesis, 23–29
  Displacement group theory, 27
  Screw-based approach, 24
  Single-opened-chain theory, 28
Structure groups, 33
Structures
  2R-2P
    CPR, 41, 241
    CRP, 41
    PCR, 41
    PRC, 248
    RCP, 40
    RPC, 41, 240
  3R-1P
    CRR, 40, 232
    RCR, 39
    RRC, 39, 229
  4R-1P
    CRU, 260
    CUR, 269
    PUU, 263
    RCU, 41
    RUC, 41, 266
    UCR, 41, 254
    UPU, 41, 257
    URC, 41, 253
    UUP, 41, 251
  5R
    RUU, 42, 281
    URU, 42, 277
    UUR, 42, 278
Swiftness, 78

Tasks, 50–57
  Guidance, 54, 138
  Pick & place, 53, 132
  Positioning, 53
Transmission quality, 73

Velocity, 48

Working range, 47, 71
Workspace, 46, 70
  Analysis, 98–101